TECHNISCHE UNIVERSITÄT DORTMUND

Electronic and spin control in functional oxide heterostructures

Eingereicht von:
Ronja Anika Hinz
geb. Heinen
geb. am 23.09.1990
in Viersen

1. Gutachterin:
Prof. Dr. Martina Müller
2. Gutachter:
Prof. Dr. Carsten Westphal

Dissertation
zur Erlangung des akademischen Grades
Doktor der Naturwissenschaften

an der

Fakultät für Physik der Technischen Universität Dortmund

Declaration of Authorship

Eidesstattliche Erklärung

Ich, Ronja Anika Hinz, geb. Heinen, geb. am 23.09.1990 in Viersen, versichere an Eides statt, dass die vorliegende Doktorarbeit eigenständig erstellt wurde und alle in Anspruch genommenen Quellen und Hilfen in der Dissertation vermerkt wurden.

Ronja Anika Hinz, Jülich, den 7. Juni 2021

Erklärung

Die vorliegende Doktorarbeit wurder weder vollständig noch in Teilen in der gegenwärtigen oder einer anderen Fassung an der Technichen Universität Dortmund oder einer anderen Hochschule in Zusammenhang mit einer staatlichen oder akademischen Prüfung bereits vorgelegt.

Ronja Anika Hinz, Jülich, den 7. Juni 2021

"Ein Gelehrter in seinem Laboratorium ist nicht nur ein Techniker; er steht auch vor den Naturgesetzen wie ein Kind vor der Märchenwelt."

Marie Curie

Abstract

Transition metal oxides exhibit a variety of physical properties due to their high tunability of spin, orbital, and charge degrees of freedom. This thesis studies two complex, transition metal oxide thin film/substrate systems, the $NiFe_2O_4$/Nb:$SrTiO_3$ (NFO/STO) and the $La_{0.3}Sr_{0.7}MnO_3$/Nb:$SrTiO_3$ (LSMO/ STO). NFO is a ferrimagnetic insulator. LSMO is a ferromagnetic half metal and below a critical thickness transitions to an insulator. However, the physical properties of those complex oxides heterostructures are often directly linked to the quality of the thin oxide film and the interactions between the oxide thin film and its substrate at the interface. In this thesis the ultra thin NFO film growth via pulsed laser deposition is optimized. First those optimized, smooth and single crystalline NFO films are studied with lab measurement methods to ensure a high film quality. In a next step their stoichiometry and crystalline occupancy is studied via hard X-ray photoemission (HAXPES) and X-ray absorption spectroscopy, which were recorded at the large scale synchrotron BESSY II, PETRA III and the DIAMOND Light source. The stoichiometry and occupancy is found to match the theoretical expectations of the NFO oxide in the inverse spinel structure. The magnetic response of the NFO/STO heterostructure is researched with the element selective X-ray magnetic circular dichroism (XMCD). The Ni and Fe cations' orbital and spin magnetic moment are extracted with the XMCD sum rules. The NFO magnetic response is largely carried by the Ni cations which is in agreement with the theoretical calculations. It is proven that the Ti cations of the STO substrate, which is near to the interface, is partially reduced and shows a non vanishing magnetic signal. Due to the proximity effect the Ti signal mimics the ferrimagnetic response of the NFO thin film. The electronic properties of Au/NFO/STO and Pt/LSMO/STO devices were investigated via in-operando HAXPES measurements. In-operando HAXPES is recording HAXPES spectra during a voltage is applied to the sample. The band alignment and band bending are investigated by applying Kraut's method to the HAXPES spectra. In the Au/NFO/STO device the band alignment and band bending at the NFO/STO interface is found to be voltage independent. The diode-like electronic behaviour of those samples is carried by the Au/NFO interface and the quality of the NFO thin films. The Pt/LSMO/STO device's electrical behaviour resembles a diode. Only the voltage backward direction shows voltage dependent band alignment and band bending. The band alignment of both oxide systems match the electrical behaviour observed in the IV-curve. The STO substrate's band bending region extends up to 7 nm into the substrate and the LSMO electronic bands are bent throughout the entire film.

In conclusion, high quality NFO films are grown on STO. These NFO films show a stoichiometry, cation structure occupancy, and magnetic response that are in agreement with theoretical expectations. Furthermore it is shown that the STO has a non - vanishing magnetic response due to the proximity effect. Even under applied voltages the band arrangement between the NFO and STO remains stable. The NFO/STO and LSMO/STO electronic behaviour are successfully described and determined by applying Kraut's model to the in-operando HAXPES spectra. This makes in-operando HAXPES a powerful tool for studying the electronic behaviour at buried oxide interfaces.

Kurzzusammenfassung

Übergangsmetalloxide weisen aufgrund ihrer hohen Abstimmbarkeit von Spin-, Orbital - und Ladungsfreiheitsgraden eine Vielzahl physikalischer Eigenschaften auf. Diese Arbeit untersucht zwei komplexe Übergangsmetalloxid Dünnschicht/ Substrat - Systeme, das $NiFe_2O_4/SrTiO_3$ (NFO/STO) und das $La_{0.3}Sr_{0.7}MnO_3/SrTiO_3$ (LSMO/STO). NFO ist ein ferrimagnetischer Isolator. LSMO ist ein ferromagnetisches Halbmetall und geht unterhalb einer kritischen Dicke in einen Isolator über. Die Eigenschaften dieser komplexen Oxidheterostrukturen hängen jedoch häufig direkt von der Qualität des dünnen Oxidfilms und den Wechselwirkungen an der Oxid-Oxid Grenzschicht ab. In dieser Arbeit wird zunächst das Wachstum von ultradünnen NFO - Filmen mittels Pulsed Laser Deposition optimiert. Diese optimierten, glatten und einkristallinen NFO Filme werden dann mit Labormessmethoden untersucht, um eine hohe Filmqualität sicherzustellen. In einem nächsten Schritt wurden ihre Stöchiometrie und ihre kristalline Besetzung mittels Hart X-ray Photoemissions- (HAXPES) und X-ray Absorptionsspektroskopie untersucht, die an den Synchrotron BESSY II, PETRA III und der DIAMOND Light Source aufgenommen wurden. Die Stöchiometrie und die Besetzung stimmen mit den theoretischen Erwartungen des NFO in der inversen Spinellstruktur überein. Die magnetische Eigenschaften der NFO/STO Heterostruktur wird mit dem elementselektiven X-ray magnetisch - circular - Dichroismus (XMCD) untersucht. Mit den XMCD - Summenregeln werden von den Ni- und Fe - Kationen das Orbital- und das Spinmoment extrahiert. Das magnetische Moment von NFO wird größtenteils von den Ni - Kationen getragen, was mit den theoretischen Berechnungen übereinstimmt. Es wird nachgewiesen, dass die Ti - Kationen des STO Substrats in der Nähe der Grenzfläche teilweise reduziert sind und ein nicht verschwindendes magnetisches Signal besitzen. Aufgrund des Proximityeffekts ahmt das Ti - Signal die ferrimagnetische Eigenschaft des NFO - Films nach. Die elektronischen Eigenschaften von Au/NFO/STO - und Pt/LSMO/STO - Heterostrukturen wurden mithilfe von in-operando HAXPES Messungen untersucht. Die Bandausrichtung und die Bandverbiegung werden untersucht, indem die HAXPES Spektren mit der Krauts Methode untersucht werden. In der Au/NFO/STO Heterostruktur ist die Bandausrichtung und die Bandverbiegung an der NFO/STO Grenzfläche spannungsunabhängig. Das elektrische Verhalten der Pt/LSMO/STO Heterostruktur ist ebenfalls diodenähnlich. Nur die Spannung-Rückwärtsrichtung zeigt eine spannungsabhängige Bandausrichtung und Bandverbiegung. Die Bandausrichtung beider Oxidsysteme stimmt mit dem in der IV-Kurve beobachteten elektrischen Verhalten überein. Die Bandverbiegung des STO erstreckt sich bis zu 7 nm in das Substrat hinein und LSMO zeigt durch den gesamten Film Bandverbiegung.

Zusammenfassend lässt sich sagen, dass die hergestellten NFO Filme eine Stöchiometrie, Kationenstrukturbesetzung und magnetische Eigenschaften besitzen, die mit den theoretischen Erwartungen übereinstimmt. Weiterhin wird gezeigt, dass der STO aufgrund des Proximityeffekts ein echtes magnetisches Moment aufweist. Auch unter angelegten Spannungen bleibt die Bandanordnung zwischen NFO und STO stabil. Das elektronische Verhalten von NFO/STO und LSMO/STO wird erfolgreich beschrieben und bestimmt, indem das Kraut-Modell auf die in-operando HAXPES Spektren angewendet wird. Dies macht in-operando HAXPES zu einem leistungsstarken Werkzeug zur Untersuchung des elektronischen Verhaltens an Oxidgrenzflächen.

Contents

List of Figures

xviii

List of Abbreviations

NFO	$NiFe_2O_4$
STO	$SrTiO_3$
LSMO	$La_{0.33}Sr_{0.66}MnO_3$
PLD	**P**ulsed **L**aser **D**eposition
AFM	**A**tomic **F**orce **M**icroscopy
XRD	**X-R**ay **D**iffraction
XRR	**X-R**ay **R**eflection
RSM	**R**eciprocal **S**pace **M**apping
SQUID	**S**uperconducting **Qu**antum Interference Device
(cp) XAS	(**c**ircular **p**olarized) **X**-ray **A**bsorption **S**pectroscopy
TEY	**T**otal **E**lectron **Y**ield
FY	**F**luorescence **Y**ield
(X)MCD	(**X**-Ray) **M**agnetic **C**ircular **D**ichroism
HAXPES	**H**ard **X**-Ray **P**hoto**E**lectron **S**pectroscopy
MEXAFS	**M**agnetic **E**xtended **X**-ray **A**bsorption **F**ine **S**tructure
EBPVD	**E**lectron **B**eam **P**hysical **V**apor **D**eposition
QMS	**Q**uadrupole **M**ass **S**pectrometer
HtStr	**H**etero**str**ucture
cl	**c**ore **l**evel

List of Symbols

B	Magnetic Field	1 Tesla (T)=10000 Oersted (Oe)
T	Temperature	K or °C
F	Laser Fluence	$\frac{mJ}{cm^2}$
p_{Ox}	Oxygen Partial Pressure	mbar
f	Laser Pulse Frequency	Hz
U	Voltage	V
I	Current	A
vh	Photon Energy	eV
E_k	Kinetic Energy	eV
E_b	Binding Energy	eV
E_c	Conduction Band Energy	eV
ΔE_c	Change in Conductions Band Energy	eV
E_v	Valence Band Energy	eV
ΔE_v	Change in Valence Band Energy	eV
E_g	Bandgap Energy	eV

Chapter 1

Introduction

Dear reader, you have just read the title of this chapter. I am faced with the task to write an introduction to my thesis that should give you a first impression of the research topic and the research field presented in this thesis. Therefore I will try answering two of the most frequently asked questions regarding my research field. Please, keep in mind that the rest of my thesis will not be written in the same manner and starting with the outline of my thesis I will write in a more suitable scientific way.

Since 2014, I have been a member of the oxide community, meaning that I am, for most of the time, actively pursuing to work with, investigate and try to understand oxide material systems. The two most prominent reactions to this are: "Oxides, do you mean rust?" if they are non - physicists, or "Do you know what the problem of oxides is? - The oxygen.", if they are physicists or anything related to it. To the non - physicists: Yes, you got it, rust is a mixture of iron oxides and water, more precisely a mixture of FeO, Fe_2O_3 and H_2O. In dependence of the oxidation state of iron and of oxygen content the properties of the iron oxides change. For example at room temperature FeO is diamagnetic, i.e. non - magnetic, while Fe_2O_3, mostly known as hematite, is weakly ferromagnetic [1]. Both materials consist of iron and oxygen, but their physical properties are fundamentally different. This relates to the joke of you physicists: You are like Schrödingers cat, right and wrong at the same time. On the one hand it can be a challenge to control the oxygen content in oxide systems [2]. On the other hand the ability to change the valency and the seemingly endless combination possibilities can result in new technology applications or even new physical phenomena.

One prominent example are resistive switching devices for non volatile memory. They are based on the fact that the controlled removal or reintroduction of oxygen into the material change the resistivity of the material [3, 4]. Thus, the material has two states, a natural "0" and "1" in computer memory, which can be written and read out by electric fields. Another example is the $LaAlO_3/SrTiO_3$ heterostructure which surprised the oxide community in 2004. Those two materials are wide band gap insulators. However, the nature of the interface between those two materials, a region of a couple of nanometers, is in fact metallic [5]. Since then many other complex oxides have been studied and exploited which resulted in a huge playground of properties and emerging phenomena [6, 7, 8]. The focus of many of these studies are transition metal oxides as they exhibit a variety of physical properties due to their

high tunability of spin, orbital and charge degrees of freedom [9, 10]. The initial way to tailor these properties is a precisely controlled growth process of single-crystalline thin film heterostructures. A second way is to force the stable oxides via electrical fields or magnetic fields into other states. Whatever way is used, many measurements have to be performed in order to get a full picture of the material system's physical properties, i.e. surface morphology, crystal structure, stoichiometry, electric and magnetic response. Most of those measurements can be done in Lab facilities but some, like element selective measurements at buried interfaces, can only be performed at large scale synchrotron facilities [11, 12].

In my thesis I studied the $NiFe_2O_4$/$SrTiO_4$ for the most part. Ideal bulk $NiFe_2O_4$ is a ferrimagnetic insulator. Thus, it is a possible candidate for spin filter applications [13]. $SrTiO_3$ is a widely used oxide as it is compatible with the current Silicon CMOS technology. This makes the introduction of oxide electronic devices into existing electronics more feasible [14, 15]. However, growing $NiFe_2O_4$ on $SrTiO_3$ is challenging because the $SrTiO_3$ exerts a strong compressive strain of 6.8% [16]. This introduces a lot of defects into the $NiFe_2O_4$ films. Thus, the optimization of the fabrication procedure is an absolute necessity. However, the main focus of my thesis is to determine a full picture of the $NiFe_2O_4$/$SrTiO_4$ system's electronic and magnetic properties (and to probe the electronic response of the $La_{0.3}Sr_{0.7}MnO_3$/ $SrTiO_3$ heterostructure). Therefore in this thesis the $NiFe_2O_4$/$SrTiO_4$ and the $La_{0.3}Sr_{0.7}MnO_3$/ $SrTiO_3$ heterostructures are investigated in great detail by element selective measurement techniques, which were performed at PETRA III, DIAMOND Light Source and BESSY II from 2016 to 2018.

Outline

The fundamental physical background of this thesis is presented in chapter 2. This includes the reporting of the oxide material properties of $SrTiO_3$, $NiFe_2O_4$ and $La_{0.7}Sr_{0.3}MnO_3$ and an introduction to the synchrotron measurement techniques X-ray absorption (XAS) and hard X-ray photoemission spectroscopy (HAXPES). Furthermore, methods are presented to extract the band alignment and band bending information at buried oxide interfaces from HAXPES measurements. By utilizing the electronic flat band model we can describe the electronic structure of the oxides.

The experimental methods in this thesis can be divided into laboratory methods and synchrotron methods. Laboratory methods refer to experiments which can be performed in house, in our own or collaboration labs. The synchrotron methods on the other hand refer to experiments, which can only be performed at a synchrotron due to the high demand in depth sensitivity, precision and photon flux. In chapter 3 a short overview of those two types of experimental methods and their set-ups used in this thesis are given.

The main focus of this thesis are the properties of the hetero structures $NiFe_2O_4$/ $SrTiO_3$ (and $La_{0.7}Sr_{0.3}MnO_3$/$SrTiO_3$), more specifically the response of their interface properties under application of external electric or magnetic fields.

A basic requirement for this thesis is the optimization of the oxide pulsed laser deposition (PLD) growth parameters in order to achieve reproducible and high quality ultra thin oxide films. Chapter 4 addresses this topic for the growth of the inverse spinel (001) $NiFe_2O_4$ on top the perovskite $Nb:SrTiO_3$. The influence of laser fluence and growth pressure composition on the film quality are probed with laboratory experimental methods and an optimal set of growth parameters is defined. In a next step the optimized NFO/STO heterostructures are taken to different synchrotron facilities. There, the chemical composition are investigated and compared to theoretical expectations.

In chapter 5, $NiFe_2O_4$ films are probed with circular polarized XAS at constant magnetic field. Thus the X-ray magnetic circular dichroism (XMCD) signal, which is the fingerprint of the cation specific magnetic response, is retrieved. By applying the MCD sum rules the cation specific orbital and spin momentum are calculated and compared to the expected theoretical values. With this knowledge, the magnetic response of the $NiFe_2O_4/SrTiO_3$ interface is probed, more specifically the magnetic response of the titanium cations in the substrate near to the $NiFe_2O_4/SrTiO_3$ interface. The Ti XAS and XMCD signals are analysed in terms of Ti cation valency, the XMCD magnetic fingerprint and the magnetic field dependence and the $NiFe_2O_4$ film thickness dependence of the XMCD signal.

Chapters 6 and 7 introduce the in-operando HAXPES measurement technique in order to directly observe the influence of an electric field on a complex oxide heterostructure. In-operando HAXPES measurements are HAXPES measurements at which a constant voltage is applied to the sample during the recording of spectra. Thus for each voltage step the band alignment and band bending at the buried oxide heterostructure interfaces can be extracted, analysed and related to the electronic behaviour of the oxide device. In the scope of this thesis, the $Au/NiFe_2O_4/SrTiO_3$ and $Pt/La_{0.7}Sr_{0.3}MnO_3/SrTiO_3$ heterostructures are investigated with this technique and the resulting electric field dependency of the band alignment and bend bending are compared to each other.

Finally the summary and an outlook for further investigations is given in chapter 8.

Chapter 2

Theoretical background

This chapter is meant to give the theoretical background information in order to follow this thesis. It is not meant to cover the presented information and topics to their full extent because this would go beyond the scope of this thesis.

2.1 Material characteristics

This section focusses on the physical properties of the complex oxides used in this thesis. The comprehension of the physical properties of bulk materials are the foundation for understanding the physical properties of ultra thin films, complex heterostructures and their interfaces. Three complex oxides will be presented: $NiFe_2O_4$, $SrTiO_3$ and $La_{0.3}Sr_{0.7}MnO_3$.

2.1.1 $NiFe_2O_4$

$NiFe_2O_4$ is an insulating ferrimagnetic oxide with a Curie temperature of $T_c = 850\,K$ which crystallises in the inverse spinel structure with a lattice constant of 8.338 Å. The spinel structure which is shown in figure 2.1 has the general formula of AB_2O_4. It has a cubic unit cell with 56 ions of which 32 are oxygen ions (O^{-2}), 16 trivalent cations (B^{3+}) and 8 divalent cations (A^{2+}). The oxygen ions form an fcc sublattice with 32 octahedral (O_h) and 64 tetrahedral (T_d) sides. 1/2 of the octahedral sides and 1/8 of the tetrahedral sides

Fe^{3+} (T_d & O_h sites)
Ni^{2+} (O_h sites)
O^{2-}
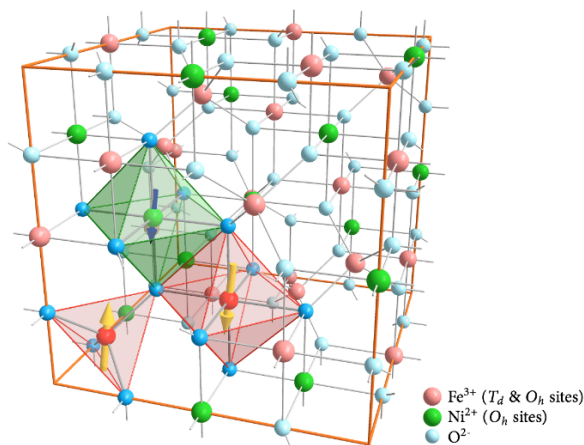
Figure 2.1: Sketch of the inverse spinel structure of $NiFe_2O_4$. The Fe^{3+} cations in red are distributed equally across the octahedral (O_h) and the tetrahedral (T_d) lattice site. The Ni^{3+} in green occupy O_h sites. Adapted from [17].
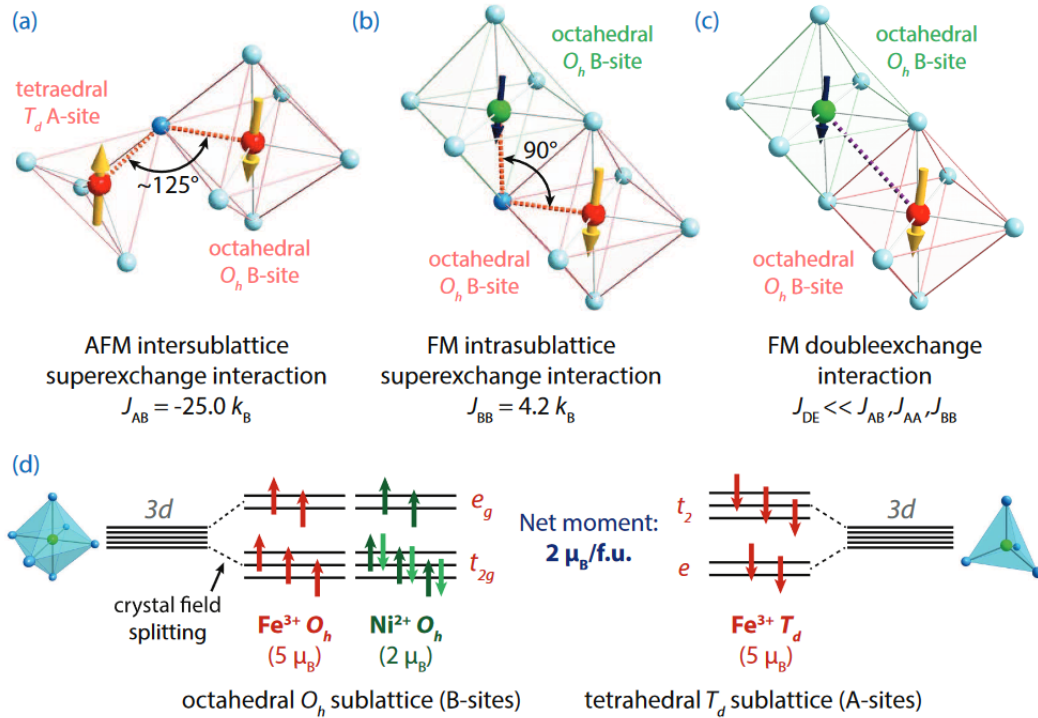
Figure 2.2: (a-c) Exchange interactions in $NiFe_2O_4$. **a)** Anti - ferromagnetic superexchange interaction between cations on the T_d and the O_h lattice sites. **b)** Ferromagnetic superexchange interaction between cations on O_h sites. **c)** Ferromagnetic double exchange interaction between cations on O_h sites. **d)** Occupation of the magnetic sublattice in the inverse spinel structure of $NiFe_2O_4$ and the splitting of the 3d levels due to the crystal field. Image adapted from [16]

are occupied. In case of the normal spinel the tetrahedral sites are occupied by the divalent A^{2+} cations ($A(T_d)$) and the octahedral sites are occupied by the trivalent B^{+3} cations ($B(O_h)$). In the unit cell of the inverse spinel, the A^{2+} occupy half of the octahedral sites ($A(O_h)$) and the B^{3+} occupy the tetrahedral ($B(T_d)$) and the other half of the octahedral sites ($B(O_h)$).

Magnetic structure

The unit cell of NFO in the inverse spinel structure includes 24 magnetic ions, 16 Fe^{3+} and 8 Ni^{2+}. In a first approximation oxides are often considered as a pure ionic system. Thus, each magnetic ion contributes to the magnetism of the unit cell. The electronic configuration of a Ni^{2+} is $[Ar]3d^8$. The 3d bands degeneracy is reduced due to the oxygen octahedron and its crystal field. Thus, the 3d bands split into the two energetically higher states e_g and into the three energetic lower states t_{2g}. According to Hund's rule and Pauli's principle the electron spins arrange themselves in the d bands, which leaves two spins unpaired and aligning parallelly in the e_g states. Thus, Ni^{2+} has a net moment of $2\,\mu_B$ per atom. For the Fe^{3+} the electronic configuration is $[Ar]3d^5$. Similar to the Ni cations the 3d bands degeneracy is reduced due to the oxygen environment and its crystal field splitting. At the octahedral sites

the 3d bands split into the two energetic higher states e_g and into the three energetic lower states t_{2g} while at the tetrahedral sites the t_{2g} and e_g degenerated states are energetically switched. In general the crystal field splitting for Fe^{3+} gives rise to the possibility of aligning the spins in all d levels (e_g and t_{2g}) parallel to each other as well as filling the energetic lower level first. In the case of NFO the parallel alignment is energetically favourable which adds up to a net moment of $5\,\mu_B$ per atom [18]. The 3d band occupation and its splitting are illustrated in the figure 2.2 **d)** for the O_h and T_d lattice sites respectively.

The magnetic response of the total NFO unit cell is gained by considering the exchange interaction between the different cations and their lattice sites. The strongest interaction can be found by considering the Goodenough-Kanamori-Anderson-Rules presented in section 2.2. The superexchange coupling mechanism couples the cation magnetic moments on the different lattice sites (O_h and T_d) via an oxygen ion. The intersublattice superexchange interaction between two Fe^{3+} cations that occupy one O_h site and one T_d site under an angle of 125° have a strong antiferromagnetic coupling (see figure 2.2 **a)**). The intrasublattice superexchange coupling between two cations occupying O_h lattice sites under an angle of 90° yield a ferromagnetic ordering (see figure 2.2 **b)**). The intrasublattice superexchange coupling between two Fe^{3+} cations occupying T_d site is antiferromagnetic. However, the latter superexchange coupling mechanism is weak and gets superimposed by the other two superexchange mechanisms [19]. Finally, the Ni^{2+} cations located at O_h sites and Fe^{3+} cations located at O_h sites couple ferromagnetically via the double exchange interaction (see figure 2.2 **c)**). The combination of all these interactions result in two ferromagnetic ordered sublattices, the octahedral and tetrahedral respectively, that align antiferromagnetically with each other. Therefore the magnetic moments of the Fe^{3+} cations that populate the octahedral and tetrahedral equally in the inverse spinel structure cancel each other out. This results in a net moment of NFO formed by the Ni^{2+} cations of $2\,\mu_B/f.u.$.

The transition metal cations 3d t_{2g} and e_g states are spherically symmetric due to the oxygen environment. The result of the spherical symmetry is that the orbital momentum of half occupied or fully occupied states vanishes [20]. In figure 2.2 **d)**, it can also be seen that the t_{2g} and e_g of each cation and each lattice site are either fully or half occupied. Thus, the total orbital momentum on each lattice site is expected to be quenched, which explains the small magneto crystalline anisotropy observed in NFO. The even occupation of possible angular momentum numbers in the 3d bands causes any effect of the spin-orbit coupling to cancel out. Therefore the spins are not locked to the alignment of orbital states which are coupled to the lattice sites, i.e. the spin alignment's direction dependence is suppressed.
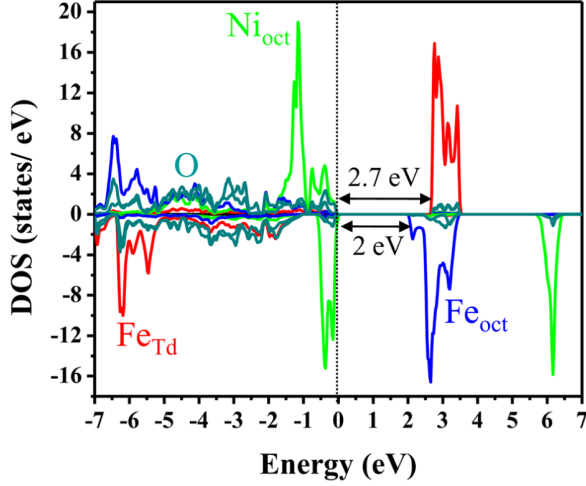
Figure 2.3: NFO's DFT calculated electron density of states. Adapted from [21]. The calculated majority and minority band gaps are $E_g^{min} = 2.1\,\text{eV}$ and $E_g^{maj} = 2.7\,\text{eV}$.

Electronic structure

The electronic structure of NFO can be calculated with the density functional theory (DFT) using the Linearized-Augmented-Plane-Wave method and Local-Orbital-Method that implements a self-interaction corrected local spin density approximation [22, 21]. Szotek *et al.* calculated the electron density of states for the NFO in inverse spinel structure and normal spinel structure [22]. The results showed that the inverse spinel structure is energetically favourable and stable. Dileep *et al.* calculated the density of states for NFO in inverse spinel structure, 50% inversion, 50% and 100% octahedra lattice site vacancies. Any deviation from the inverse spinel caused the band gap of the minority electrons E_g^{min} to decrease and the band gap of the majority electrons E_g^{maj} to increase, which resulted in a smaller overall bang gap. In figure 2.3, the density of states of the NFO in ideal inverse spinel structure calculated by Dileep *et al.* are shown. The valence band is formed by Ni^{2+} O_h states for the majority and minority electrons. The conduction band is formed by the Fe^{3+} O_h states for the minority electrons and by the Fe^{3+} T_d states for the majority electrons. This results in two distinct band gaps: The minority electrons have a calculated theoretical band gap of $E_g^{min} = 2.1\,\text{eV}$ and the majority electrons have a calculated theoretical band gap of $E_g^{maj} = 2.7\,\text{eV}$.

2.1.2   La$_{0.3}$Sr$_{0.7}$MnO$_3$

The La$_{0.7}$Sr$_{0.3}$MnO$_3$ (LSMO) studied in this thesis is part of the mixed composition manganites family R$_{1-x}$A$_x$MnO$_3$ with $0 < x < 1$. LSMO has a distorted perovskite crystal structure. The 3d transition metal Mn is located at the centre of an octahedron of oxide ions. The La and Sr cations sit on the cube's edges. Depending on the mixture of surrounding edge atoms and their difference in ions size the oxygen octahedra are buckled. This affects the symmetry of the cubic structure. At room temperature LSMO exhibits a rhombohedral or *pseudocubic* structure with a lattice constant of $a = 3.869\,\text{Å}$ and off-cubic angle of $\alpha = 89.74°$ [23].
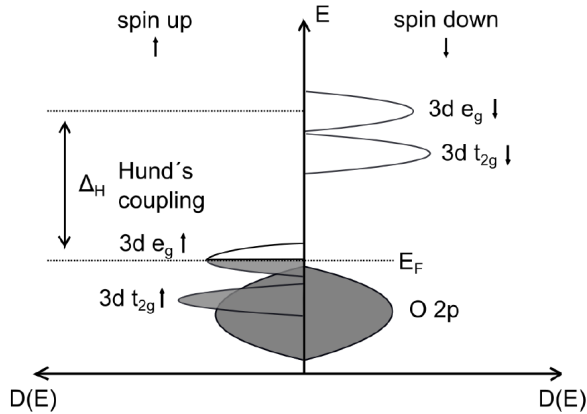
Figure 2.4: Schematic density of states $D(E)$ of ideal have metallic LSMO is shown. Modified from [24].

Electronic structure

LSMO is a mixed valence manganite which consists of tetravalent manganese Mn^{4+} and trivalent manganese Mn^{3+}. Compared to the parent compound $LaMnO_3$, the trivalent lanthanum La^{3+} is partially replaced by the bivalent strontium Sr^{2+} cations. This results in a charge disparity that will be compensated by the conversion of Mn^{3+} into Mn^{4+}. Therefore, $La_{1-x}Sr_xMnO_3$ exhibits an ionic structure and the ratio between the La and Sr cations influences the physical properties.

The electronic band structure of the $La_{0.3}Sr_{0.7}MnO_3$ shows a half metallic behaviour [25]. In figure 2.4, the schematic density of states $D(E)$ of LSMO is shown. Due to the octahedral symmetry of the oxygen anions, the 3d bands of the LSMO are split into the e_g and the t_{2g} states. For one spin orientation the Fermi level is located in the 3d e_g band. For the opposite spin orientation the Fermi level is located in a band gap. Therefore, the conductivity of LSMO will be carried by states of one spin orientation only. This inherent spin polarization of LSMO makes it a candidate for electronic devices that imply or are based on the detection of spin polarized currents.

Magnetic structure

Depending on the exact stoichiometry of $La_{1-x}Sr_xMnO_3$, different splitting of the manganese 3d-orbitals can occur. This results in a complex magnetic behaviour. Basically, the magnetic behaviour is based on two coupling mechanism: One is the superexchange interaction which couples same valence manganese cations only. The other one is the double-exchange interaction which couples manganese cations with different valence only.

The superexchange interaction is the main coupling mechanism in the parent oxide $LaMnO_3$, as it has only Mn cations of one valency without any electrons that can move freely. It is based on the coupling between two nearest-neighbour Mn^{3+} cations through a shared oxygen anion. The Mn 3d orbitals hybridize the O 2p orbitals. The virtual hopping of the O 2p electrons to the Mn 3d orbitals leads to excited states, which can result in a reduction of the energy of the system. The sign and strength of the superexchange interaction depend on the occupancy and the orbital degeneracy of the 3d
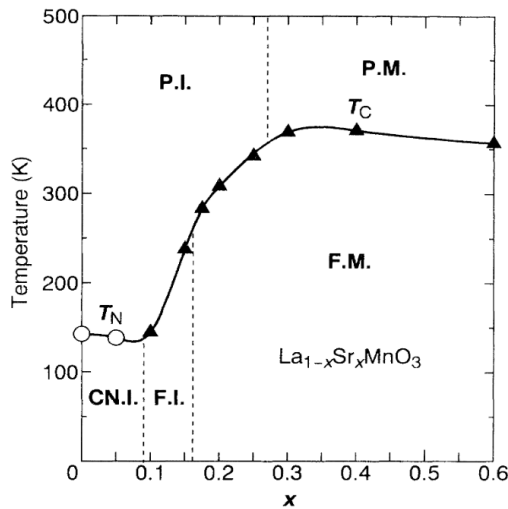
Figure 2.5: Electronic and magnetic phase diagram. 'F.I.' ferromagnetic insulator, 'F.M.' ferromagnetic metal, 'P.I.' paramagnetic insulator, 'P.M.' paramagnetic metal and 'C.N.' insulator with canted magnetic moment. Adapted from [27].

states involved and can be described with the empirically found GKA-rules described in section 2.2.

The double exchange interaction describes the exchange interaction between two manganese cations of different valence which come into existence because of the partially replacement of La^{3+} cations by Sr^{2+} cations. The free electron in the d_{z^2} orbital of the Mn^{3+} cation moves through the diamagnetic oxygen anion into the empty d_{z^2} orbital of the Mn^{4+} cation without spending any excitation energy. The electron movement into a neighbouring state is enabled by the parallel alignment of the manganese core level spins. This real electron hopping is the foundation of the good electrical conductivity and the ferromagnetic ordering observed in the LSMO [26] .

Naturally, the interplay of the superexchange and double exchange coupling mechanism crucially depend on the exact chemical composition. In figure 2.5, a phase diagram of LSMO with respect to the strontium cation part and temperature is shown. The symbol 'I' represents an insulating composition, 'M' represents a metallic composition, 'F' represents a ferromagnetic ordering and 'P' represents a a paramagnetic ordering. The composition used in this thesis has a strontium part of $x \approx 0.3$. Thus it is metallic ferromagnetic and has the maximum Curie temperature all possible compositions, which is 370 K.

Growth on $SrTiO_3$

In general, epitaxially grown LSMO thin films show different physical properties compared to their bulk counterparts. In this thesis, the a thin LSMO film is grown on top of STO. STO has a larger lattice constant than the LSMO bulk lattice constant and therefore the epitaxial LSMO film experiences a tensile strain of 0.93%. Tensile stress in LSMO films is known to distort the oxygen ion octahedron surrounding the manganese ion. This changes the overlap and hybridization of the oxygen p orbitals and the manganese d orbitals according to the Jahn-Teller distortion theory. Therefore, the tensile strain suppresses the ferromagnetic and metallic behaviour in LSMO thin
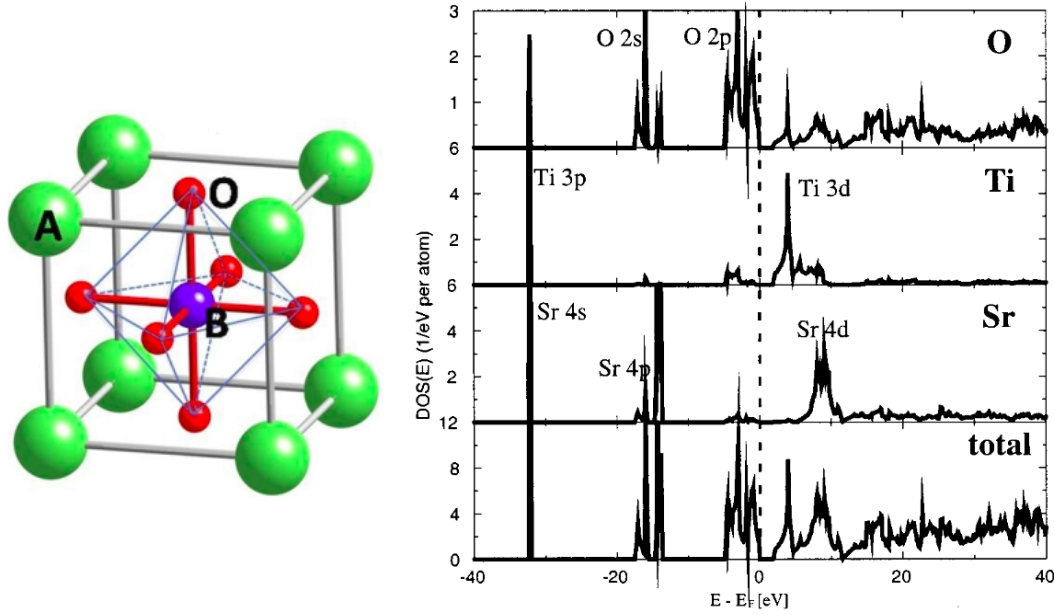
Figure 2.6: a) Sketch of the perovskite crystal structure ABO_3. **b)** Theoretical determined DOS of STO, taken from [29].

films. The result is that in ultrathin LSMO films, two critical thicknesses are observed [28]. For a film thickness of $d_1 < 3$ u.c. the LSMO film is paramagnetic and insulating. Below the film thickness of $d_2 < 9$ u.c. and larger than d_1 the LSMO film is ferromagnetic and insulating. If the LSMO thickness exceeds 9 u.c. the LSMO thin film shows its normal ferromagnetic and metallic behaviour. In the scope of this thesis an epitaxial LSMO film with a film thickness of 6 u.c. is probed, expecting an insulating and ferromagnetic behaviour.

2.1.3 SrTiO$_3$

SrTiO$_3$ (STO) is a diamagnetic and insulating transition metal oxide. At room temperature it has a cubic perovskite structure with a lattice constant of $c_{STO} = 3.905$ Å as shown in figure 2.6 **a)**. Like NFO and LSMO, STO is treated as an ionic crystal in the first approximation. The Sr^{2+} cations are located at the A-site of the perovskite, while the Ti^{4+} sits in the centre of the unit cell and of the oxygen ion octahedral. Consequently, the oxygen anions are located at the six face-centred sites. In the (100) direction STO can be regarded as an alternating stack of $(SrO)^0$ and $(TiO_2)^0$ planes. Thus a surface treatment etching procedure can provide a surface coverage of nearly only TiO_2.

In figure 2.6 **b)**, the theoretical density of states (DOS) of STO is displayed [29]. In the lowest part the total DOS of STO is shown. In the upper panels the DOS contribution of the single ions of the STO is displayed. Stoichiometric STO is a wide band gap insulator with a band gap of $E_g \approx 3.25$ eV. The Fermi level is located near to the valence band maximum. While the valence band is mostly formed by the O 2p atomic orbitals, the conduction band is

mostly build up by the Ti 3d orbitals. The result is that the electronic characteristic of STO is dominated by the titanium valence. In oxygen deficient STO the oxygen vacancies introduce electrons into the Ti 3d orbitals and yield a metallic conducting phase [30]. In the research field of resistive switching phenomena, the controlled introduction or removal of oxygen vacancies into undoped STO is used to force a localized conducting or insulating state, the "1" and "0" for possible electronic devices. In the scope of this thesis, a low percentage Nb doped STO is used. Nb doping introduces an additional free electron per Nb atom into the oxide, more precisely into the Ti 3d bands [31]. This ensures a metallic conducting substrate which is needed in order to provide a conducting substrate to perform HAXPES and XAS synchrotron measurements. At the same time the crystal structure and the magnetic response is not changed by the Nb doping.

2.2 Goodenough-Kanamori-Anderson-Rules

The Goodenough-Kanamori-Anderson-Rules (GKA-rules) are an empirically found set of rules that describe the transition and interaction between orbitals with different angular quantum numbers in complex materials [32, 33, 34].

1. The exchange interaction between partially filled or empty d shell orbitals under an cation-ligand-cation (clc) angle of 180° is strong and antiferromagnetic.

2. The exchange interaction between a partially filled and empty d shell orbital under an clc angle of 180° is ferromagnetic and weak.

3. The exchange interaction between partially filled d shell orbitals under an clc angle of 90° is ferromagnetic but weak.

These rules are often applied successfully in complex transition metal oxides to describe the interactions between the oxygen 2p orbitals and the transition metal 3d orbitals. Therefore they will be applied to the cations in the spinel structure of $NiFe_2O_4$ to describe the observed ferrimagnetic ordering. Furthermore they will be applied to the mixed valence $La_{1-x}Sr_xMnO_3$ to describe the transition of magnetic ordering.
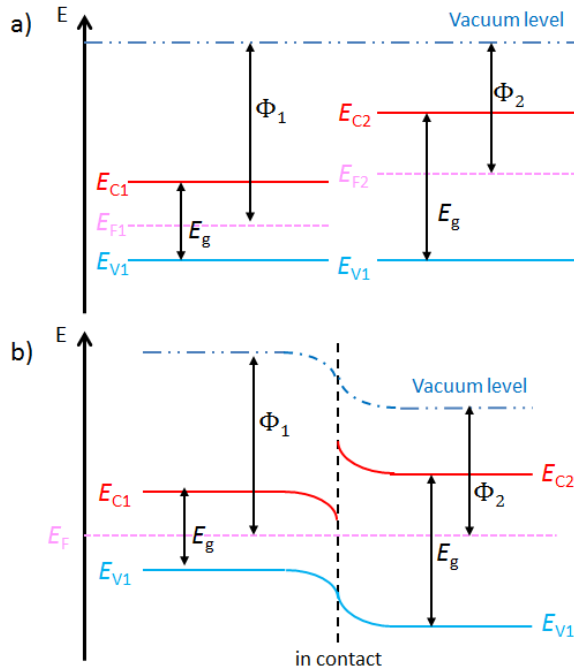
Figure 2.7: a) + b) Example of a schematic flat band structure of two semiconductors without electronic contact and with electronic contact.

2.3 The flat-band model

The true band structures of materials are highly complex and are for the most part not known precisely because of the huge influence of boundary conditions such as unit cell formation, surface boundary conditions, limitation of one dimension or defects. In favour of a first "hands on" approach, the complex band structures are broken down to the most important information: Where is the Fermi level E_F, the valence band maximum E_V and the conduction band minimum E_C and if present the band gap E_g? The result is a simplified band model with flat bands which can be found in the fundamental solid state textbooks [35, 20]. An example for this flat band model of two semiconductors is shown in figure 2.7 **a)**. This model allows to make first predictions of how a material behaves electronically.

In the scope of this thesis the simplified band model is used to study the effects of heterointerfaces on the band structure. When two materials are brought into electronic contact, the total system is confronted with two different sets of conduction band positions, valence band positions, band gaps, and positions of the Fermi level. In this case the work functions are of crucial meaning. The work function of a material is defined as the energy needed to remove one electron from the solid into the vacuum. In the picture of the simplified band model, the work function is determined by the energy difference of the vacuum level to the Fermi level. For a heterojunction a discontinuity in work function results in a violation of the conservation of energy. In this case, it would be possible to remove one electron from the material with the lower work function into the vacuum; then back into the other material with the higher work function, and finally, because they are in electronic contact, back into the first. The electron would gain the energy difference of the two work functions. In order to prevent the violation of conservation of energy,

the bands and the vacuum level have to rearrange to equalize the work functions between the materials. This rearrangement includes two main effects: **band alignment** and **band bending**. A schematic example of a band aligned and band-bent heterojunction is displayed in figure 2.7 **b)**.

When looking at the band diagram 2.7 **b)**, the energy band in a material can curve up or down near a junction. This effect is known as band bending. Band bending is caused by a local imbalance in charge neutrality at junctions consisting of semiconductor-semiconductor or semiconductor-metal transitions. If at a junction two materials with different Fermi level respectively chemical potentials come in contact, the difference in potential induces an electric field. In order to counter act the induced electrical field, the free carriers can rearrange themselves accordingly and thus align the chemical potentials at the junction. Thus a local charge imbalance, i.e. a depletion or accumulation zone, is created. Theoretically this effect can be described by solving the Poisson-Boltzmann equation 2.1 at the junction for each side utilizing the relation between the potential Φ and the conduction band E_C, $q\Phi(x) = -E_C + const$:

$$\frac{d^2\Phi(x)}{dx^2} = -\frac{\rho(x)}{\varepsilon_s} \qquad \Longrightarrow \qquad \frac{d^2E_C(x)}{dx^2} = \frac{q\rho(x)}{\varepsilon_s} \qquad (2.1)$$

Here, ε_s is the material dielectric constant, q denotes the charge and $\rho(x)$ represents the charge carrier density. In the following paragraph the solution for the n-type side of the junction, the region with the electron excess, will be discussed. The solution procedure can be applied analogously for the p-type side of the junction.

In general the following assumption will be used: First, the doping concentration is spatially independent, assuming a uniform doping. Second, the dopants are fully ionized, so all free carriers at the junction have arranged themselves. Third, the donor concentration N_D is higher than the acceptor concentration N_A because the solution of the n-type region will be discussed: $N_D \gg N_A$. Thus the charge carrier density can be written as

$$\rho(x) = q(N_D - n(x)) \qquad (2.2)$$

with $n(x)$ is denoting the local electron concentration. The local electron distribution evolves exponentially with the difference between the position dependent conduction band and the Fermi level,

$$n(x) = N_A \cdot exp\left(\frac{E_C(x) - E_F}{kT}\right) \quad . \qquad (2.3)$$

In the neutral region without any band bending $x \longrightarrow -\infty$, the electron concentration $n(x \longrightarrow -\infty)$ equals $n_{0,D} = N_D$. Thus the electron concentration

$n(x)$ can be rearranged to

$$n(x) = N_D \cdot exp\left(-\frac{E_C(x) - E_C(x \longrightarrow -\infty)}{kT}\right) \quad . \tag{2.4}$$

In a next step, the band parameter $A(x)$ is defined as

$$A(x) = \frac{E_C(x) - E_C(x \longrightarrow -\infty)}{kT} \quad . \tag{2.5}$$

Now, $n(x)$ and therefore $\rho(x)$ can be rearranged and then substituted into equation 2.1, yielding

$$\frac{d^2 A(x)}{dx^2} = \frac{q^2 N_D}{\varepsilon_s kT} \cdot \left(1 - e^{-A(x)}\right) \quad . \tag{2.6}$$

This is a non-linear differential equation. For small band bending, the $e^{-A(x)}$ term can be approximated by $1 - A(x)$. Therefore the differential equation 2.6 can be simplified to

$$\frac{d^2 A(x)}{dx^2} = \frac{q^2 N_D}{\varepsilon_s kT} \cdot A(x) \quad . \tag{2.7}$$

This is a second order differential equation and hence has two linearly independent solutions

$$A(X) \propto exp\left(\pm\frac{x}{L_D}\right) \implies E_C \propto exp\left(\pm\frac{x}{L_D}\right) \quad , \tag{2.8}$$

with L_D the Debye length defined as $L_D = \sqrt{\frac{\varepsilon kT}{q^2 N_D}}$. In conclusion it is shown that for small band bending regions, the conduction band and the valence band bend exponentially.

2.4 Hard X-ray photoelectron spectroscopy

Hard X-ray photoelectron spectroscopy (HAXPES) is a variant of the the conventional photoelectron spectroscopy (XPS) and is based on the photoelectric effect. The photoelectric effect describes the process of the emission of electrons or other free carriers when light hits a material. It was first observed by H. Hertz and correctly described by A. Einstein [36, 37]. Electrons emitted by this process are referred to as photoelectrons. In XPS measurements the target material in question gets illuminated with ideally monochromatic X-rays while simultaneously the kinetic energy of the escaped electrons from the surface is recorded with an electron energy detector. The main difference between XPS and HAXPES is the energy of the X-rays. In HAXPES measurements X-rays within an energy range of $E = 2 - 12\,keV$ are used which are usually produced at synchrotrons.
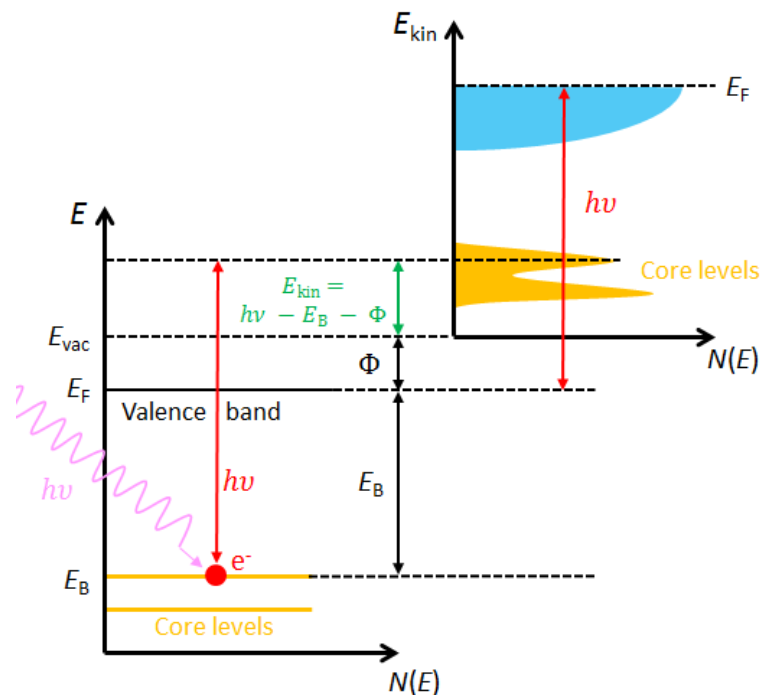
Figure 2.8: Relation between the energy levels of the sample and the XPS spectrum are shown. Adapted from [39]

One simplified description of the photoelectric effect is given by the "three-step-model" [38]. In the three-step-model the whole process describes the emission process in a single electron picture divided in consecutive three steps in order to understand the recorded photoelectron spectra. In figure 2.8 a sketch of the photoelectric effect described by the three-step-model and a resulting XPS spectrum is displayed.

In the initial step the single electron gets excited from the initial state into an unoccupied final state above the Fermi level E_F by absorption of the high energetic light $h\nu$. The excitation follows the law of conversation of energy and momentum. The probability of the excitation in dependence of the photon energy in given by Fermi's golden rule shown in equation **??**. Fermi's golden rule was discussed during the description of the XAS's working principle in chapter 2.5. In contrast to the XAS the final state must have enough energy so that the electron can escape the solid.

In the second step the excited electron travels to the surface of the solid. Thereby the electron can undergo two types of scattering: elastic and inelastic scattering. Elastic scattering changes the path of the electron. Inelastic scattering however transfers energy to the solid's lattice and thus the information of the core level's binding energy is lost. The binding energy is element - selective and is also sensitive to chemical changes of the element. The electron might still escape the solid and get detected and then contributes to the background of the XPS spectrum. The distance an electron can travel before any inelastic scattering event is limited. It is described by the inelastic mean free path (IMPF). Consequently, only surface - near electrons are detected with full information of the core levels and thus limit the information depth of the
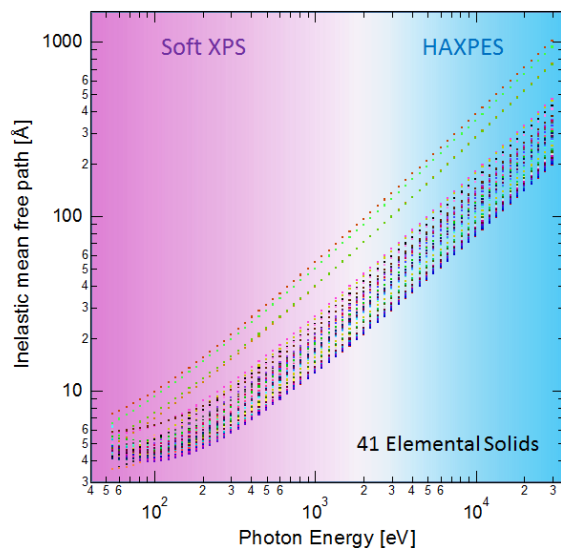
Figure 2.9: Photon energy dependence of the inelastic mean free path of 41 elemental solids. Data are taken from [40].

XPS measurement technique.

In the third and last step the electron escapes the solid into the vacuum. Therefore it has to overcome the threshold energy, which is called working function Φ. At the interface between solid and vacuum, the electron gets diffracted. Thereby the perpendicular part of the electron wave vector is altered. Hence the detected kinetic energy of the photoelectron is the initial absorbed photon energy reduced by the binding energy of the core level and reduced by the work function of the sample.

2.4.1 Depth sensitivity & information depth

Electrons travelling through a solid will scatter with the material. The scattering process is quantified by the inelastic mean free path (IMFP), which describes the average distance an electron can travel through a material without a collision. Therefore, the IMFP is material dependent and it depends on the kinetic energy of the incident light. IMPFs of 41 elemental solids and their energy dependence are shown in figure 2.9. Despite the IMPF's evident material dependence, all IMPFs show a similar behaviour in dependence of the kinetic energy. This is generally referred as "universal curve" and allows to estimate the depth sensitivity of a XPS measurement roughly. However, because it does not describe the elastic scattering effect as well, it is independent of the experimental set-up. This is also the reason why attenuation length determined by experimental measurements are not necessarily in agreement with the IMFP. In order to circumvent this issue, the emission of electrons from solids is described by the depth distribution function (EDDF) $\Phi(z, \cos(\alpha))$ [41]. The EDDF calculates the probability that a photoelectron, which originates from a depth z normal to the surface, leaves the sample surface under an angle α. If elastic scattering is negligible, an EDDF deduced
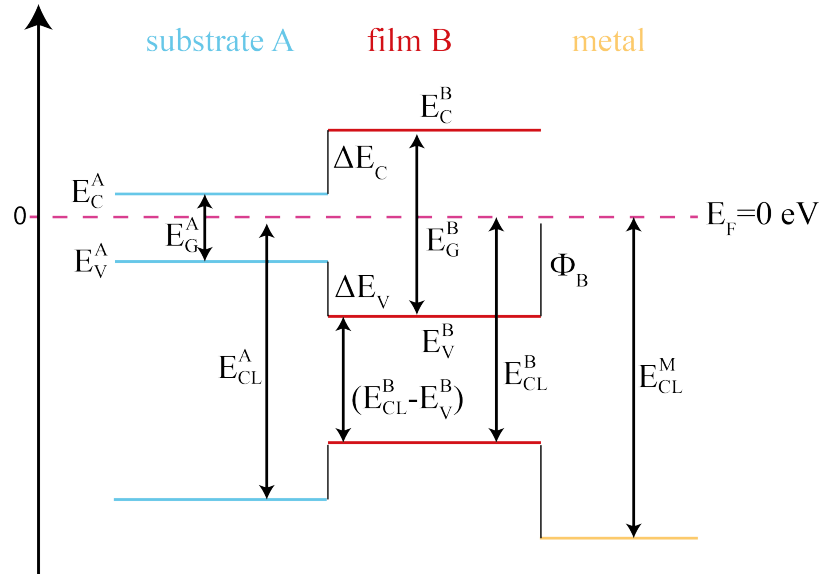
Figure 2.10: Example diagram for band alignment between to semiconductors and a metal in contact. Adapted from [43]

from the Boltzmann transport equation describes the information depth correctly [42]. The resulting EDDF equation given by equation 2.9

$$\Phi(z, \cos(\alpha)) = W(\Psi) \cdot exp\left(\frac{-z}{\lambda_{IMFP} \cdot \cos(\alpha)}\right) \quad . \tag{2.9}$$

Here $W(\Psi)$ is the differential photoelectron cross section, Ψ is the angle between the direction of the incident X-rays and the direction of the photo electron emission from the surface and λ_{IMFP} is the IMPF of the material. With the EDDF, an information depth I can be derived. The information depth I is defined as the probing depth from which a certain percentage P of electrons originate. In general, a percentage of $P = 95\,\%$ is used. The following formula is obtained

$$\frac{\int_0^{I(P)} \Phi(z, \cos(\alpha))dz}{\int_0^\infty \Phi(z, \cos(\alpha))dz} = \frac{P}{100} \iff I(P) = -\lambda_{IMFP} \cdot \cos(\alpha) \cdot ln(1 - P/100) \quad .$$

2.4.2   Band alignment in HAXPES - Kraut's model

A photoemission method for heterojunction band alignment is attributed to Kraut *et al.* [44]. Kraut's model is based on the fact that in photoemission experiments, the energy difference between the valence band maximum and a core level is a physical quantity for any given material. Thus, any shift in the valence band maximum will also result in a shift of the core levels. In figure 2.10 a band-aligned band structure based on the simplified band structure picture between a semiconductor substrate, a semiconductor film and a metal is shown. The symbols E_{CL}, E_V and E_G refer to the conduction band minimum, valence band maximum and the band gap respectively. It can be deduced that if the energy difference between the valence band and the core

level (E_{CL}) are measured, the band alignment in the valence bands ΔE_V can be determined according to the following equations for a semiconductor(A) - semiconductor(B) - junction,

$$\Delta E_V = E_V^B - E_V^A, \tag{2.10}$$

$$\Delta E_V = (E_{CL}^A - E_V^A)_{ref} - (E_{CL}^B - E_V^B)_{ref} - (E_{CL}^A - E_{CL}^B)_{int} . \tag{2.11}$$

The terms in the first and second parentheses refer to the difference between the core level and the valence band maximum in reference materials while the third term in parentheses is the difference in the core level positions of the heterostructure. If furthermore the band gap of the reference materials is known, then the band alignment in the conduction band can be deduced by

$$\Delta E_C = E_g^A - E_g^B + \Delta E_V . \tag{2.12}$$

In case of a semiconductor - metal - junction, the potential barrier height Φ_B is given by

$$\Phi_B = E_F^M - E_V^B , \tag{2.13}$$

$$\Phi_B = (E_{CL}^B - E_V^B)_{ref} - (E_{CL}^M - E_F^M)_{ref} - (E_{CL}^B - E_{CL}^M)_{int} . \tag{2.14}$$

In case of the metal, the main difference is that the valence band maximum in the second term is replaced by the position of the Fermi level. Using these equations, it is possible to extract a simplistic flat band structure of a heterostructure based on band alignment.

2.4.3 Bend bending in HAXPES

If the oxides in heterostructures are insulators or semiconductors, their surfaces, films and buried interfaces can also exhibit band bending. This band bending can be measured by photoemission spectra (PES) in terms of shifts and broadening of core levels if compared to the bulk reference spectra, provided that the core peaks are sufficiently sharp. The direction of the resulting core level shifts are consistent with the direction of the band bending. Hence a shift towards higher/lower binding energies are a result of downward/ upward band bending. In figure 2.11, originally published by Chambers *et al.* [45], a flat band picture of the (4 u.c.)LaAlO$_3$ (LAO)/STO interface is shown with (top) and without (bottom) band bending. Next to the flat band pictures, the corresponding XPS spectra of the Ti 2p$_{3/2}$ are shown. As highlighted the two Ti 2p$_{3/2}$ peaks show a different width of 0.39 eV. In order to quantify the band bending, Chambers *et al.* first estimated the information depth and the length of the depletion region at the LAO/STO interface. Based on the perovskite unit cell of STO, the information depth could be divided in nine TiO$_2$ layers. Four of these TiO$_2$ layers are in the depletion region and are therefore affected by the band bending. Chambers *et al.* furthermore assumed that these four TiO$_2$ have a fixed potential step in between, which results in
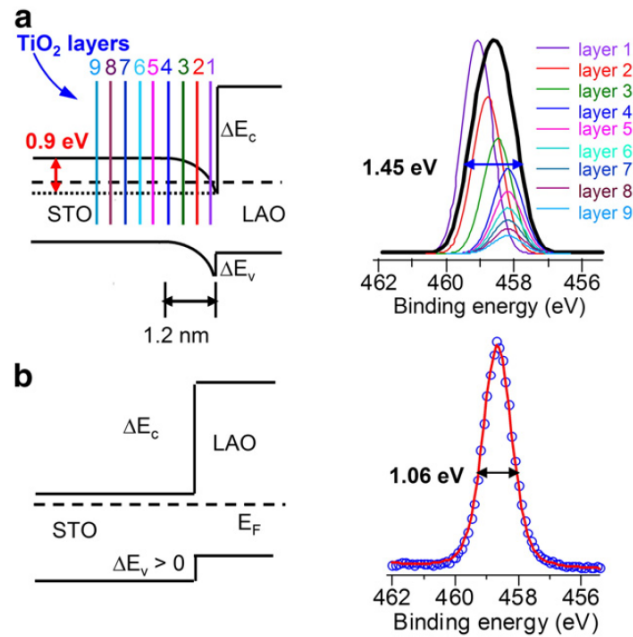
Figure 2.11: Band bending in the LaAlO$_3$/SrTiO$_3$ heterostructure taken from [45]. **a)** HAXPES spectra of the Ti 2p$_{3/2}$ peak as a function of the band bending. **b)** In comparison a not band-bent HAXPES spectra of the system.

a constant energy shift between the next neighbour TiO$_2$ layer. With this information, the XPS spectrum is built of nine reference Ti 2p$_{3/2}$ peaks, four of them shifted and all of them decreased in intensity according to the sensitivity depth. This procedure successfully recreated the observed XPS spectra.

In the scope of this thesis a synchrotron hard X-ray light source was used. The large information depth of 20-30 nm in oxides HAXPES enables the possibility to measure core level of the buried interfaces directly. However, the trade off is that the band bending region of a few nm has not such a huge intensity advantage over the not band bended region due to the high information depth. Thus, the band bending effect has a smaller influence on the HAXPES spectra. However, it is possible to profile the band bending region by changing the X-ray incident angle. Claessen *et al.* have shown at various buried interfaces that by changing the X-ray incident angle the effective information depth in the material is changed [46, 47]. This is based on the fact that at grazing incidence, the detected electrons mostly travel parallel to the surface before they escape into the vacuum. Therefore, although the travel length of electrons without scattering is unchanged, the depth of their origin does change. Thus, a smaller confined region can be probed with high energetic X-rays and high resolution. This technique trades off information depth and signal intensity for profiling buried interfaces.

2.5   X-ray absorption spectroscopy

X-ray absorption spectroscopy (XAS) describes an experiment at which the absorption of an X-ray beam as a function of photon energy $h\nu$ through a material is recorded. This transmission process is quantified by the absorption coefficient μ, the initial intensity I_0, and the thickness d of the sample. Thus the transmission intensity drops exponentially. The absorption coefficient μ can then be deduced from the following formula

$$I(h\nu) = I_0(h\nu) \cdot exp(-\mu(h\nu) \cdot x) \Leftrightarrow \mu(h\nu) = \frac{1}{x} \cdot ln\left(\frac{I_0(h\nu)}{I(h\nu)}\right).$$

However this transmission experiment is limited to thin samples because the signal of I falls below the detection limit for thick samples. Therefore the photon absorption process is detected by secondary processes in XAS measurements. Two different methods have been established. One possibility is to measure the sample fluorescence called the Fluorescence Yield (FY). The other possibility is based on the detection of secondary electrons called the Total Electron Yield (TEY). Both techniques are based on the recombination process at which the excited electrons fall back into the ground state and the energy is released. In the FY, the intensity of the fluorescence light is measured. The advantage is that the light has the same attenuation length as the incident light and thus an information depth of several μm can be achieved. Therefore this method is also called "bulk sensitive". In the TEY, the excited electrons (Auger electrons) can travel towards the sample surface and escape the sample. On the way through the sample they can excite secondary electrons which can also escape, thus forming an electron cascade. Since the electrons leave the sample, they leave a positively charged sample. If the sample is conducting the current between the ground and the sample can be measured. This current is directly related to the absorption coefficient $\mu(h\nu)$. This method is limited to the mean free path of the excited electrons and thus the information depth spans only a couple of nm. Therefore this method is considered as more "surface sensitive".

2.5.1   Fermi's golden rule

In order to understand XAS spectra in terms of shape and intensity of white lines, the photoexcitation process has to be understood. The photoexcitation process describes the interaction between light and matter, an excitation of an electron in a solid by an incoming photon. In the initial state, all electrons in the solid are in their ground state, which is the energetically preferred state. If a photon probes an electron from an atom the electron will get excited into an energetically higher unoccupied state and leaves an atom in an excited state, the final state. Theoretically, the process can be described by Fermi's Golden Rule. Fermi's golden rule describes the quantum mechanical process from transferring a system from an initial state into a final state. The state is calculated via solving the many body Hamiltonian for the electron system of the solid. If the electrons are non-interacting this Hamiltonian can be broken

down into a sum over single electron Hamiltonians. The incoming light is represented by an electromagnetic wave. This electromagnetic wave can be treated as a perturbation in the many body system of the solid. Thus the transition can be treated by perturbation theory, which can be found in the standard textbooks [48, 49]. Fermi's Golden Rule shown in equation 2.15 sums up the whole calculation process up.

$$W \sim |\langle \Phi_f | \mathbf{T} | \Phi_i \rangle|^2 \cdot \delta(E_f - E_i - h\nu) \qquad (2.15)$$

In equation 2.15, W is the transition probability, Φ_i and Φ_f are the initial and final state of the electronic system and T is the transition operator between two states. The delta function satisfies the law of the energy conservation, i.e., the difference in energy between the initial and the final state has to equal the photon energy $h\nu$. Thus it is clear that the excitation probability is highly dependent on the initial and final state. One result of Fermi's Golden Rule are the dipole selection rules. The dipole rules only cover direct transitions. They state that only transitions between the initial and final states are allowed with certain quantum numbers: $\Delta J = 0, \pm 1, \quad \Delta M_J = 0, \pm 1, \quad \Delta S = 0$.
This theoretical picture holds because in the core level spectroscopy mostly deeply bound core electrons are probed. These core electrons are are strongly localized and do nearly not overlap with the neighbouring atoms. These selective core electron excitations make the XAS (and XPS) an element selective measurement technique which is advantageous for the investigation of complex oxide systems.

2.5.2   XMCD

An extension of the X-ray absorption spectroscopy is represented by the X-ray magnetic circular dichroism (XMCD) measurement technique: If a ferromagnetic material is probed with circularly polarized light, the XAS spectra recorded with reversed magnetization or reversed polarization of light will differ. In normal XAS with unpolarized X-rays the probing photons have a random oriented spin momentum J_z. Thus, any coupling effects between the spin momentum of the incoming photon and the angular momentum of the probed atom are averaged. In XAS with circularly polarized light the incoming photons have a well defined spin angular momentum with magnetization axis parallel to the beam direction. The following XMCD process can be described in a two step model which is schematically displayed in a single electron picture in figure 2.12 [50]. First the photon's angular momentum is transferred to the core electron. In case the core electron is subject to spin-orbit coupling, which is true for any shell except the s-shell, the angular momentum of the photon is transferred to the electron. Thus, the generated photoelectron is spin polarized. In the second step the spin polarized electron occupies an empty state. However, the transition obliques Fermi's golden rule and its derived selection rules. Therefore polarized photoelectrons can only occupy states with the same spin orientation. In a ferromagnetic material the bands are spin split, e.g. there are more empty states for one spin
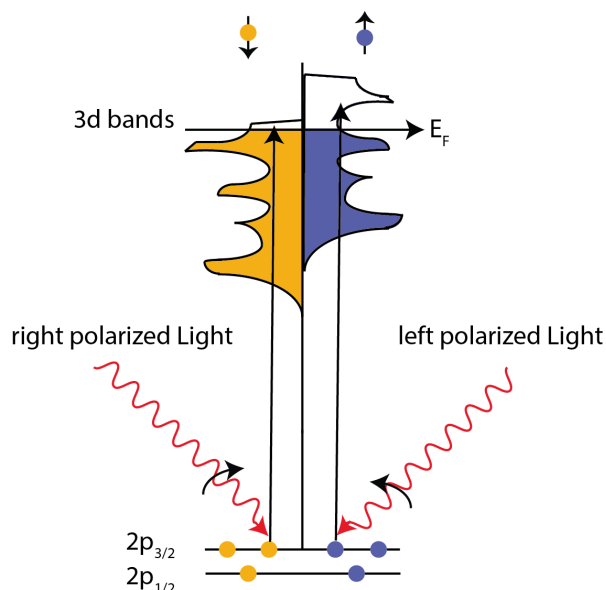
Figure 2.12: Schematic representation of the XMCD process. First the polarized X-rays create spin-polarized photoelectrons. In the second step the photo-electrons are detected by the exchange split valence shell.

direction than the other. Thus, the accepting, unoccupied band acts as a spin detector.

In the experiment, the XMCD signal is recorded by taking two XAS spectra with either reversed helicity of the X-rays or reversed magnetization of the sample. Experimentally these two sets of XAS spectra are identical. In order to detect and cancel out artefacts in the XMCD measurement, both XMCD signals can be recorded and compared to each other. The XMCD signal is then given by the difference between the two XAS spectra:

$$\mu_{XMCD}(h\nu) = \mu_-(h\nu) - \mu_+(h\nu)$$

This magnetization detection technique has the advantage that it can detect magnetic moments element - selectively. Because XAS spectra are environment sensitive the XMCD spectra are environment - sensitive as well. Thus, samples can be studied in terms of different cation species, cation distribution and stoichiometry in a given complex system.

2.6 Proximity effect

In the most general words: "The proximity effect refers to the influence that an ordered state has on a nearby system." taken from [51]. In other words, the proximity effect is a general term for the effect of emerging or transferring physical properties observed at heterointerfaces. Hetereointerfaces are interfaces formed by two different materials. One prominent case is the 2D electron gas formed at the interface of the two insulating materials $LaAlO_3$ (LAO) and $SrTiO_3$ (with a TiO_2 terminated surface), which was found by A. Ohtomo and H.Y. Hwang in 2004 [5]. The 2D electron gas was found to be stable against oxygen annealing and further TEM studies confirmed ultra - high sharp interfaces with low ion intermixing [52, 53]. The explanation up until now is that the 2D electron gas is formed due to the transition of a polar

material to a non-polar material, a result of the proximity effect [54]. In order to compensate for the polar discontinuity, i.e. the build-up of potential in the LAO film, an electronic reconstruction introduces electrons into the titanium 3d band of the STO confined at the interface.

Another well studied and still investigated proximity effect is the so called "magnetic proximity effect". It covers several different types of interfaces which all involve at least one magnetically ordered system. A highly promising system for the spintronic community is the $Pt/Y_3Fe_5O_{12}$ (YIG) system. YIG is a ferromagnetic insulator and platinum is a metal with a strong spin-orbit coupling. The exchange mechanisms at the interface results in induced spin polarization of the electrons in the platinum [55, 56]. Another high interest interface group are the superconducting - ferromagnetic interfaces. One example is the $YBa_2Cu_3O_7$(YBCO)/LSMO multilayer system at which, due to charge-transfer driven orbital ordering at the interface, the magnetic moments in the LSMO are reduced and a magnetic moment is induced into the Cu of the YBCO [51, 6].

The proximity effect can also be tracked down in oxide heterostructures. For example the EuO/STO heterostructure exhibits a proximity effect [57]. The insulating EuO is a Heisenberg ferromagnet below $T_c = 70\,°C$ and STO is diamagnetic and insulating. However, in the growth process, just Eu metal is deposited on top of the STO. The Eu is a very powerful reducing agent. Thus, oxygen is removed from the STO to build EuO, leaving oxygen vacancies which introduces free electrons in the 3d band of the titanium. As a result of the proximity effect the ferromagnetic EuO induces a magnetic moment into the titanium of the STO's interface.

Chapter 3

Experimental methods

In this chapter, the main experimental methods used to fabricate and investigate the complex oxide heterostructures (Au/) $NiFe_2O_4$/ $SrTiO_3$ and (Pt/) $La_{0.3}Sr_{0.7}MnO_3$/ $SrTiO_3$ are presented. This chapter is divided into two sections. The first section presents laboratory experimental set-ups and the second section presents the experimental methods, that are performed at synchrotons.

3.1 Laboratory methods

The laboratory methods depicted in this section are used to fabricate and characterize the samples in order to optimize the oxide film quality. Short descriptions of the general working principle and the main parameters will be presented.

3.1.1 Pulsed Laser Deposition

Complex thin oxide film growth was obtained by pulsed laser deposition (PLD). The set-up of the PLD growth chamber provided by the $PGI - 7$ is shown in figure 3.1**a)** and a schematic growth process is illustrated in figure 3.1**b)**. During PLD, the target material, which is usually a pressed, stoichiometric ceramic disc of the desired film material, gets ablated by high
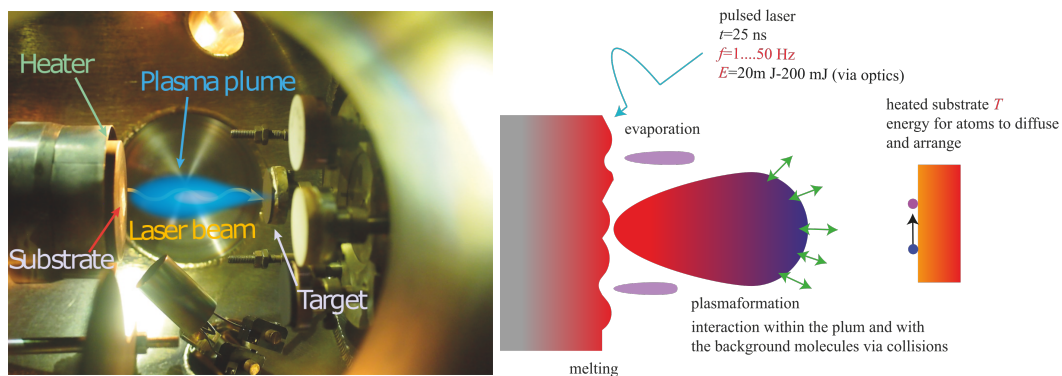
Figure 3.1: a) The pulsed laser deposition set-up in the *PGI-7* lab taken from [16]. **b)** Schematic illustration of the pulsed laser deposition and its growth parameters.

energetic nanosecond laser pulses. The deposition process takes place in controlled vacuum conditions with a base pressure of the chamber of $8 \cdot 10^{-7}$ mbar. Oxygen and Argon gas can be mixed and adjusted to chamber pressures of 10^{-2} to 10^{-5} mbar. The laser pulses are generated with a nanosecond 50 W KrF-laser with a wavelength of $\lambda = 248$ nm, pulse length of 25 ns and an adjustable repetition rate of $f = 1 - 50$ Hz. The laser spot on the target material is adjusted via a beam cutter and a lense outside of the chamber to a rectangular spot of 0.8 mm x 3.5 mm. The laser pulse is dampened by the lense and the entry window by 50%. The laser energy measured before entering the lense and the entry window provide a energy range of 50 mJ to 150 mJ. These laser pulses generate a plasma plume of neutral and ionized particles of the target. The particles of the plasma plume nucleate on the surface of the substrate, which is placed at a distance of 5.5 cm from the target. The substrates are glued with silver paste on top of a heater which make temperatures between room temperature and 750 °C available. Thus, the thermal energy of the heated substrate provides for a sufficient mobility of the atoms to move on energetically favoured positions, which results in an ordered growth. More details on the growth process can be found in Ref. [58]. The growth parameters have a strong impact on the growth and the properties of the complex oxide thin films. Thus, the laser fluence F_{dep}, the growth pressure p_{dep}, the gas mixing ratio, the substrate temperature T_{dep} and the laser pulse repetition rate f have to be optimized for each new material system.

3.1.2   Electron beam physical vapor deposition

The Electron Beam Physical Vapor Deposition (EBPVD) is used to fabricate the structure for the in-situ biasing HAXPES measurements of the oxide heterostructures in chapters 6 and 7. In figure 3.2, a sketch of the EBPVD experimental set-up is shown. Via a electric current of $I = 1 - 300$ mA, which runs through the tungsten filament, an electron beam is given off and the intensity is adjusted. A magnetic field controls the direction of the electron beam in order to hit the the target material and heat it. The target material is positioned on a water cooled holder to cool the ceramic pot and the material gets evaporated into the top direction. When the pressure in the chamber is low the target material can move freely with little collisions to the substrate material. The chamber pressure was held below $p = 10^{-6}$ mbar for the EBPVD. A Quadrapole Mass Spectrometer (QMS), which is placed near the substrate in the deposition path, measures the deposition rate and thus the thickness of the depositioned material is controlled. By using masks on top of the substrates it is possible to structure samples.

3.1.3   Atomics force microscopy

Atomic force microscopy (AFM) is used to monitor the surface properties of substrates and deposited films. The AFM images taken in this thesis were recorded in the AC-Air tapping mode of the *Asylum Cypher AFM* with non
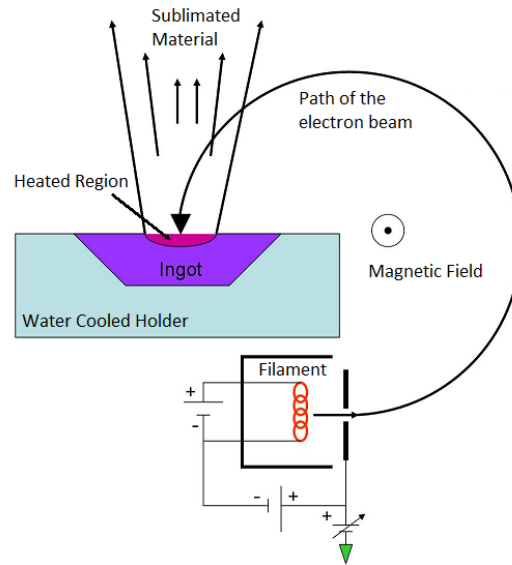
Figure 3.2: Sketch of the experimental set-up of the electron beam physical deposition taken and altered from [59].

conducting and non magnetical tips [60]. The scan parameters were always set to 5μm $\times$ 5μm scan size with 512 scan lines, a repetition rate of 5 Hz and a free amplitude of 1 V. The AFM raw data images are analysed with the *Gwyddion* software. The raw data are treated with mean plane subtraction, row aligning and a 3-point level to the largest terrace. The RMS of the largest terrace is readout as roughness. A false colour-scale from black to white is used to display the recorded z-range of the AFM images.

3.1.4 X-ray lab source measurements

X-ray lab measurements are essential tools for studying the structural properties of thin film heterostructures. The three techniques X-ray diffraction (XRD), X-ray reflectivity (XRR), and "rocking curve" were utilized at the four cycle goniometer *Philips MRD Pro* provided by *PGI-7*. The X-ray anode is monochromatized and uses a Cu anode. Through the monochromator Cu K_{α_1} and Cu K_{α_2} radiation with wavelength of $\lambda_1 = 1.540059$ Å and $\lambda_2 = 1.541070$ Å is transmitted. The intensity ratio of the Cu K_{α_1} and Cu K_{α_2} radiation is 2:1.

X-ray diffraction

X-ray Diffraction (XRD) was performed in the 2Θ - Θ Bragg-Bretano geometry. Full scans were taken from 10° to 110° in order to identify the structure and ensure the single crystallinity of the grown thin films. Due to the structure factor of the materials symmetries not all reflexes are allowed. In the case of the perovskite structure of single crystalline (001) $SrTiO_3$ only (00l) reflexes are allowed while for spinel structure of the single crystalline (001) $NiFe_2O_4$ (00l) with l restricted to even numbers are allowed. In addition to the full XRD scans, detailed XRD scans around the STO (002) and NFO (004)

reflex were measured taken from 39° to 51°. The scans were corrected to the (002) peak of the STO Cu K_{α_1} line. After extracting the reflex position of the NFO (004) reflex by fitting a Gaussian to the peak the out-of-plane lattice constant was calculated by using the Bragg's law shown in equation 3.1 [61]. The symbol n denotes the order of the reciprocal lattice vector of the corresponding reflex and equals 1 for the chosen reflexes. Due to the broadness of NFO reflexes, the two Cu K_α lines cannot be dissolved. Thus, a weighed mixed wavelength is used with $\lambda = (2\lambda_1 + \lambda_2)/3$. In equation 3.2, the inverse lattice spacing d_{hkl} and its dependence of the Miller indices (for a cubic system) are displayed.

$$n \cdot \lambda = 2 \cdot d_{hkl} \cdot sin(\Theta) \tag{3.1}$$

$$d_{hkl}^{-1} = \sqrt{\frac{h^2}{a^2} + \frac{k^2}{b^2} + \frac{l^2}{c^2}} \tag{3.2}$$

Rocking curve

In order to record a rocking curve of a reflex, the 2Θ is fixed to the ideal position and the ω angle is scanned. In theory, for an ideal single crystal with perfectly ordered atomic planes, only the set of $2\Theta - \omega$ with $\omega = \Theta$ fulfils Bragg's law and gives a result. Thus, the rocking curve would be a delta function. In reality, even for a perfect crystal, the width of the rocking curve is determined by the beam geometry and the spectral width of the source. Defects, such as dislocation density, mosaicity, curvature, misorientation, and inhomogeneity, lead to additional broadening related to more $2\Theta - \omega$ combinations fulfilling Bragg's law. Therefore, the width of the rocking curve is directly linked to the quality of the single crystal thin films.

X-ray reflectivity

The X-ray reflectivity (XRR) of a heterostructure reveals the thickness of the thin layers of thicknesses in the range of approximately 2 nm to 100 nm. XRR are recorded in the $2\Theta - \omega$ configuration with small incident angles in the range of $2\Theta \approx 0 - 7$. The X-rays are reflected from the interfaces between layers because of the difference in optical density. The reflected beams interfere with each other and produce a characteristic oscillation the Kiessig fringes in the intensity. The angle difference between two interference maxima can be used to obtain the thickness by the relation

$$d = \frac{\lambda}{2 \cdot sin(\Delta\Theta)} \qquad . \tag{3.3}$$

In this thesis, the software *X'Pert reflectivity* and *GenX* are used to determine the thickness of the oxide layer. Both programs need the information of the beam geometry, the assumed materials of the heterostructure, layer iteration, roughness and material densities in order to simulate the XRR. The roughness is extracted from the AFM measurements of substrate and deposited

film and the material densities are taken from the literature. Layer iteration and beam geometry are known.

3.1.5 Superconducting quantum interference device

For the characterization of the magnetic response of the NFO films, the Superconducting Quantum Interference Device (SQUID) is used. With a magnetic resolve of signals down to 10^{-7} emu, an MPMS XL SQUID by *Quantum Design*, provided by the JCNS-2/PGI-4, is used. The sample chamber can be cooled down to 2 K. In figure 3.3, a schematic experimental setup of the SQUID magnetometer is shown. The sample is positioned between two pick-up coils and a superconducting magnet. Above and below a counter-clockwise wound loop are positioned as second derivative coils. The coils consist of one superconducting wire and are configured to be a second derivative gradiometer. Thus, a magnetic background noise, which is measured by all four coils, will be cancelled. The sample is positioned so that the film in-plane direction is parallel to the magnetic field. The sample is moved through the pickup coils. The magnetic moment of the sample induces local changes of the magnetic flux. The SQUID acts as a linear current to voltage converter that allows to detect this change in magnetic flux as variation of the SQUID output-voltage utilizing two Josephson junctions. The voltage is then recorded as a function of the sample position. The resulting voltage curve is fitted with the theoretical curve of an ideal dipole and the magnetic moment of the sample can be extracted.
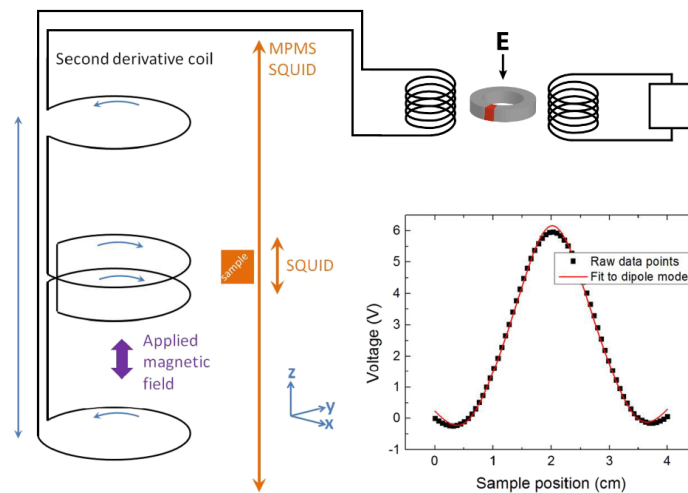
Figure 3.3: Schematic experimental setup of the SQUID magnetometer altered from [16, 62].

3.2 Synchrotron methods

The Synchrotron measurement methods described in this section are used to investigate the chemical composition, occupation and interface of the $NiFe_2O_4$ /$SrTiO_3$ heterostructures. Short descriptions of the beamline setup and the main parameters will be presented.

3.2.1 BESSY II - HAXPES

The KMC-1 beamline at BESSY II, Berlin is equipped with a hard X-ray photoelectron spectroscopy (HAXPES) endstation called HIKE. Photon energies of $h\nu$ =2 keV up to 10 keV are used to probe the sample and excite photoelectrons with high kinetic energy. The monochromator of the beamline is a double-crystal monochromator with Si (111), Si (311) and Si (422) crystals [63]. The monochromator achieves an energy resolution of ΔE =200 meV at 6 eV with the Si (422) crystal and ΔE =50 meV using Si (333) [64].
In the scope of this thesis, HAXPES measurements were performed at photon energies $h\nu$ =4 keV with the Si (311) crystals. An energy resolution of the ΔE =150 meV was achieved. The sample was mounted in normal emission configuration geometry. Passing energy was 200 eV, energy step size of 0.1 eV and depending on the core level a set number of sweeps, which were automatically added up and averaged.

3.2.2 DIAMOND - X-ray magnetic circular dichroism

X-ray absorption spectra (XAS) were recorded at the high field magnet system endstation of the I10 beamline at the *DIAMOND Light Source, Didcot*. Magnetic fields of $B = \pm14$ T and temperatures between $T = 2 - 420$ K can be applied to the samples. The magnetic field is directed along the direction of the X-ray beam [65]. Circular polarized X-rays with energies of $E = 400 - 1600$ eV are available and enable the possibility to measure dichroism effect, namely the X-Ray Magnetic Circular Dichroism (XMCD). In order to minimize the error due variations of the photon energies or film damage, multiple XAS with switching polarization are recorded. XAS are detected by total electron yield (TEY) and fluorescence yield (FY) simultaneously. The TEY is mostly surface sensitive. This is achieved by grounding the electrically isolated sample through a sensitive current amplifier. The FY gives more sensitivity to the bulk of the sample. This is achieved with two X-ray fluorescence diodes in back-scattering geometry close to the sample. The near grazing incidence geometry R =80° is chosen, as the thin oxide films are expected to have a mostly in-plane easy axis of magnetization. Hysteresis of the samples can be recorded by automatically sweeping the magnetic field and switching the X-ray polarization at each point from positive to negative for a given photon energy of strongest dichroic signal and background noise.

3.2.3   PETRA III - monochromatic reciprocal space mapping

Monochromatic reciprocal space maps (RSM) and XRDs were recorded at the High Resolution Diffraction beamline P08 at *PETRA III, DESY, Hamburg* by Florian Bertram [66]. This beamline is built to suit for investigation of bulk samples, surfaces and interfaces. A sample can be investigated with photon energies between 5 keV and 30 keV and a scanning interval of 100 eV. In the scope of this thesis the high precision 6-circle diffractometer is used. High precision measurements of strain, stress, and lattice distortions relative to the lattice parameter can be probed with variations of 10^{-4} to 10^{-6}.

3.2.4   PETRA III - in-operando HAXPES

In the scope of this thesis, in-operando hard X-Ray photoelectron spectroscopy (HAXPES) was measured at the HAXPES endstation P09 at *PETRA III, Hamburg*. Since 2018 the HAXPES endstation has been relocated at the P22 beamline at *PETRA III*. The endstation is specifically set up to make use of HAXPES in an energy range from 2.4 keV - 10.5 keV [67]. This technique is ideally suited to investigate complex material systems and buried interfaces of multilayer heterostructures. The HAXPES is recorded with a SPECS Phoibos 225 HV wide angle lens option ($\pm$ 30°) electron spectrometer. The Omicron 5-axis manipulator has an integrated Helium-cryostat. Therefore temperatures of 45 K to 400 K are achievable. Typical energy resolution ranges from 100 meV to 400 meV.

In figure 3.4 **a)**, the manipulator head with the four contact screws is shown taken from [68]. This four screws are connected with wires that lead out of the high vacuum chamber outside the hutch. The wires in the chamber have a current limit of $I \leq 2$ A. These wires can then be connected to the *Agilent B2961A/B2962A6.5 Digit Low Noise Power Source* (Agilent) [69], which is used as a voltage source. In figure 3.4 **b)** a sketch of the in-situ biasing holder and
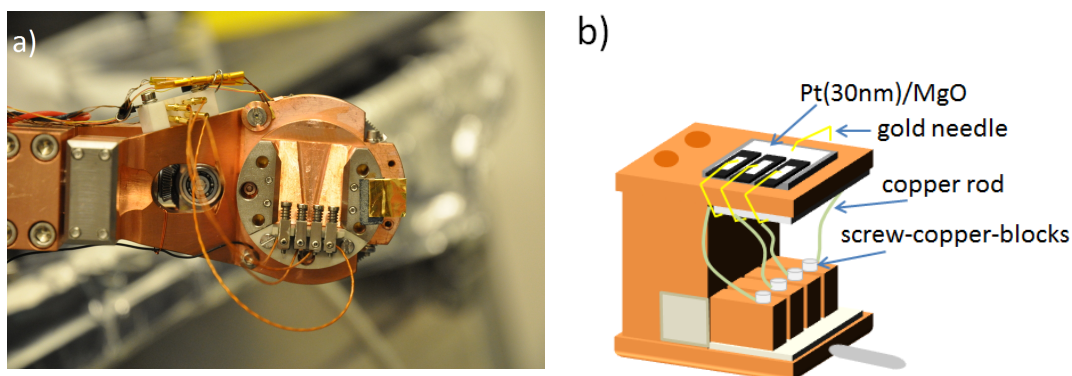
Figure 3.4: a) Manipulator head with 4-contact sample holder compartment [68]. **b)** Sketch of the in-situ biasing holder. Three samples top electrodes are connected via copper wires to the screw contacts. The fourth contact is used to background contacting via a Pt(30 nm)/MgO plate.

three contacted samples is shown. One of the contacts is set to ground, contacting the back side of the oxide heterostructures. In order to set the back sides of all oxide heterostructures to ground with a single contact and decouple it from the ground of the whole measurement set-up, the backside of the oxide heterostructures is glued via silver paste to a highly insulating, 10 mm × 10 mm MgO substrate with 30 nm of platinum (Pt(30 nm)/MgO) on top. Thus, if the platinum plate is contacted all the backsides of the heterostructures are automatically grounded. The three other contacts are used to contact the top electrodes of three separated heterostructures. They are contacted via three gold needles and copper wires to three electrically decoupled screw-copper-blocks. A constant voltage is applied between the top electrode and the backside electrode of the oxide heterostructures. Given that the backside of the sample is always grounded the voltage gets always applied to the top electrode. With applied voltage the HAXPES measurement is then recorded, termend "in-operando" HAXPES. In the scope of this thesis, the in-operando HAXPES was performed with a photon energy of $h\nu = 6$ keV at room temperature in the normal emission geometry. The energy resolution was set to 0.1 eV.

Top-electrode structuring

The structuring is a two step process: With a first mask, a 4 nm × 2 mm × 3.6 mm metal patch is grown with a film thickness of 4 nm. In the next step the sample is removed of the EBPVD and the mask is changed ex-situ for the second mask. In figure 3.5 **a)**, the dimensions of the finger structure is displayed. The fingers are 1.5 mm long and the center fingers and the space between the fingers have a width of 0.2 mm. This finger structure is deposited on top of the first deposited metal rectangular patch with a width of 40 nm. In figure 3.5 **b)** a structured and uncut oxide heterostructure is displayed.
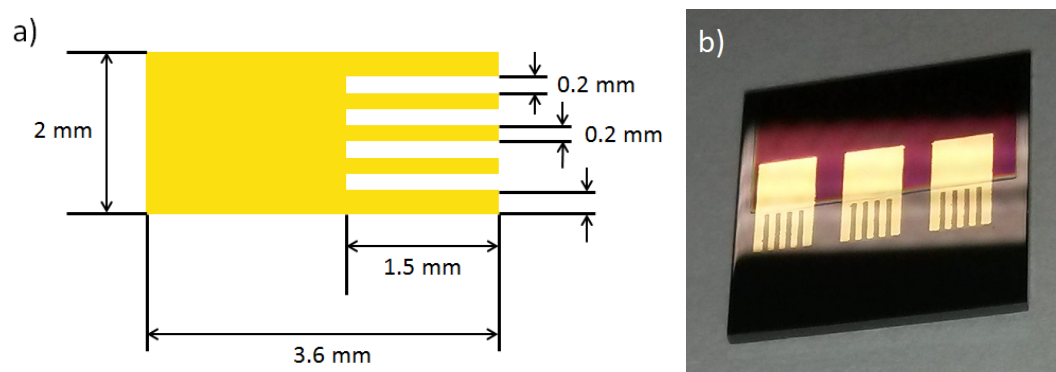
Figure 3.5: a) Finger structure dimensions. **b)** Finished structured oxide heterostructure of a not broken substrate.

Chapter 4

Growth of thin $NiFe_2O_4$ films

This chapter deals with the pulsed laser deposition (PLD) growth and the characterization of ultra thin $NiFe_2O_4$ (NFO) films grown on $SrTiO_3$ (STO). Ideally, the NFO thin films on STO should maintain bulk-like properties, in particular ferrimagnetic and insulating behaviour. The complex spinel structure of NFO is highly sensitive to structural and chemical disorder that can strongly alter its properties [70, 71]. Thus, the growth of NFO on STO is a special challenge as the NFO has a lattice constant of 8.338 Å which is more than double the size of the STO lattice constant with 3.905 Å. This results in a compressive strain of 6.8%, which can introduce defects and may also influence the chemical composition and occupation.

The chapter can be divided into two parts. In the first parts, the growth conditions of NFO, which were found by M. Hoppe *et al.* at the same PLD set-up, are rechecked and optimized if needed [72].

In the second part of this chapter, the optimized NFO/STO heterostructures are checked by hard X-ray photoelectron spectroscopy (HAXPES) recorded at BESSY II and DESY, as well as by X-Ray absorption spectroscopy (XAS) recorded at DIAMOND. Both techniques are element selective and give insights to the cation valence and the occupation of the spinel structure sites in the NFO films.

4.1 $NiFe_2O_4$ PLD growth optimization

M. Hoppe *et al.* established a single crystalline and stoichiometric growth of $NiFe_2O_4$ (NFO) on-top of $SrTiO_3$ (STO) at the same PLD set-up, which is used in this thesis. Hence, the growth conditions temperature, laser frequency, and growth pressure can be assumed to be unchanged from the previous findings, which are discussed in detail in [16].

Thus, they are kept constant at

- $T = 635\,°C$,

- $p = 3.9 \cdot 10^{-2}\,mbar$,

- $f = 2\,Hz$,

- 90 minutes annealing at growth pressure & temperature.

This leave to be set the growth conditions of laser fluence and growth pressure composition, which will be altered systematically from the starting point $F = 1.4 \frac{J}{cm^2}$ and 25:75 Ar:O$_2$ ratio. The resulting NFO films are probed with a variety of lab methods in order to find the optimal set of growth conditions that yield high quality NFO films with the desired properties in surface morphology, crystallinity and magnetic behaviour.

4.1.1   Preparation of TiO$_2$ - terminated SrTiO$_3$ substrates

In this thesis, single crystalline SrTiO$_3$ (STO) substrates in (001) orientation with a Nb doping of 0.1 % and 0.5 % are used. The substrates are supplied by *Crystec GmbH, Berlin* with polished surfaces and a miscut angle to the orientation of 0.05° to 0.1°. Due to the miscut angle and the perovskite structure, which is formed by layers of SrO and TiO$_2$ in the (001) direction, the STO comes with a characteristic step surface. However, the substrates, as they are received, have an unordered step surface consisting partially of TiO$_2$ and SrO atom configurations. In order to get a defined surface, which is built up largely of a closed TiO$_2$ surface, the Nb:STO has to undergo an etching procedure with buffered hydrofluoric acid (BHF) and an annealing step.
This etching procedure consists of two main steps. The first step is to rinse the samples with water. The SrO has a higher water affinity than TiO$_2$ and forms stable Sr(OH)$_2$ [73, 74]. Thus, the etching with BHF becomes more effective on the SrO layers than on the TiO$_2$ layers. The second step is the etching itself. The main point is to choose the right etching time. A too short etching time can result in an incomplete TiO$_2$ - surface termination and thus to a non - smooth step surface. A too long etching time produces deep etching holes of several nm [75, 76]. The 0.1%Nb:STO are etched for 90 seconds. The resulting surface morphology in the 5x5 µm AFM image of figure 4.1 **a)** shows a flat surface with uniformly evolving steps of consistent height of one STO unit cell, but it has also some etch holes. The depth of the etch holes was found by investigating line scans of the AFM image. The line scan in figure 4.1 **b)** shows consistent step heights of 3.9 Å, the height of the STO unit cell. The line scan includes an etch hole which is reflected in a deep dip of $\approx$ 2.6 nm. These uniformly flat STO surfaces are ideal for growth studies, but the deep etch holes can lead to short circuits in electrical devices. Thus, 0.5%Nb:STO was etched for 30 seconds only. The resulting surface morphology is shown in figure 4.1 **c)**. The steps evolve more unevenly, but still have a consistent height of one STO unit cell. In contrast, the etch hole depth, measured in the line scan in figure 4.1 **d)**, is only 0.9 nm making electrical devices more feasible.
The annealing step is the second main step in achieving a TiO$_2$ terminated ordered STO surface. If the temperature is too high or the annealing time is too long, step bunching will occur, i.e. a step surface with step height of more than one STO unit cell height. Is the temperature too low or the annealing time too short it will lead to unordered steps and even island are possible. The optimal annealing conditions for the doped STO samples with the orientation miscut angle of 0.05° to 0.1° are found to be a temperature
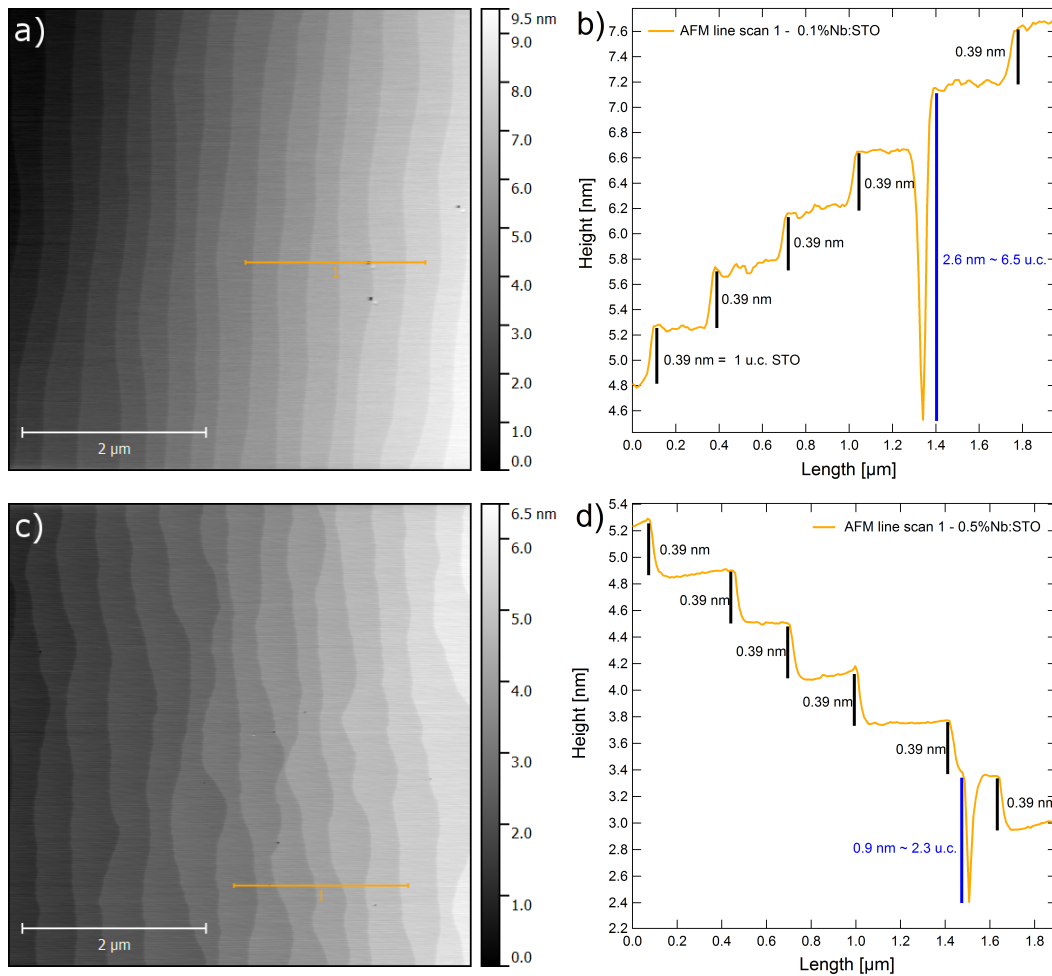
Figure 4.1: a)/c) Surface morphology of a 0.1%Nb:SrTiO$_3$/ 0.5%Nb:SrTiO$_3$ substrate after etching for 90 seconds/30 seconds and annealing recorded with the Cypher AFM. In yellow the position of the line scan is marked. **b)/d)** Line scan of the 0.1%Nb:STO/ 0.5%Nb:STO substrate averaged over 5 lines. In black the height of a STO unit cell is marked. In blue the height of an etch hole is marked.

of 950 °C and an annealing time of 2.5 hours at atmosphere with an ramping time of 1.5 hours.

4.1.2 Laser fluence: Stability of NiFe$_2$O$_4$

First the influence of the laser fluence used in the PLD growth process on the surface, structural and magnetic properties of the NFO films are investigated. In general, it is desired that the stoichiometry of the target material is transferred to the oxide film. But this is highly dependent on the right set of growth parameters as well as the target material. In some cases, it is even favourable to use a target material of a different stoichiometry and structure than the film. For example, Fe$_3$O$_3$ thin films grown on STO can be obtained by using a ceramic target of α-Fe$_2$O$_3$ [1, 77]. The laser fluence is one growth parameter that influences the strength of the ablation of the target material

and, in combination with the background growth pressure, also the cation scattering in the laser plume. One prominent example for the influence of the laser fluence can be found in the homoepitaxial growth of STO on STO where the kinetic energy of the ablated species contributes significantly to the stoichiometry of the STO films [78].

The laser fluence depends on the energy of the pulsed KrF Laser and on the spot size on the target material. The laser energy is measured before the optics and in regular time intervals in the chamber. This ensures that the measured energy can be related to the effective energy in the chamber after passing through a lens and the laser entry window. Thus, the laser fluence is gained by dividing the measured energy before the chamber by the spot size and multiply it with the ratio between the actual energy reference inside the chamber to the reference energy outside. A laser fluence series was grown at constant conditions of $p = 3.9 \cdot 10^{-2}$ mbar, $T = 635\,°C$, $f = 2\,Hz$, Ar:O$_2$ of 25:75 and a post-annealing procedure of 90 minutes in vacuum. The laser fluence range from 1.29 J/cm^2 to 1.52 J/cm^2. The resulting films are slightly increasing in thickness for increasing laser fluence from 20.5 nm to 23.0 nm.

Surface morphology

For the in-situ biasing study, which is represented in chapters 6 and 7, an atomically sharp film surface is crucial in order to diminish effects due to intermixing of film and metal electrode at the interface and varying film thickness. Thus, after the deposition of the NFO, the surface properties are measured with the *Asylum Cypher* atomic force microscope (AFM). The AFM scans are performed in squares of 5 μm x 5 μm AFM images in the AC-Air mode. In figure 4.2 AFM images of the fluence series are shown. They are ordered from the lowest laser fluence in **a)** of $F =$1.29 J/cm^2 to the highest in **d)** of $F =$1.52 J/cm^2. Within the laser fluence series all samples have in common that the characteristic step surface from the STO is transferred to the film and that the film surface is closed despite the 6.8% compressive strain from the substrate. The Root Mean Square (RMS) of the surface is taken at of the broadest step and is used as a representation of the surface roughness. The RMS for the two samples with the high fluencies is the same as the roughness of the STO substrates. A slightly increasing of the roughness can be seen with decreasing laser fluence. Especially for the lowest laser fluence the higher roughness is reflected in a softened step edges compared to the substrates and the other films.

Structural and crystallinity study

The structure and the crystallinity of the deposited NiFe$_2$O$_4$ thin films of the fluence series are studied by rocking curves and X-ray diffraction (XRD) in a $2\Theta - \Theta$ configuration with the scattering vector parallel to the surface. XRD surveys are taken from $2\Theta =$20° to 100°. All samples of the fluence series show only two film reflections at $2\Theta \approx 43$ and $2\Theta \approx 95$, which correspond to the (004) and (008) NFO reflection for a NFO film grown in (001) direction.
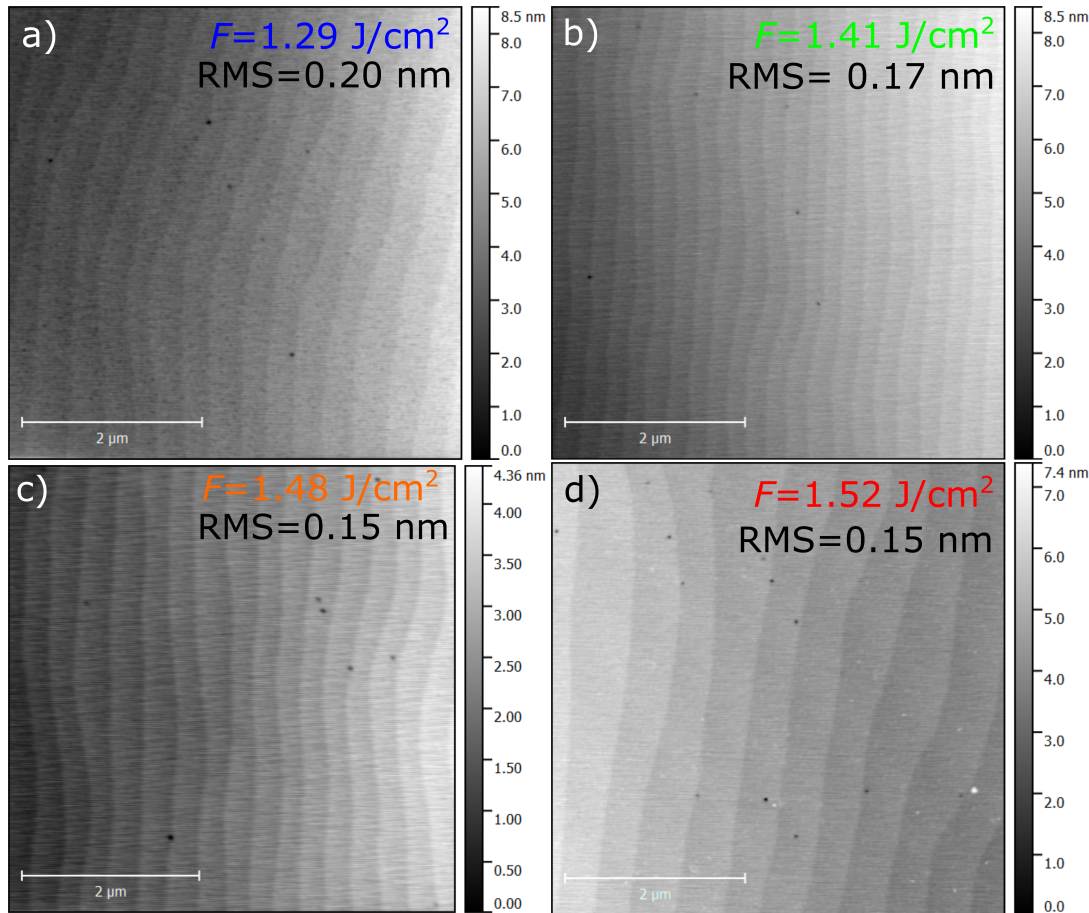
Figure 4.2: Surface morphology of (22 ± 1) nm NiFe$_2$O$_4$/SrTiO$_3$ heterostructures, which are grown at different laser fluences. The laser pulse frequency, the growth pressure and the gas mixture composition of Ar:O$_2$ are kept constant. The laser fluence increases from **a)** to **b)**. The fluence and the roughness is shown in each image.

Thus parasitic phases can be excluded in the NFO and all samples are considered as single crystalline. In figure 4.3 the XRD spectra of the NFO/STO heterostructure of the fluence series are shown. The XRD spectra are normalised to the (002) reflex of STO. The STO (002) reflex is composed of two peaks. This two peaks correspond to the Cu K α_1 and Cu K α_2 wavelengths from the Cu anode of the *Phillips MRD Pro* diffractometer and therefore can only be resolved for bulk single crystalline materials. From bottom to top the laser fluence increases for each spectra. Next to the (002) reflex of STO substrate all films show the (004) reflex of the NFO. The film peak position for a bulk NFO (004) reflex is indicated with the black line. Clearly all the NFO film peaks are shifted from the ideal bulk NFO position. After applying the Bragg equation 3.1 to the (004) NFO film peaks' positions the out-of-plane lattice constant is obtained and displayed in the inset of figure 4.3. Throughout the laser fluence series, all NFO films show a larger out-of-plane lattice constant than the NFO bulk. Even though the NFO films are 22 nm thick and should be fully relaxed, the NFO films are still influenced by the compressive
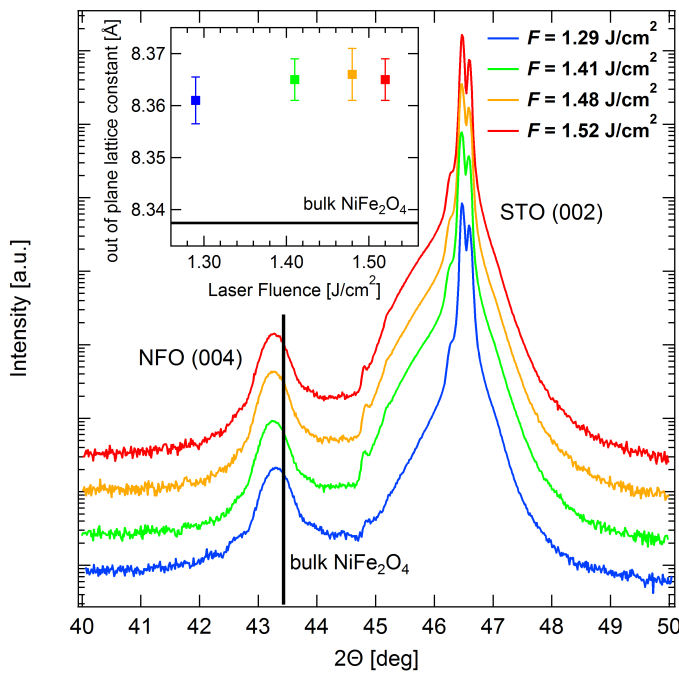
Figure 4.3: XRD scan of the (004) reflex of NiFe$_2$O$_4$ films, which are grown at various laser fluences, and the (002) reflex of SrTiO$_3$ substrate. The laser fluence increases from bottom to top. The calculated out-of-plane lattice constant are shown in the inset.

strain the STO substrate exerts. Within the fluence series, no trend in the out-of-plane lattice constant can be found. Additionally the absence of the Laue oscillations are a sign of lack of structural homogeneity and an indication for a rough interface.

In order to investigate the influence on the amount of defects rocking curves of the fluence series NFO films have been recorded. In theory for an ideal single crystal with perfectly ordered atomic planes only the set of $2\Theta - \omega$ with $\omega = \Theta$ satisfies the Bragg equation and gives a result. Thus, the rocking
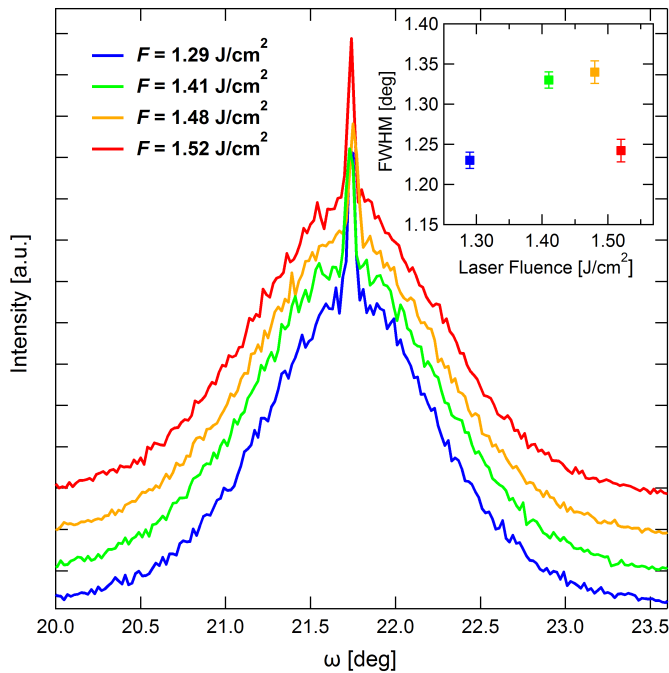
Figure 4.4: Rocking Curve of the (004) NiFe$_2$O$_4$ reflex of NiFe$_2$O$_4$ films grown at various laser fluences. The laser fluence increases from bottom to top. The FWHM of the rocking curves are shown in the inset.

curve would be a delta function. However, defects like dislocation or mosaicity create disruptions in the perfect parallelism of the atomic planes. In this case more $2\Theta - \omega$ sets fulfil the Bragg equation and thus the width of the rocking curve increases. Therefore, the width of the rocking curve is directly linked to the quality of the single crystal. In figure 4.4 the rocking curves of the fluence series with increasing laser fluence from bottom to top are displayed. The thin peaks in the center of the rocking curves can be attributed to (002) STO substrate rocking curve. The FWHM of the rocking curves of each NFO film of the fluence series was determined by fitting a Gaussian to the Rocking Curve. The obtained FWHM are plotted against the laser fluence in the inset of figure 4.4. The FWHMs scatter from 1.22 to 1.35 without any trend in the laser fluence. The FWHMs of the NFO films are quite broad and reflect the high distortion due to the increased lattice match. Still this result is consistent with NFO grown on STO in literature [72, 79, 80].

Magnetic response

In order to detect the magnetic behaviour of the NFO films of the fluence series, magnetic hysteresis were measured at SQUID. In figure 4.5, the substrate - corrected normalised magnetic hysteresis loops of the NFO films of the fluence series are displayed in the magnetic field range of $B = \pm 25\,\text{kOe}$, which emphasize the ferrimagnetic nature of NFO. The hysteresis were taken at a temperature of $T = 6\,\text{K}$, magnetic fields of $B = \pm 40\,\text{kOe}$ parallel to (100) in-plane direction. The diamagnetic contribution of the substrate was subtracted from the hysteresis loops and the remaining signal was normalised to the film volume. The detailed procedure is shown in appendix B. The
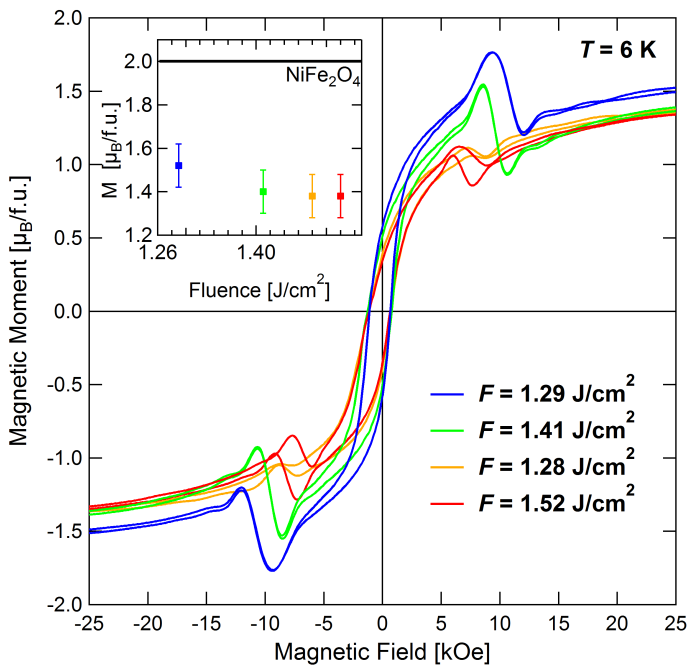
Figure 4.5: Magnetic hysteresis loops of the NiFe$_2$O$_4$ fluence series taken at $T = 6\,\text{K}$ and the magnetic field range of $B = \pm 40\,\text{kOe}$. The saturation magnetization is displayed in the inset.

jumps in the hysteresis loops at magnetic fields of $B \approx \pm 10\,\text{kOe}$ are an arte-fact of SQUID, which fails to measure the region of the zero magnetic moment intercept. Within the fluence series, the coercivity stays constant with $H_c = 870\,\text{Oe}$, which is in line with previous reported coercivity for NFO thin films [81]. The saturation magnetization of the NFO films of the fluence series is shown in the inset of figure 4.5. A slight trend towards higher saturation magnetization with lower laser fluence can be seen. However, compared to the $2\,\mu_B/\text{f.u.}$ of ideal bulk NFO, all the NFO films show a diminished saturation magnetization of $M_s =$1.3-1.5$\,\mu_B/\text{f.u.}$. This can be seen as a direct result of the high defect density of dislocations and anti-phase boundaries in the NFO films due to the high strain from the STO substrate and due to the growth process itself. A high density of dislocations results in stacking disorders and thus the superexchange interaction is suppressed and the magnetic response is weakened. Anti-phase boundaries on the other hand are formed during growth. The spins located at the boundaries of phases with different orientation are highly frustrated and thus can only align at strong magnetic fields. Therefore, the magnetic signal is dampened and the slope of the hysteresis is reduced. Combined with the observation of the missing fluence dependency of the rocking curve, it can be deduced that the defect density, mostly the density of dislocations, is quite stable while the density of the anti-phase boundaries slightly decreases with decreasing laser fluence.

Summary

In summary, the variation in laser fluence yields only small changes in the physical properties of the resulting NFO thin films. The NFO films are single-crystalline and grow along the c axes in (001) direction of the STO. The absence of Laue oscillations in the XRD and the broad rocking curves are a result of a high density of defects. Hysteresis loops measured by SQUID show ferrimagnetic behaviour in all NFO films. However, the saturation magnetization slightly reduces and the slope towards saturation magnetization becomes more shallow with increasing laser fluence. It follows from the rocking curves and the SQUID measurement that the defect density of primary dislocations only changes minimally with no trend in laser fluence. However, the density of anti- phase boundaries may decrease with decreasing laser fluence. AFM images show that the closed terrace surface of the STO substrate surface is transferred to the NFO films. However, the RMS roughness of the NFO films slightly increases with decreasing laser fluence. Thus, there is a trade-off in saturation magnetization for surface smoothness. Therefore an intermediate laser fluence of

$$F = 1.41 \quad \mu_B/\text{f.u.}$$

is used in the following experiments.
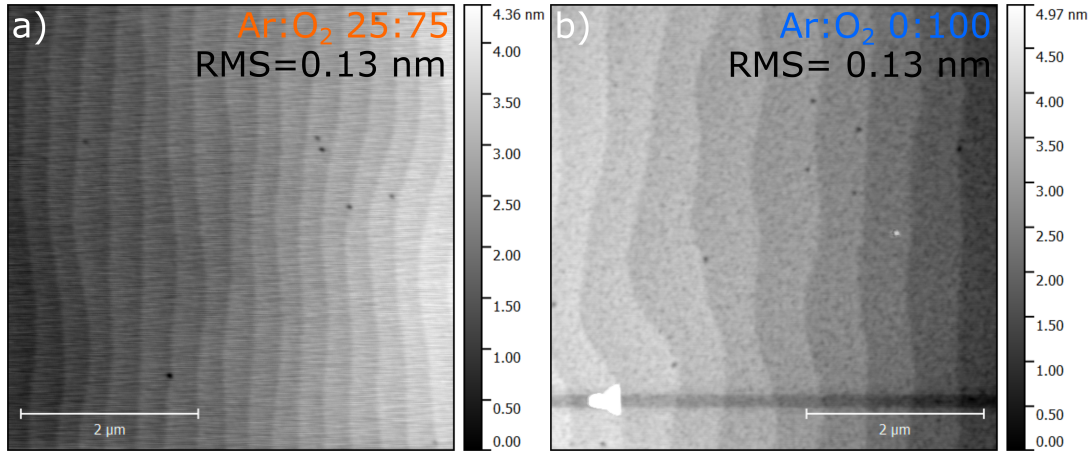
Figure 4.6: Surface morphology of NiFe$_2$O$_4$/SrTiO$_3$ heterostructures grown at **a)** 25:75 Ar:O$_2$ and **b)** 0:100 Ar:O$_2$ growth gas mixture. The growth pressure is kept constant at $p = 3.9 \cdot 10^{-2}$ mbar. The roughness is shown in each image.

4.1.3 Background pressure composition probe

The background pressure has a high impact on the growth process. If chosen poorly the growth can result in off-stoichiometric, polycrystalline or even amorphous oxide films. It acts as an oxygen supply for the growing oxide films and as a kinetic energy regulator. In simple terms if the growth pressure is high, it reduces the kinetic energy of the laser plume species and increases the number of chemical reactions between the laser plume and gas molecules. Thus, the growth pressure also influences the stoichiometry. This is a highly non-equilibrium process. In addition the laser plume dynamics is affected by the type and pressure of the gas [82]. One possibility to partially decouple the influence of growth pressure and oxygen supply from the background on the growth of oxide is to use a gas mixture. In the case of the NiFe$_2$O$_4$ (NFO) growth, M. Hoppe *et al.* identified a gas mixture of argon and oxygen with a ratio of 25:75 as optimal [72]. In the following, the background pressure is kept constant and the influence of a gas mixture ratio of 25:75 Ar:O$_2$ is compared to 0:100.

Surface morphology

After the growth procedure, the NFO films' surface properties were recorded by AFM. The AFM scans were performed in squares of 5 μm x 5 μm and in the AC-Air mode. In figure 4.6 **a)** and **b)**, the AFM images of NFO films are shown which were grown at an Ar:O$_2$ growth pressure gas mixture of 25:75 and 0:100 respectively. Again both samples show the characteristic step surface which was transferred to the film from the STO substrate. Also, the surface is closed despite the 6.8% compressive strain from the substrate. Both samples show some etching holes with similar depths of $\approx$2 nm. In addition one small and one huge contamination was measured (see figure 4.6 **b)**). Inhomogeneous contamination of the surface is usually not related to the
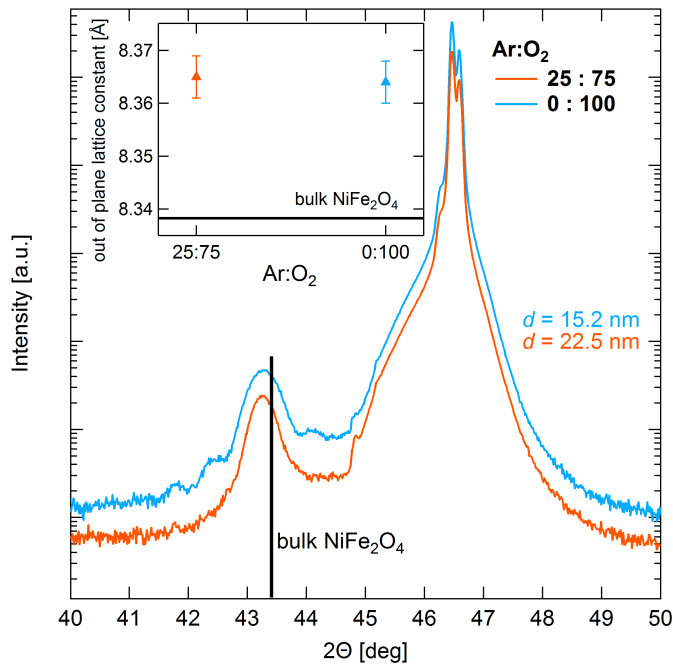
Figure 4.7: XRD scan of the (004) reflex of NiFe$_2$O$_4$ films, which are grown at the Ar:O$_2$ growth pressure compositions of 25:75 and 0:100, and (002) reflex of SrTiO$_3$ substrate are shown. The calculated out-of-plane lattice constant are displayed in the inset.

growth process but rather related to an unfortunate sample exposure to the environment. A close look on the 0:100 Ar:O$_2$ gas mixture sample reveals a somehow perforated surface, especially if compared to the 25:75 Ar:O$_2$ NFO sample. This perforated surface is directly linked to an incompletely grown layer, i.e. the growth stopped before the last layer was finished. The Root Mean Square (RMS) of the surface, which is used as a representation of the surface roughness, is identical for both films. Thus, from the surface morphology point of view the gas mixture composition ratio Ar:O$_2$ of 25:75 and 0:100 yield similarly smooth and stepped surfaces.

Crystallinity Study

The quality of the crystallinity of the 25:75 and 0:100 Ar:O$_2$ growth gas mixture NFO films are investigated and compared to each other via XRD and rocking curve measurements. In figure 4.7, the (002) STO and the (004) NFO XRD reflex of the 25:75 Ar:O$_2$ growth gas mixture in orange and of the 25:75 Ar:O$_2$ in blue are presented. Both XRD spectra are normalised to the position of the STO (002) reflex. The inset shows the determined out-of-plane lattice constant. For both growth pressure composition NFO films the out-of-plane lattice constant is identical, $c_{oop} = (8.365 \pm 0.005)$ Å within errors. This corresponds to an enlargement in lattice constant of 0.3%. Although the NFO films are mostly relaxed, the films still react to the strong compressive strain of the STO substrate with a slightly enhanced out-of-plane lattice constant. The strongest difference in the two XRD spectra are the appearance of the Laue oscillations of the (004) NFO reflex in the 0:100 Ar:O$_2$ growth gas composition. The Laue or thickness oscillations are a sign for a significantly improved structural homogeneity and crystal order [83]. Comparing the (004) NFO reflexes to each other reveals that the 0:100 Ar:O$_2$ sample has
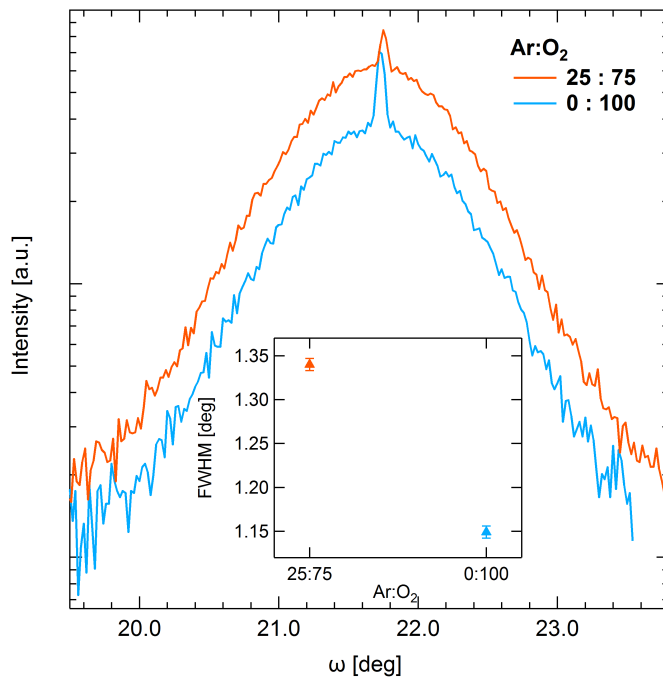
Figure 4.8: Rocking Curve of the (004) NiFe$_2$O$_4$ reflex of NiFe$_2$O$_4$ films grown at the Ar:O$_2$ growth pressure compositions of 25:75 and 0:100. The FWHM of the rocking curves are shown in the inset.

a broader reflex. The 0:100 Ar:O$_2$ growth time has been adjusted to yield 20 nm thickness according to the growth time of the 25:75 Ar:O$_2$ film. However, the XRR analysis of the 25:75 Ar:O$_2$ reveals a film thickness of 15.2 nm, a decrease of 24%. This is reflected in the broadening of the (004) NFO reflex. Therefore the growth rate must have been dropped. In general, the growth rate evolves during the PLD deposition. For NFO it was observed that the growth rate is the highest for film thicknesses below ≈10 nm, and then continuously slightly decreases until ≈30 nm. This does not fit to the XRD observation of the 0:100 Ar:O$_2$. Thus it is related to the change in the growth pressure composition, i.e. the change in the disequilibrium plume dynamics and the oxygen supply during growth. This is not surprising as it is well known that the growth pressure strongly affects the growth overall [84, 85, 86]. Therefore changing partially the gas species will also have a high impact on the whole process.

Rocking curves were recorded in order to investigate the influence of the growth gas composition on the defect density of the NFO thin films. Due to the fulfilment requirement of Bragg's law the width of the rocking curve is linked to the defects like dislocation or mosaicity, which creates disruptions in the perfect parallelism of the atomic planes. Therefore a higher rocking curve width is linked to a higher defect density. In figure 4.8 the NFO films' rocking curves grown at the Ar:O$_2$ growth pressure compositions of 25:75 in orange and 0:100 in blue are displayed. The thin peaks in the centre of the rocking curves can be attributed to (002) STO substrate rocking curve. The rocking curves' FWHM of each NFO film were determined by fitting a Gaussian to the rocking curves. The obtained FWHMs are plotted against the growth gas composition in the inset of figure 4.4. The rocking curves of the NFO films are quite broad and reflect the high distortion due to the increased
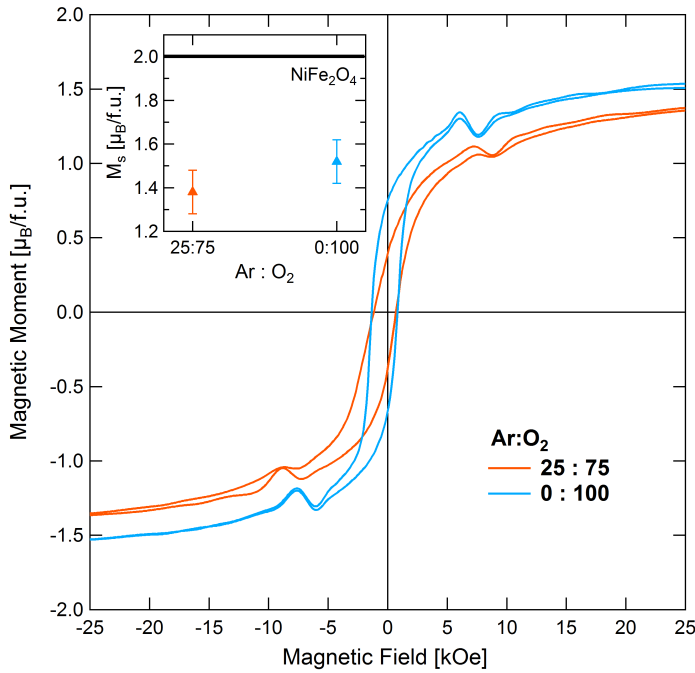
Figure 4.9: Magnetic hysteresis loops of the NiFe$_2$O$_4$ grown at the Ar:O$_2$ growth pressure compositions of 25:75 and 0:100. The hysteresis loops were taken at $T = 6$ K and the magnetic field range of $B = \pm 40$ kOe. The saturation magnetization is displayed in the inset.

lattice match. However, the FWHM of the Ar:O$_2$ growth pressure compositions of 25:75 is with 1.34° obviously larger than the 1.15° of the Ar:O$_2$ of 0:100. Thus, the defect density of the Ar:O$_2$ of 0:100 NFO film must be decreased and the film homogeneity improved. This is consisting with the previous observed Laue oscillations of the XRD measurements. Thus, from the crystallinity quality point of view the gas mixture composition ratio Ar:O$_2$ of 0:100 yield a clearly improved NFO thin films.

Magnetic response

In order to detect the magnetic response of the NFO films, magnetic hysteresis loops were measured by SQUID. The hystereses were taken at a temperature of $T = 6$ K, magnetic fields of $B = \pm 40$ kOe which were set parallel to the (100) in-plane direction. The diamagnetic contribution of the substrate was subtracted from the hysteresis loops and the remaining signal was normalised to the film volume. The detailed procedure is shown in appendix B. In figure 4.9, the NFO films' hysteresis loops grown at the Ar:O$_2$ growth pressure compositions of 25:75 in orange and 0:100 in blue are displayed in the magnetic field range of $B = \pm 25$ kOe, which emphasize the ferrimagnetic nature of NFO. Again the jumps in the hysteresis loops at magnetic fields of $B \approx \pm 10$ kOe are an artefact of SQUID like discussed in the laser fluence study. For both growth gas mixtures the coercivity stays constant with $H_c = 870$ Oe which is in line with the discussed findings in the fluence series and with previous reported coercivity for NFO thin films [81]. The saturation magnetization of the NFO films is shown in the inset of figure 4.9. The NFO film which was grown in pure oxygen has a higher saturation magnetization of $M_s = 1.6 \, \mu_B$/f.u. than the NFO film grown at Ar:O$_2$ 25:75 gas composition of $M_s = 1.4 \, \mu_B$/f.u.. This can be understood as a direct result of the decreased

defect density of dislocations and anti-phase boundaries in the NFO film. A lower density of dislocations result in less stacking disorders and thus the magnetic exchange in the NFO is less disturbed. The density of anti-phase boundaries, which are formed during growth, is also correlated to the slope of the hysteresis loop of the NFO films. The reason is that the spins located at the boundaries of phases with different orientation are highly frustrated and thus can only align at strong magnetic fields. Thus the magnetic signal gets damped and the slope of the hysteresis is reduced with respect to the density of the anti-phase boundaries. Therefore a decreased density of anti-phase boundaries leads to a steeper slope of the magnetic hysteresis like observed for the NFO film grown in pure oxygen. The improved magnetic behaviour fits well with the findings of improved crystallinity by the XRD and rocking curve.

Summary

In summary the change in growth gas composition from 25:75 Ar:O$_2$ to 0:100 Ar:O$_2$ result in improved NFO thin films. The NFO films are single-crystalline and are grown along the c-axes in (001) direction of the STO. However, the appearance of Laue oscillations in XRD and the decreased width of the rocking curve of the NFO film grown in pure oxygen are the result of a decreased defect density. On the other hand the growth rate is decreased by 24% if the NFO is grown in a pure oxygen environment. Hysteresis loops measured by SQUID show ferrimagnetic behaviour in both NFO films. The magnetic behaviour confirms the improved film quality of the 0:100 Ar:O$_2$ grown NFO film. The saturation magnetization and the slope of the hysteresis loops are increased for the NFO film grown in 100% oxygen environment. AFM recording show that the closed terrace surface of the STO substrate surface is transferred to the NFO films independent of the growth gas composition. Also there is no difference in the surface roughness for the NFO film grown in 0:100 or 25:75 Ar:O$_2$ growth gas composition. In conclusion the improved crystallinity and the improved magnetic response of the NFO film grown in pure oxygen leads to a clear choice for the growth gas composition Ar:O$_2$ = 0:100.

4.2   Synchroton study: Chemical composition and occupation of thin NiFe$_2$O$_4$ films

After the NiFe$_2$O$_4$ (NFO) PLD growth conditions are adjusted to achieve high quality thin NFO films, the chemical composition and the chemical site-occupation within the NFO thin films are investigated. For this, the NFO/STO heterostructures were taken to the Synchrotrons *BESSY II* and *DIAMOND Light Source*. At the HIKE beamline KMC-1 of *BESSY II* at the HIKE end station HAXPES measurements of thin NFO films were taken. HAXPES is an element selective probing method with a probing depth at $h\nu$ =4 keV of approximately 20 nm to 30 nm for oxides. The energy resolved recording of the photoelectrons are sensitive to the chemical information of the probed material. At the I10 of the *DIAMOND Light Source*, circularly polarized XAS of the NFO thin films were measured. In the surface sensitive TEY mode XAS measurements have a probing depth limited to approximately a couple of nanometres. The core electrons are excited to unoccupied higher energetic final states by the absorption of high energetic and high flux light. The initial and final states are strongly sensitive to chemical changes and change in the chemical environment. Thus, HAXPES and circularly polarized XAS are both powerful tools in order to investigate the chemical composition and site-occupation of thin films.

4.2.1   HAXPES study of thin NiFe$_2$O$_4$ films

One possibility to get the information about the chemical composition of thin oxide films is by analysing the hard X-ray photoelectron spectroscopy measurements (HAXPES). The HAXPES spectra of the NFO thin films were taken at the HIKE beamline at the *BESSY II*. The beam's photon energy was set to $h\nu$= 4 keV with the monochromator Si crystal set to Si (311). This results in a total resolution of ΔE= 0.15 eV [63]. The incident beam was 5° off normal to the sample which ensures to probe the whole film [46]. After each set of NFO HAXPES spectra, the Au 4f was recorded as well. Au 4f core level were used to correct the energy axis to account for energy shifts of the beam.

In figure 4.10, the Fe 2p HAXPES spectrum of a 23 nm optimized NFO thin film is displayed in red. The experimental Fe 2p is compared to background free theoretical simulations of Fe^{2+} and Fe^{3+} cations contributions at the octahedral and tetrahedral sites of the spinel structure of Fe$_3$O$_4$ taken from [87]. The experimental NFO Fe 2p spectrum shows an Fe 2p$_{3/2}$ peak at 711.0 eV and a Fe 2p$_{1/2}$ broad peak at 724.6 eV. The experimental Fe 2p positions match with the theoretical simulations of the Fe^{3+} residing on octahedral and tetrahedral sites. There is no indication of a Fe^{2+} shoulder at 709 eV at the low binding energy flank of the Fe 2p$_{3/2}$ peak. Each theoretical Fe cation line has a satellite at higher binding energies. The satellite of the experimental NFO's Fe 2p$_{3/2}$ is located at approximately 719.4 eV and the satellite of the Fe 2p$_{1/2}$ is located at approximately 733.6 eV. This satellite peaks are classified as shake-up satellites. They originate in the multi-electron nature of the target material. They generally involve a one photon transition in which one
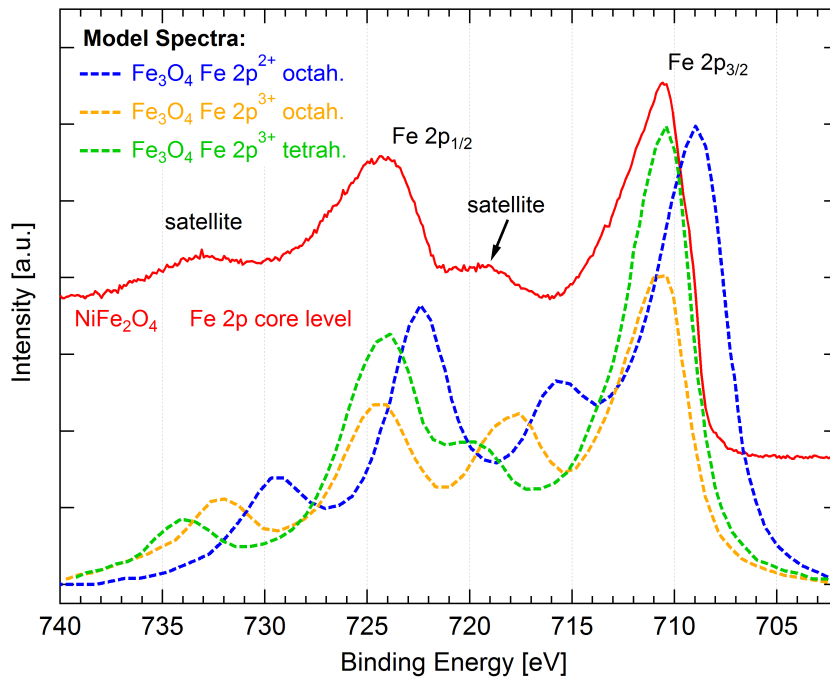
Figure 4.10: In red a Fe 2p HAXPES measured at a photon energy of $h\nu$= 4 keV of a 23 nm thin NFO film is displayed. Simulated Fe 2p spectra for Fe$_3$O$_4$ taken from [87] are shown in dashed lines.

electron is ionized while another electron is excited to a different orbital at the same time [43]. The result is a final ionic and excited state with a higher energy ground state. These satellites are also sensitive to chemical changes and occupation in the crystal lattice. In the case of NFO, the Fe $2p_{3/2}$ satellite is an often used indicator for the chemical state and the occupation [88, 1]. The position of the satellite of the Fe^{2+} on the octahedral site is roughly 716 eV while the Fe^{3+} satellites at octahedral and tetrahedral sites are at 718 eV and 720 eV respectively. In comparison there is no indication of a Fe^{2+} satellite in the experimental NFO Fe $2p_{3/2}$ line. The NFO film Fe $2p_{3/2}$ satellite is located in the region of the two Fe^{3+} satellites. From this it follows that there is no evidence of Fe^{2+} in the 23 nm NFO film and that Fe^{3+} ions occupy tetrahedral and octahedral sites of the spinel. This is in agreement with the expectation of the occupancy in the inverse spinel structure.

In figure 4.11, the Ni 2p HAXPES spectrum of a 23 nm NFO thin film is displayed and compared to Ni 2p HAXPES spectrum of Ni metal and of the NFO PLD target taken from [17]. The Ni 2p HAXPES spectrum of the NFO thin film consists of the Ni $2p_{3/2}$ peak at 855.1 eV and of the Ni $2p_{1/2}$ peak at 872.5 eV. The Ni $2p_{3/2}$ line has a sharp satellite at 861.8 eV and the Ni $2p_{1/2}$ line has a broad satellite at approximately 880 eV. The pre-edge of the Ni 2p core level at the low binding side is formed by the shoulder of the Fe 2s core level.

First the comparison to the Ni metal Ni 2p core level show a clear shift of 2.5 eV towards higher binding energies. This fits well with the expectation that the Ni is clearly existent as Ni^{2+}. Also in the NFO thin film, no shoulder
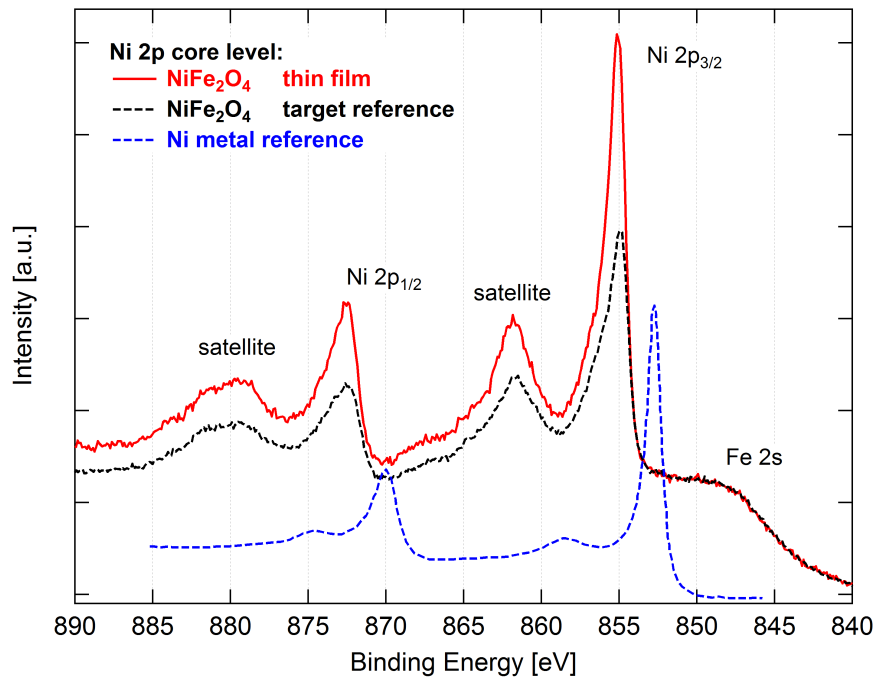
Figure 4.11: In red the Ni 2p HAXPES spectrum measured at $h\nu = 4\,\mathrm{keV}$ of a 23 nm thin NFO film is displayed. Blue dashed line is the Ni 2p HAXPES spectrum of Ni metal is taken from [90]. Black dashed line is the Ni 2p HAXPES spectrum of the NFO PLD target taken from [17].

or small peaks arise at the metal Ni $2p_3/2$ or Ni $2p_{1/2}$ positions. Therefore the formation of Ni metal clusters due to a high oxygen deficiency can be excluded [89]. The Ni 2p HAXPES spectrum of the NFO thin film are in accordance with the Ni 2p HAXPES spectrum of the stoichiometric NFO PLD target. The core level positions, the distance of core level to satellite and the intensity ratio of core level to satellite are in agreement. Consequently in the NFO film the Ni is only existing as Ni^{2+}.

4.2.2 XMCD study of thin NiFe$_2$O$_4$ films

X-ray absorption spectroscopy (XAS) is a powerful tool, which can give access to information about the composition of oxide thin films and the occupation of the ion species on the lattice sites. XAS spectra are element selective and they are sensitive to the chemical environment of the probed element. If left and right circularly polarized light is applied, the XAS spectra become spin sensitive. Subtracting the left and right circularly polarized XAS spectra from each other yields the X-ray circularly magnetic dichroism (XMCD) spectra see subsection 2.5.2. XMCD spectra are like an element selective fingerprint for a magnetic material. Given that the NFO is supposed to be ferrimagnetic, the XMCD spectra of Fe and Ni will be investigated in terms of ion valency and occupancy of the ions species.
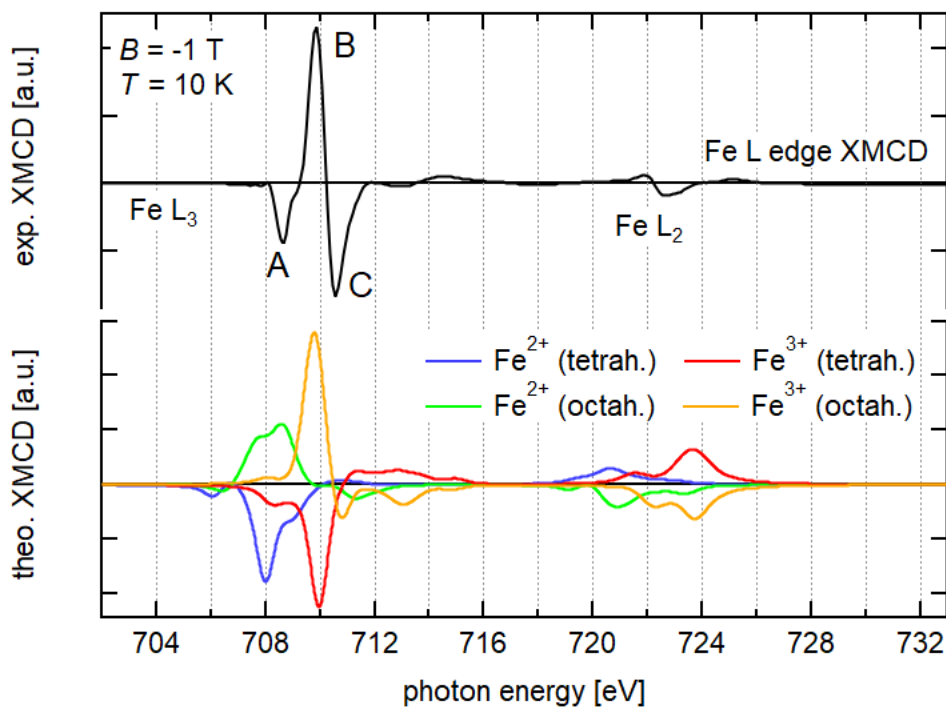
Figure 4.12: Top: Fe L edge XMCD spectrum of a 6.1 nm NFO thin film taken at $B = -1$ T and $T = 10$ K. Bottom: Fe L edge XMCD simulations of divalent and trivalent Fe ions on octahedral and tetrahedral sites of the spinel structure. These simulations were taken from [16] where they were computed by LFM calculations utilizing the software CTM4XAS.

The XAS spectra were taken at the I10 beamline of *DIAMOND Light Source*. The temperature of the sample was set to $T = 10$ K and a magnetic field of $B = -1$ T was applied to the sample. The beam was adjusted to hit the sample at near grazing incident of 80° off-normal because thin films are expected to have an in-plane easy axis of magnetization. The XAS spectra were recorded in the surface sensitive total electron yield (TEY). The recorded left and right circularly polarised XAS spectra of the Ni and Fe L edge were normalised to zero at the pre-edge and to one at the post-edge. Then the XMCD spectra were obtained by subtracting the left and right circularly polarized XAS from each other.

In figure 4.12, the Fe L edge XMCD of a 6 nm NFO thin film is shown in black at the top and calculations of site- and valency-specific Fe L edge XMCD taken from [16] are shown at the bottom. The main focus will be at the Fe L$_3$ edge XMCD because it has the strongest features. The experimental Fe L$_3$ edge XMCD has mainly three recognition features. A negative peak at the photon energy of 708.6 eV (A), a positive peak at 709.8 eV (B) and a smaller negative peak at 710.6 eV (C). In the literature, these features are often used to determine the iron species according to the occupation site and in case of Fe$_3$O$_4$ to even determine the cation ratio [1, 91]. The features A,B and C are compared to the calculated Fe L edge spectra. In case of features C and B the identification is quite clear given that only one Fe L edge spectrum has a

matching feature. Feature B is identified with the main peak of Fe^{3+} at octahedral sites of the spinel structure and feature C is identified with the main peak of Fe^{3+} at tetrahedral sites. Feature A cannot be assigned clearly. At the position of peak A, the calculated XMCD of Fe^{2+} at tetrahedral site (Fe^{2+} (T$_d$)) has its strongest feature. The calculation of the Fe^{2+} at the octahedral site can be excluded as it has a high and broad positive feature at the position of A. This applies also to the Fe^{3+} at the octahedral site which has a small positive tail at this position. But the calculations of Fe^{3+} (Fe^{3+} (T$_d$)) at tetrahedral site has a small negative peak at the position as well. Thus, the peak positions of the calculation are not a criterion for exclusion. Thus, the shape of feature A will be compared to the calculated shapes. The calculated XMCD of the Fe^{3+} (T$_d$) is a smooth small bump and has the rising shoulder of the main feature at higher photon energies. The calculated XMCD of the Fe^{2+} (T$_d$) has a sharp peak at energy position A, a small negative bump at lower photon energies and a shoulder at higher photon energies indicating a weaker overlapping peak. While the small negative bump of the Fe^{2+} (T$_d$) XMCD is not present in the experimental XMCD of the NFO thin film, the shape of the main feature with the shoulder at higher energies matches the shape of feature A. Therefore a Fe^{2+} contribution of the tetrahedral site of the spinel structure is quite likely. This is not in agreement with the theoretical expectation that the NFO should only consist of trivalent Fe ions. It also contradicts the results of the HAXPES measurements of a 23 nm thick NFO film at which no indications for Fe^{2+} cations were found. In the literature, feature A is always observed in PLD-grown NFO thin films and mostly independent of film thickness and growth procedure [16, 92, 93]. One reasonable explanation is that Fe^{2+} is only formed in small amounts at the surface of the film. HAXPES measurements of thick samples and in the normal emission configuration are bulk sensitive. Therefore if the total amount of the Fe^{2+} is too small and accumulated solely at the surface, the Fe^{2+} signal will get screened of by the Fe^{3+} for the thick NFO films. On the other hand if Fe^{2+} is at the surface even in small amounts it will most likely always be detected independently of the thickness by the surface sensitive XAS measurement in TEY mode.

Similar to the Fe L edge XAS spectra, the Ni L edge XAS spectra are also sensitive to the octahedral and tetrahedral crystal environment of the spinel structure [95]. Therefore the Ni L edge XMCD has as well its own unique magnetic fingerprint and will be used to determine the site occupation of the Ni^{2+} ions. In figure 4.13, the Ni L edge XMCD of a 6 nm NFO thin film is displayed in black at the top and calculations of site-specific Ni L edge XMCD taken from [94] are displayed at the bottom. The main focus will be at the Ni L$_3$ as it has the most distinct features [96]. The experimental Ni L$_3$ edge consists of a negative sharp peak at 853.2 eV called feature A and a positive sharp peak at 854.8 eV called feature B. The XMCD spectra of Ni^{2+} at tetrahedral site and octahedral site both show a distinct negative peak near to the energy position A with the main difference in the intensity. However, at the energy position of feature B the theoretical L edge XMCD of the Ni^{2+} at tetrahedral site has a negative contribution while the one of
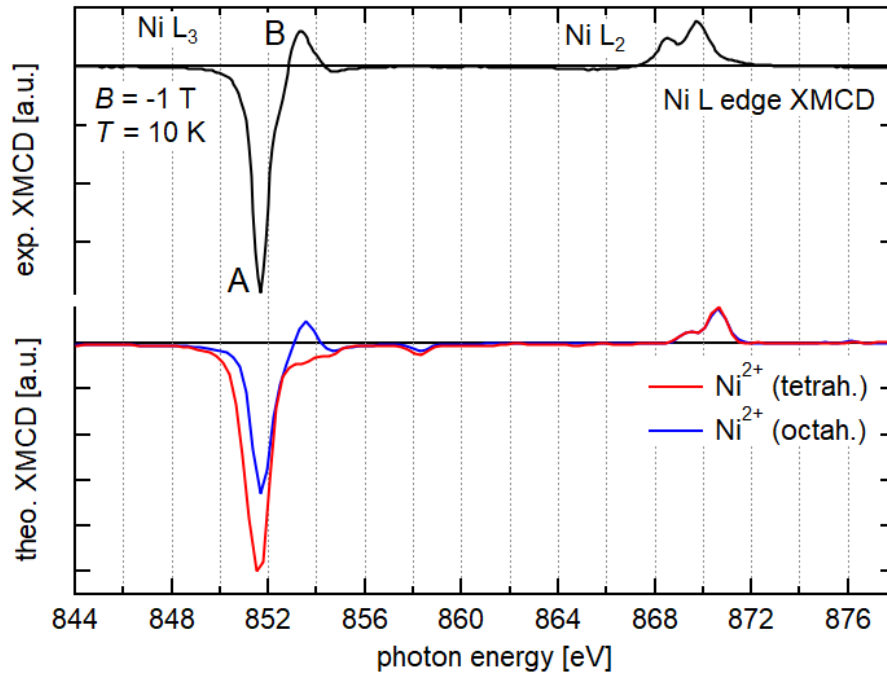
Figure 4.13: Top: Ni L edge XMCD spectrum of a 6.1 nm NFO thin film taken at $B = -1\,\text{T}$ and $T = 10\,\text{K}$. Bottem: Ni L edge XMCD calculations of divalent Ni ions on octahedral and tetrahedral sites of the spinel structure. The calculations were taken from [94] where they were computed by using first-principles configuration interaction calculations.

the Ni^{2+} at octahedral site has a positive peak. Therefore the divalent Ni ions are mostly occupying the octahedral sites. This is in agreement with the theoretical expectation of the inverse spinel structure occupation.

4.3 Summary

This chapter covered the PLD growth parameter optimization and the characterization of the resulting NFO thin films grown on top of the STO. The growth parameter foundation was taken from M. Hoppe *et al.* [72]. An NFO film series was grown with variation of the laser fluence and one with a variation in growth gas composition. The grown NFO films were investigated by AFM, XRD, rocking curves and magnetic hysteresis in order to probe the surface roughness, the crystallinity, the defect density and the magnetic response of the NFO films. The laser fluence influence is minimal and no trends could be identified within the probed range of laser fluence. The growth gas composition on the other hand clearly affects the NFO film quality. If the growth gas composition is changed from 25:75 Ar:O_2 ratio to 0:100 Ar:O_2 the crystallinity, defect density and the magnetic response are improved. Therefore the PLD growth conditions for high quality thin NFO films are found to be:

- $T = 635\,°C$,
- $p = 3.9 \cdot 10^{-2}\,\text{mbar}$,
- $f = 2\,\text{Hz}$,
- 90 minutes annealing at growth pressure & temperature,
- $F = 1.41\,\frac{J}{cm^2}$,
- $\text{Ar} : \text{O}_2 = 0 : 100$.

Next the optimized thin NFO films have been investigated in terms of cation identification and site occupation by means of HAXPES and XMCD. Ni 2p and Fe 2p HAXPES measurements of a 20 nm NFO film have been measured. It has been found that the NFO film consists of Ni^{2+} and Fe^{3+} cations, that is in agreement with the theoretical expectations. Ni L edge and Fe L edge XMCD spectra have been derived from circularly polarized XAS measurements in TEY mode of a 6 nm NFO thin film. It has been confirmed that the NFO film consists of Ni^{2+} cations that occupy the octahedral sites of the spinel structure which agrees with the theoretical expectations. Fe^{3+} cations have been found to occupy tetrahedral and octahedral sites of the spinel structure which is in line with the theory. However, also a weak signal of Fe^{2+} residing on tetrahedral sites have been found which was not detected by HAXPES measurements. This phenomenon has been mentioned in the literature. Therefore it is highly possible that the Fe^{2+} accumulates at the film surface and is not distributed evenly throughout the film.

Chapter 5

Magnetism of the NiFe$_2$O$_4$/SrTiO$_3$ heterostructure

In chapter 4 it was shown that the saturation magnetization of the NiFe$_2$O$_4$/ SrTiO$_3$ (NFO/STO) heterostructure could be optimized by the adjustment of the growth conditions. In order to extract the saturation magnetization, the magnetic response of the entire sample was measured via SQUID. However, the SQUID technique is only bulk sensitive. The element-selective magnetic response can be measured via X-Ray Magnetic Circular Dichroism (XMCD). Thus, in this chapter, the origin of the magnetization in NFO can be investigated. Furthermore the interface of the NFO/STO heterostructure can be investigated.

5.1   XMCD of NiFe$_2$O$_4$ thin films

The element-selective magnetic response of the optimized NFO thin films has been investigated at the DIAMOND Light Source at the beamline I10. The X-ray Absorptions Spectra (XAS) have been recorded with soft X-rays at a temperature of $T = 10\,\mathrm{K}$ and in the Total Electron Yield (TEY) measurement mode. The magnetic field has been set to either $B = +1\,\mathrm{T}$ or $B = -1\,\mathrm{T}$ and has been aligned to the incident beam and thus to the sample's in-plane vector (100). In order to measure the magnetic signal, the samples have been probed with left (negative) and right (positive) circularly polarized (cp) light. Figure 5.1 shows the circularly polarized XAS (cp XAS) spectra of the Fe and Ni L edge for an NFO film with a thickness of $d = 6.1\,\mathrm{nm}$ and an applied magnetic field of $B = -1\,\mathrm{T}$. The left cp XAS in blue and the right cp XAS in red are compared to each other. For both L edges, the left and right cp XAS vary in intensity distribution. In case of the Fe L edge, even the peak energy positions of the L$_3$ edge are distinct. For materials with zero net magnetic moment, left and right cp XAS are expected to be identical. In contrast, if the material has a non-zero net magnetic moment, the left and right cp XAS show distinct different intensity distributions, called dichroic behaviour. Thus, the cp XAS confirm the already known fact that the NFO thin films have a net magnetic moment.

In subsection 2.1.1, the magnetism in ideal NFO is explained to have its origin in the ferromagnetic coupling of the Ni^{2+} cations, which are residing at the octahedral sites, and in the antiferromagnetic coupling of the Fe^{3+} cations,
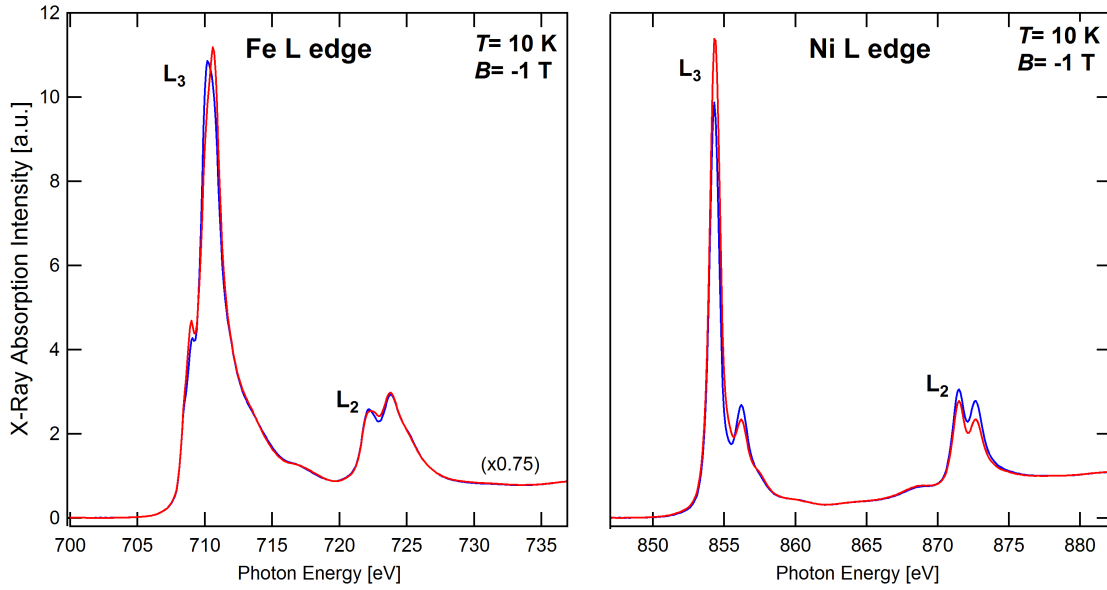
Figure 5.1: In blue the left and in red the right circularly polarized XAS of a $d = 6.3$ nm NiFe$_2$O$_4$ film. The film was measured at a magnetic field of $B = -1$ T. **a)** Iron L edge **b)** Nickel L edge.

which are residing at the tetrahedral and octahedral sites. In order to extract the information of the element specific magnetic contribution to the net magnetic moment, the magneto optical sum rules can be applied to the Ni and the Fe cp XAS. The general XMCD sum rules were derived for quantum mechanical dipole transitions of ferro- or ferrimagnetic materials by Thole *et al.* in 1992 and Carra *et al.* in 1993 [97, 98]. The sum rules displayed in equations 5.1 and 5.2 show the special case for dipole transitions from the p- to the d-states and are in this form taken from C. T. Chen *et al.* in 1995 [99].

$$m_{\text{orb}} = -\frac{2q}{3r} \cdot N_{\text{h}} \quad , \tag{5.1}$$

$$m_{\text{spin}} = \frac{2q - 3p}{r} \cdot N_{\text{h}} \cdot \left(1 + \frac{7\langle T_{\text{z}} \rangle}{2\langle S_{\text{z}} \rangle}\right)^{-1} \quad , \tag{5.2}$$

$$r = \frac{1}{2} \int_{L_{3,2}} (\mu_+ + \mu_-) \, dE \quad p = \int_{L_3} (\mu_+ - \mu_-) \, dE \quad q = \int_{L_{3,2}} (\mu_+ - \mu_-) \, dE \quad . \tag{5.3}$$

The m_{orb} and the m_{spin} refer to the orbital and the spin moment contribution to the net magnetic moment. The N_{h} is the number of holes in the d bands and has to be known in advance. The integral over the XMCD signal of the L$_3$ edge is p and the integral over the XMCD signal of the total L edge is q. The integral over the unpolarized L edge is r, which is proportional to the number of 3d valence states and usually can assumed to be the mean value of left and right cp XAS for not surface dominated ultra thin films [100]. The expectation value of the total spin is $\langle S_{\text{z}} \rangle$. The $\langle T_{\text{z}} \rangle$ is the expectation value of the magnetic dipole operator and allows for correction of the distortion of the

spin cloud by crystal field effects. For cubic, non distorted magnetic systems like ideal NFO, this term is close to zero and thus will be neglected [101]. The XMCD sum rules can be applied in case that the following conditions apply:

1. restrict to p- to d-orbital dipole transitions

2. strong spin-orbit coupling

3. no hybridization of the l shells, i.e. clear separation of L$_3$ and L$_2$ edge

The heavy 3 d transition metals iron, cobalt and nickel have shown to meet these conditions [102].

In order to apply the XMCD sum rules properly as described in [16, 99], it is crucial to determine and subtract the background of the unpolarised XAS spectra. Furthermore, the unpolarised and polarised XAS pre-edges have to be normalised to zero and the post-edges have to be normalised to one. The analysis will be discussed separately for the Fe and the Ni cations.

5.1.1   Analysis of the Fe^{3+} L edge XMCD

In section 4.2 it was qualitatively confirmed by HAXPES and XAS that the Iron cations of the NFO thin films are mostly Fe^{3+} and are occupying the octahedral as well as the tetrahedral sites of the inverse spinel structure. Thus, the Fe^{3+} cations in the NFO thin films will be treated like the Fe^{3+} cations of non-defective bulk NFO in the analysis.

Background correction of Fe^{3+} XAS

The unpolarised XAS background can be divided into two parts. The first part consists of the pre-edge background which has its origin from edges at lower energies. If the edges at lower energies are not close to the L edge and the signal of the L edge is rather large in comparison then it can be treated like a linear background and just be subtracted, which automatically sets the pre-edge to zero. For the NFO/STO heterostructure both conditions are fulfilled and the pre-edge is corrected like this. In a next step, the post edge is set to one which results in a normalised unpolarised XAS. The second part of the background are onsets of p states to the s states transitions. The most basic approach to determine this background is a fit of a two step background to the XAS L edge, where the step position corresponds to the edge peak position and the width corresponds to the *FWHM* of the edge. For the Fe L edge, the height of those two steps is generally set to the L$_3$:L$_2$ ratio of 2:1 as the total number of non-dipole transitions from the p states are expected to be of the same ratio [99].

Background modelling was performed with the software *Unifit 2016*. The detailed function and the modelling result is described in Appedix C. The position of the L$_3$ edge is found to be 710.6 eV and the L$_2$ edge is found to be at 723.4 eV. For both edges a *FWHM* of 2 eV was set. Those settings fit to results in the literature [16]. At energies larger than 735 eV of the post-edge, the background increases again. In order to model this for background

Figure 5.2: a) Unpolarised XAS of the Fe L edge of a 6.1 nm NiFe$_2$O$_4$ film measured at $T = 10$ K and $B = 1$ T with an angle of 80° of normal. The blue dashed line indicates the integral over the background corrected unpolarised XAS. **b)** XMCD spectra of the normalised polarised Fe XAS at the L edge of the same NiFe$_2$O$_4$ film. The pink dashed line corresponds to the integral over the XMCD spectrum.

removal, one additional step was implemented at the post edge at 735.5 eV with a large *FWHM* of 5 eV. The modelled background in brown solid line together with the unpolarised XAS in red solid line are shown in figure 5.2 **a)**. As blue dashed line, the integral r of the background corrected unpolarised XAS is shown. It is constant after the edge and the vertical arrow at 735.5 eV indicates were r is taken.

Orbital moment Fe^{3+}

In figure 5.2 **b)**, the XMCD signal obtained by subtracting the normalised and background corrected cp XAS from each other is displayed as a green solid line. As shown in section 4.2.2, the shape of the XMCD signal is characteristic for the Fe^{3+} cations in the spinel enviroment of the NFO. The integral over the XMCD signal is displayed as well in figure 5.2 **b)** as a pink dashed line. In order to determine the orbital momentum m_{orb}, the integral q has to be calculated, which is the total integrated magnetic signal of the L edge. Here it is taken between the energies 703 eV of 735.5 eV. After this energy the integral is nearly constant. Thus, the integral up to 735.5 eV includes all magnetic contributions of the L edge. In order to evaluate equation 5.1, the number of holes N_h in the d band of Fe^{3+} has to be known. In general this number can be deduced by subtracting the number of electrons in the d bands and from the total number of available d states, $N_h = 10 - N_e$. DFT calculations for ideal bulk NFO yield $N_h \approx 9.4 \frac{\mu_B}{\text{f.u.}}$ [92]. Thus, applying the sum rule shown in equation 5.1 results in an orbital momentum of

$$m_{orb} = (0.07 \pm 0.02) \frac{\mu_B}{\text{f.u.}}.$$

Spin moment Fe^{3+}

In order to determine the Fe^{3+}'s spin magnetic moment m_{spin} of the NFO film, the integral p over the XMCD has to be calculated. The integral p will be taken from the pre-edge of the L$_3$ edge to the minimum between the L$_3$ and L$_2$ edge in the XAS or rather to the zero point of the XMCD near to the L$_2$ edge. In figure 5.2**b)**, this point is indicated with an arrow. In combination with the previously determined integrals, q and r, the spin momentum sum rule shown in equation 5.2 results in an Fe^{3+} spin momentum of

$$m_{spin} = (0.08 \pm 0.02) \frac{\mu_B}{\text{f.u.}}.$$

5.1.2 Analysis of the Ni^{2+} L edge XMCD

In section 4.2 the Ni XAS, XMCD and HAXPES data were investigated in terms of occupation of octahedral and tetrahedral sites of the spinel structure and the valency of the Ni cations. It was qualitatively confirmed that only Ni^{2+} cations are observed and that those Ni^{2+} cations are exclusively occupying the octahedral sites like expected for ideal NFO. Thus, the Ni^{2+} XAS and XMCD will be treated like the Ni^{2+} of non-defective bulk NFO in this analysis.

Background correction of Ni^{2+}

The background of the Ni L edge will be calculated similar to the Fe L edge. A linear background will be subtracted from the pre-edge, which automatically sets the pre-edge of the unpolarised XAS to zero. The post-edge is normalised to one. However, the two-step background model for purely ionic and dipole transitions in not sufficient for the background of the Ni L edge XAS of NFO given that there is an additional continuum step at 867 eV. This continuum step refers to transitions from 2p to 4s like states [103]. These transitions are not taken into account in the derivation of the sum rules and thus will give false results if included in the sum rules. Therefore, the two-step model is modified with an additional step at the continuum step. The detailed function and the modelling result is described in appendix C. The *FWHM* of the L edges are set to 2 eV and the *FWHM* of the continuum step was found to be 2.2 eV. The positions of the L$_3$ and L$_2$ edges are found to be 854.0 eV and 871.8 eV, which matches the values found in literature [95, 103]. At the post-edge with energies larger then 785 eV, the background increases again. In order to model this one additional step was implemented at the post-edge at 885 eV with a large *FWHM* of 4 eV. The modelled background in brown solid line together with the unpolarised XAS in red solid line is shown in figure 5.3 **a)**. The integral r of the background corrected unpolarised XAS is shown in a blue dashed line. It is constant after the edge. The arrow at 884 eV indicates were r is evaluated.

Orbital moment Ni^{2+}

In figure 5.3 **b)**, the XMCD spectrum obtained by subtracting the normalised and background corrected cp XAS from each other is displayed as a green solid line. In subsection 4.2.2, the shape of the XAS signal and the XMCD signal were confirmed to be mostly from Ni^{2+} cations in the spinel environment of NFO. The integral over the Ni XMCD signal is shown in figure 5.3 with a pink dashed line. An arrow indicates the energy position after the L edge where q is evaluated. After this energy the XMCD integral is constant until 890 eV after which it is slowly decreasing again. In the literature, the integral q is taken at higher energies of 910 eV [16]. The reason for this is that the magnetic extended fine structure (MEXAFS) of the L$_3$ edge is superimposed with that of the L$_2$, resulting in an additional dichroic signal that would lead to a falsified result with the sum rules [104]. However, the MEXAFS is decreased at high excitation energies and the MEXAFS signal for L$_3$ and L$_2$ have opposite signs. Thus, if a large integration range is used, the MEXAFS signal of the L$_3$ and L$_2$ will cancel each other [16, 105]. Unfortunately, the energy ranges, which were chosen for the experiment at the DIAMOND beamline I10 are too small in order to correct this MEXFAS signal. However, if the data from the dissertation of M. Hoppe [16] are taken as a basis, then the integral q is overestimated by approximately (15±2) %. Thus the q_{ext} can be estimated with this.

In order to apply the sum rule from equation 5.1 the number of holes for the Ni^{2+} has to be known. Many-body perturbation theory combined with LDA
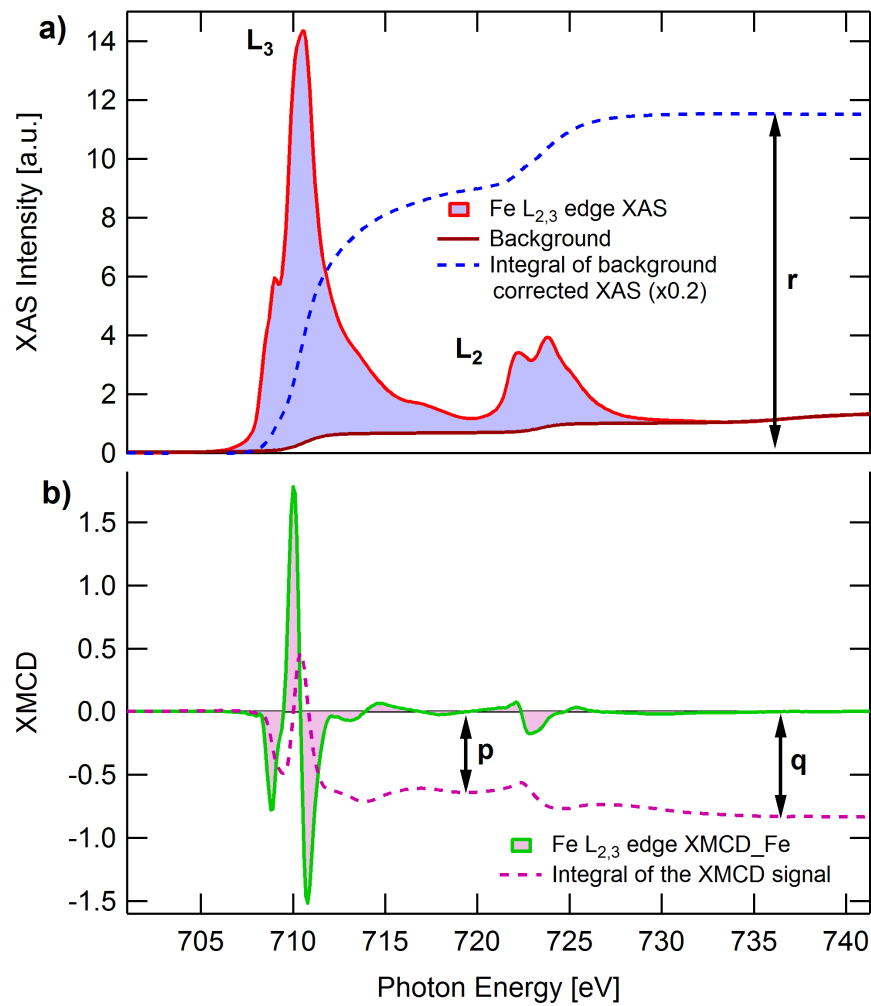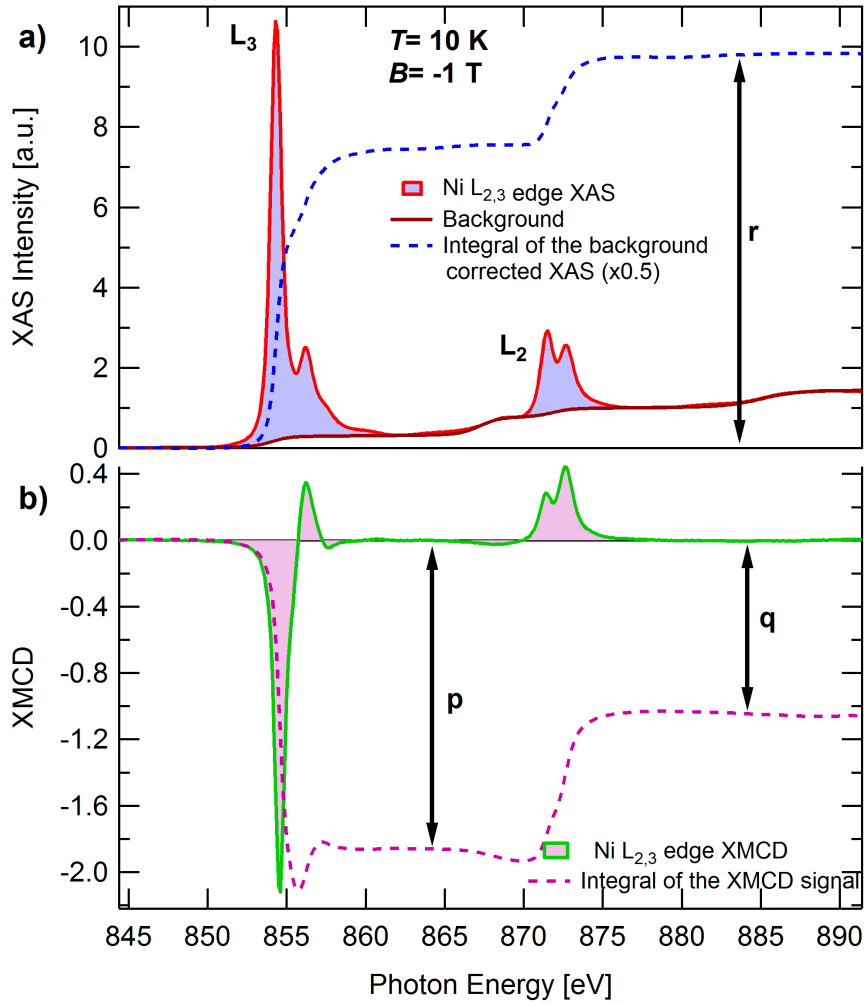
Figure 5.3: a) Unpolarised XAS of the Ni L edge of a 6.1 nm NiFe₂O₄ film measured at $T = 10\,\text{K}$ and $B = 1\,\text{T}$ with an angle of 80° off normal. The blue dashed line indicates the integral over the background corrected unpolarised XAS. **b)** XMCD spectra of the Ni L edge of the same NiFe₂O₄ film. The pink dashed line corresponds to the integral over the XMCD spectra.

correlation calculations for ideal bulk NFO give numbers of $N_h \approx 2.23\,\frac{\mu_B}{\text{f.u.}}$ in [106]. Thus, applying the sum rule results in an orbital momentum of

$$m^*_{\text{orb}} = (0.07 \pm 0.02)\,\frac{\mu_B}{\text{f.u.}} \quad .$$

Spin moment Ni²⁺

In order to determine the spin magnetic moment m_{spin} of Ni²⁺ of the NFO film the integral p over the XMCD signal originating in the L₃ edge has to be evaluated. In figure 5.3 **b)**, an arrow indicates the position between the L₃ and L₂ edge where the XMCD becomes zero and the integral is constant near

to the L$_2$ edge. In combination with the previous determined q and r integral, the sum rules shown in equation 5.2 results in a spin momentum of:

$$m^*_{\text{spin}} = (0.44 \pm 0.02)\, \frac{\mu_B}{\text{f.u.}}$$

5.1.3   Discussion of the XMCD of NiFe$_2$O$_4$ thin film

Spin and orbital magnetic moment of Fe^{3+}

In subsection 2.1.1 the electronic configuration of the Fe^{3+} cation with 3d^5 is described in detail. The d shells are half-filled and all spins are aligned parallel in the e_g and the t_{2g} states. In addition, the Fe cations are expected to occupy the antiparallel aligning tetrahedral and octahedral sites of the spinel structure equally. Thus, the spin magnetic moments of Fe cations are expected to compensate each other and should be zero [16].
The orbital magnetic moment on the other hand is highly dependent on the potential of the surrounding oxygen ions. In NiFe$_2$O$_4$ the Fe^{3+} cations are enclosed in an oxygen ions octahedral or tetrahedral. Due to the rotational symmetry, the potential of these oxygen environments can be expanded in a series of spherical harmonics. The expansion will only have nonzero terms if the quantum number m is an integer multiple of $q = 4$ octahedral and tetrahedral symmetry. As a result, the potential only couples orbital momentums states with quantum numbers m_{L1} and m_{l2} such that $m_{L2} - m_{L1} = n \cdot q$ in so far they exist. For the d-electrons there are only two states available that fulfil the conditions, $m_L = \pm 2$. However, in the cubic environment of the NiFe$_2$O$_4$ both states contribute with the same weight. Thus, the orbital momentum is expected to be quenched [50]. However, due to the two site occupation states in the spinel structure a XMCD signal should exist.
In figure 5.2, a distinct XMCD signal is shown. When applying the sum rules for the spin and the orbital magnetic moment, small magnetic moments are obtained of $m_{\text{orb}} = (0.07 \pm 0.02)\, \frac{\mu_B}{\text{f.u.}}$ and $m_{\text{spin}} = (0.08 \pm 0.02)\, \frac{\mu_B}{\text{f.u.}}$. It was shown in section 4.2 that NFO thin films mostly consist of Fe^{3+}. However, small amounts of Fe^{2+} cannot be excluded. This small amount of Fe^{2+} can be the root of the non zero spin moment because with antiparallel alignment, the moments of Fe^{2+} and Fe^{3+} cations do not compensate each other. The Fe^{2+} can also be the cause for a non vanishing orbital magnetic moment. The additional electron undergoes strong Coloumb interactions with the other electrons thus unquenching the orbital moment partially [107]. Another possibility is that the density of defects present in NFO thin films causes the non-vanishing spin and orbital magnetic moment in the Fe. The introduction of anti phase boundaries and mosaicity into the films due to the high strain of the substrate breaks the symmetry of the NFO locally. Thus, the magnetic coupling mechanisms get weakened and the symmetry based arguments of the origin of the magnetism in NFO does not hold true unambiguously.

Spin and orbital magnetic moment of Ni^{2+}

As described in subsection 2.1.1, the electronic configuration of the Ni cation in NFO is 3d^8. The t_{2g} states are all occupied and do not contribute to either spin or orbital momentum. The spins of the two remaining electrons align parallelly in the e_g states. Due to the octahedral symmetry and the equal weight of the two degenerated states in the e_g from the atomic level view, the orbital magnetic moment should be quenched to zero. The two parallelly aligned spins should result in a non-zero spin magnetic moment, which is the source of the macroscopically observed ferrimagnetism in NFO [16].
When applying the sum rules for spin and orbital magnetic moments, we obtain of $m_{\text{orb}} = (0.07 \pm 0.02)\,\frac{\mu_B}{\text{f.u.}}$ and $m_{\text{spin}} = (0.44 \pm 0.02)\,\frac{\mu_B}{\text{f.u.}}$. The non-zero spin magnetic moment agrees with the model presented in subsection 2.1.1. However, the orbital magnetic moment is also non zero and the ratio between orbital magnetic moment and spin magnetic moment is 16% $\pm$ 5%. This is in agreement within the error of the previously reported 12% $\pm$ 2% [96].

Total magnetic moment of NiFe$_2$O$_4$

The evaluation of the L edge cp XAS and the XMCD of the Ni and Fe cations with the sum rules give a total magnetic moment of

$$m_{\text{total}} = m_{\text{orb}}^{\text{Fe}} + m_{\text{spin}}^{\text{Fe}} + m_{\text{orb}}^{\text{Ni}} + m_{\text{spin}}^{\text{Ni}} \quad ,$$

$$m_{\text{total}} = (0.07 + 0.08 + 0.07 + 0.44)\,\frac{\mu_B}{\text{f.u.}} \quad ,$$

$$m_{\text{total}} = (0.67 \pm 0.04)\,\frac{\mu_B}{\text{f.u.}} \quad .$$

This total magnetic moment is approximately half of the saturation magnetization observed in optimized 20 nm thick NFO films via SQUID measurements. One reason for the low total magnetization is that the XMCD was taken at a magnetic field of $B = 1$ T at which the NFO is not saturated. This magnetic field was chosen in order to save time between switching magnetic field and switching the samples, because the measurement time was highly restricted. However, NFO is a ferrimagnet and saturates at fields of $B \gtrsim 3$ T as shown in sections 4.1.2, 4.1.3 and in literature [17, 108]. Thus, the achievable magnetization at $B = 1$ T is $m = (1.1 \pm 0.01)\,\frac{\mu_B}{\text{f.u.}}$. This corrected expectation value is still 40% higher than the total magnetic moment from the XMCD analysis. Another explanation can be found in the derivation of the XMCD rules. Those only apply for non-hybridized shells and dipole transitions from l to d shells. Literature studies about the reliability of the XMCD sum rules showed that they underestimate the ground state properties of 3d^8 systems by up to 30% [101]. Even if taken the error of the XMCD sum rules into account, the difference of the expected value to the moment of the XMCD signal do not match. Apart from internal experimental errors, the sample itself

seems to have a reduced moment. The studied sample had a film thickness of $6.1\,\text{nm} \approx 7.3\,\text{u.c.}$. One possibility could be that the reduced dimensionality of the film causes a decrease in the magnetic interactions throughout the film. Another explanation could be that the broken symmetry at the surface leads to a decreased magnetic exchange resulting in a decreased magnetic moment for the surface layer. This would of course have a higher impact on thinner films. However, in order to find a final answer, further studies have to be undertaken.

5.2   Magnetic response of the NiFe$_2$O$_4$/SrTiO$_3$ interface

In the previous section, the element-selective magnetic response of the optimized NFO thin films has been investigated by means of XMCD analysis utilizing circularly polarized soft X-Ray absorption spectra. The cp XAS have been recorded at the DIAMOND Light Source at the beamline I10. The Total Electron Yield mode of this measurement set up is rather surface sensitive with an exponential decay in probing depth of only a few nanometers [109, 110]. Thus, it is well suited to study thin NFO films with $d < 8\,\text{nm}$ as a whole. However, this exponential decrease in probing depth makes it possible to study explicitly the interface layers of the underlying substrate. The thicker the top NFO film, the less information from deep bulk STO layers contribute to the signal. However, also the substrate signal itself decreases significantly and, which necessitates a higher number of repetitions in order to reduce the background noise. Therefore in this section, first the interface XAS of Ti L edge of the STO substrate will be investigated and then the magnetic response via X-Ray magnetic circularly dichroism will be checked. All recorded XAS and the resulting XMCD spectra were recorded at a temperature of $T = 10\,\text{K}$ and an in-plane magnetic field of $B = \pm 1\,\text{T}$.

5.2.1   Thickness dependency of the titanium L edge XAS

This section focusses on the investigation of the NFO/STO interface, in particular the substrate STO's Ti L edge. The valence of the Ti cation is of importance for the properties of the STO as discussed in subsection 2.1.3. In the perovskite structure of bulk STO, the valence of the Ti cation is expected to be Ti^{4+}, which leads to a 3d^0 electronic configuration with no free electrons. Thus, the STO is insulating and diamagnetic [29]. If oxygen vacancies are introduced into STO, an additional electron will get transferred to the Ti electronic configuration and thus Ti^{4+} will convert to Ti^{3+}. This altered 3d^1 electronic configuration has a delocalized electron which changes the STO behaviour from insulating to conducting [111]. This process is often observed at the interface of oxide/STO heterostructures [112, 113].

In figure 5.4, the measured Ti L edge of a (6.1 nm) NFO/STO is shown in blue. The measurement has been taken with left cp light. Four main absorption lines can be clearly identified. The two signals on the lower energy
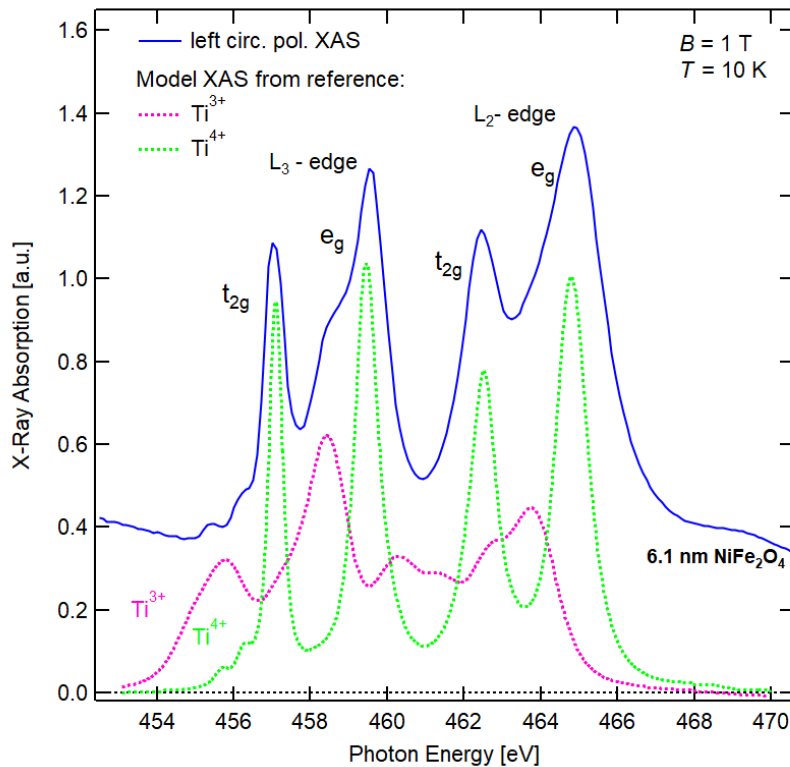
Figure 5.4: In blue averaged and aligned left circularly polarized Ti L edge XAS of a 6.1 nm NFO/STO heterostructure measured at $T = 10$ K and $B = 1$ T. In dotted lines XAS L edge reference spectra for a Ti^{3+} (pink) and Ti^{4+} (green) are displayed. Reference spectra are taken from [114].

spectrum refer to the L$_3$ edge and the two at the high energy spectrum refer to the L$_2$ edge. Each L edge is split into two energetically well separated levels which identify with the t_{2g} and e_g states at low and high energies respectively. However, on the low energy site of the L$_3$ e_g and the L$_2$ e_g, a shoulder rises. In dotted lines reference spectra of Ti^{3+} XAS in pink and Ti^{4+} XAS in green are shown, which are modelled by Lee *et al.* utilizing multiplet calculations by the *CTM4XAS* software [114]. The modelled Ti^{4+} shows crystal field split L$_3$ and L$_2$ absorption signals. The small peaks in the pre-edge of the Ti^{4+} XAS originate in particle-hole coupling [115, 116]. The Ti^{3+} the XAS is formed by more and broader absorption lines. This is due to the Coloumb interaction of the single electron for the absorption process, which partially lifts the degeneracy of the e_g and the t_{eg} levels. When the experimental data are compared to the modelled data, the four main absorption lines fit to the Ti^{4+} model XAS while the shoulders are evidence for existing Ti^{3+}. Obviously, the interface near to the 6.1 nm thick NFO consists of a mixture of both Ti^{4+} and Ti^{3+}.

Next the Ti^{3+} evolution in dependence of film thickness will be investigated. In order to do this, four films with a film thickness of 2.5 nm, 3.5 nm 4.8 nm and 6.1 nm are compared to each other. All of them were grown with the same growth parameters shown in chapter 4 and the thickness was evaluated via XRR. In figure 5.5, pre-edge corrected and zero-one normalised left

cp XAS of the four heterostructures are shown from bottom to top with increasing thickness. Black vertical lines mark the position of the Ti^{4+} L$_3$ e_g absorption line and the position of the main Ti^{3+} L$_3$ e_g absorption line. One general observation is that the titanium signal to background ratio decreases with increasing NFO film thickness, which is expected due to the thicker overlaying film. However, the Ti^{3+} to Ti^{4+} ratio increases with increasing overlaying film thickness. For the sample with the thinnest film, the Ti^{3+} is not detectable. The Ti XAS reflects the XAS of a purely Ti^{4+}. In contrast the sample with the thickest film on top has the strongest Ti^{3+} signal. This evolution can have two main origins. First possibility is that thinner films lead to an enhanced probing depth into the substrate. Thus, more of the bulk like STO contributes to the Ti XAS, which has a valence of 4+. The other possibility is that the overall amount of Ti^{3+} increases with increasing film thickness. The interface between two oxides during the growth process is thermodynamically not in equilibrium. Even though a post annealing step is applied for the oxide heterostructure to minimize oxygen vacancies in film and substrate, it can not exclude that the NFO film also takes oxygen from the substrate during the growth process. Thus, the NFO growth introduces oxygen vacancies to the substrate interface, which has also been observed for other oxides in the literature [1, 117]. While the first option definitely is a reason for the underestimation of the Ti^{3+} content at the interface, it would be quite unlikely to cover all of the Ti^{3+} because the probing depth is only a few nm [109]. Thus, a mixture of both explanations is most likely.

For the further investigation of the STO substrate's magnetic response, the NFO/STO heterostructure with the thickest film and thus the highest Ti^{3+} to Ti^{4+} ratio will be used, i.e. the 6.1 nm NFO/STO heterostructure.

5.2.2   Magnetic response of the titanium L edge

In order to observe the magnetic response of the substrate, the Ti L edge of the (6.1 nm)NFO/STO heterostructure will be measured with left and right circularly polarized light and with switching the magnetic field from $B = +1$ T to $B = -1$ T at $T = 10$ K. Only a small signal is expected due to the measurement mode and thus a high repetition rate is needed in order to lower statistically the noise of the background. Thus, for each magnetic field and each polarization, 32 Ti L edge XAS were recorded in a sequence of right-left-left-right cp XAS. The raw data and the averaging and aligning process are shown in the appendix D.

In figure 5.6 **a)**, averaged and aligned left and right cp XAS measured at $B = 1$ T of the (6.1 nm)NFO/STO heterostructure are shown. It is apparent from the picture that the left and right cp XAS are background aligned to each other. The right cp XAS has slightly smaller intensities in the L e_g states than the left cp XAS, which might be a sign of a magnetic dichroic signal. The XMCD of the Ti L edge can be found by subtracting the left cp XAS from the right cp XAS. In figure 5.6 **b)**, the XMCD for positive and negative magnetic field in red and blue are displayed. One can see a clearly on-zero XMCD signal for both field directions. Although the XMCD signal of the Ti L edge
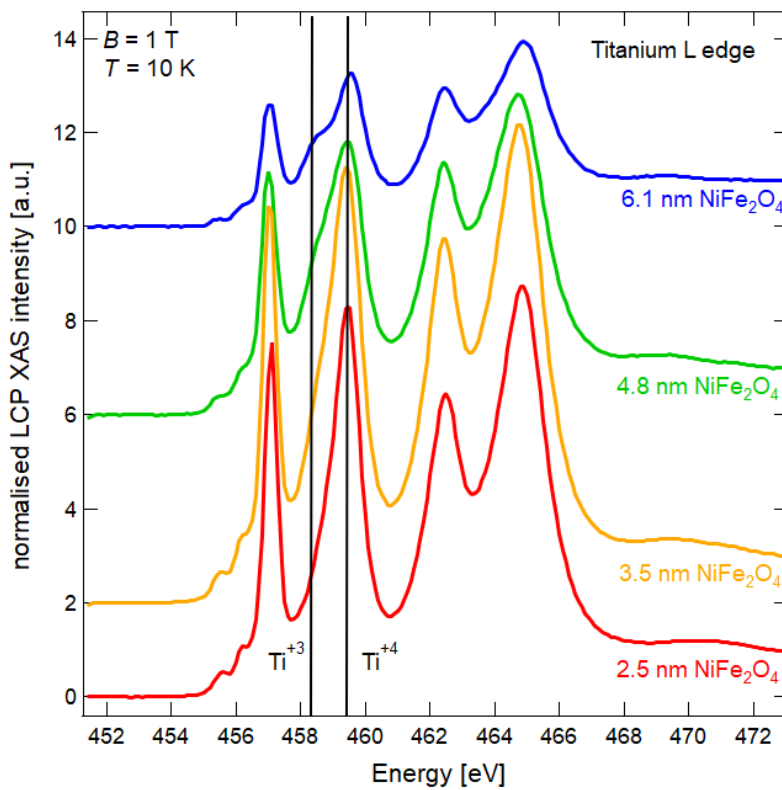
Figure 5.5: Titanium left circularly polarized XAS of the L edge for the thickness series of 2.5 nm to 6.1 nm measured at $B = 1$ T and $T = 10$ K. Marked are the L$_3$ e$_g$ edge positions of Ti^{3+} and Ti^{4+} cations.

is more than two orders of magnitude smaller than the XMCD signal of the NFO film, the signal flips when flipping the direction of the magnetic field. This is in general a strong proof for a true magnetic signal. However, if the magnetic field directions are compared to each other with regard to positive and negative XMCD signals, then both magnetic directions yield mostly positive signals, which raises the question, whether the XMCD signal is a true XMCD signal. Two effects have to be considered and both are related to the size of the XAS and the XMCD signal. The XAS in figure 5.6 **a)** clearly has a strong dominance of the background, which is reflected in the strength of the slope of the pre-edge. Those pre-edge slopes are in general dominated by the extended X-ray absorption fine structure of edges at smaller energies which themselves can have a dichroic signal here, e.g. the K edge of carbon compounds formed at the film surface [118, 119]. For strong XAS, this background slope can mostly be treated like a linear background resulting only in a small error. However, for small XAS a linear background subtraction would yield a high error. Thus, the pre-edge related linear background subtraction is applicable. In summary, the background itself can have an effect on the XMCD signal. Another point of view comes from the experiment itself. Ideally, the left and right polarized light has the same intensity but in the real experiment a tiny difference in intensity always remains [120]. Again for strong signals, this in not an issue but for small signals like this titanium
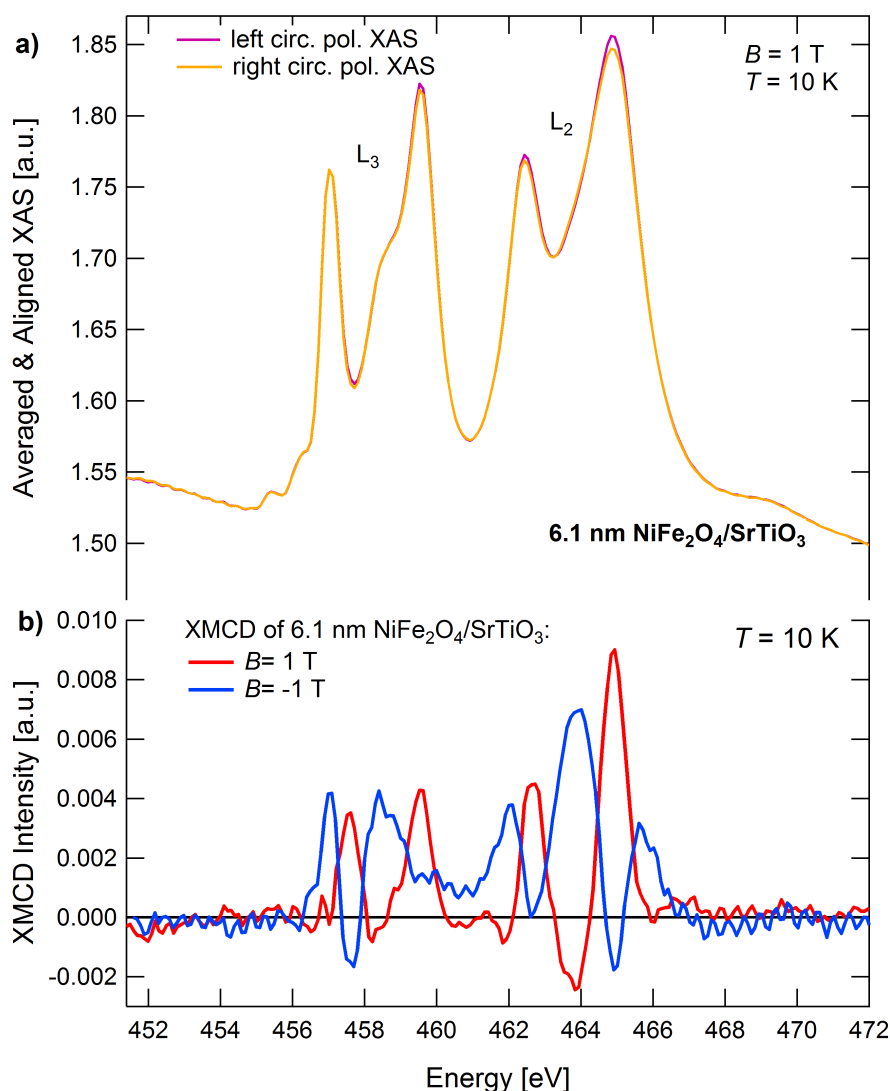
Figure 5.6: a) In orange(pink) right(left) cp XAS of the Ti L edge of a 6.1 nm NiFe$_2$O$_4$/SrTiO$_3$ heterostructure measured at $T = 10$ K and $B = 1$ T is displayed. **b)** In red the Ti XMCD spectrum measured at $B = 1$ T and in blue the XMCD spectrum measured at $B = -1$ T are displayed. The XAS were recorded at $T = 10$ K.

XAS, the tiny boost for one polarization direction can shift the overall XMCD signal slightly to all negative or all positive, regardless the direction of the magnetic field.

Another tool to test the reliability of the XMCD signal is to compare it to theoretical XMCD signals. In figure 5.7 **b)**, the experimental XMCD signal is displayed in red of the 6.1nm NFO/STO measured at $B = 1$ T. Above in figure 5.7 **a)**, theoretical reference XMCD signal for Ti^{3+} in pink and Ti^{4+} in green taken from Lee *et al.* are displayed, which are the result of multiplet calculations by the *CTM4XAS* software [114]. The experimental XMCD signal has four positive peaks covering the complete XAS energy range and one negative peak in the region of the Ti L$_2$ edge. Neither the theoretical Ti^{4+} nor the
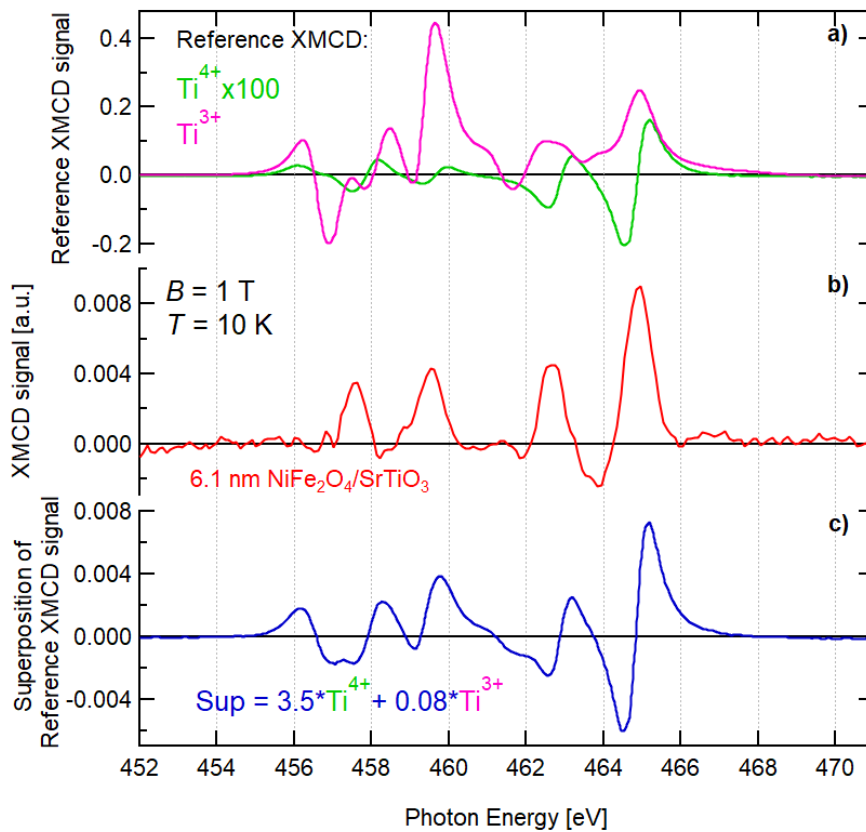
Figure 5.7: a) Reference XMCD spectra taken from [114]. In green Ti^{4+} multiplied with 100 and in pink Ti^{3+}. **b)** Ti XMCD signal obtained of the 6.1 nm thick NiFe$_2$O$_4$/SrTiO$_3$ heterostructure measured $B = 1$ T and $T = 10$ K. **c)** Superposition of the XMCD reference spectra taken from [114].

Ti^{3+} can reproduce the experimental result entirely. This is not unexpected because it was shown in subsection 5.2.1 that the Ti L edge is a composition of Ti^{4+} and Ti^{3+}. In figure 5.7 **c)**, a superposition of $3.5 \cdot$ Ti^{4+} XMCD and $0.08 \cdot$ Ti^{3+} XMCD from the reference XMCD signals shown in figure 5.7 **a)** is displayed. Although in the superposition the cross section of each Ti valency is not taken into account and the XMCD of the two valence states are only accurate for purely 3+ and 4+ valance titanium, the superposition of them reproduces the main features of the experimental XMCD signal.

The flipping of the Ti L edge XMCD signal while flipping the direction of the magnetic field and the good agreement with the superposition of the theoretical XMCD signal with strong Ti^{4+} part and small Ti^{3+} part both strongly suggest, that the Ti XMCD signal is a true XMCD signal, despite its small size. This non-vanishing XMCD signal of the Ti L edge contradicts the diamagnetic behaviour expected from ideal bulk STO. However, because of the small size of the Ti XAS and XMCD signal and the mixing of the Ti valence, the sum rules are not applied to the Ti XMCD to obtain the magnetic moment.
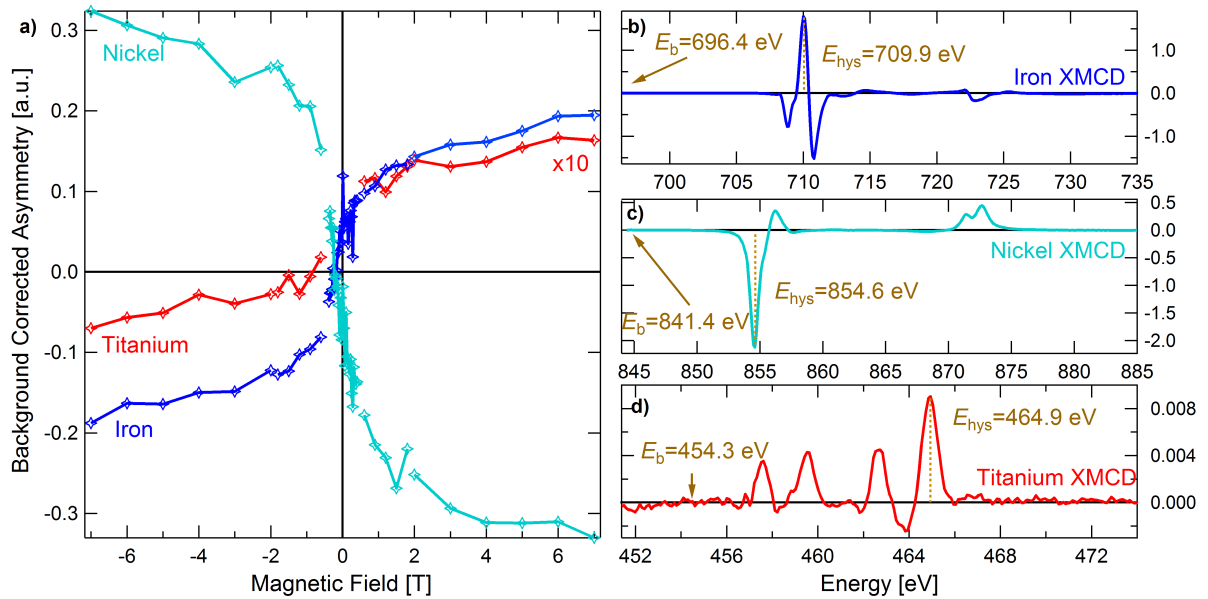
Figure 5.8: a) XMCD of a 6.1 nm NiFe$_2$O$_4$/SrTiO$_3$ heterostructure normalised to pre-edge XMCD signal for magnetic fields between $B = \pm 7$ T of Ni(cyan), Fe(blue) and Ti(red) measured at $T = 10$ K. **b)-d)** XMCD signal of Fe, Ni and Ti measured at $B = 1$ T and $T = 10$ K. The XAS energy positions for figure **a)** are marked in brown.

5.2.3 Magnetic field dependency of the NiFe$_2$O$_4$/SrTiO$_3$ heterostructure magnetic response

The nature of the magnetic response of the Ti at the interface of the NFO/STO heterostructure needs to be investigated. In contrast to the SQUID measurements of section 4.1.2 and 4.1.3, where the macroscopic magnetic response of the whole sample is measured, the magnetic field dependent XMCD can show the magnetic response element selectively. However, the full XMCD measurement for each magnetic field is time consuming, especially for the underlying STO substrate signal. Thus, instead of measuring the evolution of the total XMCD signal a energy position at which the XMCD signal is the strongest is chosen. In order to account partially for the background offset, also an energy position at the pre-edge is measured. The pre-edge XAS signal is then subtracted from the XMCD position XAS signal for each polarization direction. The energy positions, that are used for the XMCD and for the pre-edge are marked in the XMCD spectra of the L edge of Fe, Ni and Ti in figure 5.8 **b)-d)**. They were chosen according to the expected highest XMCD signal. Again by subtracting the left cp XAS signal from the right cp XAS signal the XMCD is obtained. This difference is then divided by the sum of left and right cp XAS which results in the asymmetry. At the I10 beamline in DIAMOND, magnetic fields of $B = \pm 14$ T are achievable, which is appropriate for NFO that is ferrimagnetic and thus saturates at high magnetic fields. On the other hand this strong magnet has a permanent non zero

field when it should be zero. This makes it impossible to measure the important magnetic field region around zero in detail which decreases the possible information gain. Thus reasonably, only a half hysteresis was measured and is displayed in figure 5.8 **a)**. The half hysteresis was recorded between $B = \pm 7\,\mathrm{T}$ at which the SQUID hysteresis of NFO shows only a small increasing slope. The XMCD half hysteresis shows the same behaviour, neither Ni nor the Fe are saturated yet. In the region of $B = +1\,\mathrm{T}$ to $B = -1\,\mathrm{T}$ the Ni as well as the Fe show a jump. Both characteristics fit to the ferrimagnetism observed in NFO [17, 121]. In red and multiplied by ten the Ti magnetic dependent XMCD is shown. It is quite obvious that in the region of $B = +1\,\mathrm{T}$ to $B = -1\,\mathrm{T}$ the Ti XMCD does not go through zero at zero magnetic field but instead mimics the jump from the Ni and Fe. Also in high magnetic fields, the Ti XMCD does not seem to be saturated yet which is identical to the Ni and Fe observation. This can be explained by the proximity effect in which one material can transfer its characteristics to a second material via exchange coupling at the interface. In the literature, the proximity effect was observed e.g. at the $EuO/SrTiO_3$ interface which is a ferromagnetic/diamagnetic interface at which Ti^{3+} are generated in the growth process and that these Ti^{3+} cations show the same ferromagnetic behaviour as the EuO [57]. However, a proximity effect was also observed at a diamagnetic/diamagnetic interface, the $LaAlO_3/SrTiO_3$ interface in which the coupling of oxygen vacancies and magnetic impurities are seen as the cause for the stabilized magnetic ordering [54]. Both cases might apply to the NFO/STO interface. On the one hand the Ti XMCD's magnetic field dependency shows the same magnetic behaviour as the one of the NFO XMCD which strongly supports the inducing magnetism at the magnetic/non-magnetic interface. On the other hand it is possible during the growth process, that a small amount of the Ni and the Fe might have immigrated into the STO. Thus, the magnetic order in the STO can get stabilized via coupling of the migrated NFO cations to oxygen vacancies and thus coupling to the Ti. In order to find a final answer, the cation distribution at the NFO/STO interface has to be investigated in detail, for example by transmission electron microscopy.

5.3 Summary

This chapter covered the in-plane XMCD investigation of $NiFe_2O_4/SrTiO_3$ (NFO/STO) heterostructures measured at the I10 beamline at the DIAMOND light source. In section 5.1, the XMCD signal of the Ni and Fe L edges of a 6.1 nm NFO were analysed and the sum rules were applied. The analysis revealed that the Fe contributes with small non vanishing orbital and spin magnetic moment to the total moment. This was related to non-perfect stoichiometry, i.e. small amounts of Fe^{2+}. The orbital moment for Ni is nearly completely quenched. But the spin moment of the Ni contributes heavily to the total magnetic moment of the NFO thin film which is in agreement with the theoretical expectation. However, the total magnetic moment is of $m_{\mathrm{total}} = (0.67 \pm 0.04)\,\frac{\mu_{\mathrm{B}}}{\mathrm{f.u.}}$ is roughly 40% lower than the expected value at the applied magnetic field of $B = -1\,\mathrm{T}$. This cannot be explained by the natural

error of 30% coming from the sum rules themselves and thus more investigation of the film properties are needed in order to understand this deviation. In section 5.2, the substrate XMCD signal specifically the Ti L edge was studied. Due to the surface sensitivity of the TEY recording mode, all findings are related to the interface near substrate. The Ti L edge XAS exhibit features of Ti^{4+} and Ti^{3+} cations from which only the first one is expected to be found in bulk STO. Furthermore, Ti XAS with different thick NFO top layers showed that for thicker NFO top layers the Ti^{3+} signal in the XAS gets stronger. This observation suggests an accumulation of Ti^{3+} at the interface as well as that the NFO uses the STO substrate as an oxygen reservoir during growth. The Ti L edge XMCD of the 6.1 nm NFO/STO sample was looked into in detail. It was found that the small non-zero XMCD signal flips directions when the direction of the magnetic field is flipped. The comparison with theoretical XMCD spectra of Ti^{3+} and Ti^{4+} yield that the XMCD signal is a mixture of the Ti^{3+} and Ti^{4+}. Both results support that the Ti signal is a true signal. The magnetic field dependent investigation of the XMCD signals shows that the Ti XMCD signal mimics the ferrimagnetic behaviour of the Ni and Fe of the NFO. This is explained by the proximity effect at which the ferrimagnetic NFO transfers the magnetic ordering to the Ti^{3+} of the otherwise diamagnetic STO and thus stabilizes the magnetic ordering throughout the substrate interface i.e. also in Ti^{4+}. However, deeper investigations specifically of the cation distribution throughout the interface is needed in order to find the origin of the physical properties at the NFO/STO interface.

Chapter 6

In-operando HAXPES of the Au/NiFe$_2$O$_4$/SrTiO$_3$ heterostructures

In 1980 Kraut *et al.* showed that a shift of the valence band maximum in semiconductors is directly translated into a shift of the atomic core level (cl) in XPS measurements [44]. Since then laboratory XPS and synchrotron HAXPES measurement, that are usually used in order to determine the chemical fingerprint of a sample, enable also the possibility to measure the band alignment and band bending at buried oxide interfaces [122, 123, 124]. In the oxide community, this technique is often applied in resistive switching studies of oxide devices at which first the samples are switched from a high resistive state into a low resistive state (or vice versa) and then the chemical element selective fingerprint and the new band alignment is studied at the buried oxide interfaces [11]. Thus, the relationship between the electrical behaviour, the element valency and the oxide band alignment can be studied. For new complex oxide arrangements, the interaction at buried interfaces are often unknown and theoretical calculations and descriptions are usually not available at first. Therefore HAXPES band alignment studies are an even more valuable tool to get a first description of the oxide working principles [125].

At the Petra III P09 beamline (since June 2018 P022), the band alignment studies go one step further: The chemical fingerprint, band alignment and band bending can be observed while a voltage is applied to the device, called in-operando HAXPES measurements. Thus, voltage driven chemical changes, as observed in resistive switching devices, can be studied in-operando and thus random artefacts and time driven relaxation effects can be minimized and for most samples even excluded [126]. In the field of ferroelectric complex oxide devices the polarization is influenced or even switched with applying high voltages and can be read out at low voltages. The in-operando HAXPES measurements give access to determine ferroelectric polarization changes and their effect in the band alignment [127, 128].
In the scope of this thesis, more precisely in this chapter and in chapter 7, the focus is to study the voltage dependence of the band alignment and band bending at the Au/ NiFe$_2$O$_4$/ SrTiO$_3$ heterostructures and Pt /La$_{0.7}$Sr$_{0.3}$MnO$_3$/ SrTiO$_3$ heterostructure.

6.1   Sample fabrication process & in-operando HAX-PES measurement procedure

The successful measurement of in-operando HAXPES requires firstly the samples to be contacted and therefore be structured and secondly a measurement routine that does not directly destroy the samples. The fabrication process consists of three main steps: First the fabrication process of the substrates, second the oxide growth and third the structuring process.

6.1.1   Substrate preparation

Single crystal (001) 0.5%Nb:SrTiO$_3$ with a size of 0.5 mm × 10 mm × 10 mm from *Crystec GmbH, Berlin* were used as substrates. The etching and annealing follow the procedure described in section 4.1.1. In a next step a 9 mm × 4.5 mm patch of 500 nm thick SiO$_2$ layer is sputtered on top of one half of the substrates. The sputtering was performed by the PGI-6 technician Thomas Jansen. A sputtering rate of 0.2 Å/s was applied. Next the substrate is cut into three approximately 0.5 × 3 × 10 mm^3 pieces by a diamond saw. The cut pieces are cleaned in Acetone and Isopropanol in the ultra sound bath for a couple of minutes. The cleaned and cut substrate pieces were controlled via AFM to ensure a clean surface.

6.1.2   Oxide growth

On top of the prepared substrates, thin layers of NiFe$_2$O$_4$ (NFO) are grown. Two NFO films have been investigated: a 10 nm NFO oxide film and a 2 nm NFO oxide film. The NFO films were grown with the PLD technique according to the growth optimization performed in chapter 4.

6.1.3   Structuring procedure

After the NFO films are grown, a gold contact is deposited on-top. The gold is deposited with the Electron Beam Physical Vapor Deposition (EBPVD) technique. Via the Quadrapole Mass Spectrometer (QMS) a deposition rate of 0.2 Å/s for gold was adjusted. The gold electrode spans half over the SiO$_2$ and half over the NFO/STO oxide side. The structuring pattern of the top-electrode is shown in detail in subsection 3.2.4.

6.1.4   Measurement Routine

Two Au/NFO/STO heterostructures from hereon names as "HtStr", one with a film thickness of 2 nm and one with a thickness of 10 nm, were probed with the in-operando biasing HAXPES. The HAXPES spectra were recorded in normal emission configuration, at room temperature and at a vacuum of $p < 5 \cdot 10^{-10}$ mbar at the P09 HAXPES endstation at Petra III, Hamburg. The measurement position was adjusted to a region between the 40 nm gold fingers of the top electrode. After the measurement position is optimized, the

measurement routine is started. First the HAXPES spectra of Au 4f, Fe 2p, Ni 2p, Sr 3d, Ti 2p and the valence band is recorded without applying any voltage. Next, a voltage is set by the *Agilent* voltage source, the core level(cl) regions are adjusted to the applied voltage and the whole set of HAXPES spectra and the electrical current I flowing through the device are recorded. Next the voltage is switched in sign and the measurements are repeated. In order to minimize the chance of short-outing the HtStrs, the applied voltage was stepwise enhanced and with each step the whole set of HAXPES spectra were measured. The step size of the thin 2 nm NFO HtStr is $U = 1$ V until $U = |4|$ V and $U = 2$ V for higher voltages. The step size of the 10 nm NFO HtStr is $U = 3$ V. In addition, a reference sample of gold, a 20 nm NFO film and a STO substrate was recorded for further comparison.

6.2 The electrical fingerprint of Au/NFO/STO heterostructures

At each voltage step of the in-operando HAXPES measurement the electrical current flow through the Au/NFO/STO heterostructures (HtStr) is observed in case the sample would short out. However, the information of the electrical behaviour is a side product of this measurement. If the voltage is turned on, the electrical current that flows through the HtStr, will stabilize after two to three seconds. This behaviour was observed voltage independently. For each voltage step, the stabilized current was read out from the *Agilent* voltage source and was recorded. One set of in-operando HAXPES spectra took three hours of measurement time. The current read-out slightly decreases from beginning to end of the HAXPES recording by 5% - 15%. However, no abrupt jumps were observed, which indicates a slow discharging effect. The resulting IV-curve and the wiring are shown in figure 6.1 **a)**. The Au/NFO/STO IV-curves are asymmetric. Especially for the 2 nm NFO HtStr the current slowly increases for positive voltages and strongly increases for the negative voltages. For voltages of $|U| < 2$, the current response is a plateau with only small changes in current. The 10 nm NFO HtStr's IV-curve has a similar behaviour. The current rises faster with negative voltage than with positive voltage. However, the expansion of the plateau is reduced.

The observed IV curves resemble the electrical behaviour of diodes. In figure 6.1 **b)**, a sketch of a bipolar diode is presented. In the forward direction (red), the current rises slowly until a threshold voltage. If the threshold voltage is exceeded, the current will rise strongly i.e. small variations in the voltage translate to big variations in the current. Ideally, in the backward blocking direction (blue) the electrical current flow would be zero. However, due to imperfections, a small leakage current is observed with increasing voltage. If the voltage exceeds a breakdown threshold, an avalanche current will occur and rise sharply with small voltage increase. The forward direction in the Au/NFO/STO HtStrs is identified with the negative voltage direction and the blocking direction is identified with the positive voltage direction. The
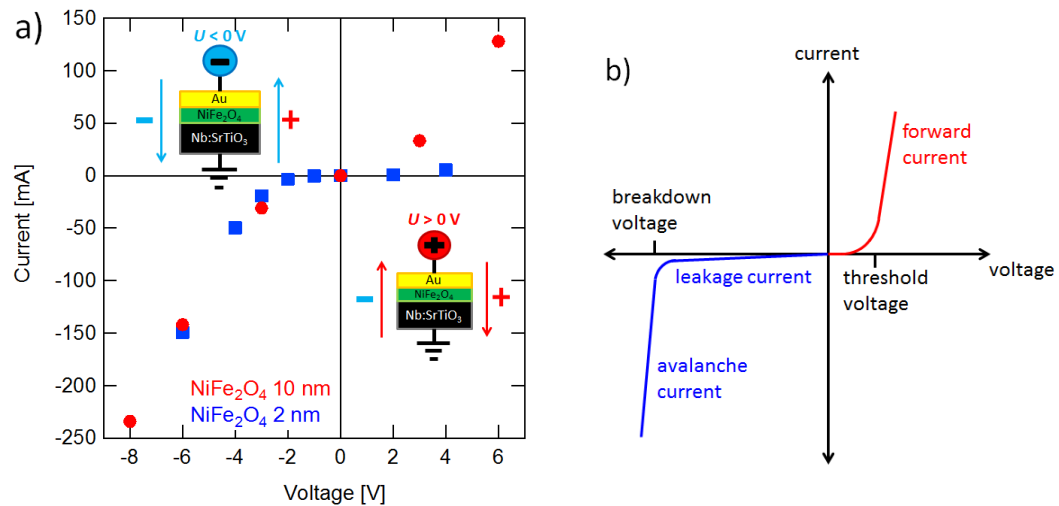
Figure 6.1: (a) Stabilized current *I* measured at each voltage step of the 2 nm (blue) and 10 nm (red) NFO heterostructures. **(b)** Sketch of an IV-curve of a diode.

question arises why the Au/NFO/STO system acts like a diode and why there are differences between the 2 nm and the 10 nm thick NFO systems. The two most basic diode systems are build up from an n-type semiconductor in contact with a metal called a Schottky-diode and an n-type semiconductor in contact with a p-type semiconductor called a pn-diode. Obviously, the gold in the Au/NFO/STO systems is a metal. Usually, the STO is an insulator. However, due to the Niobium doping the STO is conducting and thus can be treated like a heavily doped n-type semiconductor. In contrast, the NFO is expected to be an insulator with a minority spin channel direct band gap of 2.1 eV [21]. Yet the presence of defects and the thickness of the layer weakens the insulating behaviour of the NFO films and thus the NFO thin films can be treated as a semiconductor. Therefore, the two interfaces Au/NFO and NFO/STO both have the possibility to create a Schottky barrier. The analysis of the recorded HAXPES cl in terms of band alignment and band bending at those two interfaces might give information about the origin of the diode like behaviour of the Au/NFO/STO HtStrs.

6.3   Band alignment study of the Au/NFO/STO heterostructure

A photoemission method to measure heterojunction band alignment was provided by Kraut *et al.* [44]. This method is based on the fact that for a given material the energy difference between a core level (cl) and the valence band maximum is a physical quantity. Thus, any shift in the valence band maximum will also result in an equivalent shift of the cl. The method is shortly pictured in section 2.4.2 and covered by HAXPES specialised literature [43]. The bulk sensitive in-operando HAXPES measurements can be used to determine the change in band offsets of buried interfaces. Kraut's model uses the simplified flat band picture to describe the material system electronically and assumes the interfaces of the heterojunctions respectively to be abrupt. Furthermore Krauts's model does not account for inhomogeneous materials. The sharpness of oxide interfaces in general is focus of many device oriented HtStrs as the ion intermixing at the interface or dead layers can affect the quality of hetero oxide devices. In the case of PLD growth, it has been shown that even multi-layers of alternating perovskite oxides can achieve atomic flat interfaces, however it strongly depends on the set of growth parameters and the material system used [129, 130]. One requirement of these sharp interfaces is always that the virgin substrate is atomically flat to begin with. In section 4.1.1, it has been shown that the STO substrate treatment ensured such atomically flat and clean surfaces. Furthermore it has been shown in chapter 4 that atomically smooth NFO films have been achieved via PLD growth and that the step like surface structure of the STO was transferred to the NFO films. Therefore, it can be assumed that the interface between the NFO and the STO is abrupt. The gold on top of the NFO is used as an electrode. Noble metal electrodes on oxides are mostly used to prevent the electrode to oxidise and provide a good conductance. However, ion intermixing might still be an issue. Structural homogeneity of the NFO film was checked via XRD measurements. The stoichiometric homogeneity has been proofed via HAXPES measurements.

Now the band alignment and the evolution of the band alignment with applied bias of the Au/NFO/STO HtStrs will be analysed with Kraut's model. Each sample has two interfaces of interest. The first is the NFO/STO interface at which the semiconductor spinel NFO is connected to the semiconductor perovskite STO. The second one is the Au/NFO interface at which the gold metal is connected to the spinel NFO semiconductor. For each interface, Kraut's method will be applied separately. According to this model, the valence band maximum of the reference materials will be determined in a first step. In the second step the positions of the cl of the reference material and the HtStrs will be determined and then the band offset will be deduced based on equation 2.11 - 2.14.
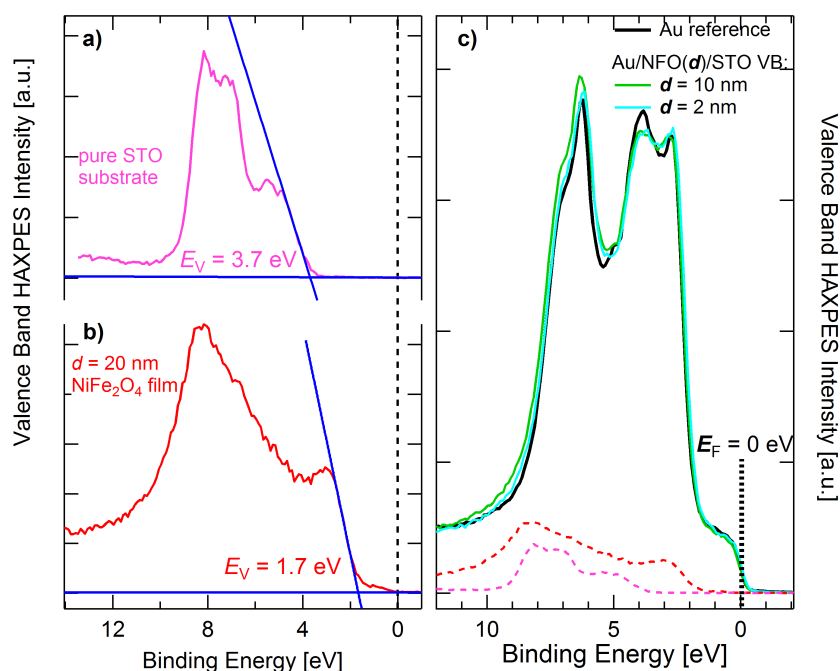
Figure 6.2: a) Valence band spectrum of a virgin Nb:STO substrate. **b)** Valence band spectrum of a reference 20 nm NFO film. The blue line indicate the edge line fit and the zero line fit. The intersection of these two fits is used as the valence band maximum. **c)** Valence band spectra of the 50 nm gold reference sample and the two Au/NFO/STO systems with NFO film thickness of 2 nm and 10 nm. In dashed lines the STO and NFO valence band spectra are presented.

6.3.1   Valence band maximum determination

An important aspect of Kraut's model is the accurate determination of the valence band maximum. A simple solution is found for metals, as the inflection point of the Fermi edge is the Fermi level by definition. However, for semiconductors the density of states at the Fermi level is is zero because the Fermi level normally lies in the band gap. Thus the situation is more complex. In the literature, two different approaches to this problem are used: One approach is based on fitting the valence band spectrum with a theoretical density of states which accounts for experimental effects by implementing a broadening function. This is highly precise in describing the composition of the valence band spectrum [131]. The disadvantage is that it also needs a high information intake: the material specific energy dependent photoemission cross-sections for each band involved in the valence band and the precise knowledge of the experimental broadening effect based on the experimental set-up. For complex oxides, these data are hard to get the hands on as the density of state is also strongly affected by oxygen deficiency and cation stoichiometry. In this thesis, the second approach is used which determines the valence band maximum by extrapolating a line from the valence band edge. Although this simplification can introduce a high uncertainty of the valence band maximum, it has the advantage that it is easily accessible

and can be used as a first hands-on approach to investigate new and complex material systems.

In figure 6.2, the valence band maximum determination of the reference STO, NFO and gold are shown. In order to determine the valence band maximum of the virgin STO substrate (fig. 6.2 **a)**) and the reference 20 nm NFO film (fig. 6.2 **b)**), the valence band edge was fit with a line and the zero offset was fit with a line. The crossing point of these two fits are the valence band maximums of the reference materials. For STO the valence band maximum is $E_v^{STO} = (3.7 \pm 0.1)\,\text{eV}$ and for the NFO the valence band maximum is $E_v^{NFO} = (1.7 \pm 0.1)\,\text{eV}$. While the STO obviously has no measured density of states near the Fermi level at $E_B = 0\,\text{eV}$ the case is different for the NFO. The NFO valence band has a long tail towards the Fermi level which hits the Fermi level with a very small density of state. This does not fit into the picture of the NFO insulator. However, the investigation of the Fe 2p cl of this specific reference sample yields that the Fe^{3+} cations of the NFO films were partially replaced by Fe^{2+}. Thus this sample is slightly off-stoichiometric and the non-zero density of states at the Fermi level is most likely a result of this off-stoichiometry. Because of this fact the NFO tail is not taken into consideration for the determination of the valence band maximum.

Figure 6.2 **c)** shows the valence band of the 50 nm Au reference and the valence bands of the two Au/NFO/STO HtStrs with NFO films of 2 nm and 10 nm film thickness. The infliction point of the Au reference Fermi foot's kinetic energy was used to determine the total photon energy in the experiment. All HAXPES cl are corrected and normalised to this measurement wherefore the Fermi level of the Au valence band is $E_f = 0\,\text{eV}$. As expected, the Au/NFO/STO HtStrs are dominated by the gold valence band and no contribution of the NFO or the STO valence band can be directly observed. However, the intensity ratio between the first main feature at $E_b \approx 7\,\text{eV}$ and the second main feature at $E_b \approx 3\,\text{eV}$ shifts towards a higher contribution of the first main feature. At this position the STO and the NFO valence band spectra have their strongest features, which indicates that this change in intensity ratio may be a result of a STO and NFO contribution.

6.3.2 Determination of the Au 4f binding energy positions

One requirement of Kraut's model is that the investigated core level (cl) are chemically stable, i.e. there are no energy shifts of cl shape changes related to a change in the element's valency. However, the in-operando HAXPES recordings of the Au 4f cl are conspicuous. With applying voltage the Au 4f cl split. If the voltage source is turned off, the Au 4f splitting disappears again. Therefore the observed splitting is not a chemical shift. In figure 6.3, the in-operando HAXPES Au 4f spectra of the Au/(10 nm)NFO/STO and the Au/(2 nm)NFO/ STO HtStrs are displayed. The measurement sequence of the in-operando HAXPES is displayed from bottom to top. In the case of the 10 nm NFO sample the splitting occurs for positive as well as for negative applied voltages. The green arrows in figure 6.3 point to the Au $4f_{7/2}$ cl with the stronger shift and the pink arrows point to the Au $4f_{7/2}$ cl with the smaller
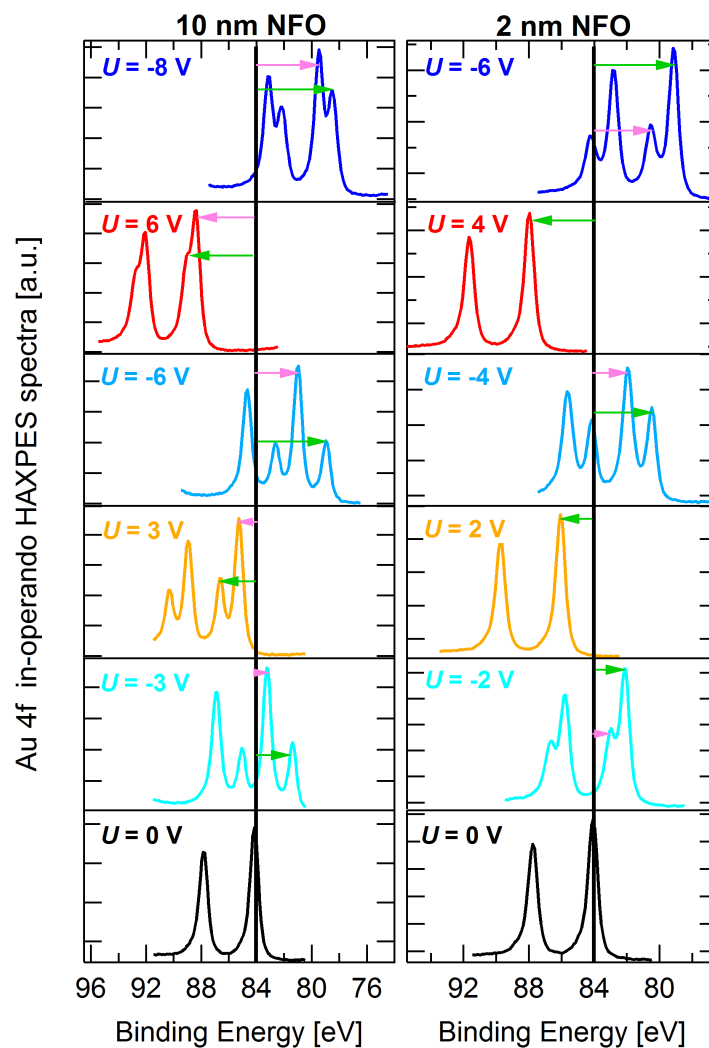
Figure 6.3: Au 4f HAXPES core level of the Au/(10 nm)NFO/STO and the Au/(2 nm)NFO/STO heterostructure in the in-operando measurements are shown. From bottom to top the measurement sequence is displayed.

shift. Within the measurement series the Au 4f$_{7/2}$ with the smaller shift has always a higher intensity. Until the voltage step of $U = -6$ V, the splitting difference seems to correlate with increasing voltages. However, at the next voltage step of $U = 6$ V, the splitting is strongly reduced and although the splitting increases for the $U = 8$ V voltage step, the splitting does not exceed to the splitting difference of the $U = -6$ V. In the case of the 2 nm NFO sample, the splitting only occurs with negative applied voltages. In addition, the intensity ratio between the split cl changes. At $U = -2$ V, the more strongly shifted Au 4f$_{7/2}$ has the higher intensity, at $U = -4$ V the tables are turned: The less shifted Au 4f$_{7/2}$ has the higher intensity and at $U = -6$ V the more strongly shifted Au 4f$_{7/2}$ has the higher intensity again.

In order to understand the origin and behaviour of the observed Au 4f splitting, the shifting distance of the Au 4f cl with respect to the $U = 0$ eV position was determined and compared to the shifts from the NFO and the STO cl. In figure 6.4, the cl shifts of the Au/(10 nm)NFO/STO sample in **a)** and of the

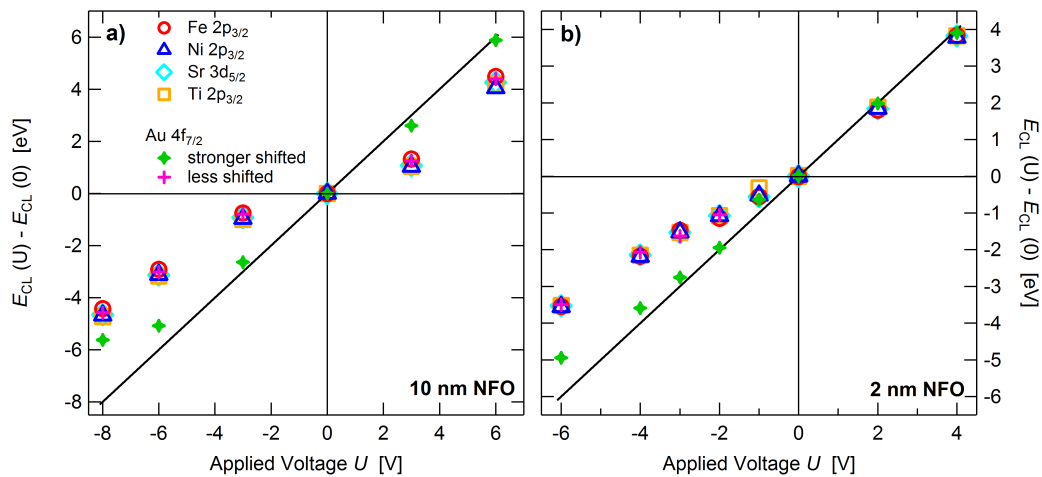**Figure 6.4:** In-operando core level shifts from origin position with respect to the applied voltage of the **a)** Au/(10 nm)NFO/STO and **b)** Au/(2 nm)NFO/STO heterostructure. The core level investigated for both heterostructures were Au $4f_{7/2}$, Fe $2p_{3/2}$, Ni $2p_{3/2}$, Ti $2p_{3/2}$ and Sr $3d_{5/2}$.

Au/(2 nm)NFO/STO sample in **b)** are plotted against the applied voltage. The black line is a guide for the eye as it indicates the maximum cl shift possible with respect to the applied voltage, the "on-potential line". In the 10 nm NFO sample the cl shifts of the NFO film and the STO substrate are the same within the error and are noticeably decreased from the on-potential-shift line. This is already a strong sign for the absence of a strong voltage dependent band alignment at the NFO/STO interface. For clarity and due to the fact that the Au $4f_{5/2}$ and the Au $4f_{7/2}$ cl show similar behaviour with nearly identical difference values the Au $4f_{5/2}$ core level is not included in figure 6.4. In case of Au 4f splitting, the less shifted cl is presented with the green diamond and the more strongly shifted cl is presented with a pink cross. The cl shift of the less shifted Au 4f cl is in agreement with the NFO and the STO cl shifts while the cl shift of the strongly shifted Au 4f cl fits the on-potential line for the most part. Similar behaviour is observed at the 2 nm NFO sample with the only difference that the the NFO and the STO cl shifts for positive voltages are following the on-potential-shift line as well. But for both HtStrs the following rule applies: One Au 4f cl is on the same potential as the NFO and STO and one Au 4f cl is (for the most parts) on the potential of the voltage source. Thus it appears that two types of gold contacting are observed. One is contacted via the gold finger of the gold electrode and is at the potential of the voltage source. One is not connected to the gold fingers but is in contact to the NFO. The thin 4 nm gold layer in between the fingers, the position at which the HAXPES spectra are recorded, is not a closed surface. This explanation is also in agreement with the missing splitting of the Au 4f spectra at positive voltages of the 2 nm NFO sample. The NFO and STO cl are at the same potential as the gold electrode. Thus the gold film connected to the gold fingers experiences the potential of the gold electrode and the gold film not connected to the gold fingers but to the NFO experiences the potential of the

NFO film. A literature search confirms the theory as closed ultra thin gold films are mostly only observed down to a thickness of ≈ 7 nm [132]. Thus for the calculations of the potential barrier height between the valence band maximum of NFO and the Fermi level of Au the "more strongly shifted" Au $4f_{7/2}$ cl is used.

6.3.3 Au/NFO & NFO/STO interface

In order to determine the band alignment by Kraut's method, in a next step the core level (cl) positions of the reference materials and of the heterostructures (HtStr) have to be identified. In a first step the cl of interest were background corrected. For the Au/NFO/STO HtStr the background correction of the Fe 2p cl was more complex because the Fe 2p background was highly influenced by the Au 4s and the Au $4p_{1/2}$ cl. The background was modelled with a Lorentz function fitted to the low binding energy flank of the Au 4s and a linear dependence fitted to the pre-edge of the Fe 2p cl. The detailed procedure is described in appendix E. In the second step the cl of interest were fitted with a Gauss function in the region around the peak. Although for Kraut's model a single material specific cl is sufficient, two cl were chosen for the NFO and the STO. Thus the cl of interest are Au $4f_{7/2}$, Ni $2p_{3/2}$ and Fe $2p_{3/2}$, Ti $2p_{3/2}$ and the Sr $3d_{5/2}$ as this cl are sharp and have the strongest intensity signal. An example of the fitting process is shown in appendix F. While undertaking the fitting procedures, the cl spectra are checked for any sign of chemical change as the latter would lead to a falsified result in the band alignment determination. Neither the Ni 2p and Fe 2p in the NFO nor the Ti 2p and Sr 3d cl spectra of STO show any sign of a chemical change. Therefore, within the detection limit of the HAXPES measurements, the NFO and STO are chemically stable and Kraut's model can be applied to them as well.

Now the general equations from section 2.4.2 of Kraut's model will be applied and thus the potential barrier height Φ_B at the Au/NFO interface and the valence band offset ΔE_V at the NFO/STO interface will be determined as follows

$$\Phi_B = (E_{Cl}^{Au})_{ref} - (E_{CL}^{NFO} - E_V^{NFO})_{ref} + (E_{CL}^{NFO} - E_{CL}^{Au})_{int} \quad,$$

$$\Delta E_V = (E_{CL}^{STO} - E_V^{STO})_{ref} - (E_{CL}^{NFO} - E_V^{NFO})_{ref} - (E_{CL}^{STO} - E_{CL}^{NFO})_{int} \quad.$$

The brackets marked with "ref" refer to the cl and valence band maxima of the reference material and the brackets marked with "int" refer to the cl measured in the HtStr. The formula of Φ_B is compromised because the Fermi level of gold was set to zero as normalization. Φ_B and ΔE_V could be calculated with any cl combination of the involved materials. Therefore the potential barrier height Φ_B is calculated once by the cl combination of Ni $2p_{3/2}$ - Au $4f_{7/2}$ and once by the Fe $2p_{3/2}$ - Au $4f_{7/2}$. In case of the valence band offset ΔE_V determination, two cl of the NFO, namely the Fe $2p_{3/2}$ and the Ni $2p_{3/2}$, and

two cl of the STO, namely the Sr $3d_{5/2}$ and the Ti $2p_{3/2}$, are available which results in four possible cl combinations. The calculated Φ_B and ΔE_V are then just averaged to get a final result. One important aspect is the significance of the calculated potential barrier and band offset value. The Gauss fitting routine of the cl positions resulted in position errors in the range of 0.01 eV to 0.08 eV depending on the sharpness and the overall noise of the probed cl. However, this fitting error is below the experimental energy resolution of the HAXPES spectra of $\delta E = 0.1$ eV, which is the lower limit for an error on the energy scale. Thus, the error of the cl position is set to $\sigma_{CL} = 0.1$ eV. By error propagation calculation the error on Φ_B and ΔE_V for one cl combination thus is 0.24 eV. Thus, the error on the averages is then $\sigma_{\Phi_B} = 0.17$ eV and $\sigma_{\Delta E_V} = 0.12$ eV.

The conduction band offset, also known as the Schottky barrier height, can be deduced from the valence band offset and the band gaps of the probed materials. In the literature, the band gap of STO is found to be an indirect band gap at the Γ point with $E_g = 3.25$ eV [29]. However, a literature search for stochiometric ideal NFO gave a variety of theoretical results for the size of the direct minority band gap. It varies from as little as 1 eV [22] over 1.6 eV [106] towards as much as 2.1 eV for the minority electrons [21]. But the theoretically determined NFO band gap values do not scatter arbitrarily in the literature. In general it can be observed that the more recent the published paper is, the higher the NFO band gap. Naturally, it is expected that the theoretical predictions improve over time as more experimental information on the physical characteristics of a system can be used to confirm and improve the theoretical calculations. Thus, the band gaps used for the calculation of the conduction band offset are taken from K. Dileep *et al.* [21] with the band gap of the minority electrons $E_g^{Min} = 2.1$ eV and the band gap of the majority electrons $E_g^{Maj} = 2.7$ eV.

In figure 6.5, the voltage dependent results for the potential barrier height and the valence band offset of the Au/(2 nm)NFO/ STO and Au/(10 nm)NFO /STO HtStrs are displayed. The overall voltage dependence of the physical quantities does not change with the NFO film thickness. Starting with the valence band offset between the valence band maximum of STO and NFO (VBO): The four cl combinations lead to valence band offsets that are in agreement with each other within the error. The average value is shown in black. Neither the 10 nm nor the 2 nm NFO HtStr show a voltage dependence in the VBO. This indicates already that the interface between the NFO and STO is stable and electrically robust. In a conventional pn-junction, the band alignment and band bending occur in order to account for the charge neutrality. Electrons flow from the n-type (donor) region into the p-type (acceptor) region and vice versa the holes. This leaves oppositely charged localized ions in the respective region and a static electric field appears. This electric field and the charge redistribution cause local band alignment and band bending. However, if an external electric field is applied, another force pulls the electrical charge carriers, reduces or enhances the internal electric field at the
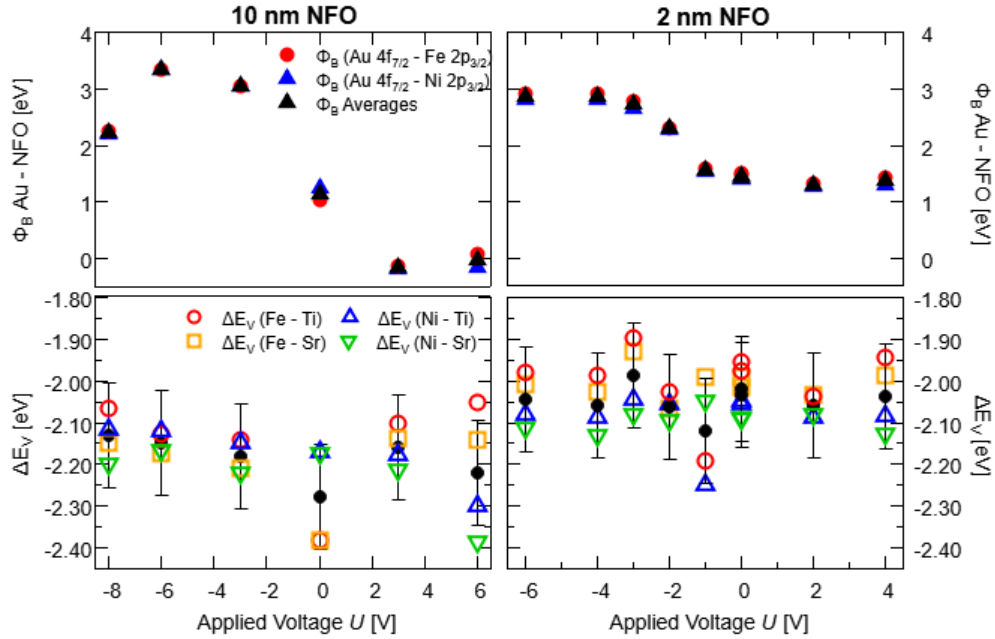
Figure 6.5: Top to bottom: Voltage dependent potential barrier height and valence band offset calculated by Kraut's model of the Au/(10 nm)NFO/STO in the left and the Au/(2 nm)NFO/STO heterostructure in the right are shown.

interface. Therefore a change in the band alignment and band bending is observed. As mentioned before this behaviour is not observed at the NFO/STO interface. Therefore it can be excluded that there is a strong polarized depletion region at the NFO/STO interface. The negative algebraic sign of the VBO indicates that the STO valence band maximum lies below the NFO valence band maximum.

The potential barrier height Φ_B between the valence band maximum E_V of NFO and the Fermi level E_F of gold shows voltage dependent behaviour. For both NFO films, the barrier height first increases with small negative voltages and then saturates at high negative voltages. With positive voltages the 10 nm NFO film's barrier height first decreases and then saturates at high positive voltages, too. In case of the 2 nm NFO the barrier height decreases only marginally. Another difference between the 10 nm and the 2 nm NFO film is the saturation barrier height. For positive voltages the 2 nm NFO film saturates at approximately 1.3 eV while the 10 nm NFO saturates at much lower barrier heights of nearly 0 eV. If the breakdown at $U = -8$ V is excluded the 10 nm and 2 nm NFO film saturate for negative voltages at nearly the same potential barrier height of approximately 3 eV. This voltage dependence clearly indicates that the electronic behaviour is mediated at the Au/NFO interface and therefore that the electrode has a significant influence. There is a strong polarized depletion region at the Au/NFO interface that adjust to external applied electrical fields. Thus, the difference in Φ_B evolution between the 2 nm and the 10 nm NFO HtStr is also influenced by the quality of the gold film. Like discussed before the gold electrodes are not
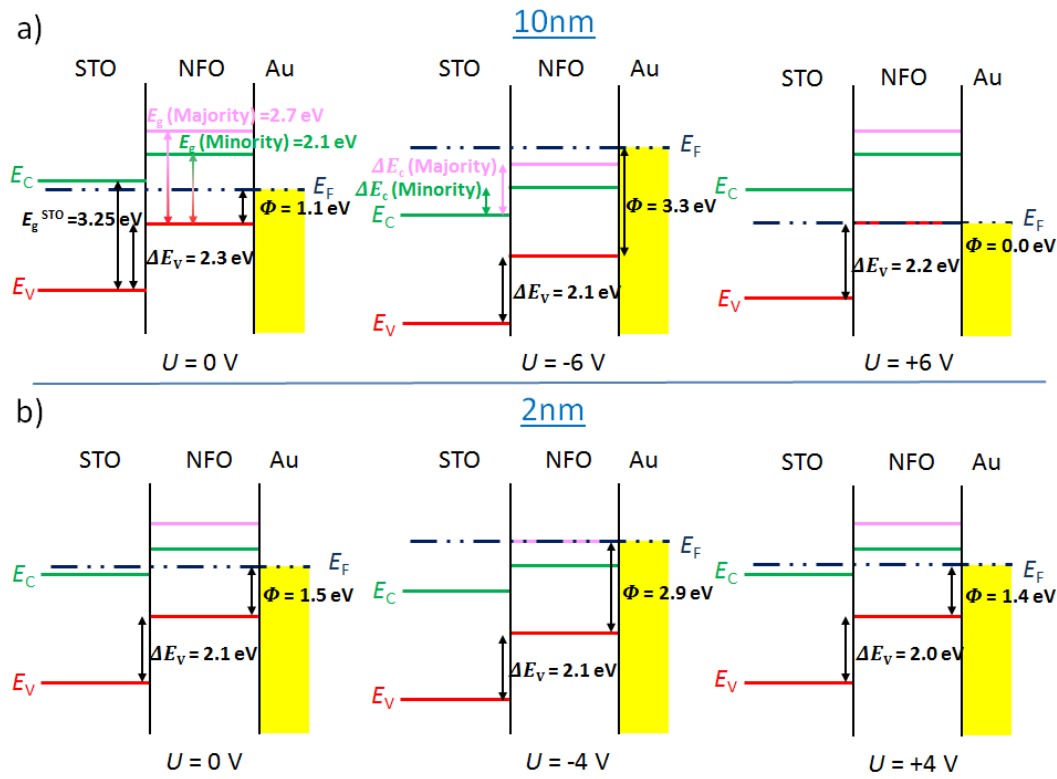
Figure 6.6: a) Sketch of the band alignment of the 10 nm NFO heterostructure for $U = 0, -6, 6$ V. **b)** Sketch of the band alignment of the 2 nm NFO heterostructure for $U = 0, -4, 4$ V.

closed. Although the sample preparation was done thoroughly, slight differences in gold film thickness might lead to a 'more' closed surface and thus cause slightly changes in the electronic behaviour. The positive algebraic sign of the Φ_B means that the Fermi level is above the valence band maximum.

In figure 6.6, the band alignment of the two Au/NFO/STO HtStrs is illustrated with a flat band diagram at zero voltage and the highest positive and highest negative applied voltage for each system. The dashed black line marks the position of the Fermi level E_F throughout the HtStr. The red line is the valence band maximum E_V of the STO and NFO respectively. The green line is the reconstructed position of the conduction band minimum E_C in STO. In NFO, the green line marks the position of the E_C of the minority charge carriers and the pink line marks the position of the E_C of the majority charge carriers. The flat band diagram at $U = 0$ V of the two Au/NFO/STO HtStrs shows the same configuration. The E_V of NFO lays below the Fermi level and the E_V of the STO lays below the E_V of NFO. Furthermore, the NFO's E_C of minority and majority charge carriers lay above the Fermi level. The E_C of STO is located close to the Fermi level. The last fact is attributed to the donor doping of the STO, which induces donor states near the conduction band into the band gap of STO. Although for both HtStrs the E_F lies in the band gap, the E_F in the 2 nm NFO HtStr is near to the E_C while the E_F in the 10 nm NFO HtStr is located in the centre of the band gap. Thus the Schottky

barrier height which is defined as the energy difference between the E_C and the E_F is higher for the 10 nm NFO HtStr. The higher film thickness and the higher Schottky barrier of the 10 nm NFO HtStr might lead to the conclusion for the electron transport that electron tunnelling through the film or inducing electrons into the conduction band of the NFO should be more difficult. But the IV curve of both NFO HtStrs showed the similar trend for applied negative voltages, at which the electrons move from the gold electrode into the STO. For positive voltages, at which the electrons move from the STO into the gold electrode, it was even shown that the 10 nm NFO HtStr has an even lower voltage onset and thus a better electrical conductivity. The result of the IV curves are in agreement with the observed band alignments with applied voltage, which were determined with Kraut's model. For negative voltages the potential barrier Φ_B increases which results in conduction bands falling below the Fermi level E_F. This results in a conducting channel. For positive voltages and 10 nm NFO film thickness the potential barrier Φ_B is decreased nearly to zero. Thus the Fermi level E_F and the valence band maximum are on one energy level and together with the in gap states of the Nb dopant in the STO create again a conducting channel. For positive voltage and 2 nm NFO film thickness the band alignment stays constant within the error and thus no conducting channel is formed. While the IV curves and the band alignments are in agreement with each other the question still stands why this samples are different, in particular why does the 10 nm NFO HtStr show better conductivity than the 2 nm NFO HtStr?

Chemical changes can be excluded as an explanation as there is no evidence for a chemical difference between the two HtStrs in the HAXPES data. One possibility is that the gold electrode produces this effect. In case that the 2 nm NFO HtStr has less gold surface "in-contact", the thinner NFO film might experience less of the electrical field. This can result in a weaker distinct depletion region at the Au/NFO interface and therefore minimize the band alignment. Thus the conduction channel might not be achieved. However, in the Au 4f HAXPES spectra the gold "in-contact" has a big contribution and in the band alignment determination only the gold "in-contact" is of interest. Therefore it is highly unlikely that the worse diode like behaviour of the 10 nm NFO HtStrs is solely based on the electrodes. Another possibility is that the quality of the 2 nm NFO film is better than the quality of the 10 nm NFO film, i.e. the defect distribution is different or different types of defects are on hand. This is a quite uncommon thought because electric devices based on thin oxide films tend to have a lower breakdown voltage with decreasing film thickness. It is commonly excepted that the reason for this is an increased defect density in ultra thin film and that this defects connect to each other and form a destructing conducting channel between the anode and the cathode [133, 134, 135]. However, there is no breakdown observed in the 2 nm NFO film. Instead the IV curve shows a well pronounced diode-like behaviour which is expected for a metal-insulator-metal device.
So let us assume for the moment there is a difference in the defect distribution or in defect types. The 10 nm NFO film has more defects that create

states within the band gap. Thus, the electrons do not have to be injected into the conduction band of the NFO or tunnel through the whole NFO film thickness. Instead they have to overcome the energy to get into the in gap defect states. Thus, with respect to the defect density the electrons are either just directly injected into the defect density band (high defect density) or they tunnel from one defect state to the next defect state (low defect state) which is often referred to as Poole-Frenkel-emission [136]. In total this would result in an enhanced probability of electrons to travel through the NFO film. In case of the 2 nm NFO film the diminished defect density only allows for the conventional electron injection into the NFO conduction band or tunnelling through the NFO film. Therefore the thin NFO acts as a barrier and a more pronounced diode-like electronic behaviour is observed.

The question arises, why should there be less defects and or different defect types in the ultra thin film? It can be safely assumed that the defects of the first layer unit cell are created in order to accommodate the growth of NFO on STO. Thus, defects like anti phase boundaries or interstitials should be present in 2 nm as well as in the 10 nm NFO film. Because of the gold electrode on top of NFO, it can also be assumed that the same amount of defects should be found in the last NFO layer in both samples. The main difference should be found in between the interface layers. Obviously there are not many "in-between" layers in the 2 nm NFO film and there are definitively more in the 10 nm NFO film. Just due to the longer growth time alone, more defects like interstitials, foreign ions or misplaced cations can form in the NFO. Another factor is that one-dimensional and two-dimensional defects like dislocations, stacking errors or mosaicity have just more space to evolve. Also the huge lattice mismatch between the NFO and its STO substrate may affect the defect distribution. In order to relax the film and reduce the energy build-up due to the compressive strain of the substrate, the film incorporates defects. The NFO films relax fully at film thicknesses beyond 2 nm. Thus, it might be possible that the 10 nm film has different and even more defects than the 2 nm film. However, there is no direct proof of any of these theoretical thoughts yet. More experiments are recommended to focus on the reliability of the gold electrode for example with AFM measurements and on the reproducibility of the samples and their IV curve. Further steps should be taken to measure the defect d ensity and identify the types of defects and their densities with respect to NFO film thickness. This might be achieved with tunnelling electron microscopy.
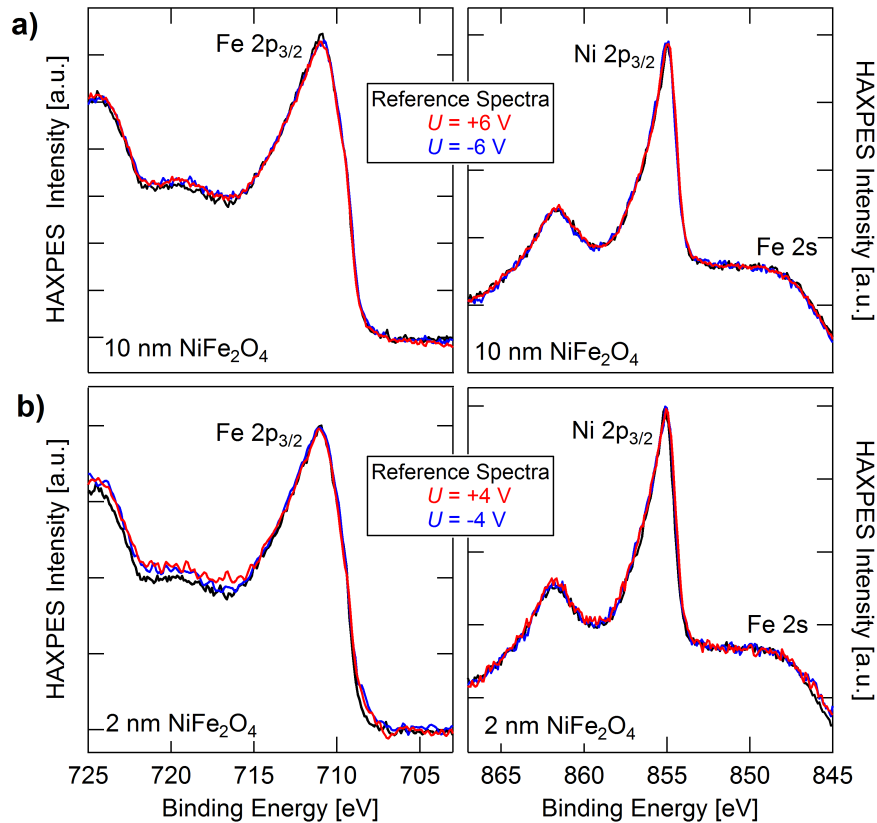
Figure 6.7: In-operando Fe 2p$_{3/2}$ and Ni 2p$_{3/2}$ core level comparison to NFO bulk reference spectra: **a)** for the Au/(2 nm)NFO/STO and **b)** for the Au/(10 nm)NFO/STO heterostructure.

6.4   Band bending study of the Au/NFO/STO heterostructure

Band bending can occur at any material interface due to the necessity of charge neutrality and energy conservation law. Due to the very short electron screening length in metals the band bending region is very small. Thus band bending is almost always observed and investigated in semiconductors or insulators.

In the following sections the band bending of the NFO electronic bands at the Au/NFO and at the NFO/STO interface as well as the band bending of the STO electronic bands at the NFO/STO interface is studied and presented.

6.4.1   Band bending in NFO

In order to identify the band bending that occurs in the NFO thin films the in-operando HAXPES spectra are compared to NFO reference spectra of bulk like thick NFO films in which the band bending at the NFO/STO interface has only a negligible contribution. In figure 6.7 **a)** and **b)**, the comparison with the NFO HAXPES reference spectra of representative Fe 2p$_{3/2}$ and Ni 2p$_{3/2}$ core level (cl) of the 10 nm NFO and the 2 nm NFO HtStr are shown.

The HAXPES cl with positive in-operando voltage are shown in red and the ones with negative in-operando voltage are shown in blue. The reference spectra of a 25 nm NFO film are shown in black. For comparison reasons the in-operando HAXPES spectra are shifted to the position of the reference spectra. The energy shifts are discussed in subsection 6.3.2. A slight difference in the Fe $2p_{3/2}$ pre-edge of the 2 nm NFO sample can be attributed to the noisy background. Also the height shift in the Fe 2p satellite of the 2 nm NFO sample is consistent with the varying and increasing background contribution towards higher binding energies.

A clear sign of band bending is the occurrence of peak broadening, shoulders or even additional peaks which cannot be related to a change in valency of the respectively cl. As shown in subsection 4.2.1, a reduction of Fe iron valency would result in a strong change of the Fe $2p_{3/2}$'s satellite peak and it would result in a rising shoulder at the low binding energy region. The same argumentation applies to the Ni $2p_{3/2}$ cl. Neither the Fe $2p_{3/2}$ cl nor the Ni $2p_{3/2}$ cl show any sign of broadening, change in satellite, or rising shoulders in the probed HtStrs. In fact they could be fitting mirror images of the reference spectra within the sensitivity of the HAXPES measurement. Therefore it can be concluded that the band bending at either interface of the NFO electronic bands is negligible or possibly even vanishing. Also there is also no evidence for a voltage dependency of any band bending. The NFO electronic bands can be assumed to be flat throughout the entire film and for any applied voltage.

6.4.2 Band bending in STO

Analogously to the previous band bending study in the NFO film, firstly any band bending in the STO at the NFO/STO interface has to be identified. Therefore the Ti 2p cl of the Au/NFO/STO HtStrs are compared to a STO substrate reference Ti 2p HAXPES cl in order to detect any change in the cl shape. In figure 6.8, the Ti 2p cl of the two Au/NFO/STO samples at positive in-operando voltage (red) and at negative in-operando voltage (blue) are compared to the STO substrate reference Ti 2p HAXPES spectrum (black). For comparison reasons, the in-operando HAXPES spectra are shifted to the position of the reference spectra. The energy shifts are discussed in subsection 6.3.2.

Both Au/NFO/STO HtStrs have Ti 2p spectra for the positive and negative in-operando voltages, which are identical within the sensitivity of the HAXPES measurements. However, they show a clear change in shape of the Ti 2p cl. While the high binding energy side of the Ti $2p_{3/2}$ cl is still matching the Ti $2p_{3/2}$ of the reference, the low binding energy side gets broad. In contrast to the symmetric STO reference Ti 2p cl, the Ti 2p cl of the Au/NFO/STO are obviously asymmetric. This asymmetry is not the result of a Ti^{3+} contribution, as the energy position of the Ti^{3+}'s Ti $2p_{3/2}$ peak would be at a lower binding energy of 457.9 eV [137]. Therefore the Ti 2p cl's shape change is true evidence of the band bending. But the observed band bending is voltage independent within the sensitivity of the HAXPES measurement. This fits to
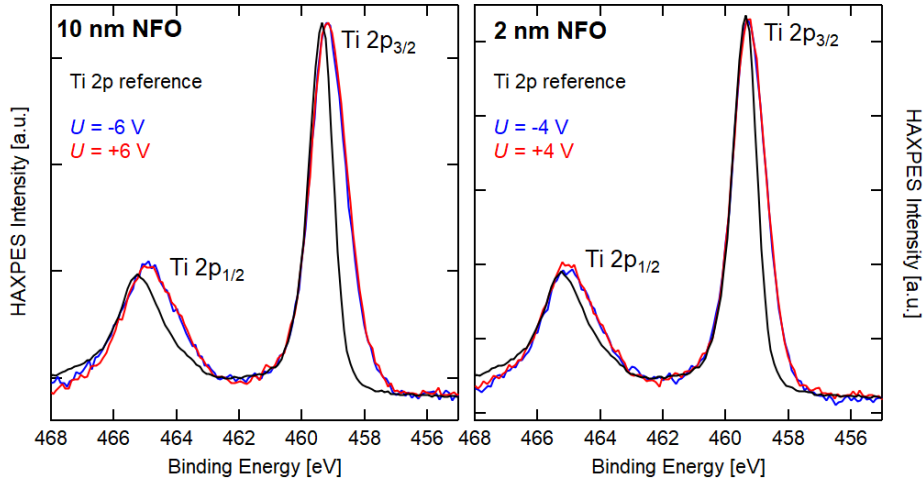
Figure 6.8: In-operando Ti 2p core level comparison to STO substrate HAXPES spectra: **Left** for the Au/(10 nm)NFO/STO and **Right** for the Au/(2 nm)NFO/STO heterostructure.

the observed voltage independent band alignment at the NFO/STO interface as shown in the previous section.

In order to determine the band bending region size and the band bending strength in the STO, the Ti 2p cl of the HtStr will be remodelled. The model is based on three main assumption:

1. The band bending is the strongest at the interface and zero in the bulk of the material. It decreases exponentially. Derivation see section 2.3.

2. A measured HAXPES cl spectrum is the sum of HAXPES cl of each unit cell within the detection depth [45].

3. The 1 unit cell HAXPES cl spectrum is identical to the HAXPES cl of the pure bulk reference.

Thus, any HAXPES cl $I(E)$ can be written as

$$I(E) = \sum_{j=0}^{\text{detection depth}} I_{\text{mat ref}}(E + BB_{\text{shift}}) \cdot exp\left(-\frac{j \cdot a_{\text{material}}}{\lambda_{\text{material}}}\right) \quad . \qquad (6.1)$$

The intensity spectrum $I_{\text{mat ref}}(E + BB_{\text{shift}})$ is the reference bulk HAXPES cl, in this case the Ti 2p HAXPES cl of a clean STO substrate. Furthermore the ith contribution is weakened due to the path the photo electrons have to travel towards the surface (see section 2.4.1). This is expressed by the exponential part in equation 6.1, that includes the travelled path of the photo electrons $j \cdot a_{\text{material}}$, with a_{material} the lattice constant, and the material specific inelastic mean free path (IMFP) $\lambda_{\text{material}}$. The lattice constant of STO is $a_{\text{STO}} = 3.905\,\text{Å}$. Within the groups of oxides the IMFP at a specific photon energy does not vary strongly [138]. Therefore for the purpose of the band bending modelling

a IMPF for STO of $\lambda_{STO} = 9\,$nm is used. Within Kraut's model any shift in the valence band maximum energy position is directly mirrored in a energy shift of the HAXPES cl (see 2.4.2). The band bending is a depth dependent shift of the valence band maximum and conduction band minimum. This translates into a depth dependent band bending shift BB_{shift} of the cl,

$$BB_{shift}(j) = E_{BB\,max} \cdot exp\left(-\frac{j \cdot a_{material}}{\lambda_{BB}}\right) \quad . \tag{6.2}$$

The band bending shift is the strongest with $E_{BB\,max}$ at the interface with $i = 0$ and the band bending shift becomes negligible small for distances d from the interface of $d > 3 \cdot \lambda_{BB}$. The λ_{BB} defines the strength and depth of the band bending shift. Hence three main parameter have to be optimized to get a model that fits optimally to the band bended HAXPES cl: The maximum band bending shift $E_{BB\,max}$, the size of the band bending region $3 \cdot \lambda_{BB}$ and the detection depth. In the case of the Ti 2p cl modelling the detection depth is strongly decreased due to the 4 nm Au film and the NFO film on top. For the 10 nm NFO HtStr roughly 50% of the intensity is lost due to the short IMPF of $\lambda(6000eV) = 5\,$nm in the gold film and roughly another 30% of the intensity is lost due to the film thickness which is assumed to be nearly the same as the IMPF for oxides with $\lambda_{oxide} = 9\,$nm. Furthermore a small experimental intensity loss cannot be excluded. The result is an upper limit for the detection depth at the 10 nm NFO HtStr of roughly 7 nm. A similar argumentation can be applied to the 2 nm NFO HtStr, with the only difference that the thinner NFO film results in a smaller intensity loss. Therefore the upper limit of the detection depth is given by 10 nm.

The modelling had to be performed for each HtStr once because of the voltage independence of the Ti 2p cl. Table 6.1 shows the parameter which yield the best modelling result.
The detection depth of for the 2 nm NFO HtStr is found to be more than two times higher with 22 u.c.$\approx 8.6\,$nm than the detection depth of the 10 nm NFO HtStr with 10 u.c.$\approx 3.9\,$nm which matches the expectations. The maximum band bending $E_{BB\,max}$ differs only slightly between the samples and the negative sign of $E_{BB\,max}$ corresponds to upward band bending. However, the size of the band bending region differs strongly. With a λ_{BB} of 2.5 nm in the 2 nm NFO HtStr, the electronic bands relax slower towards the bulk band alignment value and the band bending region extends approximately

	detection depth [# u.c.]	$E_{BB\,max}$ [eV]	λ_{BB} [nm]
Au/(2 nm)NFO/STO	22 ($\approx 8.6\,$nm)	-1.1	2.5
Au/(10 nm)NFO/STO	10 ($\approx 3.9\,$nm)	-1.2	1.5

Table 6.1: Voltage independent band bending modelling results for the Ti 2p core level at the Au/NFO/STO heterostructures.
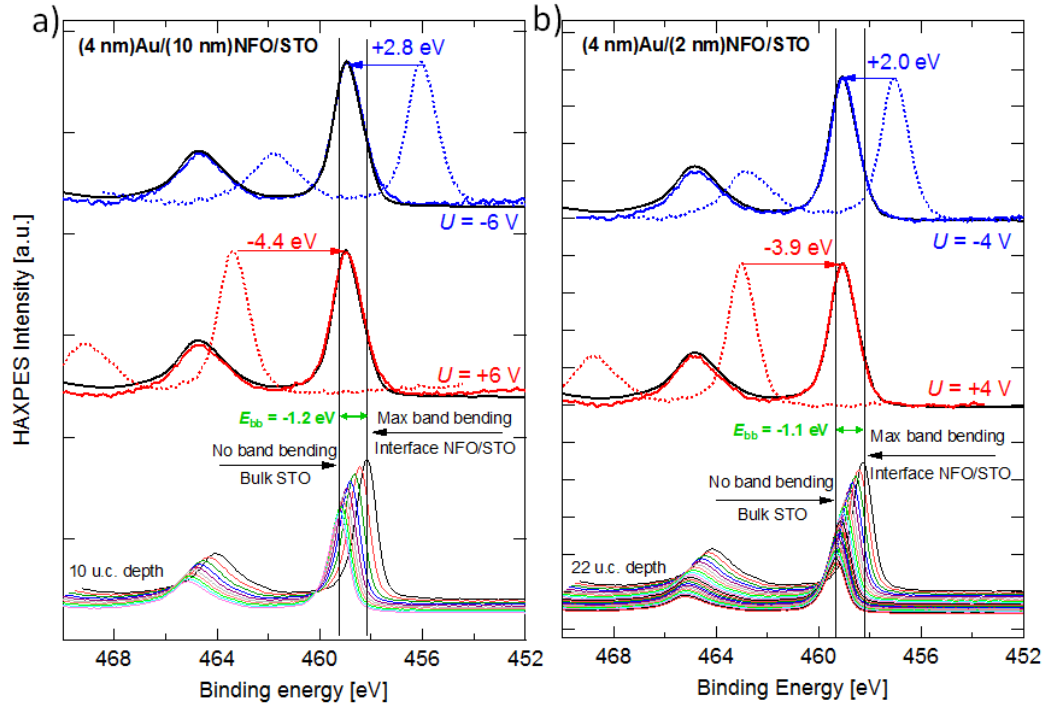
Figure 6.9: (a) Au/ (10 nm)NFO/ STO and **(b)** Au/ (2 nm)NFO/ STO: The band bending modelled Ti 2p core level (black) are presented together with the band bending shifted single unit cell core level contributions. The modelled Ti 2p core level is compared to one positive (red) and one negative (blue) in-operando HAXPES measurement. The core levels are scaled.

$3 \cdot \lambda_{BB} = 7.5$ nm in to the STO substrate. With a λ_{BB} of 1.5 nm in the 10 nm NFO HtStr the electronic bands relax faster towards the bulk band alignment value and the band bending region extends approximately $3 \cdot \lambda_{BB} = 4.5$ nm in to the STO substrate.

In figure 6.9, the band bending modelled Ti 2p HAXPES cl (black) are presented together with the shifted single unit cell HAXPES cl contributions for the respective NFO HtStrs. The modelled Ti 2p HAXPES cl are compared to one positive (red) and one negative (blue) in-operando HAXPES measurement. In order to make the comparison, the Ti 2p cl are shifted to the energy position of the modelled Ti 2p cl. The one modelled Ti 2p cl for each HtStr matches in shape and width the positive and negative in-operando HAXPES measurements of the respective sample. This supports the observation of a voltage independent band bending at the NFO/STO interface and that in fact the band bending can be modelled using Kraut's theory and assuming that the HAXPES measurements can be seen as a sum of single unit cell contributions. Although the band bending strength for both NFO HtStrs is nearly the same, the larger λ_{BB} of the 2 nm NFO HtStr means that the band bending extends further into the STO. In figure 6.9 this translates into smaller energy shifts between the single unit cell contributions. The black vertical lines in figure 6.9 indicate at the low binding energy position the strongest band bending shifted unit cell contribution and at the high binding

energy position relaxed STO energy position without band bending influ-
ence. The summed up modelled Ti 2p cl energy position is near to but not
exactly the relaxed STO energy position. Therefore it can be assumed that
the band alignment calculations of the previous section are influenced by the
band bending. Thus, the band alignment should be treated as a local aver-
aged band alignment of the STO that is near to the interface. The dotted red
and blue cl represent the not- shifted HAXPES measurements. For both NFO
HtStrs, the energy shift between the positive in-operando Ti 2p measurement
and the modelled Ti 2p is larger than the energy shift between the negative
in-operando Ti 2p measurement and the modelled Ti 2p. For the 10 nm NFO
HtStr, the energy shift is below the applied in-operando voltage. In the 2 nm
NFO HtStr, the energy shift of the positive in-operando voltage measurement
is at the potential while the energy shift of the negative in-operando voltage
measurement is also below the the applied in-operando voltage. This fits to
the observation of the NFO band alignment section figure 6.4. Within Kraut's
model, this observed voltage driven energy shift translates into a valence
band maximum shift in the respective direction. Thus, although the band
alignment between the NFO and STO is constant within the error, the total
valence band maximum shift is in fact not constant and is voltage dependent.

6.5   Summary

Section 6.3 of this chapter focussed on the determination of the voltage de-
pendent band alignment at the buried interfaces of the Au/NFO/STO Ht-
Strs. By consequently applying Kraut's model, the band alignment at the
Au/NFO and the NFO/STO interface was extracted from the HAXPES spec-
tra at each voltage step. It has been shown that the band alignment at the
NFO/STO interface is voltage independent. In contrast, the band alignment
at the Au/NFO interface has been shown to be voltage dependent. Further-
more, the voltage dependent band alignment at the Au/NFO interface is in
agreement with the diode like Au/NFO/STO IV-curves for each HtStr. This
supports the ansatz that the NFO and STO electronic bands can be described
in a first approximation with a semiconductor flat band model. Thus the
diode like electronic behaviour is a result of the voltage dependent Schottky
barrier at the Au/NFO interface and the properties of the Au electrode and
the NFO oxide film. Surprisingly, the band alignment at zero voltage lacks
the possibility to predict the electronic behaviour or the voltage dependency
of the band alignment at a HtStr. Moreover the NFO film thickness, qual-
ity of the electrode and the quality of the NFO thin film determine the elec-
tronic behaviour and change the observed band alignments. Especially the
Au/(10 nm)NFO/STO HtStr is supposedly dominated by the defect density
and defect chemistry of the NFO thin film while the Au/(2 nm)NFO/STO
HtStr is dominated by the film thickness and the insulting properties of NFO.

Section 6.4 of this chapter investigated the voltage dependent band bending
at the buried interfaces of the Au/NFO/STO HtStrs. First the NFO film of
the Au/NFO/STO HtStrs were checked for any sign related to band bending

by comparing the Ni 2p and Fe 2p HtStr cl to NFO bulk reference cl. It was found that neither the 2 nm nor the 10 nm NFO HtStr shows cl broadening or a shoulder rising. In fact they fit to the bulk reference cl. Thus there is no band bending in the NFO films and their electronic bands are flat. In contrast to the NFO film the Ti 2p cl of the STO substrate are clearly broadened in both samples. However, the observed band bending is voltage independent, which is in agreement with the observation of the band alignment studies. In a next step, the Ti 2p cl were modelled by using a sum of exponentially shifted, depth dependent single unit cell contributions. The resulting Ti 2p cl correspond to an upward band bending and are in agreement with the Ti 2p measurements in both NFO HtStrs. The band bending strength in the STO is the same in both NFO HtStrs. However, the band bending region of the 2 nm is $3 \cdot \lambda_{BB} = 7.5$ nm and thus clearly larger than the band bending region of the 10 nm NFO HtStr with $3 \cdot \lambda_{BB} = 4.5$ nm.

Chapter 7

In-operando HAXPES of the Pt/La$_{0.67}$Sr$_{0.33}$MnO$_3$/SrTiO$_3$ heterostructure

In the previous three chapters of this thesis, the NFO/STO complex oxide system was investigated in terms of NFO thin film properties and NFO/STO interface properties. More precisely, the dependencies of the growth conditions, of the magnetic field, and of the electric field were probed. In this chapter, a second material system, namely the La$_{0.67}$Sr$_{0.33}$MnO$_3$/Nb:STO (LSMO/STO) heterostructure, is probed with the in-operando HAXPES measurement technique. LSMO is a versatile material that can change its physical characteristics with film thickness, substrate strain, temperature, oxygen vacancy density and with the La/Sr ratio (overview in sec. 2.1.2). Due to its physical properties it is a well studied and still actively researched material system in terms of future electronic applications. Thus this chapter focusses at the electric field dependency of the band alignment and bend bending in the Pt/LSMO/STO heterostructure (HtStr).

7.1 Sample fabrication process & in-operando HAXPES measurement procedure

The successful measurement of in-operando HAXPES requires the samples to be contacted and therefore be structured and secondly a measurement routine that does not directly destroy the samples. The fabrication process consists of three main steps: First the fabrication process of the substrates, second the oxide growth, and third the structuring process.

7.1.1 Substrate preparation

Single crystal (001) 0.5%Nb:SrTiO$_3$ with a size of 0.5 mm $\times$ 10 mm $\times$ 10 mm from *Crystec GmbH, Berlin* has been used as substrates. The etching and annealing follow the procedure described in section 4.1.1. In a next step, a 9 mm $\times$ 4.5 mm patch of 500 nm thick SiO$_2$ layer is sputtered on top of one side of the substrates. The sputtering has been performed by the PGI-6 technician Thomas Jansen. A sputtering rate of 0.2 Å/s has been applied. Next the substrate is cut into three approximately 0.5 $\times$ 3 $\times$ 10 mm^3 pieces with SiO$_2$ on

one side by a diamond saw. The cut pieces are cleaned in Acetone and Iso-propanol in the ultra sound bath for a couple of minutes. The cleaned and cut substrate pieces have been controlled via AFM to ensure a clean surface.

7.1.2 Oxide growth

On top of one prepared substrate a 6 u.c. LSMO film is grown. The LSMO film has been provided by Marek Wilhelm, a fellow PhD student from the PGI-6. The LSMO film has been grown with the PLD technique as well. The LSMO growth has been monitored during growth with a high pressure reflection high-energy electron diffraction (RHEED). The LSMO grows in a layer-by-layer growth mode. Therefore the RHEED detects oscillations and each oscillation corresponds to a fully grown unit cell layer. The PLD growth parameters are as follows:

- $T = 700\,°C$ with $50\,°C$ /min ramp,
- $p = 0.223$ mbar in oxygen,
- $f = 5$ Hz,
- annealing at 500 mbar oxygen until $T < 130\,°C$,
- $F = 3.3$ J/cm^3.

7.1.3 Structuring procedure

After the LSMO film is grown, a platinum metal contact is ex-situ deposited on top. The Pt is deposited with the EBPVD technique. A deposition rate of of $0.1\,\text{Å/s}$ for platinum has been adjusted via QMS. The platinum electrode spans half over the SiO$_2$ and half over the LSMO/STO oxide side. The structuring pattern of the top-electrode is shown in detail in subsection 3.2.4.

7.1.4 Measurement routine

A Pt/La$_{0.67}$Sr$_{0.33}$MnO$_3$ (LSMO)/Nb:STO HtStr with a LSMO film thickness of 6 .u.c. ≈ 2.4 nm has been investigated with the in-operando biasing HAX-PES. The HAXPES spectra have been recorded in normal emission configu-ration, at room temperature, and at a vacuum of $p < 5 \cdot 10^{-10}$ mbar at the P09 HAXPES endstation at PETRA III, Hamburg. The measurement position has been adjusted to a region between the 50 nm Pt fingers of the top elec-trode. After the measurement position is optimized the measurement routine is started. First the HAXPES spectra of Pt 4f, Mn 2p, La 3d, Sr 3d, Ti 2p and the valence band is recorded without applying any voltage. Next a voltage is set by the *Agilent* voltage source, the core level (cl) regions are adjusted to the applied voltage and the whole set of HAXPES spectra are recorded. Next the voltage is switched in sign and the HAXPES measurements are repeated. In order to minimize the chance of short-outing the HtStrs, the applied voltage has been increased stepwise and with each step, the whole set of HAXPES spectra has been measured. The step size of the LSMO HtStr is $U = \pm 1$ V
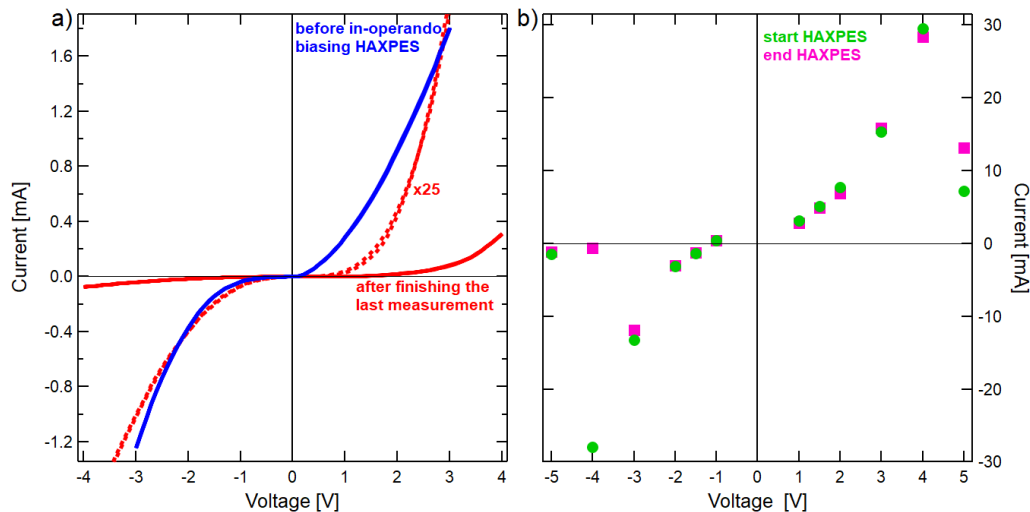
Figure 7.1: a) IV curves measured with the Agilent voltage source of the Pt/(6 u.c.)LSMO/Nb:STO. In blue the IV curve before the in-operando biasing HAXPES measurements, in red afterwards. The red dashed line is the afterwards IV curve multiplied by 25. **b)** Current recorded at each in-operando voltage step. In green at the beginning of each measurement step, in pink at the end of the measurement step.

with an additional measurement point at $|U| = 1.5\,$V. Additionally, a reference sample of platinum, a 20 nm LSMO film, a 6 u.c. LSMO film and a STO substrate has been measured with HAXPES for further comparison.

7.2   The electrical fingerprint of the Pt/LSMO/STO device

Before the start and after end of the whole in-operando HAXPES measurement series, an IV curve has been measured with the build-in function of the *Agilent* voltage source. The voltage step size has been 0.1 V and the measurement time per step has been 10 msec. In figure 7.1 **a)**, the two IV curves are displayed. Obviously the two measurements are not matching and are not identical by scaling the afterwards IV curve up to the before IV curve. This indicates that the HtStr or the measurement set-up has changed at some point during the measurements. However, the general behaviour of the current does not change. The IV curves are asymmetric. In the positive voltage region, the current increases more strongly than in the negative region. At the 'virgin' IV curve there is a plateau region between $U = -0.7\,$V and $U = 0.1\,$V. At the IV curve after the HAXPES measurements the region expands from $U = -1.5\,$V to $U = 2\,$V. The observed IV curves resemble the electrical behaviour of diodes. The positive voltage direction is in agreement with the forward direction of a diode and the negative voltage direction is in agreement with the blocking direction. Ideally, the electrical current flow blocking

direction would be zero. However, due to imperfections and the small thickness of the LSMO film, a small leakage current is observed with increasing voltage. Like the NFO, the LSMO is with a thickness of 6 u.c. regarded as a ferromagnetic insulator. Yet the presence of defects and the thickness of the layer weakens the insulating behaviour of the LSMO film. Thus the LSMO thin film can be treated as a semiconductor. Therefore, comparable to the Au/NFO/STO system, the Pt/LSMO/STO fulfils also the requirements to build a diode. However, the question arises when and why the IV characteristic of the HtStr changes.

When the voltage is turned on, the current through the HtStr will decrease slowly over time. This behaviour has been observed voltage independently. Therefore, for each voltage step, the current at the beginning and at the end of the measurement is read out from the *Agilent* voltage source. One set of in-operando HAXPES spectra takes 2.5 hours of measurement time. The resulting IV-curve and the wiring are shown in figure 7.1 **b)**. In general the current that has been recorded during the measurement is higher than the current of the IV curve measured before and after the HAXPES measurements. It has been also observed that the current needs two to three seconds to stabilize before the slow decrease starts. Therefore the discrepancy in total current might be attributed to the measurement time per step due to accumulation effects. In spite of the slowly decreasing current the 'in-operando' IV curve follows clearly the shape of the IV curve measured prior to the HAXPES measurements in size and increasing behaviour. However, at $U = -4$ V the current collapses during the measurement. The measurement at $U = 5$ V shows a strong rise in current during the 2.5 hour of the measurement but is in-line with the IV curve recorded after the HAXPES measurements. Also the current recorded at $U = -5$ V is in agreement with the IV curve recorded afterwards. The question arises, what is the reason for the Pt/LSMO/STO HtStr changing its electrical behaviour. LSMO is an oxide which can show RedOx switching behaviour. This means that the oxygen content of the LSMO crucially influences the electrical behaviour of the LSMO thin film. It is a reversible process that changes the LSMO from a high resistive state into a low resistive state. However, van Dijken *et al.* [139] and Wilhelm *et al.* [140] show independently that the switching only appears in small areas of a couple of µm in diameter near a sharp tip at voltage. Therefore the total energy per area is a lot higher in the literature than in the Pt/LSMO/STO system studied here. It is even more important that the switching from the low resistance state into the high resistance state happens at positive voltages. The result of the Pt/LSMO/STO systems is in disagreement with the observations in the literature. Therefore an observation of a resistive switching process is highly unlikely. Another possibility is that the platinum electrode has been damaged. In this case the contact Pt and LSMO is not optimal any more and thus the resistivity rises depending on the size of the damage. Thus the $U = \pm 5$ V will be excluded in order to get a clean, full picture of the Pt/LSMO/STO interfaces in terms of band alignment and band bending at the two interface of the Pt/LSMO/STO HtStr.

7.3 Band alignment study of the Pt/LSMO/heterostructure

In analogy to the Au/NFO/STO HtStrs in section 6.3, the band alignment and the evolution of the band alignment with applied bias of the (4 nm)Pt/ (6 u.c.)LSMO/ STO HtStr will be investigated by means of applying Kraut's model to the in-operando HAXPES measurements of this system. This sample has two interfaces of interest. First, the LSMO/STO interface at which the semiconductor perovskite LSMO is connected to the semiconductor perovskite STO. Second, the Pt/LSMO interface at which the platinum metal is connected to the perovskite LSMO semiconductor. For each interface, Kraut's method will be applied separately. According to this model, the valence band maximum of the reference materials will be determined in a first step. In the second step, the positions of the core level (cl) of the reference material and the HtStrs will be determined and then the band offset will be deduced on equation 2.11 to 2.14.

7.3.1 Valence band maximum determination

In analogy to the discussion in section 6.3, the Fermi level of the platinum is determined by the infliction point of the Fermi foot and the valence band maximum in the LSMO is determined via a linear extrapolation of the valence band edge. The valence band maximum of the STO is already discussed and displayed in figure 6.2. In figure 7.2 **a)**, the HAXPES valence band spectrum of the 40 nm platinum reference sample is displayed. The Fermi foot at the low binding energy side was fitted with a Fermi function. The position of the Fermi level was found to be $E_f = (-0.02 \pm 0.10)$ eV. This Fermi level is not zero by default because all in-operando HAXPES cl were corrected and normalised to the gold Fermi edge. The valence band spectrum of the Pt/LSMO/STO sample is shown in red. In comparison to the Pt reference, the Pt/LSMO/STO valence band spectrum is completely dominated by the strong platinum valence band signal. However, a slight shift between the platinum reference spectrum and the HtStr spectrum can be observed, which is a first sign of the band alignment in this system.

In figure 7.2 **b)**, the HAXPES valence band spectra of a 20 nm LSMO film in blue and a 6 u.c. LSMO film in green, both grown on top of STO, are displayed. Despite the decreased intensity in the spectrum of the 6 u.c. LSMO film, the two spectra share the same features and shape. The found shape and features are in agreement with other valence band studies of LSMO from the literature [141]. However, the 6 u.c. LSMO film is clearly shifted towards higher binding energies with respect to the 20 nm film. The shift of the strongest intensity feature is pointed out by the blue and green dashed lines and is roughly 1 eV in size. Two different reasons might lead to this result. First the 6 u.c. LSMO film is roughly just one-tenth of the thickness of the 20 nm film. In combination with the high probing depth of HAXPES measurements it is reasonable that there is a stronger contribution of the STO valence band in the 6 u.c. LSMO valence band than in the 20 nm
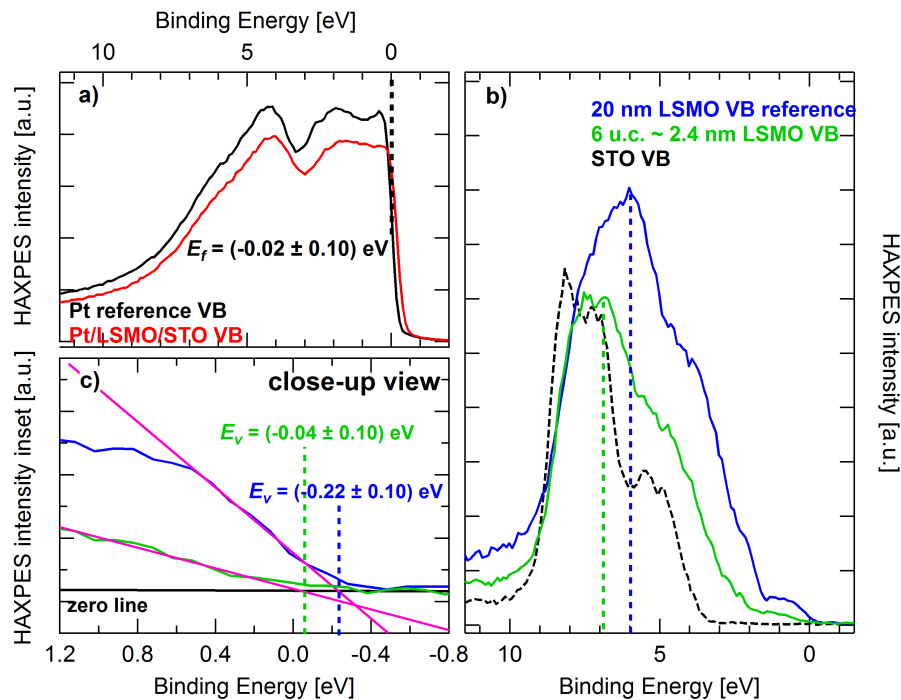
Figure 7.2: a) Pt valence band spectra compared to the Pt/LSMO/STO valence band spectra. **b)** Reference valence spectra of a 20 nm and 6 u.c. $\approx$ 2.4 nm LSMO film. **c)** Determination of the valence band maximum of the 20 nm and the 6 u.c. LSMO film.

LSMO film. The reference STO valence band spectrum is shown in dashed lines for comparison. The main feature of the STO reference is positioned at slightly higher binding energies with respect to the main feature of the LSMO spectra. Thus, a contribution of the STO should result in a shift towards higher binding energies. The second reason is that the 6 u.c. and the 20 nm LSMO film are expected to be different in nature. It is well known that LSMO changes its physical properties depending on the lanthanum and strontium stoichiometry [27] and that the HAXPES valence band differs for the different LSMO compositions [142]. However, the physical properties of LSMO do also depend on the LSMO film thickness in the ultra thin film limit [28]. Below the critical thickness of 3 u.c., LSMO (La$_{0.7}$Sr$_{0.3}$MnO$_3$) is known to be insulating and paramagnetic. If the first critical thickness is exceeded LSMO becomes ferromagnetic but remains insulating. If the film thickness is larger than $\approx$ 9 u.c., the LSMO film becomes conducting. Therefore the 6 u.c. LSMO film is expected to be ferromagnetic and insulating whereas the 20 nm LSMO film is expected to be ferromagnetic and conducting. This would also result in a shift of the 6 u.c. LSMO valence band spectrum towards higher bending energies due to a missing density of states at the Fermi level for insulators.

In figure 7.2 **c)**, a close-up view of the 6 u.c. and 20 nm LSMO valence band edges at roughly 0.5 eV of are shown. The valence band spectrum of the 6 u.c. LSMO film has basically no density of state at the Fermi level in contrast to

the 20 nm LSMO film which is reflected in the negative valence band maximum. The extrapolation of the valence band edges yield a valence band maximum of $E_v = (-0.04 \pm 0.10)$ eV for the 6 u.c. LSMO film and a valence band maximum of $E_v = (-0.22 \pm 0.10)$ eV for the 20 nm LSMO. The direction of the shift fits with the phenomena described before but the shift of the valence band maximum is significantly smaller than the 1 eV shift of strongest intensity feature of the valence band discussed before. This might be evidence that the STO valence band strongly contributes to the measured valence band as the pure STO valence band spectrum has no density of states below ≈ 3.7 eV. Therefore the shift in the valence band maxima might either be caused by the difference in thickness or caused by band alignment of the LSMO and the underlying STO. Now the question is which reference spectrum and thus which valence band maximum should be used in the further analysis. On the one hand, the 20 nm LSMO film is supposed to have different electrical properties due to the difference in film thickness. This fact is expected to result in a difference in the valence bands and thus the 20 nm film is not a good pure material reference for a 6 u.c. LSMO film. On the other hand, the 6 u.c. LSMO film is really thin and the valence band spectrum will most likely be aligned with the STO substrate to some degree and thus not a pure material reference either. In summary, neither of the LSMO films can truly satisfy the requirements for Kraut's band alignment analysis. However, even though the 20 nm LSMO reference cannot be used to discriminate between valence band offsets caused by band alignment of the thin LSMO/STO interface and valence band offsets caused by the reduced film thickness, it can still be used as a reference for the evolution of the band alignment with applied bias. Thus the change in band alignment can still be tracked. Therefore the valence band maximum of the 20 nm LSMO reference is used in the following analysis.

7.3.2 Pt/LSMO & LSMO/STO interface

In order to apply Kraut's method, the core level (cl) positions of the reference materials and the HtStr have to be identified. In a first step, the background of cl of interest has to be corrected. At the Pt/LSMO/STO HtStr the background correction of the Mn 2p cl is a challenging task: The Mn 2p background is not only highly influenced by the Pt 4s and the Pt $4p_{1/2}$ cl background, but also by a Pt $4p_{1/2}$ satellite direct at the position of the Mn2 p cl. Therefore the Mn 2p background is corrected by subtracting a Pt HAXPES reference after fitting it in the region including the Pt 4s and the Pt $4p_{1/2}$ cl to the Mn 2p cl and the survey of the HtStr. The detailed procedure is described in appendix E. In the second step, the energy position of the cl of interest has to be determined. Therefore the cl is fitted with a Gauss function in the region around the peak maximum. Although for Kraut's model a single material specific cl is sufficient, two cl are chosen for the LSMO. The Sr 3d cl has to be excluded because the Sr cations belong to LSMO as well as to STO. Thus the cl of interest are Pt $4f_{7/2}$, Mn $2p_{3/2}$ and La $3d_{5/2}$ and Ti $2p_{3/2}$ as this cl are sharp and have the strongest intensity signal. An example of the fitting process is shown in appendix F. While undertaking the fitting procedures, the
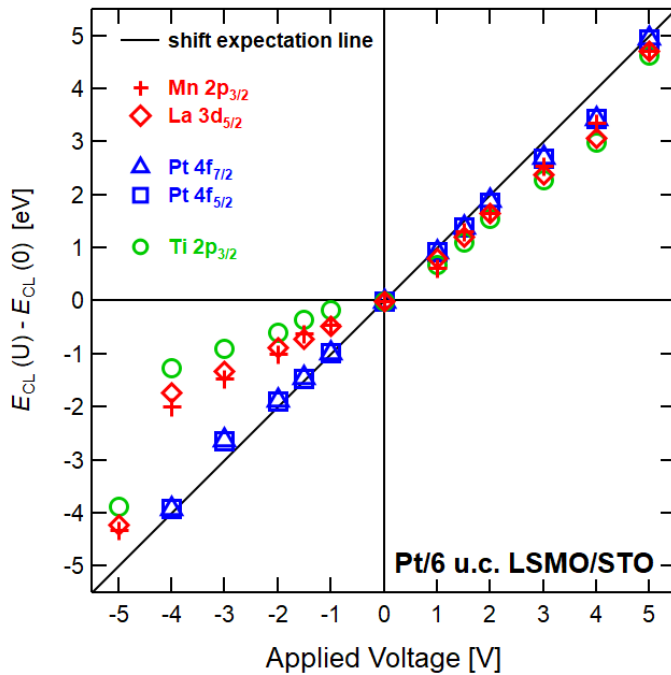
Figure 7.3: In-operando HAXPES core level shifts between the zero applied voltage position and the applied voltage position of the Pt/(6 u.c.)LSMO/STO heterostructure. The core levels investigated are Pt 4f$_{7/2}$ and Pt 4f$_{5/2}$ in blue, Mn 2p$_{3/2}$, La 3d$_{5/2}$ in red and Ti 2p$_{3/2}$ in green.

cl spectra are checked for any sign of chemical change as a chemical change would lead to a falsified result in the band alignment determination. Neither the Mn 2p and La 3d in the LSMO nor the Ti 2p cl spectra of STO show any sign of chemical change. Therefore, within the detection limit of the HAXPES measurements, the LSMO and STO are chemically stable and Kraut's model can be applied.

In the Pt 4f cl, no splitting of the Pt 4f cl is observed with applied voltage. Thus it can be concluded that the 4 nm Pt electrode is closed, in agreement with the critical thickness in platinum on top of oxides [143].

The foundation of Kraut's method is that any valence band shift due to band alignment is also observed as a shift in the cl energy positions. It follows from this that the valence band alignment at a HtStr interface can be reconstructed by cl and valence band maxima of the reference spectra and the observation of the cl positions in the HtStr. Now by calculating the energy difference between the cl of the HtStr with in-situ biasing voltage and the same cl with zero in-situ biasing voltage, the voltage dependency of the band alignment at the interface can be observed. In figure 7.3, those distances between the Pt/LSMO/STO HtStr's cl with applied voltage and its cl position at zero voltage are plotted as a function of the applied voltage. The black line serves as a guide to the eye and indicates the energy position at which a cl lays on the applied potential. The platinum cl differences are shown in blue, the LSMO ones are shown in red and the STO ones are shown in green. In the positive in-situ biasing voltage region the cl differences are all changing minimally with applied voltage and the cl differences of Pt, LSMO and STO are nearly the same at each voltage step. Therefore the band alignment at the Pt/LSMO and LSMO/STO interfaces are only influenced marginally with

positive applied voltages. In the negative in-situ biasing voltage region the cl difference of Pt are voltage independent, in fact the cl difference equals the applied voltage for the most parts. The LSMO and STO cl differences on the other hand are voltage dependent. Their deviation from the "on-potential" line increases with increasing in-situ biasing voltage. Thus the cl differences distance between the platinum and the LSMO and STO increase while the distance between the STO and LSMO only increase minimally by comparison. Therefore a strong voltage dependent band alignment can be expected for the negative in-situ voltage region. The IV curve showed that the electrical signature of the HtStr was changed drastically at the end of the $U = -4\,\text{V}$ in-operando HAXPES measurement. This is mirrored in the differences of the in-operando HAXPES cl at $U = \pm 5\,\text{V}$. The cl difference distances between the Pt, LSMO and STO shrink drastically. The cl differences themselves are near to the on potential line.

Now Kraut's model will be applied to the Pt/LSMO and LSMO/STO interface by utilizing the general equations for the valence band offsets from section 2.4.2. Thus the potential barrier height between the valence band and the Fermi level Φ_B at the Pt/LSMO interface and the valence band offset ΔE_V at the LSMO/STO interface will be determined as follows

$$\Phi_\text{B} = (E_\text{Cl}^\text{Pt} - E_\text{F}^\text{Pt})_\text{ref} - (E_\text{CL}^\text{LSMO} - E_\text{V}^\text{LSMO})_\text{ref} + (E_\text{CL}^\text{LSMO} - E_\text{CL}^\text{Pt})_\text{int} \quad ,$$

$$\Delta E_\text{V} = (E_\text{CL}^\text{STO} - E_\text{V}^\text{STO})_\text{ref} - (E_\text{CL}^\text{LSMO} - E_\text{V}^\text{LSMO})_\text{ref} - (E_\text{CL}^\text{STO} - E_\text{CL}^\text{LSMO})_\text{int} \quad .$$

The brackets marked with "ref" refer to the cl and valence band maxima of the reference material and the brackets marked with "int" refer to the cl measured in the HtStr. The cl are all normalized to the gold Fermi level, thus the Fermi level of the platinum E_F^Pt is not per definition zero, only within the errors. Now in a next step, the Φ_B and ΔE_V could be calculated with any cl combination of the involved materials. The potential barrier height Φ_B is calculated using the cl combination of Mn $2p_{3/2}$ - Pt $4f_{7/2}$, Mn $2p_{3/2}$ - Pt $4f_{5/2}$ and by the La $3d_{5/2}$ - Pt $4f_{7/2}$, La $3d_{5/2}$ - Pt $4f_{5/2}$, in total four cl combinations. In case of the valence band offset ΔE_V determination two cl of the LSMO, namely the Mn $2p_{3/2}$ and the La $3d_{5/2}$, and one cl of the STO, namely the Ti $2p_{3/2}$, are used which results in two cl combinations. The calculated Φ_B and ΔE_V are then averaged to get a final result. One important aspect is the significance of the calculated potential barrier and band offset value. The Gauss fitting routine of the cl positions resulted in position errors in the range of 0.01 eV to 0.09 eV depending on the sharpness and the overall noise of the probed cl. However, this fitting error is below the experimental energy resolution of the HAXPES spectra of $\delta E = 0.1\,\text{eV}$, which is the lower limit for an error on the energy scale. Thus the error of the cl position is set to $\sigma_\text{CL} = 0.1$ eV. By error propagation calculation, the error on Φ_B and ΔE_V for a one cl combination thus is 0.24 eV. Thus the error on the average values is then $\sigma_{\Phi_\text{B}} = 0.12$ eV and $\sigma_{\Delta E_\text{V}} = 0.17$ eV.
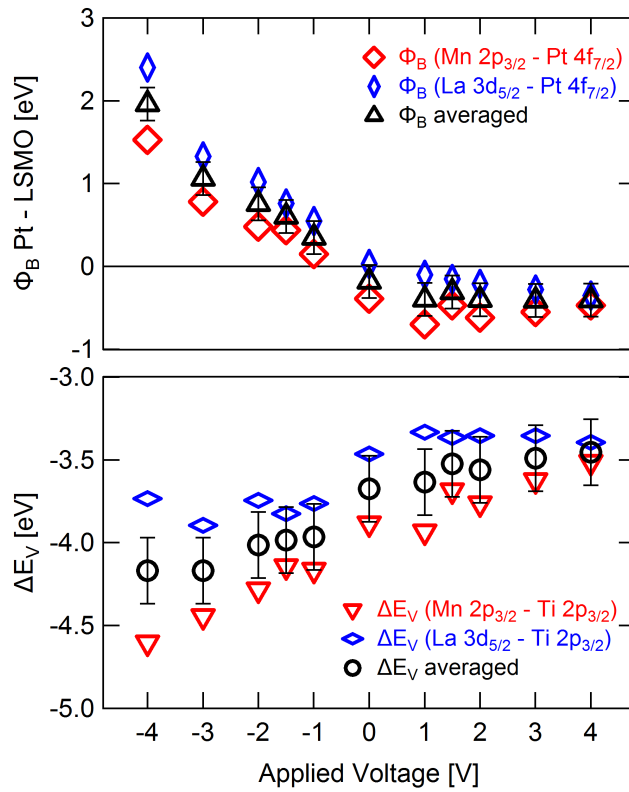
Figure 7.4: Calculated by Kraut's model of the Pt/(6 u.c.)LSMO/STO: Top: Voltage dependent potential barrier height between Pt's E_F and LSMO's valence band maximum. Bottom: Voltage dependent valence band offset between valence band maximum of LSMO and STO.

In figure 7.4, the potential barrier height Φ_B between the valence band maximum of LSMO and the Fermi level of Pt in the top figure and the valence band offset between the valence band maxima of LSMO and STO in the bottom figure are displayed. The barrier height Φ_B has been calculated from the Mn $2p_{3/2}$ cl, which is over all smaller than the Φ_B calculated from the La $3d_{5/2}$ cl. The same observation is found in the valence band offset ΔE_V. This is clearly not a random scattering but rather a constant gap between the values calculated by the Mn $2p_{3/2}$ and the values calculated by La $3d_{5/2}$ cl. There is no obvious physical explanation for this difference on hand as the choice of the cl should not affect the outcome of Kraut's model. One possible explanation might be that the background correction of the Mn 2p cl might have resulted in an undesired shift biased in one direction of the Mn 2p cl position. The Mn 2p background removal is based on the fact that the Pt satellite, which lays in the region of the Mn 2p cl, has a constant distance to the Pt cl and does not change its shape if the Pt does not change its valency. Any shift or shape change of this satellite would result in a wrong background subtraction which could introduce an Mn 2p cl shift. There was however no indication of a chemical change in the Pt and therefore no obvious reason to assume any change in the Pt satellite. Thus the further discussion will continue to average over all values, but the error will be adjusted to $\sigma_{aver} = 0.2$ eV for both the potential barrier height and the valence band offset.

At zero applied voltage and in the positive in-operando voltage region, the averaged potential barrier height Φ_B is negative and is constant within the

error. This means that the Fermi level of Pt is below the valence band maximum of LSMO which results in a conduction channel between the Pt and the LSMO. The same behaviour is also observed in the valence band offset ΔE_V between the valence band of the LSMO and STO. Within the error, the valence band offset at the LSMO/STO interface stays constant for applied positive voltages. The valence band maximum of STO is approximately 3.7 eV below the valence band maximum of LSMO at zero applied voltage and approximately 3.5 eV below the valence band maximum of LSMO at $U = +4$ V. Both values are larger than the band gap of STO of $E_g = 3.25$ eV. The consequence is a conduction channel between the valence band of LSMO and the conduction band of STO. Thus, a conduction channel from the doped STO into the metal Pt is achieved for all positive applied in-operando voltages. This is in agreement with the observation of the IV-curve in which the positive voltage region is identified as the forward direction of a diode. In the forward direction of a diode, the external electrical field is opposed to the internal electric field produced by the depletion region at the Pt/LSMO and LSMO/STO interface. Thus, the depletion region shrinks and vanishes if the bands align energetically at the same level. In case of the Pt/LSMO/STO HtStr, the conduction band minimum of STO and the valence band maximum of LSMO are already at the same energy level. Thus the bands do not need to align. The resulting flat band scheme is shown in figure 7.5. The dashed black line marks the position of the Fermi level E_F throughout the HtStr. The red line is the valence band maximum E_V of the STO and LSMO respectively. The green line is the reconstructed position of the conduction band minimum E_C in STO. There is no line indicating the reconstructed position of the LSMO conduction band minimum for the following reason. As described before, the band alignment at $U = 0$ V and at $U = +4$ V do not differ. In the LSMO theory description in subsection 2.1.2 it was presented that LSMO is in general a half metal and thus does not have a bad gap. However, below a critical thickness of 9 u.c., the LSMO becomes insulating, i.e. a bad conductor due to the exchange interactions adjustments whose are also expressed in the diode like behaviour. Although this is a well studied phenomenon ([28, 144]) there is no information about the evolution of a band gap in LSMO ultrathin film published and available. Thus there will be no conduction band of LSMO in the flat band diagram scheme of the Pt/LSMO/STO HtStr.

In the negative voltage region in figure 7.4, the Φ_B at the Pt/LSMO interface increases strongly with increasing negative in-operando voltage and its sign is switched already at $U = -1$ V. This means that the Fermi level of Pt is above the valence band maximum of LSMO. The valence band offset ΔE_V at the LSMO/STO interface also increases with increasing negative applied voltage, albeit not as strong as the Φ_B. However, the sign of the ΔE_V does not change. Thus the valence band maximum of STO lays far below the valence band maximum of the STO and the offset even increases with increasing negative voltage. The resulting flat band scheme for $U = -4$ V is shown in figure 7.5. In terms of a diode in the reverse voltage direction, the external electrical field is aligned with the internal electrical of the interface's depletion region. Thus, the depletion region extends and the bands align and bend in order

to preserve charge neutrality. However, without the knowledge of the band gap of LSMO, the full picture for the band alignment at the Pt/LSMO/STO HtStr is missing.

It is known from the Schottky diode that the avalanche current in the negative voltage direction has its onset once the band alignment and band bending gets steep and the conduction band of the semiconductor gets below the Fermi level. In this case the electrons can tunnel directly from the Pt Fermi level through the thin Schottky barrier into the conduction band of the semiconductor. From the IV curve of the Pt/LSMO/STO HtStr it is known that the avalanche current in the negative direction has its onset on $U \approx -1$ V. At $U = -1$ V, the Φ_B has a value of ≈ 0.35 V. Thus, following this argumentation, the 6 u.c. LSMO film might at least have a band gap of $E_g \approx 0.35$ eV. After the onset of the avalanche, the current starts increasing strongly due to the increasing in band alignment, the further narrowing of the Schottky barrier and thus the increase in tunnel probability. This is in agreement with the evolution of the Φ_B and ΔE_V observed in the Pt/LSMO/STO HtStr.

7.4 Band bending study of the Pt/LSMO/STO heterostructure

Band bending can occur at any material interface due to the necessity of charge neutrality and energy conservation law. However, due to the very short electron screening length in metals, the band bending region is very small. Thus band bending is in general observed and investigated in semiconductors or insulators. LSMO is a mixed valence oxide that - depending on the chemical composition, the structure, and on the film thickness - changes its properties. As mentioned before, the LSMO study in this chapter is expected to be ferromagnetic and insulating.

In the following sections, the band bending of the LSMO electronic bands at the Pt/LSMO and at the LSMO/STO interface as well as the band bending of the STO electronic bands at the LSMO/STO interface will be studied and presented.
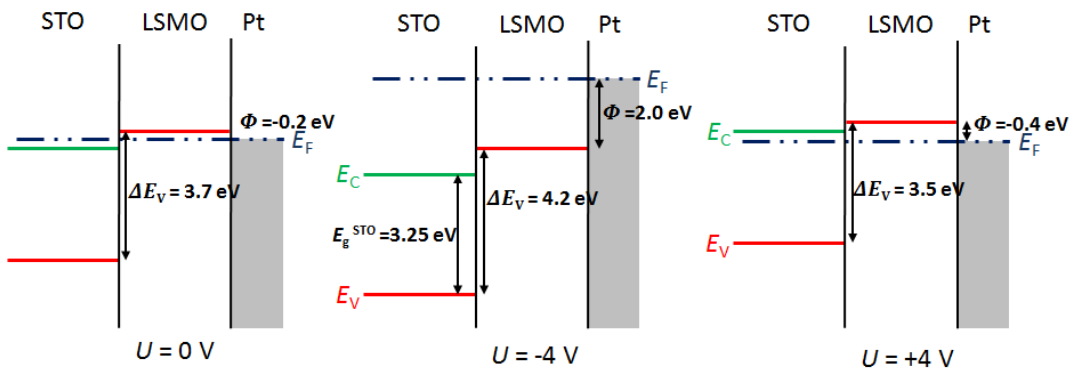
Figure 7.5: Sketch of the band alignment of the Pt/(6 u.c.)LSMO/STO heterostructure for $U = 0, -4, +4$ V.

(4 nm) Pt/ (2.3 nm) LSMO /STO
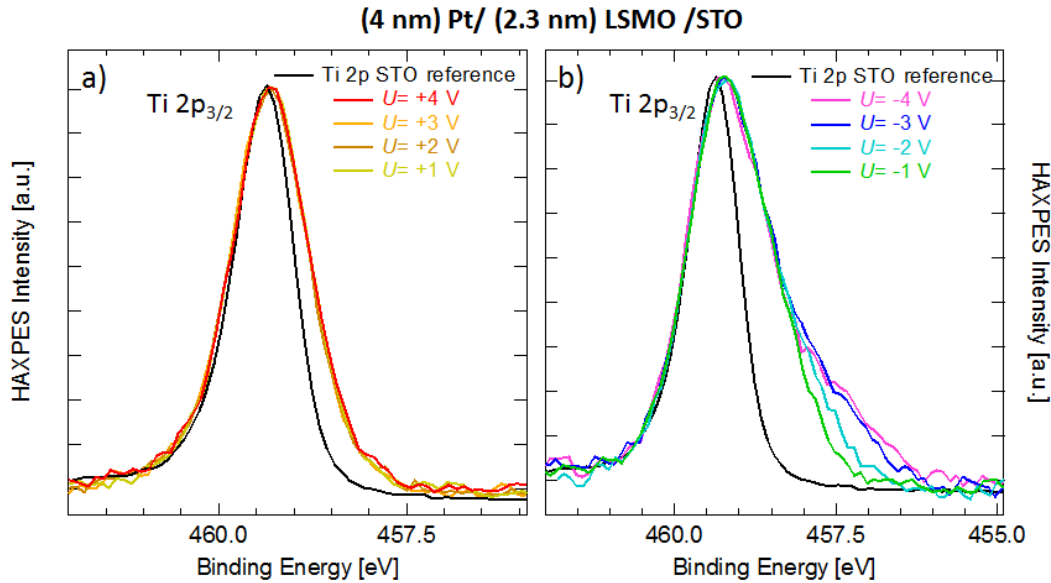
Figure 7.6: Comparison of the in-operando Ti $2p_{3/2}$ core level in the Pt/LSMO/STO heterostructure to the Ti $2p_{3/2}$ core level of a reference STO substrate. Positive applied voltage in **a)** and negative applied voltage in **b)**.

7.4.1   Band bending in STO

In order to identify the band bending that occurs in the STO of the HtStr, the in-operando HAXPES the Ti $2p_{3/2}$ core level (cl) spectra are compared to STO substrate reference spectra. Thus any change in shape can be identified.

In figure 7.6 **a)** and **b)**, the positive and negative in-operando Ti $2p_{3/2}$ cl spectra are compared to the Ti $2p_{3/2}$ of a reference STO substrate. For comparison reasons, the in-operando cl spectra are shifted to the STO substrate cl position. For positive and negative in-operando voltages the Ti $2p_{3/2}$ cl are clearly broadened. However for positive voltages there is no evidence for a voltage dependency. In contrast, for negative voltages there is clearly a shoulder increasing with increasing voltage at the low binding energy flank. Thus, for each negative voltage step, the Ti 2p has to be modelled separately while for the positive voltage region one single Ti 2p modelling has to be performed.

In subsection 6.4.2, a band bending model is introduced that is based on the assumption that the measured HAXPES cl can be represented by a sum of the single unit cell contributions. Utilizing Kraut's theory, each single unit cell contribution is a shifted bulk reference that is damped by an exponential expression with respect to the depth from the interface. The band bending shift is the strongest with $E_{BB\,max}$ at the interface with $i = 0$ and the band bending shift becomes negligible small for distances d from the interface with $d > 3 \cdot \lambda_{BB}$. The resulted formula of the model from equation 6.1 and 6.2 are summarized below

$$I(E) = \sum_{j=0}^{\substack{\text{\# u.c. detection depth}}} I_{\text{mat ref}}(E + BB_{\text{shift}}) \cdot exp\left(-\frac{j \cdot a_{\text{material}}}{\lambda_{\text{material}}}\right) \quad,$$

$$BB_{\text{shift}}(j) = E_{\text{BB max}} \cdot exp\left(-\frac{j \cdot a_{\text{material}}}{\lambda_{\text{BB}}}\right) \quad.$$

The parameter a_{material} is the lattice constant and $\lambda_{\text{material}}$ is the inelastic mean free path (IMFP). The lattice constant of STO is $a_{\text{STO}} = 3.905$ Å and the IMFP of STO is $\lambda_{\text{STO}} \approx 9$ nm. Based on the intensity damping of 4 nm Pt and the 6 u.c. LSMO on top of the STO the detection depth into the STO was found to be ≈ 22 u.c.. The modelled band bending region damping factor λ_{BB} and the modelled maximum band bending shift $E_{\text{BB max}}$ are shown in table 7.1. For the Ti 2p$_{3/2}$ cl with positive applied in-operando voltages and the zero applied voltage case, indeed one modelled Ti 2p cl is found to fit the data. This is in agreement with the observation made in the band alignment studies of the Pt/LSMO/STO HtStr in subsection 7.3.2. The band alignment was found to be voltage independent for positive applied voltages and it does not change compared to the zero voltage case. Thus in the forward direction of the Pt/LSMO/STO device the band bending at the LSMO/STO interface in the STO is voltage independent. With a λ_{BB} of 2.2 nm, the band bending region extends approximately $3 \cdot \lambda_{\text{BB}} = 6.6$ nm into the STO. The maximum band bending at the interface is 1 eV and due to the negative sign this is upward band bending. In case of the Ti 2p$_{3/2}$ cl with negative applied in-operando voltages, the strength of the band bending $E_{\text{BB max}}$ increases with increasing voltage while the band bending region λ_{BB} shrinks. Therefore the upward band bending gets more steep but also relaxes faster to the STO bulk value. However, the band bending region first increases from 2.2 nm at zero voltage to 3.0 nm at $U = -1$ V before it starts decreasing and falls below the 2.2 nm at $U = 3$ V. This behaviour is clearly connected to the rising shoulder at the low binding energy flank of the Ti 2p$_{3/2}$ cl. Overall, the voltage dependency of the band bending at negative voltages is in agreement with the observation of the voltage dependency of the band alignment.

voltage [V]	$E_{\text{BB max}}$ [eV]	λ_{BB} [nm]
-4	-2.5	1.9
-3	-2.2	2.1
-2	-1.8	2.4
-1	-1.6	3.0
0	-1.0	2.2
$0 < V < +5$	-1.0	2.2

Table 7.1: Voltage dependent band bending modelling results for the Ti 2p core level at the Pt/ (6 u.c.)LSMO/ STO heterostructure. Detection depth is 22 u.c into the STO.
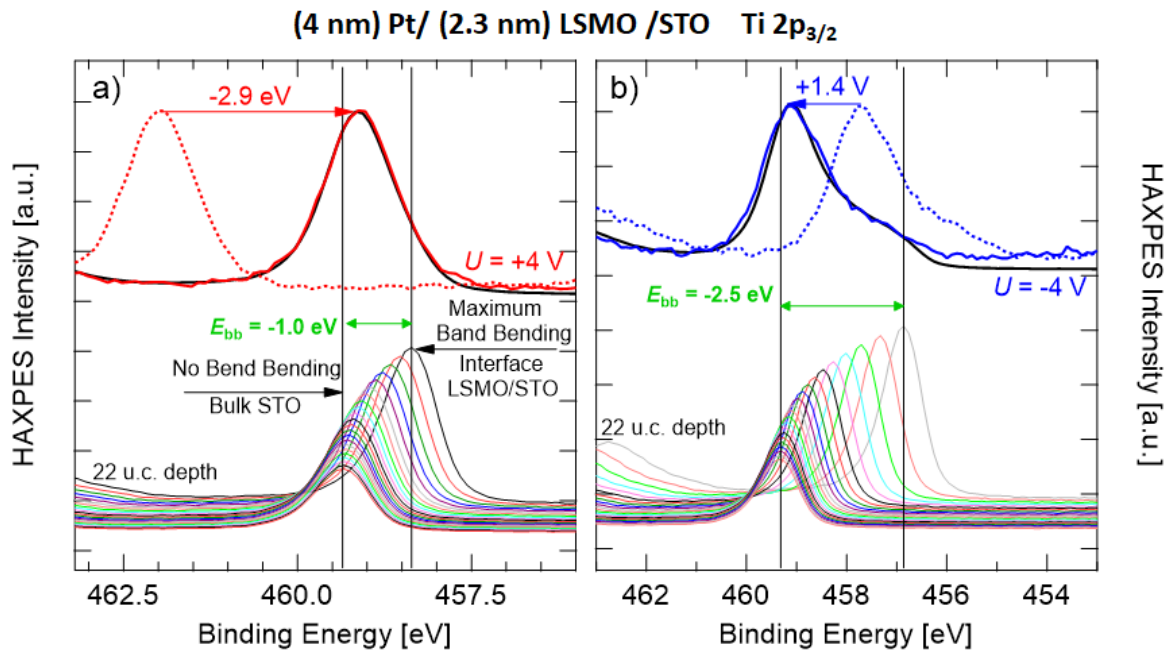
Figure 7.7: (4 nm)Pt/ (2.3 nm)LSMO/ STO: The band bending modelled Ti 2p core level (black) are presented together with the band bending shifted single unit cell core level contributions. The modelled Ti 2p core level for $U = +4$ V in **(a)** and for $U = -4$ V in**(b)** is compared to the HAXPES measurements. The core level are scaled.

In figure 7.7 **a)** and **b)**, the band bending modelled Ti 2p HAXPES cl (black) for the $U = +4$ V and $U = -4$ V are presented together with the shifted single unit cell HAXPES cl contributions. The modelled Ti 2p HAXPES cl are compared to the respective in-operando HAXPES measurements. In order to make the comparison, the Ti 2p cl are shifted to the energy position of the modelled Ti 2p cl. The $U = +4$ V Ti $2p_{3/2}$ cl model fits in shape and width to the HAXPES measurement. The $U = -4$ V Ti $2p_{3/2}$ cl model assembles a shape very similar to the actual HAXPES measurement: One broad main feature and at the low binding energy flank a growing shoulder. The shape of the shoulder fits to the HAXPES measurement in intensity and width. However, the width of the main feature is smaller and thus does not match perfectly to the measurement. During the procedure of the modelling routine it became clear that either the shoulder or the width of the main feature can be modelled perfectly. In case of a nice fitting main feature width however, the shoulder is too high in intensity and thus does not fit to the measurement. One possible explanation is that for strong band bending the assumptions for the model break down partially. In section 2.3, the exponential band bending term was derived for small band bending strengths. A correct and more complex description might lead to a better modelling routine. Nevertheless the band bending modelling procedure used in this section still can recreate the overall cl shape and thus fulfils its purpose.

In a next step the single unit cell contribution arrangement between the $U = +4$ V and the $U = -4$ V HAXPES model are compared to each other. The

two arrangements, that consist both of 22 single unit cell contributions, differ strongly. The band bending model translates a bigger band bending strength $E_{BB\,max}$ into bigger energy steps between the single unit cell contributions that are near the interface. Also, a larger band bending region λ_{BB} means that more single unit cell contribution experience an energy shift due to the band bending. This is exactly observed in the case of $U = -4\,V$ in comparison to the $U = +4\,V$ case. The unshifted Ti 2p$_{3/2}$ cl measurements are shown in dotted lines. The energy shift between the positive in-operando Ti 2p measurement and the modelled Ti 2p is larger than the energy shift between the negative in-operando Ti 2p measurement and the modelled Ti 2p. However, for both measurements the observed shift is smaller than the applied voltage. This observation is in agreement with the findings in figure 7.3. Within Kraut's model, this voltage driven energy shift of the electron cl translates into a valence band maximum shift in the respective direction which is the base of the band alignment studies. However, in comparison to the energy position of the bulk STO Ti 2p$_{3/2}$, both Ti 2p$_{3/2}$ model cl energy positions are shifted towards smaller binding energies. Thus it can be assumed that the band alignment calculations of the previous section are influenced by the band bending. Therefore the band alignment can be treated as a local averaged band alignment of the STO that is near to the interface.

7.4.2 Band bending in LSMO

Analogously, to the previous band bending study in the STO substrate of the Pt/LSMO/STO HtStr, firstly any band bending in the LSMO thin film has to be identified. Therefore a LSMO specific cl of the Pt/LSMO/STO HtStr has to be compared to the same type of cl of a LSMO reference sample in terms of band bending induced broadening or shape change. Due to the facts that the uncorrected Mn 2p HAXPES cl are overlapping with a Pt satellite peak, the overall signal is weak and any background corrections, the Mn 2p cl is not suited to study the band bending. Therefore the La 3d cl is chosen to study the band bending in the 6 u.c. LSMO thin film. Ideally the La 3d HAXPES cl of a LSMO sample would be taken as a reference, so that the LSMO electronic band would not not be affected by the band bending at the LSMO/STO interface. However, bulk LSMO is metallic while the 6 u.c. LSMO thin film is insulating. This can introduce intensity and shape differences as well [142]. Thus, the La 3d cl of a 6 u.c.LSMO/STO reference sample will be used as a reference. Although the band bending at the LSMO/STO interface is expected to influence the electronic bands of the 6 u.c. LSMO thin film, the voltage dependency of the band bending can be tracked without changes due to a change in the LSMO physical properties.

In figure 7.8 **a)** and **b)**, the positive and negative in-operando La 3d$_{5/2}$ cl spectra are compared to the La 3d$_{5/2}$ cl of a reference 6 .c. LSMO thin film. For comparison reasons, the in-operando cl spectra are shifted to the reference 6 .c. LSMO cl position. Neither a shape change nor a broadening are observed for any of the positive in-operando La 3d$_{5/2}$ cl. Therefore a positive voltage dependency of the band bending in the LSMO thin film can be

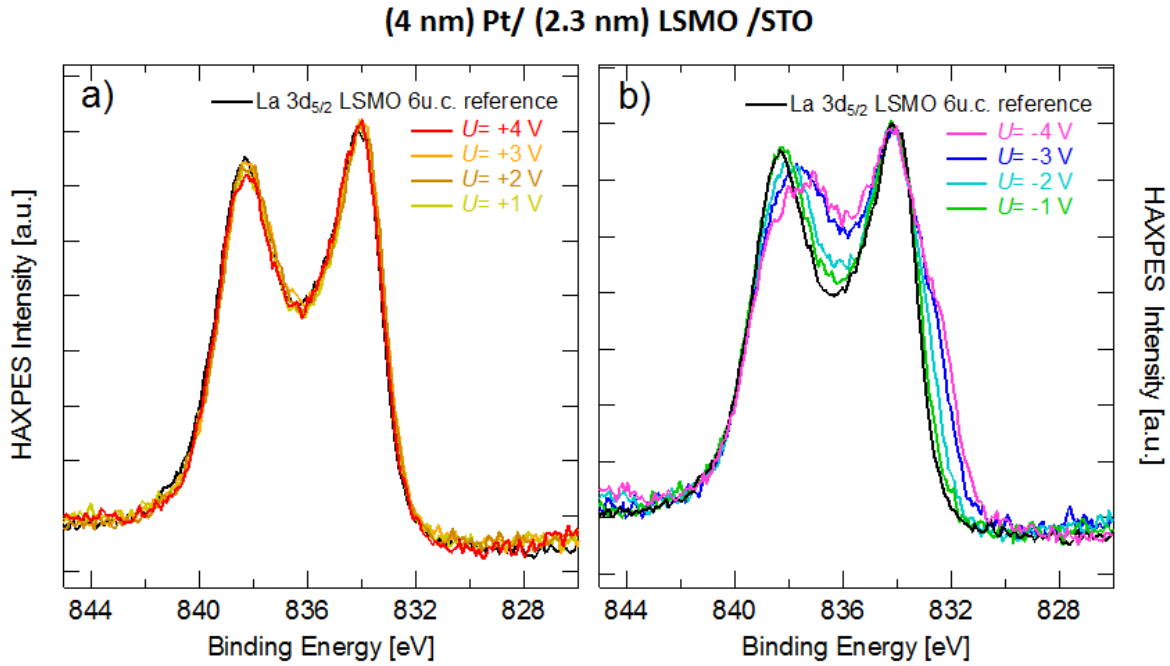**(4 nm) Pt/ (2.3 nm) LSMO /STO**

Figure 7.8: Comparison of the in-operando La $3d_{5/2}$ core level in the Pt/LSMO/STO heterostructure to the La $3d_{5/2}$ core level of a 6 u.c. LSMO thin film reference. Positive applied voltage in **a)** and negative applied voltage in **b)**.

excluded. In contrast, the negative in-operando La $3d_{5/2}$cl clearly shows a voltage dependency. By increasing the negative applied voltage the peaks of the La $3d_{5/2}$ cl's double peak structure increase in width and the intensity ratio changes towards a higher contribution of the second peak at lower binding energies. Additionally, a shoulder at the low binding energy flank arises. This is not a result of a partially changed La valency as the La $3d_{5/2}$ cl shape change as the growing shoulder disappear if the voltage is turned off. Therefore the negative La $3d_{5/2}$ cl will be modelled, analogously to the Ti $2p_{3/2}$ cl, with the band bending model introduced in section 6.4.2.

The detection depth into the LSMO is given by the LSMO film thickness due to the high depth sensitivity of the HAXPES measurement and the low LSMO film thickness. Thus the La $3d_{5/2}$ cl model will be the sum of exactly six single unit cell contributions. The reference La $3d_{5/2}$ cl is given by the La $3d_{5/2}$ cl of the 6 u.c. LSMO/STO HtStr. The LSMO lattice constant is $a_{LSMO} = 3.869$ Å and the IMFP of LSMO is taken from the literature, $\lambda_{LSMO} = 8$ nm [145].

The modelled band bending region size λ_{BB} and the modelled maximum band bending shifts $E_{BB\,max}$ of the negative in-operando voltage La $3d_{52}$ cl are shown in table 7.2. The maximum band bending shift $E_{BB\,max}$ increases with increasing negative applied voltage. The band bending region size however only increases once from $\lambda_{BB} = 1.0$ nm at $U = -1$ V to $\lambda_{BB} = 1.3$ nm at $U = -2$ V and stays constant for higher negative applied voltages. Both values of λ_{BB} lead to a band bending region $3 \cdot \lambda_{BB}$ that of course exceeds the LSMO film thickness $d_{LSMO} = 6$ u.c. ≈ 2.3 nm. Therefore all single unit cell contributions are shifted by the band bending effect and the bulk relaxation

voltage [V]	$E_{\text{BB max}}$ [eV]	λ_{BB} [nm]
-4	-3.2	1.3
-3	-2.7	1.3
-2	-1.8	1.3
-1	-1.0	1.0

Table 7.2: Voltage dependent band bending modelling results for the La 3d core level at the Pt/ (6 u.c.)LSMO/ STO heterostructure. Detection depth is 6 u.c. LSMO film.

energy position is not achieved. Therefore the voltage dependency of the band bending in the LSMO film is reflected in the voltage dependency of the maximum band bending shifts $E_{\text{BB max}}$. An increased $E_{\text{BB max}}$ with a constant band bending region results in a larger energy step size between the single unit cell contributions. Also the negative sign of the $E_{\text{BB max}}$ refers to an upwards band bending in the LSMO thin film. In conclusion the modelling strongly suggests that the LSMO thin film does in fact not exist in a flat band situation for negative applied voltages. Furthermore, the LSMO thin film's electronic bands have a positive slope, i.e. the electronic bands of LSMO lie energetically higher at the Pt/LSMO interface than at the LSMO/STO interface.

In figure 7.9, the La 3d$_{5/2}$ HAXPES measurement at $U = -4$ V (blue), its La 3d$_{5/2}$ cl band bending model (black) and the single unit cell contributions are shown. The model and the experiment are in agreement with each other. A dotted line shows the unshifted La 3d$_{5/2}$ in-operando HAXPES measurement. The shift between the La 3d$_{5/2}$ model and the La 3d$_{5/2}$ in-operando
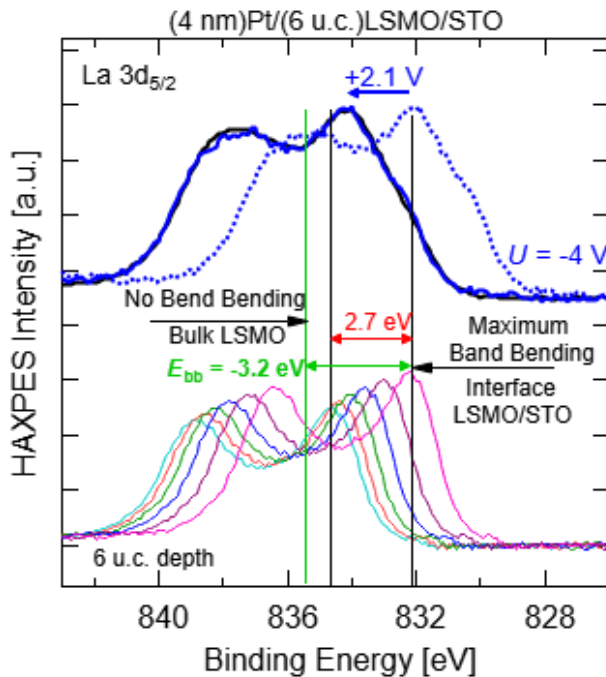
Figure 7.9: (4 nm)Pt/ (2.3 nm)LSMO/ STO: Showcase of the $U = -4$ V La 3d$_{5/2}$ HAXPES measurement, its band bending modelled La 3d$_{5/2}$ core level (black) and the single unit cell core level contributions. The core levels are scaled.

HAXPES measurement is smaller than the applied voltage. This observation is in agreement with the findings in figure 7.3. Within Kraut's model this voltage driven energy shift of the electron cl translates into a valence band maximum shift in the respective direction which is the base of the band alignment studies. The black vertical line at the lower binding energies mark the energy position of the most band bending shifted single unit cell contribution at the Pt/LSMO interface. The black line at the higher binding energies mark the energy position of the less band bending shifted single unit cell contribution at the LSMO/STO interface. The summed up total band bending model HAXPES signal lies in between those two lines. The actual energy position of the La $3d_{5/2}$ cl of the LSMO reference not influenced by band bending is marked with the green vertical line and lies at even higher binding energies. This fits to picture of not flat electronic bands introduced above. Thus, is can be safely assumed that the band alignment calculations of the previous section are influenced by the band bending at negative applied voltages. Therefore the band alignment at the LSMO/STO and the Pt/LSMO interface have to be treated as a local averaged band alignment.

7.5   Summary

Section 7.3 of this chapter has focussed on the determination of the voltage dependent band alignment at the buried interfaces of the Pt/LSMO/STO heterostructure (HtStr). By consequently applying Kraut's model the band alignments at the Pt/LSMO and the LSMO/STO interface have been extracted from the HAXPES spectra at each voltage step of the in-operando HAXPES measurements. It has been shown that the band alignment at the LSMO/STO interface and at the Pt/LSMO interface has a voltage dependency at negative in-operando voltages. In contrast, the band alignment at both interfaces for positive in-operando voltages are only weakly voltage dependent. The comparison between the diode like behaviour in the IV curve of the Pt/LSMO/STO HtStr and the Schottky diode and its working principle resulted in a lower limit for the band gap in the LSMO thin film of $E_{\mathrm{g}} \approx 0.35\,\mathrm{eV}$. In case that the minimum of the LSMO band gap is indeed correct, the extracted band alignment of the Pt/LSMO/STO HtStr is in agreement with the diode like electronic behaviour shown in the IV curve. This supports the ansatz that the LSMO and STO electronic bands can be described in a first approximation with a semiconductor flat band model. Also the band alignment at zero voltage lacks the possibility to predict the electronic behaviour or the voltage dependency of the band alignment at the Pt/LSMO/STO HtStr. Moreover the LSMO film thickness, mixed ion valency ratio, quality of the electrode and the quality of the thin LSMO film determine the electronic behaviour and the observed band alignments.

Section 7.4 of this chapter has investigated the voltage dependent band bending at the buried interfaces of the Pt/LSMO/STO HtStr. First, the STO substrate of the Pt/LSMO/STO HtStr has been checked for any sign related to band bending by comparing the Ti $2p_{3/2}$ cl to STO substrate reference Ti $2p_{3/2}$

cl. It has been found that the Ti 2p$_{3/2}$ is influenced by band bending. A constant band bending has been observed for positive in-operando voltages and a voltage dependency has been observed for the negative in-operando voltages. In a next step the Ti 2p$_{3/2}$ cl have been modelled by using a sum of exponentially shifted, depth dependent single unit cell contributions. Due to the strong band bending, the band bending model partially breaks down. However, the overall shape can still be recreated. The resulting Ti 2p$_{3/2}$ core levels correspond to an upward band bending and are in agreement with the Ti 2p$_{3/2}$ measurements. Second, the LSMO thin film has been checked for any sign related to band bending by comparing the La 3d$_{5/2}$ cl to LSMO 6 u.c. reference La 3d$_{5/2}$ cl. A voltage dependent band bending is observed in the negative in-operando HAXPES measurements. Analogously in a next step the La 3d$_{5/2}$ cl have been modelled by using a sum of six exponentially shifted, depth dependent single unit cell contributions. The resulting La 3d$_{5/2}$ cl correspond to an upward band bending. The band bending study of the LSMO film suggest a not flat band case for the LSMO film, instead nearly linear electronic bands with positive slope, i.e. the electronic bands are energetically higher at the Pt/LSMO interface and lower at the LSMO/STO interface.

Chapter 8

Conclusion and Outlook

Conclusion: Growth & Synchrotron Studies

Chapter 4 has covered the successful PLD growth parameter optimization and the characterization of the resulting NFO thin films grown on top of the STO. In order to optimize the PLD growth parameters one NFO film series has been grown with variation of the laser fluence and one with a variation in gas composition. The NFO films' properties have been investigated in terms of surface roughness, crystallinity, defect density, and magnetic response. The laser fluence influence is minimal and no trends could be identified within the probed range of laser fluence. The gas composition applied during growth on the other hand clearly affects the NFO film quality. If the gas composition is changed from a 25:75 $Ar:O_2$ ratio to a 0:100 $Ar:O_2$ the crystallinity, defect density, and the magnetic response are improved. The resulting improved NFO thin films are smooth, single crystalline and grow along the c axes in (001) direction of the STO.

In a next step the optimized NFO films have been investigated in terms of cation valency and site occupation by means of HAXPES and XMCD. Ni 2p and Fe 2p HAXPES and Ni L edge and Fe L edge XMCD spectra have been measured. It has been found that the NFO films consist of Ni^{2+} cations and Fe^{3+} that occupy the octahedral sites of the spinel structure, which is in agreement with the theoretical expectations. However, also a weak signal of Fe^{2+} residing on tetrahedral sites is found in the XMCD signal, which has been not detected by HAXPES measurements. This is also observed by the literature and seems to be a film thickness independent observation. Thus it is highly possible that the Fe^{2+} accumulates at the film surface.

Conclusion: Magnetic Response At The $NiFe_2O_4/SrTiO_3$ Heterostructure

Chapter 5 has covered the in-plane XMCD investigation of NFO/STO heterostructures (HtStr) measured at the I10 beamline at the DIAMOND light source. The XMCD signal of the Ni L and Fe L edges of a 6.1 nm NFO have been analysed and the XMCD sum rules have been applied. The analysis has revealed that the Fe contributes to the total magnetic moment with a small non vanishing orbital and spin magnetic moment. This has been related to the small amount of Fe^{2+} which contributes to the Fe moments. The orbital moment of Ni is nearly completely quenched and the spin moment of

the nickel contributes heavily to the total magnetic moment of the NFO film which is in agreement with the theory. The total magnetic moment at the applied magnetic field of $B = -1\,\mathrm{T}$ is $m_{\mathrm{total}} = (0.67 \pm 0.04)\,\frac{\mu_{\mathrm{B}}}{\mathrm{f.u.}}$, so roughly 40% lower than the expectation value. This cannot be explained by the internal error of 30% from the sum rules and thus more investigation of the film properties are needed in order to understand this deviation.

The magnetic response of the STO substrate has been investigated by analysing the Ti L edge XKCD signal. Due to the surface sensitivity of the TEY recording mode, all findings are related to the interface near the substrate. The Ti L edge XAS exhibits features of Ti^{4+} and Ti^{3+} cations, from which only the first one is expected to be found in bulk STO. The investigation of the XAS Ti L edge of a NFO film thickness series shows that thicker top layers result in a stronger Ti^{3+} contribution which suggests an accumulation of Ti^{3+} at the interface and that the NFO extracts oxygen from the STO during growth. A non zero true Ti XMCD signal is found which is not expected to be found in bulk STO. The comparison with theoretical XMCD spectra of Ti^{3+} and Ti^{4+} yield that the Ti XMCD is a mixture of the Ti^{3+} and Ti^{4+}. Furthermore the Ti XMCD is magnetic field dependent and mimics the ferrimagnetic behaviour of the Ni and Fe XMCD. This is explained by the proximity effect at which the ferrimagnetic NFO transfers the magnetic ordering to the Ti^{3+}. However, further investigations specifically of the cation distribution across the interface are needed in order to find the origin of the physical properties at the NFO/STO interface.

Conclusion: In-Operando HAXPES Band Alignment Studies

Sections 6.3 and 7.3 of this thesis has focussed on the determination of the voltage dependent band alignment at the buried interfaces of the Au/NFO/ STO and the Pt/LSMO/STO heterostructures. By consequently applying Kraut's model the band alignment at the Au/NFO and the NFO/STO interfaces and the Pt/LSMO and LSMO/STO interfaces have been extracted from the HAXPES spectra at each voltage step. In the Au/NFO/STO HtStr, it has been shown that the band alignment at the NFO/STO interface is voltage independent but the band alignment at the Au/NFO interface is voltage dependent. The voltage dependent band alignment at the Au/NFO interface is in agreement with the diode like Au/NFO/STO IV-curves for each HtStr. In the Pt/LSMO/STO HtStr, it has been shown that the band alignment at the LSMO/STO and at the Pt/LSMO interface has a voltage dependency at negative in-operando voltages, but both interfaces show no voltage dependency for positive in-operando voltages. The comparison between the diode like behaviour in the IV curve of the Pt/LSMO/STO HtStr and the Schottky diode and its working principle has resulted in a lower limit for the band gap in the LSMO thin film of $E_{\mathrm{g}} \approx 0.35\,\mathrm{eV}$. In this case, the extracted band alignment of the Pt/LSMO/STO HtStr is also in agreement with the diode like electronic behaviour shown in the IV curve. This supports the ansatz that the NFO, LSMO and STO electronic bands can be described in a first

approximation with a semiconductor flat band model in a first approximation. Furthermore, is has been found for both HtStr that the band alignment at zero voltage lacks the possibility to predict the electronic behaviour or the voltage dependency of the band alignment. The electronic behaviour in those two different material systems strongly depend on the quality of the electrode and the oxide thin film properties, i.e. film thickness, stoichiometry, and defect density. In conclusion, the band alignment determination by Kraut's method enables oxide HtStrs to link the electronic behaviour shown in IV curves to the respectively electronic band alignment at the buried interfaces.

Conclusion: In-Operando HAXPES Band Bending Studies

Sections 6.4 and 7.4 have investigated the voltage dependent band bending at the buried interfaces of the Au/NFO/STO HtStrs and the Pt/LSMO/STO HtStr. In a first step, the oxide film and oxide substrate core level (cl) have been compared to cl spectra of reference materials and checked for any sign related to band bending, i.e. cl broadening or any kind of shape change. It has been found that there is no sign of voltage dependent band bending in the Fe 2p and Ni 2p cl of the NFO film. Thus, the NFO electronic bands can be assumed to be flat. In contrast, in the La 3d cl of the LSMO film, a voltage dependent band bending is observed for negative in-operando voltages. The STO substrate Ti cl shows band bending effects in the LSMO and the NFO HtStrs. However, a voltage dependency of the band bending is only observed for negative applied in-operando voltages at the STO in the LSMO HtStr. The voltage dependency of the STO band bending is in agreement with the observation of the band alignment voltage dependency for both samples. In a next step, the cl HAXPES spectra that have been influenced by band bending have been modelled by using a sum of exponentially shifted, depth dependent single unit cell contribution. The modelled spectra fit in shape and intensity to the experimental measurements. The modelled Ti cl of the Au/NFO/STO HtStr, the modelled Ti cl of the Pt/LSMO/STO HtStr, and the modelled La 3d cl of the Pt/LSMO/STO HtStr all correspond to upward band bending. The band bending region of the HtStrs in the STO varies between $3 \cdot \lambda_{BB} = 4.5\,\text{nm}$ in the 10 nm NFO HtStr and $3 \cdot \lambda_{BB} = 9\,\text{nm}$ in the LMSO HtStr at $U = -1\,\text{V}$. The band bending study of the LSMO film suggest a not flat band case for the LSMO film, but rather nearly linear electronic bands with positive slope. Furthermore, it has been been shown that due to the strong band bending the band bending model partially breaks down. However, the overall shape can still be recreated. In conclusion, the in-operando HAXPES measurements enable us to track the voltage dependent band bending and the extraction of the band bending region and strength.

Outlook

This outlook will point out some of the open questions and new suggestions for future research particular on the NFO/STO oxide heterostructure system.

Many results of this thesis suggest a high influence and dependency of the defect types and defects density at the NFO thin film's physical properties. However, a full picture on the defect types and their respective defect density is still missing. The direct experimental way to identify and get an estimation of the defect density is by observation of the defects and simply counting them. This can be done via the high-angle annular dark field transmission electron microscopy measurements that result in two-dimensional images of the atomic grid.

As discussed in subsection 6.3.3, the band alignment of the conduction band minimum via Kraut's method can be deduced from the valence band offset and the material specific band gap. Literature research gave varying theoretical results for the ideal NFO band gap. However, a full series of experimentally determined NFO band gaps in the vicinity of defects and film thickness reduction has not been reported yet. Thus the investigation of NFO film thickness dependent band gaps via angle-resolved photoemission spectra measurement technique should be a future goal.

Another main result of this thesis is that the titanium cations of the STO near to the NFO/STO interface have partially a valency of 3+ instead of the 4+ for bulk STO. Furthermore, the Ti XMCD measurement yielded a non-vanishing magnetic signal that mimics the NFO magnetic field dependency. A next step towards spinoxide-electronics would be to grow NFO thin films on undoped STO and check the interface by Hall measurements for a conducting state, i.e. a pseudo two-dimensional electron or hole gas. In case a conducting state exists, there is the possibility of spin polarization, i.e. magnetic ordering of the conducting state and further studies on this topic should be conducted.

Appendix A

Nb:SrTiO$_3$ substrate treatment

The following procedure as been taken over from literature [146, 76, 147] and has been optimized in constant evaluation of the AFM morphology and in constant exchange with the group members of the *PGI-7*. The etching procedure has been performed at a wet etch bank of the clean room of the *PGI-7* to ensure human safety during the etching process and to ensure optimal clean surfaces of the substrates after the etching procedure. NFO and LSMO have been grown on 0.1%Nb:STO and 0.5%Nb:STO. The substrate treatment solely differs in the etching time.

1. 3 minutes in acetone in a supersonic bath adjusted to the lowest level

2. 3 minutes in isopropanol in a supersonic bath adjusted to the lowest level

3. blowing the samples dry with nitrogen after the isopropanol bath

4. 3 minutes in deionised water in a supersonic bath adjusted to the lowest level

5. blowing the samples dry with nitrogen after the water bath

6. etching each sample 0.1%Nb:STO (0.5%Nb:STO) for 90 seconds (30 seconds) in buffered hydrofluoric acid

7. rinsing the samples in deionised water

8. blowing the samples dry wit nitrogen after the deionised water bath

9. 3 minutes in acetone in a supersonic bath adjusted to the lowest level

10. 3 minutes in isopropanol in a supersonic bath adjusted to the lowest level

11. blowing the samples dry with nitrogen after the isopropanol bath

12. annealing the samples at 950 °C, at normal atmosphere for 2.5 hours with a temperature ramp of 1.5 hours

Appendix B

Background Subtraction and Normalisation Of The SQUID Hysteresis Loops

The SQUID measurements measure the magnetic signal of the entire heterostructure in the not volume normalised unit emu. In the case of the NFO/STO heterostructure this results in an open hysteresis loop of the NFO and an overplayed diamagnetic contribution of the STO like shown in figure B.2 with the blue data. First step is the normalisation of the raw data to the volume of the NFO film. Therefore it is necessary to determine the film thickness. XRR measurements can provide this information. In figure B.1, a XRR measurement of a thick NFO/STO heterostructure is shown in red. The thickness is determined by simulating the XRR signal. In figure B.1 a by the *X'Pert Reflectivity* software simulated XRR signal is shown. XRR simulation matches the XRR measurement. The resulting thickness 23 nm. The in-plane size of the NFO/STO heterostructure is given by the size of the STO substrate which are provided by *Crystec GmbH* with a standard size of 5 mm x 5 mm. Thus, the magnetic signal can be normalised to the volume changing the unit from emu to μ_B/f.u.. The formula for the normalisation is displayed in equation B.1 with $A[mm^2]$ the in-plane area of the heterostructure in mm², $d[nm]$ the thickness of the film in nm, f the number of the chemical formula units per unit cell, $V[\text{Å}^3]$ the volume of the unit cell in Å and $m[emu]$ the magnetic signal in emu.

$$m[\mu_B/\text{f.u.}] = \frac{m[\text{emu}] \cdot V[\text{Å}^3] \cdot 1.078282309 \cdot 10^5}{f \cdot d[\text{nm}] \cdot A[\text{mm}^2]} \tag{B.1}$$

In the next step, the diamagnetic magnetic response of the STO has to be determined and subtracted of the measurement. Therefore the magnetic signal is fitted with a line at magnetic field of $B > \pm 30$ kOe at which the diamagnetic signal is dominant. Then a line through the origin is subtracted with a mean slope of the fitted lines of the positive and negative magnetic field regions. The origin line in red and the resulting corrected NFO signal in pink are shown in figure B.2.
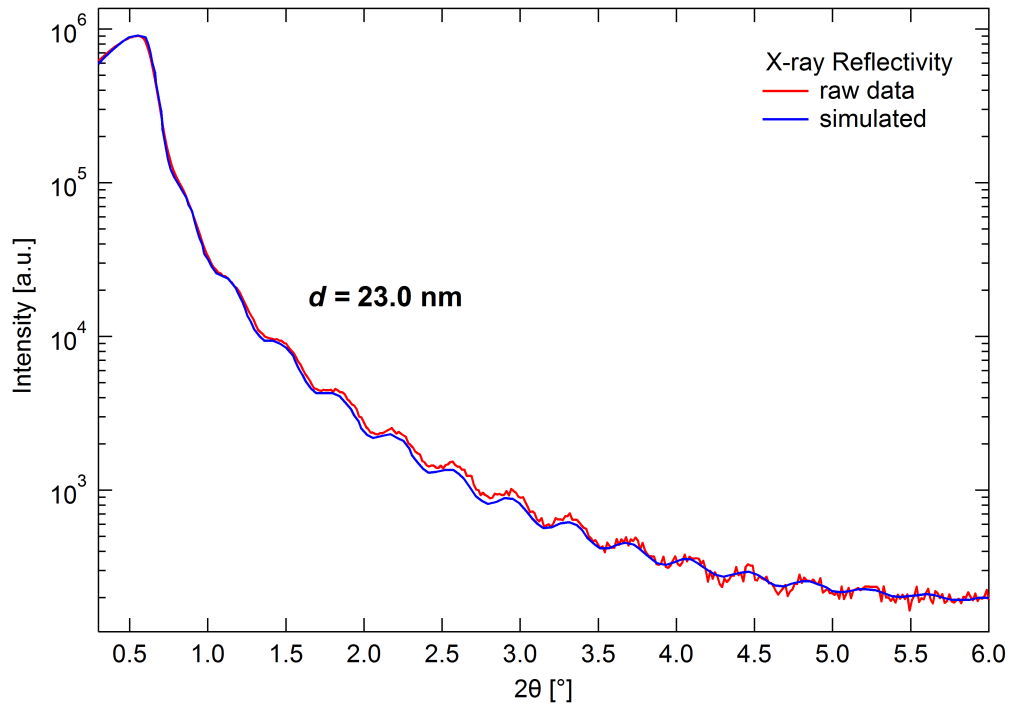
Figure B.1: In red a XRR measurement of a 23 nm NFO/STO heterostructure is shown. In blue the *X'Pert* simulation of the heterostructure is displayed.
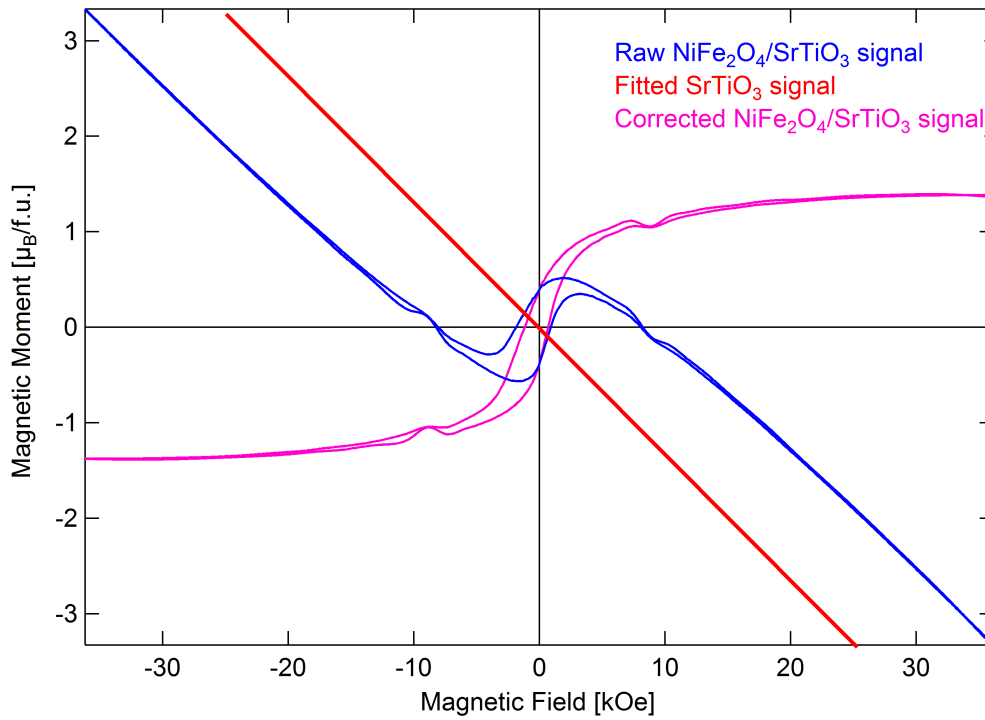
Figure B.2: SQUID magnetic hysteresis at $T = 6\,\mathrm{K}$ of a raw NFO/STO heterostructure (blue), a fitted STO signal (red) and a corrected NFO/STO signal (pink).

Appendix C

XAS Background Fitting by Unifit 2016

The XAS background calculation used in chapter 5.1 has been performed with the Unifit 2016 software and its build-in XAS background fit. The fit function implemented is taken from [148] and is a step function mixed with an arctan function. The fit function used in this thesis and the resulting parameters will be shortly sketched and the formulas are taken from the Unifit manual 2016 [149].

The XAS background fit function shown in equation C.1 is a superposition of a constant background a and a sum over step and Arctangent functions. The step function B''' displayed in equation C.2 consists of two parts one error function and one Arctangent function. Thus it is ensured that long slopes at the edges can be modelled correctly by enhancing the influence of the Arctangent function. The mixing ratio of these two functions is giving by M_{vs} and the height of the step is implemented with h_s.

$$B(E) = a + \sum_{\text{steps}} B'''_{\text{step}}(E) \tag{C.1}$$

$$B'''(E) = \frac{h_s}{2} + h_s \cdot \left(\frac{1}{2} \cdot (1 - M_{vs}) \cdot erf(E) + M_{vs} \cdot \frac{1}{\pi} \cdot arctan(E) \right) \tag{C.2}$$

In order to evaluated the error function refeq:error for the fitting process the error function is tailored for different energy regions at the position E_{erf}. Shown in equation C.4 is E_{erf} which is the energy position E_{step} of the step normalised to the $FWHM$ of the step given by $2\beta_{step}$ assuming the approximation $1.2 \approx ln(\sqrt{4\pi})$.

$$erf = \frac{2}{\pi} \cdot \int_0^E e^{-\tau^2} d\tau \tag{C.3}$$

$$E_{erf} = \frac{E_{step}}{1.2\beta_{step}} \tag{C.4}$$

The tailored error functions used in the software are displayed in equations C.5 to C.7.

$$erf \approx \frac{2}{\sqrt{\pi}} \cdot \left(E_{erf} - \frac{E_{erf}^3}{3} + \frac{E_{erf}^5}{10} - \frac{E_{erf}^7}{42} \right) \qquad 0 < E_{erf} < 1 \qquad (C.5)$$

$$erf \approx 1 - \frac{e^{-E_{erf}^2}}{\sqrt{\pi} \left(E_{erf} + \cfrac{1}{2E_{erf} + \cfrac{2}{E_{erf} + \cfrac{3}{2E_{erf}}}} \right)} \qquad E_{erf} \geq 1 \qquad (C.6)$$

$$erf(E) = -erf(-E) \qquad E_{erf} \leq 0 \qquad (C.7)$$

The Arctangent function is calculated at the energy position of the step function normalised to the width (see equation C.8).

$$arctan(E) = arctan\left(\frac{E - E_{step}}{\beta_{step}} \right) \qquad (C.8)$$

C.1   Fitting the Fe^{3+} XAS L edge

The fit results of XAS background of the Fe L edge are shown in table C.1. The fit parameter a is due to normalisation of the unpolarised XAS zero.

Table C.1: Fe L Edge Background Fit

Step	Position E_{step} [eV]	Height h_s [eV]	FWHM $\approx 2\beta_{step}$ [eV]	Erf-Arc mixing M_{vs}
L_3	709.2	0.66	2	0.5
L_2	722.0	0.34	2	0.5
Post edge	735.5	0.34	5	0.5

C.2   Fitting the Ni^{2+} XAS L edge

The fit results of XAS background of the Ni L edge are shown in table C.2. The fit parameter a is due to normalisation of the unpolarised XAS zero.

Table C.2: Ni L Edge Background Fit

Step	Position E_{step} [eV]	Height h_s [eV]	FWHM $\approx 2\beta_{step}$ [eV]	Erf-Arc mixing M_{vs}
L_3	854.0	0.32	2	0.5
Inter Edge	867.2	0.49	2.2	0.75
L_2	871.8	0.20	2	0.5
Post edge	886.0	0.46	4	0.5

Appendix D

Titanium XAS Preprocessing

In figure D.1**(a)** the titanium L edge raw data measured at $T = 10\,\mathrm{K}$ with $B = \pm1\,\mathrm{T}$ are displayed. 32 XAS for each polarization at each magnetic field have been recorded in a measurement sequence of pnnp with n referring to negative/left polarized light and p referring to positive/right polarized light. For both magnetization directions the time evolution yields an increased of the background offset until it saturates. However, the signal to background ratio is not affected by the increasing background offset which means that beam damage could not be observed. Thus, the 32 XAS were added to each other and divided by 32.

The averaged absorption spectra are displayed in figure D.1**b)**. The left and right circular polarized XAS have a linear energy dependent offset to each other. In order to correct the background difference the XAS will be aligned with respect to each other, i.e. the right circular polarized XAS will be background corrected by the left circular polarized light. First, the right cp XAS is divided by the left cp XAS. This pre-step is shown in pink in figure D.1**b)**. Then a line is fitted to the ratio from the lowest energy position possible to the highest energy position which is indicated by the green arrows. Then the right cp XAS will be divided by this background line. Thus, the two cp XAS will be aligned with respect to each other. The resulting circular polarized XAS are shown in figure D.1**c)**.
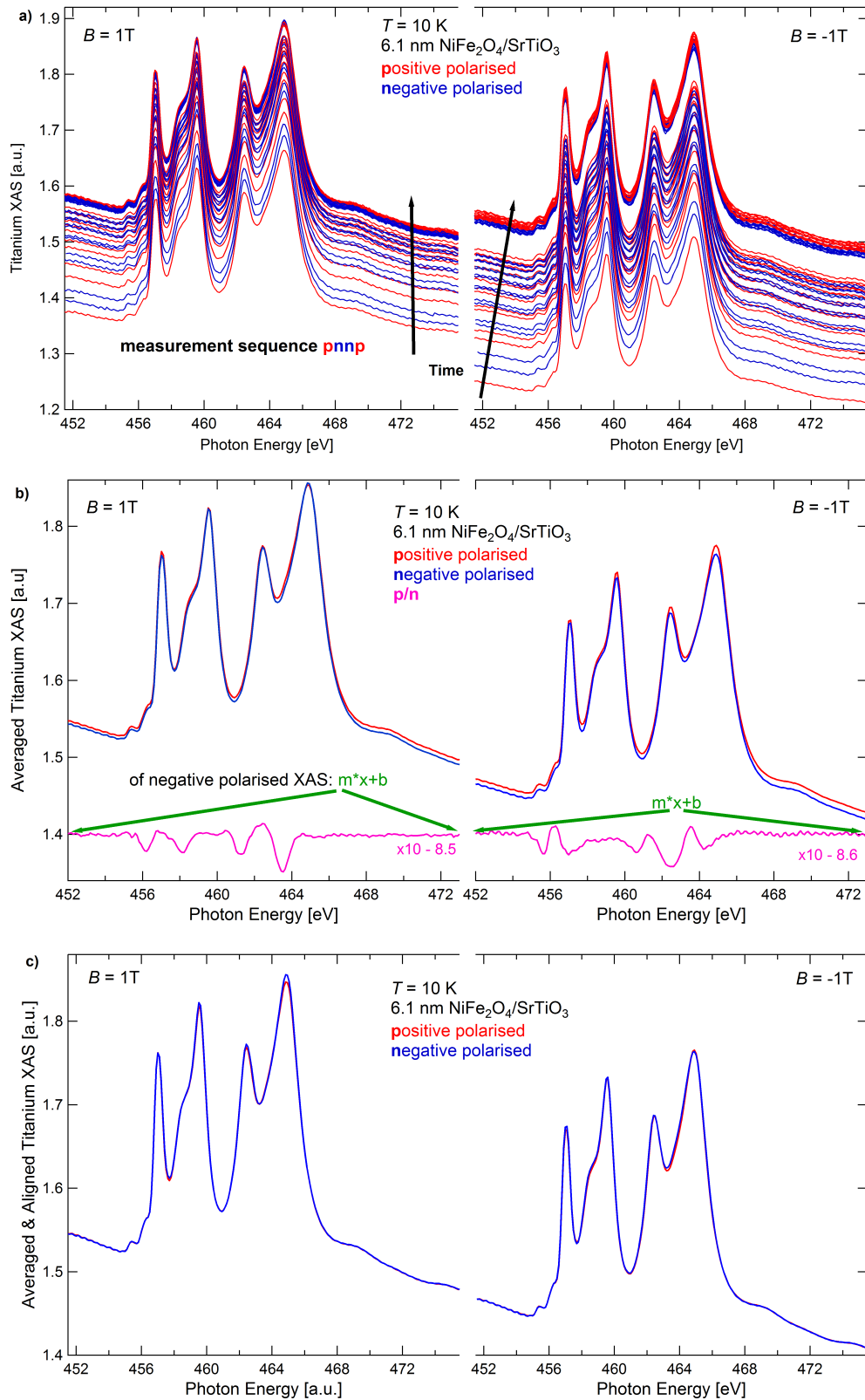
Figure D.1: (a) Left(blue) and right(red) circular polarized Titanium L edge XAS raw data measured at $T = 10\,\text{K}$ for a 6.1 nm $\text{NiFe}_2\text{O}_4/\text{SrTiO}_3$ for Left $B = 1\,\text{T}$ and right $B = -1\,\text{T}$. **(b)** Averaged XAS spectra from the raw data. In green dashed lines the background line of the negative polarised XAS is marked. **(c)** The negative averaged Titanium XAS and the positive averaged Titanium XAS which is normalised to the background line of the negative polarised XAS are shown.

Appendix E

Background Correction Of The Fe 2p & Mn 2p In-Operando HAXPES Core Level

E.1 Background Correction of the Fe 2p

The HAXPES measurement of the Fe 2p core level of the Au(4 nm)/NFO(2 nm/ 10 nm)/0.5 %Nb:STO heterostructure is always flanked by the Au 4s and the Au $4p_{1/2}$ core levels. Therefore the background of the Fe 2p core level is strongly affected by the Au core levels. In figure E.1 a) a HAXPES survey with the Au core level and a Fe 2p detail scan of Au(4 nm)/NFO(10 nm)/ 0.5 %Nb:STO heterostructure is displayed. In order to remove the Au background the survey is fitted. Three different fitting routines were tested to fit the region between the pre-edge of the Fe 2p to the Au 4s flank: First a single line, second a logarithmic and line combination and third a Lorentz and line
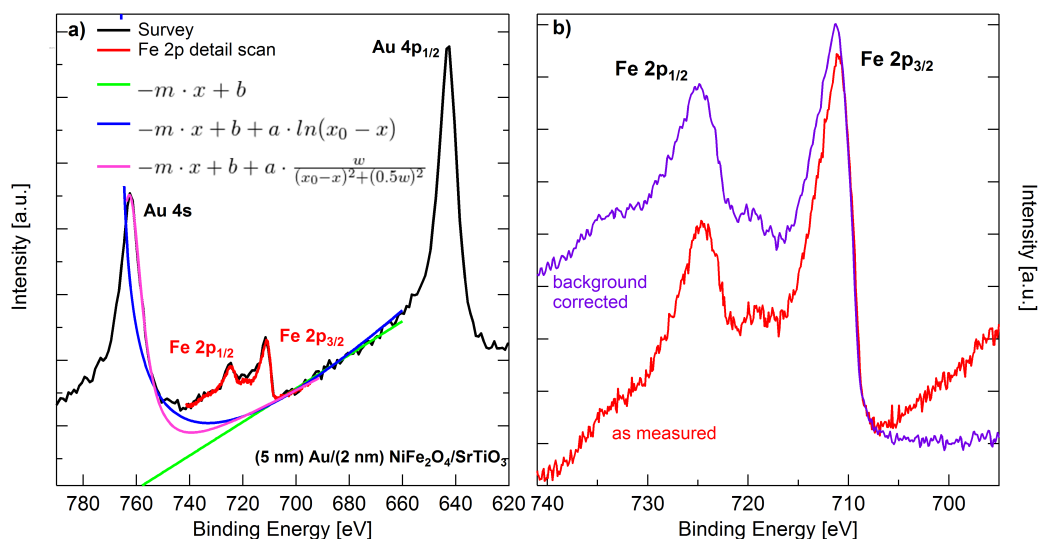
Figure E.1: a) HAXPES survey in black and Fe 2p core level in red of a Au(4 nm) /NFO(10 nm)/0.5 %Nb:STO heterostructure. A line fit in green, a line and logarithmic function fit in blue and a line and Lorentz function fit in pink of the Fe 2p background are displayed. **b)** Fe 2p detail spectra as measured in red and background corrected in violet.

combination. All three results of the fitting routine are displayed in figure E.1 a). The line fit fits well in the pre-edge of the Fe 2p, however it fails the post-edge region. The logarithmic and line function combination underestimates the influence of the Au 4s flank and thus is also not suitable. The line and lorenz function combination fits the best. In figure E.1 b) the as measured and by the line and Lorentz function fitted background corrected Fe 2p core level are shown. The background corrected Fe 2p core level fits the Fe 2p core level discussed in section 4.2.1.

E.2   Background Correction of the Mn 2p

The HAXPES measurement of the Mn 2p core level of the Pt(4 nm)/LSMO (6 u.c.)/0.5 %Nb:STO heterostructure is flanked by the Pt 4s and the Pt $4p_{1/2}$ core levels. Therefore the background of the Mn 2p core level is strongly affected by the Pt core levels. In figure E.2 **a)**, the Mn 2p HAXPES spectrum as measured is shown in blue as well as the survey of the heterostructure in black. The Mn 2p peak is flanked by the Pt 4s and Pt $4p_{1/2}$ core level. Therefore the Mn 2p core level is strongly affected by those two core level. In order to remove the background caused by the overlaying platinum film a reference 40 nm platinum film of the binding energy region was recorded. At the exact position of the Mn 2p core level the platinum HAXPES spectrum has a satellite. Thus, the background can not be assumed to be linear for background removal. The background is modelled by utilizing the platinum reference spectrum. The platinum reference spectrum is fitted in the region around the Pt 4s peak as the Pt 4s peak and its flanks are not influenced by the
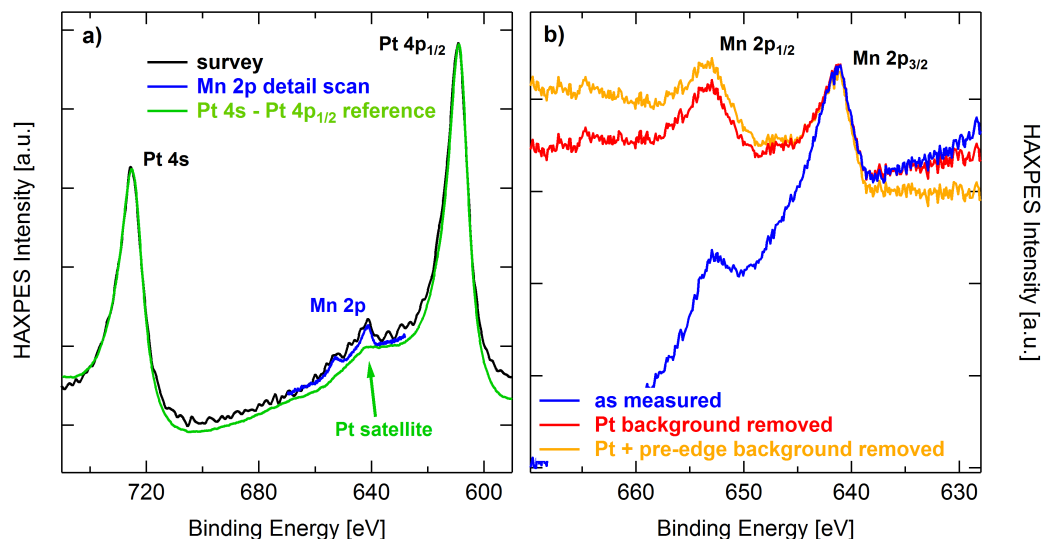
Figure E.2: a) HAXPES survey in black and Mn 2p core level in blue of a Pt(4 nm)/ LSMO(6 u.c.)/0.5 %Nb:STO heterostructure. A Pt reference spectra was fitted to the Pt 4s core level shown in green. **b)** Mn 2p detail spectra as measured in blue, Pt background corrected Mn 2p in orange and Pt + pre-edge corrected Mn 2p spectrum in red.

Mn 2p core level. After the fitting procedure the adapted platinum reference spectrum is subtracted from the as measured Mn 2p spectrum. In figure E.2 **b)** as measured and the Pt background corrected Mn 2p spectra are displayed in blue and red. However, the pre-edge of the corrected Mn 2p spectrum has still a linear behaviour. Therefore in a second step the Pt corrected Mn 2p pre-edge is fitted by a line and the line is subtracted from the Mn 2p core level spectrum. The result is shown in E.2 **b)** in orange.

Appendix F

Core Level Position Determination

In chapter 6 and 7 the HAXPES core level have to be determined in order extract the valence band offset at the metal-oxide and the oxide-oxide interface with Kraut's model. Here one example for the Au/(10 nm)NFO/STO and one for the Pt/(6 u.c.)LSMO/STO heterostructure is presented.

F.1 Au/NFO/STO Heterostructure
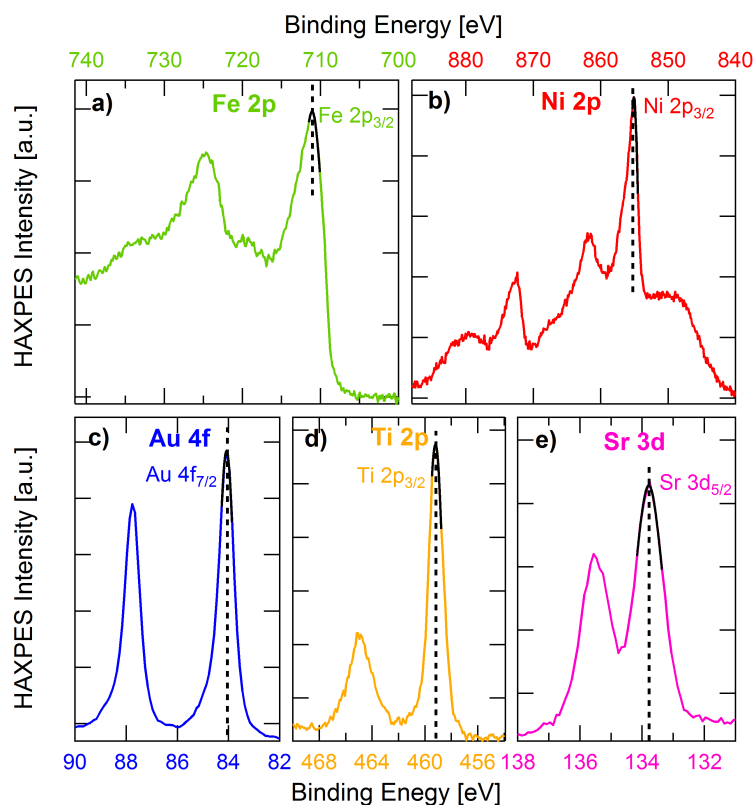
Figure F.1: Core level position determination of the HAXPES core level of the Au/(10 nm)NFO/STO heterostructure without biasing. Core level were fitted with a Gauss function in the region of the peak of interest. **a)** Background corrected Fe 2p core level, **b)** Ni 2p core level, **c)** Au 4f core level, **d)** Ti 2p core level and **e)** Sr 3d core level.

For the Au/(10 nm)NFO/STO heterostructure the core level positions of interest are Fe $2p_{3_2}$, Ni $2p_{3/2}$, Au $4f_{7/2}$, Ti $2p_{3_2}$ and Sr $3d_{5/2}$. The core level of interest were fitted with a Gauss function in the region around the intensity maximum. In figure F.1 the fits of the core level are shown in black and the core level positions are marked with a black dashed line.

F.2 Pt/LSMO/STO Heterostructure
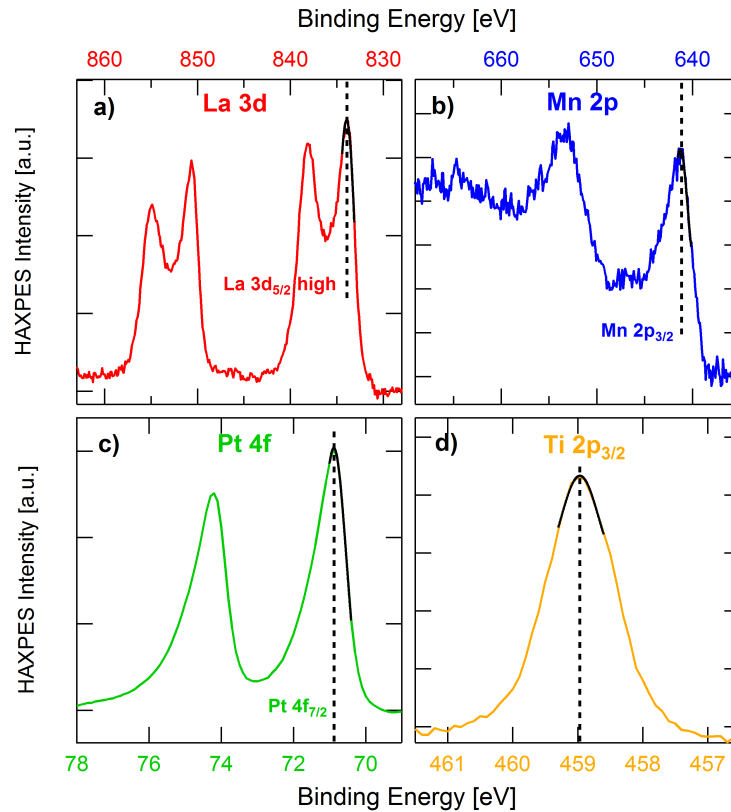
Figure F.2: Core level position determination of the HAXPES core level of the Pt/(6 u.c.)LSMO/STO heterostructure without biasing. Core level were fitted with a Gauss function in the region of the peak of interest.**a)** Linear background corrected La 3d core level, **b)** Background corrected Mn 2p core level, **c)** Pt 4f core level and **d)** Ti $2p_{3/2}$ core level.

For the Pt/(6 u.c.)LSMO/STO heterostructure the core level positions of interest are La $3d_{5_2}$ at lower binding energy but with higher intensity, the Mn $2p_{3/2}$, Pt $4f_{7/2}$ and Ti $2p_{3/2}$. The core level of interest were fitted with a Gauss function in the region around the intensity maximum. In figure F.2 the fits of the core level are shown in black and the core level positions are marked with a black dashed line.

Bibliography

[1] Mai Hussein Hamed et al. "Tunable Magnetic Phases at Fe_3O_4/$SrTiO_3$ Oxide Interfaces". In: *ACS Applied Materials & Interfaces* 11.7 (Feb. 20, 2019), pp. 7576–7583. ISSN: 1944-8244. DOI: `10.1021/acsami.8b20625`.

[2] Patrick Lömker. "Interfacing Eu0 in confined oxide and metal heterostructures". In: *Schriften des Forschungszentrums Jülich / Reihe Schlüsseltechnologien;174* (2018). In collab. with Technische Universität Dortmund and Technische Universität Dortmund. DOI: `10.17877/DE290 R-19124`.

[3] Daniele Ielmini and Rainer Waser, eds. *Resistive Switching: From Fundamentals of Nanoionic Redox Processes to Memristive Device Applications*. Weinheim, Germany: Wiley-VCH Verlag GmbH & Co. KGaA, June 22, 2016. ISBN: 978-3-527-68087-0 978-3-527-33417-9. DOI: `10.1002/97835 27680870`.

[4] Rainer Waser. *Nanoelectronics and Information Technology*. Wiley-VCH, May 6, 2012. ISBN: 978-3-527-40927-3.

[5] A. Ohtomo and H. Y. Hwang. "A high-mobility electron gas at the $LaAlO_3$/$SrTiO_3$ heterointerface". In: *Nature* 427.6973 (Jan. 2004), 423 -426. ISSN: 0028-0836, 1476-4687. DOI: `10.1038/nature02308`.

[6] C. L. Prajapat et al. "Proximity effects across oxide-interfaces of superconductor -insulator- ferromagnet hybrid heterostructure". In: *Scientific Reports* 8.1 (Dec. 2018). ISSN: 2045-2322. DOI: `10.1038/s41598-01 8-22036-y`.

[7] S. Crossley et al. "All-oxide ferromagnetic resonance and spin pumping with $SrIrO_3$". In: *Phys. Rev. B* 100 (11 Sept. 2019), p. 115163. DOI: `1 0.1103/PhysRevB.100.115163`.

[8] Felix Gunkel and Rainer Waser. "The role of defects at functional interfaces between polar and non-polar perovskite oxides". PhD thesis. Publikationsserver der RWTH Aachen University, 2013. DOI: `4765`.

[9] Felix Gunkel et al. "Mobility Modulation and Suppression of Defect Formation in Two-Dimensional Electron Systems by Charge-Transfer Management". In: *ACS Applied Materials & Interfaces* 9.12 (Mar. 29, 2017), pp. 10888–10896. ISSN: 1944-8244, 1944-8252. DOI: `10.1021/a csami.7b00905`.

[10]   M. Minnekaev et al. "Structural, ferroelectric, electronic and transport properties of $BaTiO_3$/Pt heterostructures grown on MgO(001)". In: *Microelectronic Engineering*. Insulating Films on Semiconductors 2013 109 (Sept. 2013), pp. 227–231. ISSN: 0167-9317. DOI: 10.1016/j.mee.2013.03.077.

[11]   A. Zenkevich et al. "Electronic and electrical properties of functional interfaces studied by hard X-ray photoemission". In: *Journal of Electron Spectroscopy and Related Phenomena* 190 (Oct. 2013), pp. 302–308. ISSN: 03682048. DOI: 10.1016/j.elspec.2013.08.003.

[12]   J. Chakhalian et al. "Magnetism at the interface between ferromagnetic and superconducting oxides". In: *Nature Physics* 2.4 (Apr. 2006), pp. 244–248. ISSN: 1745-2473. DOI: 10.1038/nphys272.

[13]   Nuala M. Caffrey et al. "Spin - filtering efficiency of ferrimagnetic spinels $CoFe_2O_4$ and $NiFe_2O_4$". In: *Physical Review B* 87.2 (Jan. 25, 2013). ISSN: 1098-0121, 1550-235X. DOI: 10.1103/PhysRevB.87.024419.

[14]   Hiroyuki Mori and Hiroshi Ishiwara. "Epitaxial Growth of $SrTiO_3$ Films on Si(100) Substrates Using a Focused Electron Beam Evaporation Method". In: *Japanese Journal of Applied Physics* 30 (Part 2, No. 8A Aug. 1, 1991), pp. L1415–L1417. ISSN: 0021-4922. DOI: 10.1143/JJAP.30.L1415.

[15]   Bum Ki Moon and Hiroshi Ishiwara. "Roles of Buffer Layers in Epitaxial Growth of **$SrTiO_3$** Films on Silicon Substrates". In: *Japanese Journal of Applied Physics* 33 (Part 1, No. 3A Mar. 15, 1994), pp. 1472–1477. ISSN: 0021-4922, 1347-4065. DOI: 10.1143/JJAP.33.1472.

[16]   Michael Hoppe. *Magnetic, structural, and electronic properties of $NiFe_2O_4$ ultrathin films*. In collab. with Universität Duisburg-Essen. Schriften des Forschungszentrums Jülich Reihe Schlüsseltechnologien Band 118. Jülich: Forschungszentrum Jülich, 2016. 118 pp. ISBN: 978-3-95806-122-4.

[17]   Michael Hoppe et al. "Enhanced ferrimagnetism in auxetic $NiFe_2O_4$ in the crossover to the ultrathin-film limit". In: *Phys. Rev. B* 91 (5 2015), p. 054418. DOI: 10.1103/PhysRevB.91.054418.

[18]   H Perron et al. "Structural investigation and electronic properties of the nickel ferrite $NiFe_2O_4$: a periodic density functional theory approach". In: *Journal of Physics: Condensed Matter* 19.34 (Aug. 29, 2007), p. 346219. ISSN: 0953-8984, 1361-648X. DOI: 10.1088/0953-8984/19/34/346219.

[19]   Sam Jin Kim et al. "Moessbauer studies of superexchange interactions in $NiFe_2O_4$". In: *Journal of the Korean physical society* 36.6 (2000), pp. 430–434. ISSN: ISSN 0374-4884.

[20]   N.W. Ashcroft and N.D. Mermin. *Solid State Physics*. Cengage Learning, 2011. ISBN: 978-81-315-0052-1.

[21] K. Dileep et al. "Probing optical band gaps at the nanoscale in $NiFe_2O_4$ and $CoFe_2O_4$ epitaxial films by high resolution electron energy loss spectroscopy". In: *Journal of Applied Physics* 116.10 (Sept. 14, 2014), p. 103505. ISSN: 0021-8979, 1089-7550. DOI: 10.1063/1.4895059.

[22] Z. Szotek et al. "Electronic structures of normal and inverse spinel ferrites from first principles". In: *Physical Review B* 74.17 (Nov. 28, 2006), p. 174431. DOI: 10.1103/PhysRevB.74.174431.

[23] A. Hammouche, E. Siebert, and A. Hammou. "Crystallographic, thermal and electrochemical properties of the system $La_{1-x}Sr_xMnO_3$ for high temperature solid electrolyte fuel cells". In: *Materials Research Bulletin* 24.3 (Mar. 1989), pp. 367–380. ISSN: 00255408. DOI: 10.1016/0025-5408(89)90223-7.

[24] M Viret et al. "Spin polarised tunnelling as a probe of half metallic ferromagnetism in mixed-valence manganites". In: *Journal of Magnetism and Magnetic Materials* 198-199 (June 1999), pp. 1–5. ISSN: 03048853. DOI: 10.1016/S0304-8853(98)00589-7.

[25] J.-H. Park et al. "Direct evidence for a half-metallic ferromagnet". In: *Nature* 392.6678 (Apr. 1998), pp. 794–796. ISSN: 0028-0836, 1476-4687. DOI: 10.1038/33883.

[26] Clarence Zener. "Interaction between the d -Shells in the Transition Metals. II. Ferromagnetic Compounds of Manganese with Perovskite Structure". In: *Physical Review* 82.3 (May 1, 1951), pp. 403–405. ISSN: 0031-899X. DOI: 10.1103/PhysRev.82.403.

[27] A. Urushibara et al. "Insulator-metal transition and giant magnetoresistance in $La_{1-x}Sr_xMnO_3$". In: *Physical Review B* 51.20 (May 15, 1995), pp. 14103–14109. ISSN: 0163-1829, 1095-3795. DOI: 10.1103/PhysRevB.51.14103.

[28] M. Huijben et al. "Critical thickness and orbital ordering in ultrathin $La_{0.7}Sr_{0.3}MnO_3$ films". In: *Physical Review B* 78.9 (Sept. 16, 2008). ISSN: 1098-0121, 1550-235X. DOI: 10.1103/PhysRevB.78.094413.

[29] K. van Benthem, C. Elsässer, and R. H. French. "Bulk electronic structure of $SrTiO_3$: Experiment and theory". In: *Journal of Applied Physics* 90.12 (Dec. 15, 2001), pp. 6156–6164. ISSN: 0021-8979, 1089-7550. DOI: 10.1063/1.1415766.

[30] Roger A. De Souza et al. "Behavior of oxygen vacancies in single-crystal $SrTiO_3$: Equilibrium distribution and diffusion kinetics". In: *Physical Review B* 85.17 (May 24, 2012). ISSN: 1098-0121, 1550-235X. DOI: 10.1103/PhysRevB.85.174109.

[31] J. Karczewski et al. "Electrical and structural properties of Nb-doped $SrTiO_3$ ceramics". In: *Journal of Electroceramics* 24.4 (June 2010), pp. 326–330. ISSN: 1385-3449, 1573-8663. DOI: 10.1007/s10832-009-9578-7.

[32] Alarich Weiss. "John B. Goodenough: Magnetism and the Chemical Bond. Interscience Publishers. New York, London 1963. 393 Seiten, 89 Abbildungen. Preis: DM 95 s." In: *Berichte der Bunsengesellschaft für physikalische Chemie* 68.10 (Dec. 1964), pp. 996–996. ISSN: 00059021. DOI: 10.1002/bbpc.19640681015.

[33] Junjiro Kanamori. In: *Journal of Physics and Chemistry of Solids* 10.2 (July 1959), pp. 87–98. ISSN: 00223697. DOI: 10.1016/0022-3697(59)90061-7.

[34] Philip W. Anderson. "Theory of Magnetic Exchange Interactions: Exchange in Insulators and Semiconductors". In: *Solid State Physics*. Vol. 14. Elsevier, 1963, pp. 99–214. ISBN: 978-0-12-607714-8. DOI: 10.1016/S0081-1947(08)60260-X.

[35] R. Gross and A. Marx. *Festkörperphysik*. Oldenbourg Wissenschaftsverlag, 2012. ISBN: 978-3-486-71294-0.

[36] H. Hertz. "Ueber einen Einfluss des ultravioletten Lichtes auf die electrische Entladung". In: *Annalen der Physik und Chemie* 267.8 (1887), pp. 983–1000. ISSN: 00033804, 15213889. DOI: 10.1002/andp.18872670827.

[37] A. Einstein. "Über einen die Erzeugung und Verwandlung des Lichtes betreffenden heuristischen Gesichtspunkt". In: *Annalen der Physik* 322.6 (1905), pp. 132–148. ISSN: 00033804, 15213889. DOI: 10.1002/andp.19053220607.

[38] C. Berglund and W. Spicer. "Photoemission Studies of Copper and Silver: Experiment". In: *Physical Review* 136.4 (Nov. 16, 1964), A1044–A1064. DOI: 10.1103/PhysRev.136.A1044.

[39] Stefan Hüfner. *Photoelectron spectroscopy: principles and applications ; with 28 tables*. OCLC: 248558676. Berlin: Springer, 2003. ISBN: 978-3-540-41802-3 978-3-642-07520-9.

[40] S. Tanuma, C. J. Powell, and D. R. Penn. "Calculations of electron inelastic mean free paths". In: *Surface and Interface Analysis* 37.1 (2005), pp. 1–14. ISSN: 1096-9918. DOI: 10.1002/sia.1997.

[41] A. Jablonski and C. J. Powell. "Information depth and the mean escape depth in Auger electron spectroscopy and x-ray photoelectron spectroscopy". In: *Journal of Vacuum Science & Technology A* 21.1 (Jan. 1, 2003), pp. 274–283. ISSN: 0734-2101, 1520-8559. DOI: 10.1116/1.1538370.

[42] A. Jablonski, I. S. Tilinin, and C. J. Powell. "Mean escape depth of signal photoelectrons from amorphous and polycrystalline solids". In: *Physical Review B* 54.15 (Oct. 15, 1996), pp. 10927–10937. DOI: 10.1103/PhysRevB.54.10927.

[43] Joseph C. Woicik, ed. *Hard x-ray photoelectron spectroscopy (HAXPES)*. Springer series in surface sciences volume 59. OCLC: 944194755. Cham Heidelberg New York Dordrecht London: Springer, 2016. 571 pp. ISBN: 978-3-319-24041-1 978-3-319-79572-0 978-3-319-24043-5.

[44] E. A. Kraut et al. "Precise Determination of the Valence-Band Edge in X-Ray Photoemission Spectra: Application to Measurement of Semiconductor Interface Potentials". In: *Physical Review Letters* 44.24 (June 16, 1980), pp. 1620–1623. ISSN: 0031-9007. DOI: `10.1103/PhysRevLett.44.1620`.

[45] L. Qiao et al. "Cation mixing, band offsets and electric fields at $LaAlO_3$ / $SrTiO_3$(001) heterojunctions with variable La:Al atom ratio". In: *Surface Science* 605.15 (Aug. 2011), pp. 1381–1387. ISSN: 00396028. DOI: `10.1016/j.susc.2011.04.035`.

[46] R Claessen et al. "Hard x-ray photoelectron spectroscopy of oxide hybrid and heterostructures: a new method for the study of buried interfaces". In: *New Journal of Physics* 11.12 (Dec. 11, 2009), p. 125007. ISSN: 1367-2630. DOI: `10.1088/1367-2630/11/12/125007`.

[47] P. Schütz et al. "Band bending and alignment at the spinel/perovskite γ-Al_2O_3 / $SrTiO_3$ heterointerface". In: *Physical Review B* 91.16 (Apr. 10, 2015). ISSN: 1098-0121, 1550-235X. DOI: `10.1103/PhysRevB.91.165118`.

[48] C. Cohen-Tannoudji, B. Diu, and F. Laloë. *Quantenmechanik*. Quantenmechanik Bd. 2. Walter de Gruyter, 2010. ISBN: 978-3-11-022460-3.

[49] C. Cohen-Tannoudji, B. Diu, and F. Laloë. *Quantenmechanik*. de Gruyter, 2009. ISBN: 978-3-11-021519-9.

[50] Joachim Stöhr and Hans Christoph Siegmann. *Magnetism: From Fundamentals to Nanoscale Dynamics*. Springer Series in Solid-State Sciences. Berlin Heidelberg: Springer-Verlag, 2006. ISBN: 978-3-540-30282-7.

[51] R.M. White and D.J. Friedman. "Theory of the magnetic proximity effect". In: *Journal of Magnetism and Magnetic Materials* 49.1 (Mar. 1985), pp. 117–123. ISSN: 03048853. DOI: `10.1016/0304-8853(85)90109-X`.

[52] C. L. Jia et al. "Oxygen octahedron reconstruction in the $LaAlO_3$/$SrTiO_3$ heterointerfaces investigated using aberration-corrected ultrahigh -resolution transmission electron microscopy". In: *Physical Review B* 79.8 (Feb. 12, 2009). ISSN: 1098-0121, 1550-235X. DOI: `10.1103/PhysRevB.79.081405`.

[53] Claudia Cantoni et al. "Electron Transfer and Ionic Displacements at the Origin of the 2D Electron Gas at the LAO/STO Interface: Direct Measurements with Atomic-Column Spatial Resolution". In: *Advanced Materials* 24.29 (2012), pp. 3952–3957. DOI: `10.1002/adma.201200667`.

[54] M. Salluzzo et al. "Origin of Interface Magnetism in $BiMnO_3$ / $SrTiO_3$ and $LaAlO_3$ / $SrTiO_3$ Heterostructures". In: *Physical Review Letters* 111.8 (Aug. 22, 2013). ISSN: 0031-9007, 1079-7114. DOI: `10.1103/PhysRevLett.111.087204`.

[55] S. Y. Huang et al. "Transport Magnetic Proximity Effects in Platinum". In: *Physical Review Letters* 109.10 (Sept. 7, 2012). ISSN: 0031-9007, 1079-7114. DOI: `10.1103/PhysRevLett.109.107204`.

[56] S. H. Nie et al. "Ferromagnetic Interfacial Interaction and the Proximity Effect in a Co_2FeAl / (Ga,Mn) As Bilayer". In: *Physical Review Letters* 111.2 (July 9, 2013). ISSN: 0031-9007, 1079-7114. DOI: `10.1103/PhysRevLett.111.027203`.

[57] Kristy J. Kormondy et al. "Large positive linear magnetoresistance in the two-dimensional t2g electron gas at the $EuO/SrTiO_3$ interface". In: *Scientific Reports* 8.1 (Dec. 2018). ISSN: 2045-2322. DOI: `10.1038/s41598-018-26017-z`.

[58] Douglas B. Chrisey and Graham K. Hubler. *Pulsed Laser Deposition of Thin Films*. Google-Books-ID: 0Oh_QgAACAAJ. Wiley, June 21, 1994. 648 pp. ISBN: 978-0-471-59218-1.

[59] *Electron-beam physical vapor deposition*. en. Page Version ID: 810393269. Nov. 2017.

[60] *Arrow NCR*. URL: `https://afmprobes.asylumresearch.com/arrow-ncr.html` (visited on 03/25/2019).

[61] Dieter Meschede. *Gerthsen Physik*. 2004.

[62] Z. Boekelheide and C. L. Dennis. "Artifacts in magnetic measurements of fluid samples". In: *AIP Advances* 6.8 (Aug. 2016), p. 085201. ISSN: 2158-3226. DOI: `10.1063/1.4960457`.

[63] F. Schaefers, M. Mertin, and M. Gorgoi. "KMC-1: A high resolution and high flux soft x-ray beamline at BESSY". In: *Review of Scientific Instruments* 78.12 (Dec. 2007), p. 123102. ISSN: 0034-6748, 1089-7623. DOI: `10.1063/1.2808334`.

[64] M. Gorgoi et al. "The high kinetic energy photoelectron spectroscopy facility at BESSY progress and first results". In: *Nuclear Instruments and Methods in Physics Research Section A: Accelerators, Spectrometers, Detectors and Associated Equipment* 601.1 (Mar. 2009), pp. 48–53. ISSN: 01689002. DOI: `10.1016/j.nima.2008.12.244`.

[65] *High Field Magnet - Magnetic Materials - Diamond Light Source*. URL: `https://www.diamond.ac.uk/Instruments/Magnetic-Materials/I10/magnet.html` (visited on 08/06/2019).

[66] O. H. Seeck et al. "The high-resolution diffraction beamline P08 at PETRA III". In: *Journal of Synchrotron Radiation* 19.1 (Jan. 1, 2012), pp. 30–38. ISSN: 0909-0495. DOI: `10.1107/S0909049511047236`.

[67] C. Schlueter et al. "The new dedicated HAXPES beamline P22 at PETRAIII". In: Proceedings of the 13th international conference on synchrotron radiation instrumantation – SRI2018. Taipei, Taiwan, 2019, p. 040010. DOI: `10.1063/1.5084611`.

[68] *P22 Hard X-ray Photoelectron Spectroscopy*. URL: `http://photon-science.desy.de/facilities/petra_iii/beamlines/p22_haxpes/index_eng.html` (visited on 08/06/2019).

[69] *Agilent B2961A/B2962A6.5 Digit Low Noise Power Source*. URL: https://www.alliedelec.com/m/d/35bb9646022d69a230d38b8553a1d7c3.pdf (visited on 08/12/2019).

[70] F. Rigato et al. "Strain-induced stabilization of new magnetic spinel structures in epitaxial oxide heterostructures". In: *Materials Science and Engineering: B* 144.1 (Nov. 2007), pp. 43–48. ISSN: 09215107. DOI: 10.1016/j.mseb.2007.07.102.

[71] S. Venzke et al. "Epitaxial growth and magnetic behavior of $NiFe_2O_4$ thin films". In: *Journal of Materials Research* 11.5 (May 1996), pp. 1187–1198. ISSN: 0884-2914, 2044-5326. DOI: 10.1557/JMR.1996.0153.

[72] M. Hoppe et al. "Wide-Range Structural and Chemical Stability of the Magnetic Oxide $NiFe_2O_4$ Grown by O_2-Assisted Pulsed Laser Deposition". In: *IEEE Transactions on Magnetics* 50.11 (Nov. 2014), pp. 1–4. ISSN: 0018-9464. DOI: 10.1109/TMAG.2014.2322378.

[73] Koichiro Iwahori et al. "Effect of water adsorption on microscopic friction force on $SrTiO_3$(001)". In: *Journal of Applied Physics* 93.6 (Mar. 15, 2003), pp. 3223–3227. ISSN: 0021-8979, 1089-7550. DOI: 10.1063/1.1540223.

[74] Hannes Guhl, Wolfram Miller, and Karsten Reuter. "Water adsorption and dissociation on $SrTiO_3$ (001) revisited: A density functional theory study". In: *Physical Review B* 81.15 (Apr. 28, 2010). ISSN: 1098-0121, 1550-235X. DOI: 10.1103/PhysRevB.81.155455.

[75] Xu Wang. "Atomic force microscopy studies of $SrTiO_3$ (001) substrates treated by chemical etching and annealing in oxygen". In: *Science in China Series G* 48.4 (2005), p. 459. ISSN: 1672-1799. DOI: 10.1360/04yw0181.

[76] A. Biswas et al. "Universal Ti-rich termination of atomically flat $SrTiO_3$ (001), (110), and (111) surfaces". In: *Applied Physics Letters* 98.5 (Jan. 31, 2011), p. 051904. ISSN: 0003-6951, 1077-3118. DOI: 10.1063/1.3549860.

[77] A. Hamie et al. "Investigation of high quality magnetite thin films grown on $SrTiO_3$(001) substrates by pulsed laser deposition". In: *Thin Solid Films* 525 (Dec. 2012), pp. 115–120. ISSN: 00406090. DOI: 10.1016/j.tsf.2012.10.076.

[78] G. Z. Liu, Q. Y. Lei, and X. X. Xi. "Stoichiometry of $SrTiO_3$ films grown by pulsed laser deposition". In: *Applied Physics Letters* 100.20 (May 14, 2012), p. 202902. ISSN: 0003-6951, 1077-3118. DOI: 10.1063/1.4717984.

[79] Y. Suzuki et al. "Magnetic properties of epitaxial ferrite multilayer films". In: *Journal of Applied Physics* 79.8 (1996), p. 5923. ISSN: 00218979. DOI: 10.1063/1.361844.

[80] Ulrike Lüders et al. "Enhanced magnetic moment and conductive be-
      havior in $NiFe_2O_4$ spinel ultrathin films". In: *Physical Review B* 71.13
      (Apr. 25, 2005). ISSN: 1098-0121, 1550-235X. DOI: `10.1103/PhysRevB.7`
      `1.134419`.

[81] Kuldeep Chand Verma et al. "Structural, microstructural and mag-
      netic properties of $NiFe_2O_4$, $CoFe_2O_4$ and $MnFe_2O_4$ nanoferrite thin
      films". In: *Journal of Magnetism and Magnetic Materials* 323.24 (Dec.
      2011), pp. 3271–3275. ISSN: 03048853. DOI: `10.1016/j.jmmm.2011`
      `.07.029`.

[82] Christof W Schneider and Thomas Lippert. *Laser Ablation and Thin
      Film Deposition*. 2019. URL: `https://www.psi.ch/sites/default/fi`
      `les/import/lmx-interfaces/BooksEN/christof-book.pdf` (visited
      on 06/17/2019).

[83] G. K. Pálsson, A. R. Rennie, and B. Hjörvarsson. "Examination of the
      reliability of x-ray techniques for determining hydrogen-induced vol-
      ume changes". In: *Physical Review B* 78.10 (Sept. 29, 2008). ISSN: 1098-
      0121, 1550-235X. DOI: `10.1103/PhysRevB.78.104118`.

[84] Rik Groenen et al. "Research Update: Stoichiometry controlled oxide
      thin film growth by pulsed laser deposition". In: *APL Materials* 3.7
      (July 2015), p. 070701. ISSN: 2166-532X. DOI: `10.1063/1.4926933`.

[85] A. K. Kunti et al. "Oxygen partial pressure induced effects on the
      microstructure and the luminescence properties of pulsed laser de-
      posited TiO_2 thin films". In: *AIP Advances* 7.1 (Jan. 2017), p. 015021.
      ISSN: 2158-3226. DOI: `10.1063/1.4973721`.

[86] Yeong Jae Shin et al. "Oxygen Partial Pressure during Pulsed Laser
      Deposition: Deterministic Role on Thermodynamic Stability of Atomic
      Termination Sequence at $SrRuO_3$ /$BaTiO_3$ Interface". In: *ACS Applied
      Materials & Interfaces* 9.32 (Aug. 16, 2017), pp. 27305–27312. ISSN: 1944-
      8244, 1944-8252. DOI: `10.1021/acsami.7b07813`.

[87] T. Fujii et al. "*In situ* XPS analysis of various iron oxide films grown
      by NO 2 -assisted molecular-beam epitaxy". In: *Physical Review B* 59.4
      (Jan. 15, 1999), pp. 3195–3202. ISSN: 0163-1829, 1095-3795. DOI: `10.11`
      `03/PhysRevB.59.3195`.

[88] Toru Yamashita and Peter Hayes. "Analysis of XPS spectra of Fe^{2+}
      and Fe^{3+} ions in oxide materials". In: *Applied Surface Science* 254.8
      (Feb. 2008), pp. 2441–2449. ISSN: 01694332. DOI: `10.1016/j.apsusc.2`
      `007.09.063`.

[89] G. Hassnain Jaffari et al. "Influence of oxygen vacancies on the elec-
      tronic structure and magnetic properties of $NiFe_2O_4$ thin films". In:
      Journal of Applied Physics 111.9 (May 2012), p. 093906. ISSN: 0021-8979,
      1089-7550. DOI: `10.1063/1.4704690`.

[90] O. Karis et al. "High-kinetic-energy photoemission spectroscopy of Ni at 1s : 6-eV satellite at 4 eV". In: *Physical Review B* 78.23 (Dec. 30, 2008), p. 233105. ISSN: 1098-0121, 1550-235X. DOI: `10.1103/PhysRevB.78.23 3105`.

[91] Carolin Schmitz-Antoniak et al. "Reversed ageing of Fe_3O_4 nanoparticles by hydrogen plasma". In: *Scientific Reports* 6.1 (Aug. 2016). ISSN: 2045-2322. DOI: `10.1038/srep20897`.

[92] C. Klewe et al. "Physical characteristics and cation distribution of $NiFe_2O_4$ thin films with high resistivity prepared by reactive co-sputtering". In: *Journal of Applied Physics* 115.12 (Mar. 28, 2014). ISSN: 0021-8979, 1089-7550. DOI: `10.1063/1.4869400`.

[93] Brett Leedahl et al. "Tunability of room - temperature ferromagnetism in spintronic semiconductors through nonmagnetic atoms". In: *Physical Review B* 96.4 (July 10, 2017), p. 045202. ISSN: 2469-9950, 2469-9969. DOI: `10.1103/PhysRevB.96.045202`.

[94] Hidekazu Ikeno. "First-principles analysis of X-ray magnetic circular dichroism for transition metal complex oxides". In: *Journal of Applied Physics* 120.14 (Oct. 14, 2016), p. 142104. ISSN: 0021-8979, 1089-7550. DOI: `10.1063/1.4961713`.

[95] R J O Mossanek et al. "Effects of Ni vacancies and crystallite size on the O 1s and Ni 2p x-ray absorption spectra of nanocrystalline NiO". In: *Journal of Physics: Condensed Matter* 25.49 (Dec. 11, 2013), p. 495506. ISSN: 0953-8984, 1361-648X. DOI: `10.1088/0953-8984/25/49/495506`.

[96] G. van der Laan et al. "Orbital polarization in $NiFe_2O_4$ measured by Ni-2p X-ray magnetic circular dichroism". In: *Physical Review B* 59.6 (Feb. 1, 1999), pp. 4314–4321. ISSN: 0163-1829, 1095-3795. DOI: `10.110 3/PhysRevB.59.4314`.

[97] B. T. Thole et al. "X-ray circular dichroism as a probe of orbital magnetization". In: *Physical Review Letters* 68.12 (Mar. 23, 1992), pp. 1943–1946. ISSN: 0031-9007. DOI: `10.1103/PhysRevLett.68.1943`.

[98] Paolo Carra et al. "X-ray circular dichroism and local magnetic fields". In: *Physical Review Letters* 70.5 (Feb. 1, 1993), pp. 694–697. ISSN: 0031-9007. DOI: `10.1103/PhysRevLett.70.694`.

[99] C. T. Chen et al. "Experimental Confirmation of the X-Ray Magnetic Circular Dichroism Sum Rules for Iron and Cobalt". In: *Physical Review Letters* 75.1 (July 3, 1995), pp. 152–155. ISSN: 0031-9007, 1079-7114. DOI: `10.1103/PhysRevLett.75.152`.

[100] Ruqian Wu, Dingsheng Wang, and A. J. Freeman. "First principles investigation of the validity and range of applicability of the x-ray magnetic circular dichroism sum rule". In: *Physical Review Letters* 71.21 (Nov. 22, 1993), pp. 3581–3584. ISSN: 0031-9007. DOI: `10.1103/Phys RevLett.71.3581`.

[101] Cinthia Piamonteze, Piter Miedema, and Frank M. F. de Groot. "Accuracy of the spin sum rule in XMCD for the transition-metal L edges from manganese to copper". In: *Physical Review B* 80.18 (Nov. 10, 2009). ISSN: 1098-0121, 1550-235X. DOI: `10.1103/PhysRevB.80.184410`.

[102] E. Goering *. "X-ray magnetic circular dichroism sum rule correction for the light transition metals". In: *Philosophical Magazine* 85.25 (Sept. 2005), pp. 2895–2911. ISSN: 1478-6435, 1478-6443. DOI: `10.1080/14786 430500155221`.

[103] G. van der Laan et al. "Comparison of x-ray absorption with x-ray photoemission of nickel dihalides and NiO". In: *Physical Review B* 33.6 (Mar. 15, 1986), pp. 4253–4263. ISSN: 0163-1829. DOI: `10.1103/PhysRe vB.33.4253`.

[104] D. Ahlers, K. Attenkofer, and G. Schütz. "Spin-dependent extended x-ray absorption fine structure in magnetic oxides". In: *Journal of Applied Physics* 83.11 (June 1998), pp. 7085–7087. ISSN: 0021-8979, 1089-7550. DOI: `10.1063/1.367854`.

[105] E Goering et al. "Vanishing Fe 3d orbital moments in single-crystalline magnetite". In: *Europhysics Letters (EPL)* 73.1 (Jan. 2006), pp. 97–103. ISSN: 0295-5075, 1286-4854. DOI: `10.1209/epl/i2005-10359-8`.

[106] Markus Meinert and Günter Reiss. "Electronic structure and optical band gap determination of $NiFe_2O_4$". In: *Journal of Physics: Condensed Matter* 26.11 (Mar. 19, 2014), p. 115503. ISSN: 0953-8984, 1361-648X. DOI: `10.1088/0953-8984/26/11/115503`.

[107] D. J. Huang et al. "Spin and Orbital Magnetic Moments of Fe_3O_4". In: *Physical Review Letters* 93.7 (Aug. 2004). ISSN: 0031-9007, 1079-7114. DOI: `10.1103/PhysRevLett.93.077204`.

[108] Gagan Dixit et al. "Structural and magnetic behaviour of $NiFe_2O_4$ thin film grown by pulsed laser deposition". In: *APPL PHYS* 48 (2010), p. 5.

[109] M. Abbate et al. "Probing depth of soft x-ray absorption spectroscopy measured in total-electron-yield mode". In: *Surface and Interface Analysis* 18.1 (Jan. 1992), pp. 65–69. ISSN: 0142-2421, 1096-9918. DOI: `10.10 02/sia.740180111`.

[110] Bradley H Frazer et al. "The probing depth of total electron yield in the sub-keV range: TEY-XAS and X-PEEM". In: *Surface Science* 537.1 (July 2003), pp. 161–167. ISSN: 00396028. DOI: `10.1016/S0039-6028(0 3)00613-7`.

[111] Ho Nyung Lee et al. "Growth control of oxygen stoichiometry in homoepitaxial $SrTiO_3$ films by pulsed laser epitaxy in high vacuum". In: *Scientific Reports* 6.1 (Apr. 2016). ISSN: 2045-2322. DOI: `10.1038/srep1 9941`.

[112] P. Catrou et al. "Effect of oxygen vacancies at the $Fe/SrTiO_3$ (001) interface: Schottky barrier and surface electron accumulation layer". In: *Physical Review B* 98.11 (Sept. 4, 2018). ISSN: 2469-9950, 2469-9969. DOI: `10.1103/PhysRevB.98.115402`.

[113] Alexey Kalabukhov et al. "Effect of oxygen vacancies in the $SrTiO_3$ substrate on the electrical properties of the $LaAlO_3$ $SrTiO_3$ interface". In: *Physical Review B* 75.12 (Mar. 19, 2007), p. 121404. DOI: `10.1103/PhysRevB.75.121404`.

[114] J.-S. Lee et al. "Titanium d_{xy} ferromagnetism at the $LaAlO_3/SrTiO_3$ interface". In: *Nature Materials* 12.8 (Aug. 2013), pp. 703–706. ISSN: 1476-1122, 1476-4660. DOI: `10.1038/nmat3674`.

[115] F. M. F. de Groot et al. "$L_{2,3}$ x-ray-absorption edges of d_0 compounds: K^+, Ca^{2+}, Sc^{3+}, and Ti^{4+} in O_h (octahedral) symmetry". In: *Physical Review B* 41.2 (Jan. 15, 1990), pp. 928–937. ISSN: 0163-1829, 1095-3795. DOI: `10.1103/PhysRevB.41.928`.

[116] Peter Krüger. "Multichannel multiple scattering calculation of $L_{2,3}$ - edge spectra of TiO_2 and $SrTiO_3$: Importance of multiplet coupling and band structure". In: *Physical Review B* 81.12 (Mar. 24, 2010). ISSN: 1098-0121, 1550-235X. DOI: `10.1103/PhysRevB.81.125121`.

[117] Patrick Lömker et al. "Two-dimensional electron system at the magnetically tunable EuO / $SrTiO_3$ interface". In: *Physical Review Materials* 1.6 (Nov. 14, 2017). ISSN: 2475-9953. DOI: `10.1103/PhysRevMaterials.1.062001`.

[118] E. McCafferty and J. P. Wightman. "Determination of the concentration of surface hydroxyl groups on metal oxide films by a quantitative XPS method". In: *Surface and Interface Analysis* 26.8 (July 1, 1998), pp. 549–564. ISSN: 1096-9918. DOI: `10.1002/(SICI)1096-9918(199807)26:8<549::AID-SIA396>3.0.CO;2-Q`.

[119] D. J. Miller, M. C. Biesinger, and N. S. McIntyre. "Interactions of CO_2 and CO at fractional atmosphere pressures with iron and iron oxide surfaces: one possible mechanism for surface contamination?" In: *Surface and Interface Analysis* 33.4 (Apr. 2002), pp. 299–305. ISSN: 0142-2421, 1096-9918. DOI: `10.1002/sia.1188`.

[120] T. A. W. Beale et al. "RASOR: An advanced instrument for soft x-ray reflectivity and diffraction". In: *Review of Scientific Instruments* 81.7 (July 2010), p. 073904. ISSN: 0034-6748, 1089-7623. DOI: `10.1063/1.3458004`.

[121] *Handbook of Magnetic Materials*. Elsevier, 1995, pp. 189–324. ISBN: 978-0444822321.

[122] E. A. Kraut et al. "Semiconductor core-level to valence-band maximum binding-energy differences: Precise determination by x-ray photoelectron spectroscopy". In: *Physical Review B* 28.4 (Aug. 15, 1983), pp. 1965–1977. ISSN: 0163-1829. DOI: `10.1103/PhysRevB.28.1965`.

[123] Haibo Fan et al. "Band alignment of TiO_2 /FTO interface determined by X-ray photoelectron spectroscopy: Effect of annealing". In: *AIP Advances* 6.1 (Jan. 2016), p. 015314. ISSN: 2158-3226. DOI: `10.1063/1.4941040`.

[124] Shanshan Chen et al. "X-ray photoelectron spectroscopy study of energy - band alignments of ZnO on buffer layer Lu_2O_3". In: *Physics Letters A* 380.7 (Feb. 2016), pp. 970–972. ISSN: 03759601. DOI: `10.1016/j.physleta.2015.12.038`.

[125] C. Lenser et al. "Band alignment at memristive metal-oxide interfaces investigated by hard x-ray photoemission spectroscopy". In: *Physical Review B* 90.11 (Sept. 26, 2014). ISSN: 1098-0121, 1550-235X. DOI: `10.1103/PhysRevB.90.115312`.

[126] Thomas Bertaud et al. "*In-operando* and non-destructive analysis of the resistive switching in the Ti/HfO_2 /TiN-based system by hard x-ray photoelectron spectroscopy". In: *Applied Physics Letters* 101.14 (Oct. 2012), p. 143501. ISSN: 0003-6951, 1077-3118. DOI: `10.1063/1.4756897`.

[127] Yury Matveyev et al. "Effect of Polarization Reversal in Ferroelectric $TiN/Hf_{0.5}Zr_{0.5}O_2$ /TiN Devices on Electronic Conditions at Interfaces Studied in Operando by Hard X-ray Photoemission Spectroscopy". In: *ACS Applied Materials & Interfaces* 9.49 (Dec. 13, 2017), pp. 43370–43376. ISSN: 1944-8244, 1944-8252. DOI: `10.1021/acsami.7b14369`.

[128] J. E. Rault et al. "Interface electronic structure in a metal/ferroelectric heterostructure under applied bias". In: *Physical Review B* 87.15 (Apr. 26, 2013). ISSN: 1098-0121, 1550-235X. DOI: `10.1103/PhysRevB.87.155146`.

[129] L. F. Kourkoutis et al. "Microscopic origins for stabilizing room - temperature ferromagnetism in ultrathin manganite layers". In: *Proceedings of the National Academy of Sciences* 107.26 (June 29, 2010), pp. 11682–11685. ISSN: 0027-8424, 1091-6490. DOI: `10.1073/pnas.1005693107`.

[130] Felix Gunkel et al. "Ordering and Phase Control in Epitaxial Double-Perovskite Catalysts for the Oxygen Evolution Reaction". In: *ACS Catalysis* 7.10 (Oct. 6, 2017), pp. 7029–7037. ISSN: 2155-5435, 2155-5435. DOI: `10.1021/acscatal.7b02036`.

[131] J. C. Woicik et al. "Hybridization and Bond-Orbital Components in Site-Specific X-Ray Photoelectron Spectra of Rutile TiO_2". In: *Physical Review Letters* 89.7 (July 26, 2002). ISSN: 0031-9007, 1079-7114. DOI: `10.1103/PhysRevLett.89.077401`.

[132] Anna Kossoy et al. "Optical and Structural Properties of Ultra-thin Gold Films". In: *Advanced Optical Materials* 3.1 (Jan. 2015), pp. 71–77. ISSN: 21951071. DOI: `10.1002/adom.201400345`.

[133] D. J. DiMaria and J. H. Stathis. "Explanation for the oxide thickness dependence of breakdown characteristics of metal -oxide -semiconductor structures". In: *Applied Physics Letters* 70.20 (May 19, 1997), pp. 2708–2710. ISSN: 0003-6951, 1077-3118. DOI: `10.1063/1.118999`.

[134] J.H. Stathis. "Physical and predictive models of ultrathin oxide reliability in CMOS devices and circuits". In: *IEEE Transactions on Device and Materials Reliability* 1.1 (Mar. 2001), pp. 43–59. ISSN: 1530-4388, 1558-2574. DOI: 10.1109/7298.946459.

[135] Hannes Klumbies et al. "Thickness dependent barrier performance of permeation barriers made from atomic layer deposited alumina for organic devices". In: *Organic Electronics* 17 (Feb. 2015), pp. 138–143. ISSN: 15661199. DOI: 10.1016/j.orgel.2014.12.003.

[136] Fu-Chien Chiu. "A Review on Conduction Mechanisms in Dielectric Films". In: *Advances in Materials Science and Engineering* 2014 (2014), pp. 1–18. ISSN: 1687-8434, 1687-8442. DOI: 10.1155/2014/578168.

[137] A.R. Chourasia and D.R. Chopra. "X-ray photoelectron study of TiN/ SiO_2 and TiN/Si interfaces". In: *Thin Solid Films* 266.2 (Oct. 1995), pp. 298–301. ISSN: 00406090. DOI: 10.1016/0040-6090(95)06651-9.

[138] Sherena G. Johnson. *NIST Standard Reference Database 100*. NIST. Aug. 26, 2010. URL: https://www.nist.gov/srd/nist-standard-reference-database-100 (visited on 11/09/2019).

[139] Lide Yao, Sampo Inkinen, and Sebastiaan van Dijken. "Direct observation of oxygen vacancy-driven structural and resistive phase transitions in $La_{2/3}Sr_{1/3}MnO_3$". In: *Nature Communications* 8.1 (Apr. 2017). ISSN: 2041-1723. DOI: 10.1038/ncomms14544.

[140] Marek Wilhelm et al. "Photoemission electron microscopy of magneto-ionic effects in $La_{0.7}Sr_{0.3}MnO_3$". In: *APL Materials* 8.11 (Nov. 1, 2020), p. 111102. ISSN: 2166-532X. DOI: 10.1063/5.0022150.

[141] C. Schlueter et al. "Evidence of electronic band redistribution in $La_{0.65}Sr_{0.35}MnO_{3-d}$ by hard x-ray photoelectron spectroscopy". In: *Physical Review B* 86.15 (Oct. 1, 2012). ISSN: 1098-0121, 1550-235X. DOI: 10.1103/PhysRevB.86.155102.

[142] T. Hishida et al. "Empirical relationship between x-ray photoemission spectra and electrical conductivity in a colossal magnetoresistive manganite $La_{1-x}Sr_xMnO_3$". In: *Journal of Applied Physics* 113.23 (June 21, 2013), p. 233702. ISSN: 0021-8979, 1089-7550. DOI: 10.1063/1.4811372.

[143] Hyo Jin K. Kim et al. "Electrical Properties of Ultrathin Platinum Films by Plasma-Enhanced Atomic Layer Deposition". In: *ACS Applied Materials & Interfaces* 11.9 (Mar. 6, 2019), pp. 9594–9599. ISSN: 1944-8244, 1944-8252. DOI: 10.1021/acsami.8b21054.

[144] M. Wilhelm. "Evolution of magnetic and electronic properties at critical thicknesses of $LaSrMnO_3$ films". MA thesis. University Düsseldorf, 2017.

[145] S Majumdar et al. "Analysis of electronic structure and its effect on magnetic properties in (001) and (110) oriented $La_{0.7}Sr_{0.3}MnO_3$ thin films". In: *Journal of Physics: Condensed Matter* 25.37 (Sept. 18, 2013), p. 376003. ISSN: 0953-8984, 1361-648X. DOI: `10.1088/0953-8984/25/37/376003`.

[146] J. G. Connell et al. "Preparation of atomically flat $SrTiO_3$ surfaces using a deionized-water leaching and thermal annealing procedure". In: *Applied Physics Letters* 101.25 (Dec. 17, 2012), p. 251607. ISSN: 0003-6951, 1077-3118. DOI: `10.1063/1.4773052`.

[147] Florian Gellé et al. "Guideline to atomically flat TiO_2-terminated $SrTiO_3$ (001) surfaces". In: *Surface Science* 677 (Nov. 2018), pp. 39–45. ISSN: 00396028. DOI: `10.1016/j.susc.2018.06.001`.

[148] D. A. Outka et al. "The orientation of Langmuir–Blodgett monolayers using NEXAFS". In: *The Journal of Chemical Physics* 88.6 (Mar. 15, 1988), pp. 4076–4087. ISSN: 0021-9606, 1089-7690. DOI: `10.1063/1.453862`.

[149] Ronald Hesse. *Unifit for Windows - Spectrum processing, Analysis and Presentation Software for XPS and XAS Version 2016*. Oct. 3, 2015. URL: `http://www.unifit-software.de/PDF/Manual-unifit2016.pdf` (visited on 03/06/2019).

Acknowledgements

Zum Schluss: Es gibt einen Menschen, der nichts lieber auf dieser Welt erlebt hätte als mich promovieren zu sehen und der leider nicht das Glück hat, dies miterleben zu dürfen. Liebe Mama, danke für dein Vertrauen in mich und meine Fähigkeiten, danke, dass du mir die Freiheit gegeben hast meinen schulischen und beruflichen Werdegang selbst zu gestalten und selbst dafür Verantwortung zu übernehmen. Ich danke dir, dass du nie an mir gezweifelt hast und mir damit das Selbstbewusstsein gegeben hast, um das mich viele Menschen beneiden. Ich wünschte, du könntest das hier noch lesen.